

8-2017

VOLUMETRIC, MAGNETIC RESONANCE-VISIBLE, AND RADIATION-SENSITIVE DETECTORS FOR MAGNETIC RESONANCE IMAGE-GUIDED RADIATION THERAPY

Hannah J. Lee

Follow this and additional works at: https://digitalcommons.library.tmc.edu/utgsbs_dissertations

 Part of the [Biological and Chemical Physics Commons](#), and the [Medical Biophysics Commons](#)

Recommended Citation

Lee, Hannah J., "VOLUMETRIC, MAGNETIC RESONANCE-VISIBLE, AND RADIATION-SENSITIVE DETECTORS FOR MAGNETIC RESONANCE IMAGE-GUIDED RADIATION THERAPY" (2017). *The University of Texas MD Anderson Cancer Center UTHealth Graduate School of Biomedical Sciences Dissertations and Theses (Open Access)*. 803.

https://digitalcommons.library.tmc.edu/utgsbs_dissertations/803

This Dissertation (PhD) is brought to you for free and open access by the The University of Texas MD Anderson Cancer Center UTHealth Graduate School of Biomedical Sciences at DigitalCommons@TMC. It has been accepted for inclusion in The University of Texas MD Anderson Cancer Center UTHealth Graduate School of Biomedical Sciences Dissertations and Theses (Open Access) by an authorized administrator of DigitalCommons@TMC. For more information, please contact digitalcommons@library.tmc.edu.

VOLUMETRIC, MAGNETIC RESONANCE-VISIBLE, AND RADIATION-SENSITIVE
DETECTORS FOR MAGNETIC RESONANCE IMAGE-GUIDED RADIATION THERAPY

by

Hannah Jungeun Lee

APPROVED:

Geoffrey S. Ibbott, Ph.D.
Advisory Professor

Laurence E. Court, Ph.D.

Brian P. Hobbs, Ph.D.

Gabriel O. Sawakuchi, Ph.D.

Keila E. Torres, M.D., Ph.D.

Jihong Wang, Ph.D.

APPROVED:

Dean, The University of Texas
MD Anderson Cancer Center UTHHealth Graduate School of Biomedical Sciences

VOLUMETRIC, MAGNETIC RESONANCE-VISIBLE, AND RADIATION-SENSITIVE
DETECTORS FOR MAGNETIC RESONANCE IMAGE-GUIDED RADIATION THERAPY

A

DISSERTATION

Presented to the Faculty of
The University of Texas
MD Anderson Cancer Center UTHealth
Graduate School of Biomedical Sciences

in Partial Fulfillment
of the Requirements
for the Degree of

DOCTOR OF PHILOSOPHY

by

Hannah Jungeun Lee
Houston, Texas

August, 2017

Dedication

To my family and boyfriend

For always believing in me and loving me

To my friends

For getting through it together

To Binky and Dolly

For always being there for me

Acknowledgements

This dissertation work would not have been possible with any other advisor than Dr. Geoffrey S. Ibbott. He was always patient and never told me “no, don’t try that”. If it weren’t for him, I never would have been able to try out ideas that others told me weren’t worth trying, leading to new discoveries! He always found optimism in any situation and introduced me to the world, literally, of medical physics and 3D dosimetry. I will always be grateful to him for allowing me to pursue my dreams, always having my back, and putting up with my stubbornness.

I would like to thank all of the current, old, and new members of the Ibbott lab: “DMOS Mom” Ryan Grant Lafratta, Gye Won (Diane) Choi, Yvonne Roed, Mitchell Carroll, Mamdooh Alqathami, Slade Klawikowski, and all of the many summer and rotating students we have had. I wouldn’t have been able to get through this without such a supportive lab group as ours. I’d also like to thank other current and old members of the department and division that have helped me in the last five years: Daniel O’Brien, Ashley Rubinstein, Kelly Tharp, Francois Therriault-Proulx, Stephanie Lampe, Nina Garcia, Lawrence Bronk, Yelin Suh, Eun Young Han, Peter Park, Zhifei Wen, Michelle Mathis, and so many others. I’d like to thank my committee members, Laurence Court, Brian Hobbs, Gabriel Sawakuchi, Keila Torres, and Jihong Wang, for always giving me a chance to step back from my work and view it from another perspective.

I will be forever grateful for having the opportunity to work on the MR-Linac and all of the people who came with it, especially Gary Bosco and Mo Kadbi for giving me their time and help whenever I needed it. I really owe you guys a beer or two or three! I am also thankful for all of the support from these people: James Dolan, Stefan Pencea, Sneha Cloake, Greg Smith, Ray Thomas, Max Thibodeau, and others from Elekta and Philips. The MR-Linac couldn’t have come with a better team to work with!

Lastly, I would like to thank my friends and family for their support and love over the last five years. My classmate Xenia Fave has been through all of the ups and downs of graduate school with me, and I hope we continue our gchat sessions throughout our careers! My lab mates have really become a second family in Houston to me. Thank you for being there with me for the stressful and fun parts of being a wet lab! My sanity would not have survived without the limitless love and support of my parents, brother, boyfriend, and “kids” Binky and Dolly. Thank you for never giving up on me, pushing me to my best, and always taking care of me. I apologize for the days and nights that I have physically been there but “not there” because of my work, and I hope that I can always be there for you in the same way you have for me!

Thank you all for making these last five years fly by and a time to remember!

VOLUMETRIC, MAGNETIC RESONANCE-VISIBLE, AND RADIATION-SENSITIVE
DETECTORS FOR MAGNETIC RESONANCE IMAGE-GUIDED RADIATION THERAPY

Hannah Jungeun Lee

Advisory Professor: Geoffrey S. Ibbott, Ph.D.

Due to the superior soft-tissue contrast of magnetic resonance imaging (MRI) compared to conventional computed tomography (CT) and other on-board imaging techniques, several groups have integrated MRI and radiation treatment machine systems. The advent of MR image-guided radiation therapy (MR-IGRT) using systems, such as the 1.5 MRI – 7 MV linear accelerator (MR-Linac), now allow for improved soft-tissue on-board imaging for patient position and tumor target localization verification and the ability to assess functional biological tissue characteristics with MRI, all without increasing the patient radiation burden.

However, with the advantages of MRI guidance in MR-IGRT came the dosimetric challenges of the presence of a strong magnetic field. When the magnetic field is oriented perpendicular to the radiation beam, Lorentz forces act on secondary electrons causing hot and cold spots at tissue transition areas. These interactions with the magnetic field cause perturbations of the dose distribution in three dimensions. Current vendor-supplied electronic quality assurance tools can provide at best quasi-3D sampling of the dose distribution and cannot be MR imaged. As a result, there was a growing need for volumetric, MR-visible, and radiation-sensitive detectors for MR-IGRT applications. To fill this need for volumetric dose quality assurance, this dissertation work investigated existing and novel formulations of radiochromic gel dosimeters. After the optimal radiochromic gel formulation was identified, it was characterized for dose linearity, radiological properties, reproducibility, time stability, energy dependence, reusability, dose rate dependence, fractionation dependence, gel matrix dependence, and diffusion. Next, strong magnetic field and gradient field/radiofrequency effects on the

response of 3D dosimeters were assessed along with other MR considerations that were and were not specific to MR-IGRT systems. Finally, heterogeneous and homogeneous 3D dosimeters were used for end-to-end testing with a variety of Monaco TPS plans.

This dissertation work contributed significantly to the fields of 3D dosimetry, MR-IGRT, and radiation physics: the first proof of concept of real-time 2D and 3D dose acquisition during irradiation was presented, a novel radiochromic gel dosimeter and its reusable version were presented and characterized, and the first full end-to-end testing including adaptive planning using daily MR images of the 3D dosimeters was presented. Overall, the feasibility and benefit of MR-visible and radiation-sensitive 3D dosimeters were presented in this dissertation work for MR-IGRT applications.

Table of Contents

Approval page	i
Title page	ii
Dedication	iii
Acknowledgements	iv
Abstract	vi
Table of Contents	viii
List of Illustrations	x
List of Tables	xix
Chapter 1 – Introduction	1
1.1 Integrated magnetic resonance imaging – radiation therapy systems	1
1.2 Three-dimensional dosimetry	5
1.3 Outline of the dissertation	11
Chapter 2 – Comparison of radiochromic systems for MR-IGRT applications	13
2.1 Rationale	13
2.2 Iron(II) oxidation gel formulations	14
2.2.1 Dosimeter fabrication	14
2.2.2 Optical methods	16
2.2.3 Magnetic resonance methods	17
2.2.3 Iron(II) oxidation results and discussion	17
2.3 Iron(III) reduction gel formulations	23
2.3.2 Iron(III) reduction results and discussion	25
2.4 Summary	38
Chapter 3 – Characterization of optimal radiochromic formulation	39
3.1 Rationale	39
3.2 Dose linearity	39
3.2.1 Optical linearity	39
3.2.2 Post-irradiation MR linearity	42
3.2.3 Real-time MR linearity	42

3.3 Radiological properties	45
3.4 Reproducibility	47
3.5 Time stability	48
3.6 Energy dependence	50
3.7 Reusability	52
3.8 Dose rate dependence	53
3.9 Fractionation dependence	55
3.10 Gel matrix dependence and diffusion	57
3.11 Summary	62
Chapter 4 – Magnetic field effects on volumetric dosimeters	64
4.1 Rationale	64
4.2 Strong magnetic field dependence	64
4.3 Gradient and radiofrequency field dependence	70
4.4 Other MR considerations	71
4.5 Summary	81
Chapter 5 – Volumetric phantom study	82
5.1 Rationale	82
5.2 Heterogeneous rFOX phantom results and discussion	84
5.3 Homogeneous FXG phantom and ArcCHECK-MR results and discussion	110
5.4 Summary	120
Chapter 6 – Conclusion	123
6.1 Summary and conclusion	123
6.3 Future works	124
Bibliography	127
VITA	149

List of Illustrations

Figure 1: Illustrations of a) the pre-clinical 1.5 T MRI – 7 MV linear accelerator (linac) (MR-Linac, Elekta, AB, Stockholm, Sweden) (Raaymakers BW, Lagendijk JJW, Overweg J, Kok JGM, Raaijmakers AJE, Kerkhof EM, van der Put RW, Meijsing I, Crijs SPM, Benedosso F, van Vulpen M, de Graaff CHW, Allen J, Brown KJ (2009) Integrating a 1.5 T MRI scanner with a 6 MV accelerator: proof of concept. *Phys Med Biol* 54:N229–N237. doi: 10.1088/0031-9155/54/12/N01) (© Institute of Physics and Engineering in Medicine. Reproduced by permission of IOP Publishing. All rights reserved.), b) the 1.0 T MRI with 6 MV linac in Sydney for inline (left) and perpendicular (right) configurations (Keall PJ, Barton M, Crozier S (2014) The Australian Magnetic Resonance Imaging–Linac Program. *Semin Radiat Oncol* 24:203–206. doi: 10.1016/j.semradonc.2014.02.015) (© Seminars in Radiation Oncology. Reproduced by permission of Elsevier. All rights reserved.), c) the 0.5 T with 6 MV Aurora RTTM (MagnetTx) (Fallone BG (2014) The Rotating Biplanar Linac–Magnetic Resonance Imaging System. *Semin Radiat Oncol* 24:200–202. doi: 10.1016/j.semradonc.2014.02.011) (© Seminars in Radiation Oncology. Reproduced by permission of Elsevier. All rights reserved.), and d) the 0.35 T with cobalt-60 or linac MRIdian (Viewray, Inc.) (Mutic S, Dempsey JF (2014) The ViewRay System: Magnetic Resonance–Guided and Controlled Radiotherapy. *Semin Radiat Oncol* 24:196–199. doi: 10.1016/j.semradonc.2014.02.008) (© Seminars in Radiation Oncology. Reproduced by permission of Elsevier. All rights reserved.). 3

Figure 2: Monte Carlo calculated point spread kernels of secondary electrons for a) 0 T, b) 0.2 T, c) 0.75 T, and d) 1.5 T magnetic field strengths (Raaijmakers AJE, Raaymakers BW, Lagendijk JJW (2008) Magnetic-field-induced dose effects in MR-guided radiotherapy systems: dependence on the magnetic field strength. *Phys Med Biol* 53:909–23. doi: 10.1088/0031-9155/53/4/006) (© Institute of Physics and Engineering in Medicine. Reproduced by permission of IOP Publishing. All rights reserved.). 5

Figure 3: a) Pictures of physical dosimeters where A – FOX, B – FCX, C – FPX, and D – FXG. The top half of each gel was not irradiated, and the bottom half was irradiated to approximately 17 Gy. b) Snapshots of bFFE acquisitions with TR/TE = 5/2.4 ms. c) Post-irradiation acquisitions with TSE TR/TE = 500/20 ms. MR images shown with color instead of grayscale to emphasize contrast. 18

Figure 4: Relative MR signal intensities during real-time acquisition of a) FOX, b) FCX, c) FPX, and d) FXG. The orange shaded regions indicate beam-on times. Linear fits in the beam-on sections are also indicated. The error bars in Figure 4 represent the propagated standard deviation from the regions of interest measured within the irradiated region and outside the irradiated region in each dosimeter. 19

Figure 5: Optical response of FOX and FXG. a) Spectral response of FOX, b) linear optical response of FOX at spectral peaks of 430 nm and 585 nm ($R^2 = 0.9944$ and 0.9978 , respectively), c) spectral response of FXG, and d) linear optical response of FXG at spectral peaks of 445 nm and 585 nm ($R^2 = 0.9930$ and 0.9844 , respectively). The error bars in the

calibration curves were smaller than the symbols and represented the standard deviation of three spectrophotometer readings per sample. 21

Figure 6: Sample of FCST in solution (without gelatin) with a) un-irradiated iron(II)-containing sample and b) approximately 40 Gy irradiated iron(III)-containing sample using Co-60 source showing color change from a) colorless to b) blood red characteristic of thiocyanate indicators in the presence of iron(III). 22

Figure 7: a) Pictures of physical dosimeters where A – FOST, B – FCST, C – FPST, and D – FASST. The top half of each gel was not irradiated, and the bottom half was irradiated to approximately 17 Gy. b) Snapshots of bFFE acquisitions with TR/TE = 5/2.4 ms. c) Post-irradiation acquisitions with TSE TR/TE = 500/20 ms. MR images shown with color instead of grayscale to emphasize contrast. 23

Figure 8: Post-irradiation response of TBG in solution (no gelatin). a) Pictures of TBG irradiated to 0, 5, 10, 20, 40, and 60 Gy using a Co-60 source immediately post-irradiation, 3 hours post-irradiation, and 72 hours post-irradiation. b) Spectral response of TBG 72 hours after irradiation. c) Calibration curve of TBG 72 hours after irradiation at the spectral peak 690 nm. The error bars in the calibration curve were smaller than the symbols and represented the standard deviation of three spectrophotometer readings per sample. 27

Figure 9: MR images of TBG. a) TBG in 2 wt % gelatin pre-irradiation, b) TBG in 2 wt % gelatin post-irradiation of approximately 30 Gy, c) TBG in 3 wt % gelatin pre-irradiation, and d) TBG in 3 wt % gelatin post-irradiation of approximately 30 Gy. 28

Figure 10: a) TBG incorporated into sodium polyacrylate ball prior to UV exposure, b) TBG post UV exposure, c) TBG incorporated into sodium polyacrylate powder prior to UV exposure, d) TBG post UV exposure, e) TBG incorporated into Encapso® K rubber prior to UV exposure, f) TBG post UV exposure, g) side view of e, and h) side view of f. 29

Figure 11: Post-irradiation response of FT in solution. a) Pictures of FT irradiated to 0, 5, 10, 20, 40, and 60 Gy using a Co-60 source immediately post-irradiation, 3 hours post-irradiation, 48 hours post-irradiation, and 96 hours post-irradiation. b) Spectral response of FT 96 hours after irradiation. c) Calibration curve of FT 96 hours after irradiation at the spectral peak 650 nm. The error bars in the calibration curve were smaller than the symbols and represented the standard deviation of three spectrophotometer readings per sample. 30

Figure 12: a) FT in solution showing color change from colorless clear to dark green with increasing UV exposure, b) FT incorporated into Encapso® K rubber prior to UV exposure, c) FT post UV exposure (yellow color change), d) side view of b, and e) side view of c. 31

Figure 13: a) Spectral response of FO immediately after irradiation (inset image shows FO before irradiation – yellow and after irradiation – red). c) Calibration curve of FO at the spectral peak 650 nm. The error bars in the calibration curve represented the standard deviation of spectrophotometer measurements averaged for three cuvettes per dose level. 32

Figure 14: Oxygen dependence test of FO in solution by O₂ degassing with N₂ for 10 minutes. a) Calibration curves of FO with and without O₂ and b) example set-up for degassing with N₂

into the solution with a vent (actual set-up was covered to prevent light affecting the samples). The error bars in the calibration curves represented the standard deviation of spectrophotometer measurements averaged for three cuvettes per dose level. 33

Figure 15: Dose rate dependence of FO. The error bars in the calibration curve represented the standard deviation of spectrophotometer measurements averaged for three cuvettes per dose level. 34

Figure 16: a) Calibration curves of FO in solution (no gelatin) after storage at room temperature (RT) and 4 °C (4C) for 1 week compared to immediately prior to irradiation and b) after storage for 2 weeks. The error bars in the calibration curves represented the standard deviation of spectrophotometer measurements averaged for three cuvettes per dose level. 35

Figure 17: Gelatin percentage dependence on FO sensitivity (inset image shows differences in OD of samples prior to irradiations depending on gelatin percentage). The error bars in the calibration curves represented the standard deviation of spectrophotometer measurements averaged for three cuvettes per dose level. 36

Figure 18: a) Pictures of physical dosimeters where A – FO, B – FCO, C – FB, and D – FCB. The top half of each gel was not irradiated, and the bottom half was irradiated to approximately 34 Gy. b) Snapshots of bFFE acquisitions with TR/TE = 5/2.4 ms. c) Post-irradiation acquisitions with TSE TR/TE = 500/20 ms. MR images shown with color instead of grayscale to emphasize contrast. 37

Figure 19: a) FO incorporated into Encapso® K rubber prior to UV exposure, b) FO post UV exposure (red color change), c) side view of a, and d) side view of b. 38

Figure 20: a) Representative absorption spectra of un-irradiated and irradiated FOX, b) un-irradiated yellow FOX on the left and irradiated purple FOX on the right, c) background subtracted spectrum with peaks at 440 nm and 585 nm, d) calibration curve at 440 nm, and e) calibration curve at 585 nm. The error bars in the calibration curves represented the standard deviation of spectrophotometer measurements averaged for three cuvettes per dose level. .. 40

Figure 21: a) Spectral response of rFOX immediately (as realistically possible) after irradiation with peaks at 432 nm and 585 nm. Calibration curves at 432 nm b) immediately post-irradiation, d) 24 hours post-irradiation, f) 48 hours post-irradiation, h) 72 hours post-irradiation, and j) 96 hours post-irradiation. Calibration curves at 585 nm c) immediately, e) 24 hours, g) 48 hours, i) 72 hours, and k) 96 hours. The error bars in the calibration curves represented the standard deviation of spectrophotometer measurements averaged for three cuvettes per dose level. 41

Figure 22: Post-irradiation MR linearity of rFOX. The error bars represent the standard deviation from the regions of interest measured within the irradiated region in each dosimeter. 42

Figure 23: Real-time MR signal intensity linearity with dose for a) FOX in gelatin, b) FOX in gelatin and agarose), and c) rFOX in gelatin and agarose. The error bars represent the

propagated standard deviation from the regions of interest measured within the irradiated region and outside the irradiated region in each dosimeter. 44

Figure 24: Interaction properties for water and FOX. 45

Figure 25: a) Mass attenuation coefficient ratio, b) mass energy absorption coefficient ratio, and stopping power ratios (collisional, radiative, and total) for FOX and water..... 46

Figure 26: Reproducibility testing for FOX. a) Intra-batch variability with 10 irradiations from one batch of approximately 4 Gy (measured at spectral peak of 440 nm), b) intra-batch variability (585 nm), c) inter-batch variability from 6 batches (440 nm), and d) inter-batch variability (585 nm). The error bars in the calibration curves represented the standard deviation of spectrophotometer measurements averaged for three cuvettes per dose level. 48

Figure 27: The effect of repeat spectrophotometer xenon lamp exposures on consecutive optical read-out of FO gel measured at 512 nm. The center dotted line represents the mean value from the 30 readings. The surrounding dotted lines show the bounds from the mean value considering the standard deviation of the 30 readings. The increase in net OD with repeat exposure to the xenon lamp was found to be linear ($R^2 = 0.987$). 49

Figure 28: Time stability of FOX measured for 4 Gy (red triangles), 0 Gy (blue squares), and net 4 Gy (black diamonds) when stored at a) room temperature (measured at spectral peak 440 nm), b) room temperature (585 nm), c) 4 °C (440 nm), and d) 4 °C (585 nm). The error bars in the curves represented the standard deviation of spectrophotometer measurements averaged for three cuvettes per time point and per dose level. 50

Figure 29: Energy dependence of FOX relative to net OD measured for 7 MV (MR-Linac). The error bars in the curves represented the standard deviation of spectrophotometer measurements averaged for three cuvettes per irradiation. 51

Figure 30: Reproducibility of net MR signal intensity response shown for rFOX irradiated with approximately 10 Gy each time with at least 24 hours separating each repeat irradiation. The relative net MR signal intensity was calculated as the irradiated region's signal intensity divided by the un-irradiated region's signal intensity for each repeat irradiation. The error bars represent the propagated standard deviation from the regions of interest measured within the irradiated region and outside the irradiated region in each dosimeter. 52

Figure 31: Dose rate dependence of a) FOX and b) rFOX. c) Example MR images of rFOX with no CE and T1 CE acquisitions. MR images acquired with no CE were smoother with lower standard deviation. The relative values were calculated as the net value divided by the net value at 100% gun duty cycle. The error bars in a) represent the standard deviation of spectrophotometer measurements averaged for three cuvettes per dose level and b) represent the propagated standard deviation from the regions of interest measured within the irradiated region and outside the irradiated region in each dosimeter. 54

Figure 32: Fractionation dependence of a) FOX and b) rFOX. The relative net OD values were calculated as the net value divided by the net value at 12 Gy x 1. The error bars in a) represent the standard deviation of spectrophotometer measurements averaged for three cuvettes per

irradiation and b) represent the standard deviation from the regions of interest measured within the irradiated region in each dosimeter (raw MR signal intensity given here). 56

Figure 33: Gel matrix dependence. Post-irradiation T1-weighted images (TR/TE = 500/20 ms) of a) FOX in gelatin (4 wt %), b) FOX in gelatin (3 wt %) and agarose (1 wt %), and c) rFOX in gelatin (3 wt %) and agarose (1 wt %). 57

Figure 34: Diffusion of signal for a) FOX in gelatin, b) FOX in gelatin and agarose, and c) rFOX in gelatin and agarose for up to 28 days. 59

Figure 35: rFOX reversal of raw MR signal intensity. a) Change in signal up to 28 days and b) zoomed in view to first 24 hours. The decrease in signal in the first two hours was found to be linear. The error bars represent the standard deviation from the regions of interest measured within the irradiated region at each time point. 61

Figure 36: a) Schematic of electromagnet and location of phantoms when inserted between pole caps with the directions of the B_0 field and radiation beam noted; b) acrylic phantoms with cuvette inserts used for FOX irradiations (sample cuvette in insert). Black dots in phantom and in sample cuvette indicate region of optical measurement using a spectrophotometer in relation to the radiation field (shaded region); and c) profile of 1.5 T B_0 field strength in between pole faces (50 mm) of electromagnet. The error bars represent the standard deviation from three readings of the B_0 field strength. 66

Figure 37: a) net OD versus dose linear calibration curves without ($R^2 = 1.00$) and with ($R^2 = 1.00$) 1.5 T B_0 field at spectral peak of 440 nm, b) linear calibration curves ($R^2 = 1.00$) at spectral peak of 585 nm, and c) net OD for FOX dosimeters at 440 nm and 585 nm for varying lengths of time in the 1.5 T B_0 field during irradiation to 4 Gy absorbed dose. The error bars represented the standard deviation of spectrophotometer measurements averaged for three cuvettes per data point. 68

Figure 38: a) net OD versus dose linear calibration curves without and with 1.5 T B_0 field in MR-Linac at spectral peak of 440 nm and b) linear calibration curves at spectral peak of 585 nm. The error bars in the curves represented the standard deviation of spectrophotometer measurements averaged for three cuvettes per data point. 70

Figure 39: Assessment of potential B_1 /RF dependence on FOX gel using 4 different real-time bFFE sequences at both 440 nm and 585 nm optical peaks: A) no real-time MRI during irradiation, B) TR/TE = 8/3.6 ms, $B_1 = 20 \mu\text{T}$, maximum gradient mode, $\text{dB}/\text{dt} = 20.5 \text{ T/s}$, C) TR/TE = 8/3.6 ms, $B_1 = 20 \mu\text{T}$, regular gradient mode, $\text{dB}/\text{dt} = 7.3 \text{ T/s}$, and D) TR/TE = 8/3.6 ms, $B_1 = 3 \mu\text{T}$, maximum gradient mode, $\text{dB}/\text{dt} = 14.0 \text{ T/s}$. Values for B, C, and D were normalized to A for both wavelengths. All real-time acquisitions had temporal resolutions of 400 ms. The error bars represented the standard deviation of spectrophotometer measurements averaged for three cuvettes per data point. 71

Figure 40: Real-time relative MR signal intensity for a) NSA = 1, b) NSA = 2, c) NSA = 3, and d) NSA = 4. The temporal resolution for NSA = 1, 2, 3, and 4 were 231 ms, 476 ms, 710 ms, and 947 ms, respectively. The orange shaded regions indicate beam on times. The red lines indicate the relative MR signal intensity in the irradiated region and the blue lines show the

intensity in the un-irradiated region. The error bars represent the propagated standard deviation from the regions of interest measured within the irradiated region and outside the irradiated region in each dosimeter. 73

Figure 41: Real-time relative MR signal intensity for NSA = 2 with temporal resolution of 476 ms demonstrating stability of signal intensity pre-irradiation and post-irradiation for up to 10 minutes and 20 minutes, respectively. The orange shaded region indicates beam-on time. The error bars represent the propagated standard deviation from the regions of interest measured within the irradiated region and outside the irradiated region in each dosimeter. 74

Figure 42: FOX gel used for 3D dose acquisition in an 85 mm diameter and 60 mm tall PET container. Post-irradiated T₁-weighted images are shown to the right of the physical dosimeter (irradiated and imaged in MR-Linac). 75

Figure 43: Real-time snapshot of FOX gel showing regions of interest used to assess un-irradiated and irradiated regions. Images were acquired using a bFFE sequence of TR/TE = 4.4/2.2 ms with 12 slices per acquisition, NSA = 1, and temporal resolution of 1800 ms. The red line indicates the relative MR signal intensity in the irradiated region and the blue line shows the signal in the un-irradiated region. The error bars represent the propagated standard deviation from the regions of interest measured within the irradiated region and outside the irradiated region. 75

Figure 44: Real-time volumetric snapshots of FOX gel after irradiating to approximately a) 0 Gy, b) 5 Gy, c) 10 Gy, d) 15 Gy, e) 20 Gy, f) 25 Gy, and g) 30 Gy delivered to the center of the gel. The first 10 Gy were delivered with gantry angle 0° and the last 20 Gy with gantry angle 270°. 76

Figure 45: a) MR images of FOX gels in 16 oz, 12 oz, and 4 oz containers pre-irradiation and post-irradiation and b) MR signal intensities of those images. The error bars represent the standard deviation from the regions of interest measured within the pre-irradiated and post-irradiated regions in each dosimeter. 77

Figure 46: a) MR images of FOX gels for gantry angles 0°, 90°, 180°, and 270° pre-irradiation and post-irradiation and b) MR signal intensities of those images. The error bars represent the standard deviation from the regions of interest measured within the pre-irradiated and post-irradiated regions in each dosimeter. 78

Figure 47: Examples of MRI artifacts. a) Fold over artifacts that could be remedied with suppression oversampling or increased field of view, b) Gibbs ringing artifact that could be reduced in the gel on the right but could never be completely removed due to arising from the fundamental consequence of using Fourier transform to reconstruct MR signals into images, c) zipper artifact that generally occurs with radiofrequency contamination from electronic devices occurred with spin echo sequences in PET plastic (with gel or water) and remedied on the right with a turbo spin echo sequence, and d) MR artifact due to super glue on bottom of jar (regardless of gel or water) but not present when hot glue was used. Central black region was due to brass ball bearing. 80

Figure 48: a) and b) The anthropomorphic Rando phantom imaged in the 1.5 T MR-Linac using the following parameters: 300 slices with FOV of 400 x 400 x 300 mm³, reconstructed voxel 0.83 x 0.83 x 1 mm³, T1-weighted TR/TE = 11/4.6 ms, 3D FFE, and 30° flip angle. c) and d) CT of same phantom. 83

Figure 49: Pictures of head and neck phantom and rFOX inserts. a) rFOX inside of phantom, b) rFOX outside of phantom, c) example of 1.3 cm diameter heterogeneous component in rFOX, and d) example of 3.0 cm diameter heterogeneous component in rFOX (purple regions were irradiated areas). 85

Figure 50: CT number to electron density conversion. 86

Figure 51: Overall MR-Linac workflow. First, make a reference TPS plan from the CT. Next, fuse the daily MRI with the CT and make an adapted plan. Next, deliver this plan and obtain a post-irradiation MRI. Finally, compare the relative delivered dose with the planned dose. .. 88

Figure 52: a) T2-weighted MRI, b) T1-weighted T1CE MRI, and c) T1-weighted no CE MRI. 89

Figure 53: “Subject Hierarchy” in 3D Slicer. 91

Figure 54: “Subtract Scalar Volumes” in 3D Slicer. 92

Figure 55: “Transforms” in 3D Slicer. 93

Figure 56: “Simple Filters” in 3D Slicer. 94

Figure 57: “Subject Hierarchy” to convert to RT dose volume in 3D Slicer. 95

Figure 58: “Dose Comparison” in 3D Slicer. 96

Figure 59: a) Planned dose overlaid on CT image, b) calculated relative dose from rFOX (T1 CE, NSA = 1) with no post-processing filter, c) MedianImageFilter radius 1, d) MedianImageFilter radius 2, e) MedianImageFilter radius 3, f) MedianImageFilter radius 4, and g) MedianImageFilter radius 5. The central region of rFOX that appears like a hot spot is due to the heterogeneous component and was not used for dose comparisons since that region cannot be scaled appropriately. 98

Figure 60: a) Planned dose overlaid on CT image, b) calculated relative dose from rFOX (T1 CE, NSA = 1) with no post-processing filter, c) MeanImageFilter radius 1, d) MeanImageFilter radius 2, e) MeanImageFilter radius 3, f) MeanImageFilter radius 4, and g) MeanImageFilter radius 5. The central region of rFOX that appears like a hot spot is due to the heterogeneous component and was not used for dose comparisons since that region cannot be scaled appropriately. 98

Figure 61: a) CT of rFOX with 1.3 cm solution insert, b) T2-weighted image, c) T1-weighted T1 CE image, d) T1-weighted no CE image, e) Monaco TPS dose overlaid on CT, f) T2-weighted relative dose (non-linear dose so not analyzed with gamma criteria), g) T1 CE relative

dose, h) no CE relative dose, i) gamma map of T2-weighted dose, j) gamma map of T1 CE dose, and k) gamma map of no CE dose..... 101

Figure 62: a) CT of rFOX with 1.3 cm gel insert, b) T1-weighted T1 CE image, c) T1-weighted no CE image, d) Monaco TPS dose overlaid on CT, e) T1 CE relative dose, f) no CE relative dose, g) gamma map of T1 CE dose, and h) gamma map of no CE dose. 103

Figure 63: a) CT of rFOX with 1.3 cm air insert, b) T1-weighted T1 CE image, c) T1-weighted no CE image, d) Monaco TPS dose overlaid on CT, e) T1 CE relative dose, f) no CE relative dose, g) gamma map of T1 CE dose, and h) gamma map of no CE dose. 105

Figure 64: a) CT of rFOX with 3.0 cm air insert, b) T1-weighted T1 CE image, c) T1-weighted no CE image, d) Monaco TPS dose overlaid on CT, e) T1 CE relative dose, f) no CE relative dose, g) gamma map of T1 CE dose, and h) gamma map of no CE dose. 107

Figure 65: a) CT of uniform rFOX with no heterogeneous insert, b) T1-weighted T1 CE image, c) T1-weighted no CE image, d) Monaco TPS dose overlaid on CT, e) T1 CE relative dose, f) no CE relative dose, g) gamma map of T1 CE dose, and h) gamma map of no CE dose. ... 109

Figure 66: a) and b) Images of ArcCHECK-MR showing locations of radio-opaque ceramic BB markers, c) view of BB on EPID with gantry angle at 0° (BB should be in center of field of view if positioned correctly, side BBs not visible in this acquisition due to size of EPID field of view), d) view of BB on EPID with gantry angle at 90° or 270° (BBs should be centered and overlap if positioned correctly), e) example of mis-aligned ArcCHECK-MR with BBs not overlapping, f) CT of BB used for initial isocenter positioning in Monaco TPS, and g) CT of BBs on ArcCHECK-MR used for initial isocenter positioning in Monaco TPS..... 112

Figure 67: a) CT of large uniform FXG, b) T1-weighted T1 CE image, c) Monaco TPS dose overlaid on CT, d) T1 CE relative dose, e) gamma map of T1 CE dose, f) Monaco TPS dose on CT of ArcCHECK-MR, and g) delivered and planned relative dose comparisons for AP PA TG-119 plan. 115

Figure 68: a) CT of large uniform FXG, b) T1-weighted T1 CE image, c) Monaco TPS dose overlaid on CT, d) T1 CE relative dose, e) gamma map of T1 CE dose, f) Monaco TPS dose on CT of ArcCHECK-MR, and g) delivered and planned relative dose comparisons for MultiTarget TG-119 plan..... 116

Figure 69: a) CT of large uniform FXG, b) T1-weighted T1 CE image, c) Monaco TPS dose overlaid on CT, d) T1 CE relative dose, e) gamma map of T1 CE dose, f) Monaco TPS dose on CT of ArcCHECK-MR, and g) delivered and planned relative dose comparisons for Prostate TG-119 plan. 117

Figure 70: a) CT of large uniform FXG, b) T1-weighted T1 CE image, c) Monaco TPS dose overlaid on CT, d) T1 CE relative dose, e) gamma map of T1 CE dose, f) Monaco TPS dose on CT of ArcCHECK-MR, and g) delivered and planned relative dose comparisons for Head/Neck TG-119 plan. 118

Figure 71: a) CT of large uniform FXG, b) T1-weighted T1 CE image, c) T1-weighted no CE image, d) T2-weighted image, e) Monaco TPS dose overlaid on CT, f) T1 CE relative dose, g) no CE relative dose, h) T2-weighted relative dose, i) gamma map of T1 CE dose, j) gamma map of no CE dose, k) gamma map of T2-weighted dose, l) Monaco TPS dose on CT of ArcCHECK-MR, and m) delivered and planned relative dose comparisons for C-Shape TG-119 plan..... 119

List of Tables

Table 1: Chemical components of FXG formulation.	15
Table 2: Chemical components of FOX formulation.	15
Table 3: Chemical components of FCX formulation.....	15
Table 4: Chemical components of FPX formulation.	16
Table 5: Chemical components of TBG formulation.	24
Table 6: Chemical components of FT formulation.....	25
Table 7: Chemical components of FO formulation.	25
Table 8: Iron(III) combinations for investigation in the MR-Linac.	36
Table 9: Slopes of radiation field edge over time for FOX and rFOX.	60
Table 10: Percent differences in slopes of radiation field edge over time for FOX and rFOX relative to slope measured at 14 min post-irradiation for FOX and 0 min post-irradiation for rFOX.	60
Table 11: Gel matrixes tested for FOX formulation.....	62
Table 12: Fusion translation coordinates for MRI with CT.....	89
Table 13: 3D gamma pass rates for heterogeneous rFOX phantom with 1.3 cm solution insert with image post-processing. Pass rates above the 80% cutoff are highlighted in green.	98
Table 14: 3D gamma pass rates for heterogeneous rFOX phantom with 1.3 cm solution insert. Pass rates above the 80% cutoff are highlighted in green.	100
Table 15: 3D gamma pass rates for heterogeneous rFOX phantom with 1.3 cm gel insert. Pass rates above the 80% cutoff are highlighted in green.....	102
Table 16: 3D gamma pass rates for heterogeneous rFOX phantom with 1.3 cm air insert. Pass rates above the 80% cutoff are highlighted in green.....	104
Table 17: 3D gamma pass rates for heterogeneous rFOX phantom with 3.0 cm air insert. Pass rates above the 80% cutoff are highlighted in green.....	106
Table 18: 3D gamma pass rates for homogeneous rFOX phantom. Pass rates above the 80% cutoff are highlighted in green.	108

Table 19: 3D gamma pass rates for TG-119 plans. Pass rates above the 80% cutoff are highlighted in green.	114
--	-----

Chapter 1 – Introduction

1.1 Integrated magnetic resonance imaging – radiation therapy systems

Prior to delivering patient radiation treatments, conventional treatments utilize some form of on-board imaging technique, both to ensure the consistency of the daily overall positioning of the patient as well as ensuring that the tumor target is within the radiation beam path. These imaging techniques include on-board megavoltage (MV) and kilovoltage (kV) imagers, cone beam computed tomography (CBCT), CT on rails, time-of-flight (ToF) cameras, and more sophisticated combinations of x-rays and cameras such as the Brainlab ExacTrac® [1–12]. However, MV and kV images provide poor soft-tissue contrast compared to magnetic resonance imaging (MRI) and rely largely on bony anatomy for patient positioning, assuming that the tumor has not moved relative to the bony anatomy. These conventional techniques also add to the overall radiation burden of the patient, which is especially of concern for pediatric patients. ToF cameras and other similar techniques only utilize the surface of the patient, again assuming that the tumor has not moved relative to the patient skin. However, tumors do not always behave idealistically and are known to change shape, move due to surrounding organs during treatment, and move due to overall patient weight changes between treatment fractions [13–18]. While patient immobilization techniques are used to help mitigate set-up uncertainties, several of these changes cannot be controlled. These changes can occur between the time of CT simulation and radiation treatment, daily due to inherent patient motion such as breathing, and gradually throughout treatment due to patient weight changes or disease progression or shrinkage. Larger planning target volumes (PTVs) have been implemented to account for tumor localization errors at the cost of unnecessarily irradiating adjacent normal tissues and organs at risk. Attempts have been made to mitigate these concerns with the use of fiducials, acquiring CTs more frequently during the course of treatment, and breath-hold and gating techniques to account for respiratory motion. However, the use of MRI is superior to such methods for soft tissue targets that may not necessarily track

according to bony anatomy or skin surface motion without adding any radiation burden to the patient, and the integration of MRI has been proposed by several groups for these reasons.

Due to the superior soft-tissue contrast of MRI compared to conventional computed tomography (CT) and cone-beam CT, several groups have designed integrated MRI with radiation treatment machine systems. These include the pre-clinical 1.5 T MRI – 7 MV linear accelerator (linac) (MR-Linac, Elekta, AB, Stockholm, Sweden), a prototype system combining a 1.0 T MRI with a 6 MV linac (Ingram Institute, Sydney, Australia), the Aurora RT™ 0.5 T magnet with 6 MV linac (MagnetTx, Saskatchewan, Canada), and the MRIdian™ 0.35 T magnet with cobalt-60 (Viewray, Inc., Oakwood Village, Ohio, USA) (Figure 1) [19–23]. Both the Elekta MR-Linac and the Viewray MRIdian consist of a radiation beam perpendicular to the MRI magnetic field. The Elekta MR-Linac and the Viewray MRIdian both orient their radiation sources (linac assembly or cobalt-60 sources) on a rotating gantry surrounding the MRI. The Viewray MRIdian consists of a split magnet design to allow for a lower source beam energy whereas the Elekta MR-Linac requires the flattening filter free (FFF) radiation beam to pass through the cryostat. In the Elekta MR-Linac, active magnetic shielding is used around the linac, and the magnet design reduces the fringe field to minimize any magnetic field effects on the accelerator components. The Sydney MRI-linac is designed to function with the linac component switching between parallel and perpendicular configurations with respect to the magnetic field. The MagnetTx Aurora RT™ consists of a cryogen free bi-planar rotating magnet with the linac oriented parallel to the MRI magnetic field. Unlike the other aforementioned systems, the MagnetTx Aurora RT™ is designed with concurrent rotation of the linac and MRI components. The Sydney MRI-linac and the MagnetTx Aurora RT™ have the advantages of positioning the radiation beam parallel to the MRI magnetic field, therefore reducing influences of the magnetic field on the radiation dose distribution. The disadvantages of the Viewray MRIdian and MagnetTx Aurora RT™ are their lower magnetic field strengths, 0.35 T and 0.5 T, respectively, reducing the MRI signal-to-noise ratio (SNR), overall image quality, and potential for advanced functional MRI techniques. However, the lower magnetic field strengths do have the advantage of minimal influences on electronic devices, medical

devices such as MR-compatible pacemakers, and simplifying dosimetry as a result of less influence on secondary charged particles. While the Sydney MRI-linac combines the stronger magnetic field strength advantage of the Elekta MR-Linac along with its dual orientation possibility, this system has not yet been developed into a functional product to date. For several of the mentioned reasons, the University of Texas MD Anderson Cancer Center obtained the 2nd worldwide and 1st North American Elekta MR-Linac system and is the main MR-IGRT system discussed in this dissertation work.

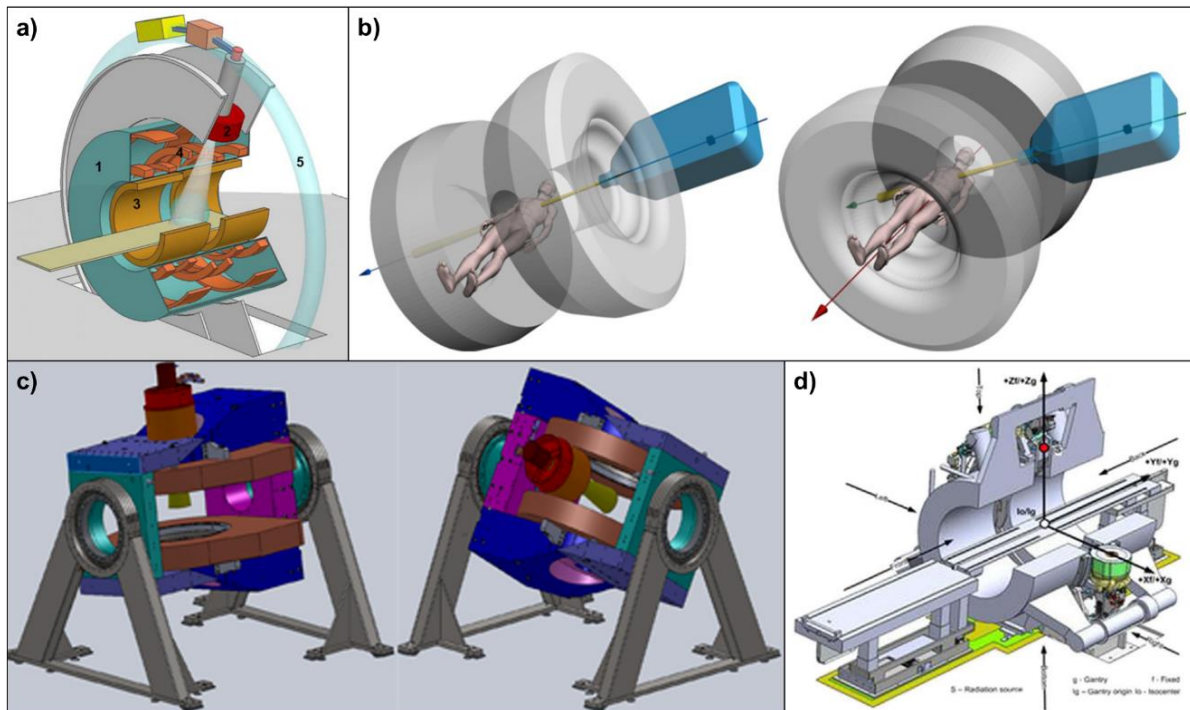


Figure 1: Illustrations of a) the pre-clinical 1.5 T MRI – 7 MV linear accelerator (linac) (MR-Linac, Elekta, AB, Stockholm, Sweden) (Raaymakers BW, Lagendijk JJW, Overweg J, Kok JGM, Raaijmakers AJE, Kerkhof EM, van der Put RW, Meijsing I, Crijns SPM, Benedosso F, van Vulpen M, de Graaff CHW, Allen J, Brown KJ (2009) Integrating a 1.5 T MRI scanner with a 6 MV accelerator: proof of concept. *Phys Med Biol* 54:N229–N237. doi: 10.1088/0031-9155/54/12/N01) (© Institute of Physics and Engineering in Medicine. Reproduced by permission of IOP Publishing. All rights reserved.), b) the 1.0 T MRI with 6 MV linac in Sydney for inline (left) and perpendicular (right) configurations (Keall PJ, Barton M, Crozier S (2014) The Australian Magnetic Resonance Imaging–Linac Program. *Semin Radiat Oncol* 24:203–206. doi: 10.1016/j.semradonc.2014.02.015) (© Seminars in Radiation Oncology. Reproduced by permission of Elsevier. All rights reserved.), c) the 0.5 T with 6 MV Aurora RTTM (MagnetX) (Fallone BG (2014) The Rotating Biplanar Linac–Magnetic Resonance Imaging System. *Semin Radiat Oncol* 24:200–202. doi: 10.1016/j.semradonc.2014.02.011) (© Seminars in Radiation Oncology. Reproduced by permission of Elsevier. All rights reserved.), and d) the 0.35 T with cobalt-60 or linac MRIdian (Viewray, Inc.) (Mutic S, Dempsey JF (2014) The ViewRay System: Magnetic Resonance–Guided and Controlled Radiotherapy. *Semin Radiat Oncol* 24:196–199. doi: 10.1016/j.semradonc.2014.02.008) (© Seminars in Radiation Oncology. Reproduced by permission of Elsevier. All rights reserved.).

Compared to conventional on-board imaging acquired for patient position verification on a linac, MRI has numerous advantages: a variety of acquisition parameters and resulting image contrast to more accurately localize soft tissues; the ability to reflect functional biological tissue characteristics such as tissue oxygenation and perfusion; and the ability to image without increasing the patient radiation burden [24–35]. The integration of MRI with radiation treatment machine systems will especially benefit patients with soft tissue lesions that are more difficult to track using conventional on-board techniques [36–38]. Encouraging preliminary patient data have been presented for pancreas and gastrointestinal sites using the MRIdian [39, 40]. Furthermore, the integration of MRI with radiation treatment machine systems is not limited to the daily advantage of patient and tumor tracking. As mentioned previously, MRI can provide valuable functional imaging to assess tumor morphology and response to radiation treatment. Predicting the radiation treatment response for each patient using functional MRI techniques could enable more personalized and daily adaptive treatments, therefore making it possible to deliver higher rates of curative treatment while minimizing normal tissue toxicities. MRI may be able to provide more accurate target delineation for certain tumor sites during treatment planning, and creating pseudo-CT data sets from only MRI are under development [41–50].

With the advantages of real-time MRI guidance came the dosimetric challenges of the presence of a strong magnetic field. The focus of this dissertation work was for the 1.5 T – 7 MV Elekta MR-Linac. As mentioned previously, the MR-Linac system consists of a radiation beam perpendicular to the strong magnetic field, with the linac components mounted on a rotating gantry around the MRI (Figure 1). When the magnetic field is oriented perpendicular to the radiation beam, Lorentz forces act on secondary electrons causing hot and cold spots at tissue transition areas, such as a radiation beam exiting from tissue into air (Figure 2 shows Monte Carlo calculated point spread kernels of secondary electrons at different magnetic field strengths) [51–58]. These changes in the electrons' trajectories in the magnetic field cause perturbations of the dose distribution in three dimensions throughout heterogeneities present in human anatomy, such as areas including the trachea and sinuses. Conventional quality assurance tools include point measurements using ionization chambers,

thermoluminescent dosimeters, and optically stimulated luminescence detectors, planar measurements using film or 2D arrays such as the Sun Nuclear IC Profiler and PTW Starcheck, and quasi-3D arrays using the Sun Nuclear ArcCHECK. Vendors are beginning to supply magnetic field-compatible quality assurance tools, but these can provide at best quasi-3D sampling of the dose distribution [59]. Along with the newfound possibility for real-time MRI during irradiation, integrated MRI with radiation treatment machine systems have increased the clinical interest for water-equivalent volumetric dosimeters.

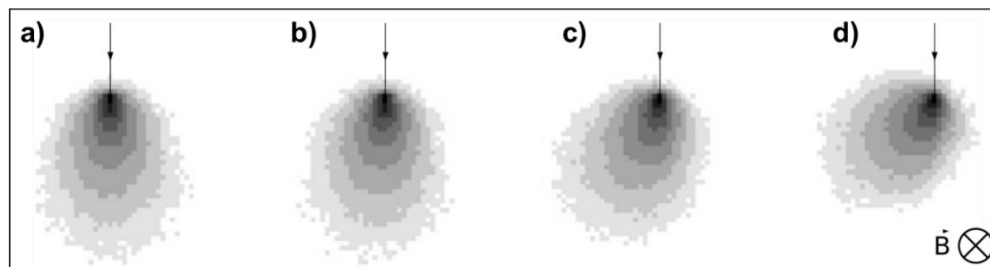


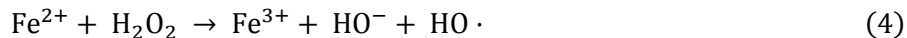
Figure 2: Monte Carlo calculated point spread kernels of secondary electrons for a) 0 T, b) 0.2 T, c) 0.75 T, and d) 1.5 T magnetic field strengths (Raaijmakers AJE, Raaymakers BW, Lagendijk JJW (2008) Magnetic-field-induced dose effects in MR-guided radiotherapy systems: dependence on the magnetic field strength. *Phys Med Biol* 53:909–23. doi: 10.1088/0031-9155/53/4/006) (© Institute of Physics and Engineering in Medicine. Reproduced by permission of IOP Publishing. All rights reserved.).

1.2 Three-dimensional dosimetry

The introduction of using chemicals that react to byproducts of ionizing radiation in a medium to measure radiation dose dates back to at least 1927 when Fricke and Morse presented ferrous sulfate solutions [60]. Since then, such chemical formulations have been incorporated into matrixes allowing for volumetric or three-dimensional (3D) measurements of radiation dose (dosimeters). Currently existing 3D dosimeters can generally be classified into 3 categories: radiochromic gels, polymer gels, and radiochromic plastics.

Radiochromic gels respond to the absorption of radiation dose by producing an optically readable response. The most common radiochromic gel formulations are based on Fricke and Morse's works [60, 61]. The chemical foundation of formulations based on this work relies on the conversion

of iron(II) (ferrous, Fe^{2+}) to iron(III) (ferric, Fe^{3+}) due to radiolysis of water producing $\text{H}\cdot$, $\text{HO}\cdot$, H_2 , and H_2O_2 and can be described by the following equations in the presence of oxygen:



giving the overall yield (G = molecules formed per 100 electron volt (eV) absorbed) of iron(III):

$$G(\text{Fe}^{3+}) = 3G(\text{H}\cdot) + G(\text{HO}\cdot) + 2G(\text{H}_2\text{O}_2) \quad (6)$$

[62]. The production of iron(III) after absorption of radiation can also be related to dose with the following relationship:

$$\Delta[\text{Fe}^{3+}] = \frac{D \cdot G(\text{Fe}^{3+}) \cdot 10\rho}{N_A \cdot e} \quad (7)$$

where D is radiation dose, ρ is the density in kg/liter, N_A is Avogadro's number (the number of units in one mole of any substance, 6.022×10^{23}), and e is the number of Joules per eV [63]. As can be seen in equation (7), the dose absorbed by an irradiated Fricke gel can be directly related to the change in concentration of iron(III). Radiochromic gels' response to radiation can be read out using optical or magnetic resonance methods. Optically, the yield or concentration of iron(III) can be related to dose with the following relationship:

$$D = \frac{N_A \cdot e}{\rho \cdot l \cdot G(\text{Fe}^{3+})} \cdot \frac{OD(D) - OD(0)}{\epsilon_m} \quad (8)$$

where l is the optical path length (1 cm for standard cuvettes), OD is the optical density, and ϵ_m is the molar extinction coefficient for iron(III) [63]. The OD of a material is related to the intensity of light after attenuation through the material, as explained by the Beer-Lambert Law:

$$I(\lambda) = I_0(\lambda) \cdot e^{-\mu(\lambda)x} \quad (9)$$

where $I_0(\lambda)$ is the initial light intensity for a given wavelength and μ is the linear attenuation coefficient (cm^{-1}). OD can then be calculated using the following relationship:

$$OD = -\log_{10}\left(\frac{I}{I_0}\right)/\text{sample length} = \text{absorbance}/\text{sample length} \quad (10)$$

where OD has the unit of cm^{-1} . OD by definition is a measure of absorbance and includes both absorption and scattering of light. Transmittance, on the other hand, is equal to the final light intensity divided by the initial light intensity. A material will absorb light when the energy of the light matches the available energy states in the atoms and molecules; otherwise, the light will scatter in a different direction from the incident light.

Due to paramagnetic differences between ferrous (iron(II)) and ferric (iron(III)) ions of iron, un-irradiated and irradiated Fricke gels can also be quantified using MR signals. The differences in the number of unpaired electrons and structure of complex formation for the iron ions affect the magnetic moment (can be simplified to spin only magnetic moment) and magnetic susceptibility of the material and are proportional to $\sqrt{n(n+2)}$ and $n(n+2)$, respectively, where n is the number of unpaired electrons [64]. Spin-lattice relaxation rate R_1 ($=1/T_1$ where T_1 is the longitudinal relaxation time) radiation-induced changes can be detected on MRI [60, 65–69]. The signal intensity of an MR image is proportional to the following relationship:

$$S \propto 1 - e^{-\left(\frac{t}{T_1}\right)} \quad (11)$$

where S is the signal intensity, t is time, and T_1 is such that the signal decreases to 63% (or $1-e^{-1}$) of its initial value. The relaxation rate R_1 is dose dependent and can be related to the concentration of iron(III) with the following equation:

$$R_1(D) = \left\{ (r_{eff}^{3+} - r^{2+}) \cdot G(Fe^{3+}) \cdot \frac{10\rho}{e \cdot N_A} \right\} \cdot D + R_1(0) \quad (12)$$

where $R_1(0)$ is the relaxation rate of the un-irradiated dosimeter, r^{3+} is the relaxation enhancement parameter (or relaxivity) for iron(III) and r^{2+} is the relaxivity for iron(II) [63]. The relaxivity for iron(III) is an effective relaxivity since it is dependent on the gel matrix that in turn, affects the complex

formation and hydration of iron(III). The relaxivities in relation to the dipole-dipole interactions (both scalar and dipolar coupling between nuclear and electron spins) in the material between water proton nuclear spins and paramagnetic ions were mathematically described under Solomon-Bloembergen-Morgan (SBM) theory of relaxation [70–72]. The gyromagnetic ratio of electrons is larger than that of the hydrogen proton, resulting in a quadratically larger interaction between an electron in the iron ion and the proton versus the interaction between two protons. The unpaired electrons of any paramagnetic material cause fluctuations in the local magnetic field, resulting in changes to the relaxivities. The SBM theory has since been expanded upon, such as using the Lipari-Szabo correction, the modified Florence approach, and the Swedish slow-motion theory to further explain paramagnetic related relaxivities [73–77]. While this explicit relationship in equation (12) is only true for iron(II) and iron(III) in solution and the relaxation models become more complex in a gel matrix, equation (12) still holds true for Fricke gels incorporated into any gel matrix as the new spin environments are incorporated through the relaxation rate of the un-irradiated dosimeter $R_1(0)$ [63]. The linear relationships between R_1 and radiation dose and MR signal intensity (arbitrary unit) and radiation dose have previously been reported, and equation (12) can be rearranged to more clearly demonstrate the relationship between net R_1 and dose:

$$D = \frac{N_A \cdot e}{10\rho \cdot G(Fe^{3+})} \cdot \frac{R_1(D) - R_1(0)}{r_{eff}^{3+} - r^{2+}} \quad (13)$$

[78–81]. Using an MRI system, the $R_1(D)$ or $T_1(D)$ values can be calculated using a series of sequences, the gold standard being inversion recovery. The MR signal as a function of T_1 can be expressed as the following from Bloch equation derivations:

$$S = k \cdot [H] \cdot (1 - 2e^{-TI/T_1} + e^{-TR/T_1}) \quad (14)$$

where k is a scaling factor, $[H]$ is the proton spin density, TI is the inversion time, and TR is the repetition time (time interval that inversion recovery sequence is repeated). However, these sequences can take upwards of 20 minutes for a single slice using the inversion recovery methodology, during which time the iron ions would be diffusing. While faster techniques exist, including Look-Locker and

Modified Look-Locker Imaging (MOLLI), these were not yet available on the MR-Linac system at the time of this dissertation work. Since the goal of this dissertation work was to identify and develop a suitable volumetric gel for MR-IGRT and to demonstrate the proof of concept of applying the gel to MR-IGRT systems, the signal intensities from T1-weighted images were used rather than acquiring a long series of MR images to quantitatively calculate R_1 or T_1 values. As previously mentioned, both the linear relationships between R_1 and radiation dose and MR signal intensity (arbitrary unit) and radiation dose have been reported for iron-based Fricke-type gels [78–81]. The iron-containing Fricke gels also produce a multi-exponential change in spin-spin relaxation rate R_2 ($=1/T_2$ where T_2 is the transverse decay time) to radiation; the R_2 responses of Fricke gels are not typically used for radiation dose assessment due to this more complex and smaller magnitude relationship [82]. The signal intensity of an MR image is proportional with the following relationship:

$$S \propto e^{-\left(\frac{t}{T_2}\right)} \quad (15)$$

where S is the signal intensity, t is time, and T_2 is such that the signal decreases to 37% (or e^{-1}) of its initial value. The more complex quantification of R_2 in comparison with dose for Fricke gels required dividing the relaxation rate behaviors into multiple parameters since multiple proton species (bulk water, bound water, tightly bound proton species, and other gel attributed hydroxyl groups) were required to explain this relaxation in Fricke gels [82]. The original Fricke gels have been modified with the addition of reporter compounds, most notably xylenol orange, producing Fricke xylenol orange gels (FXG), and exploration of gel matrixes outside of gelatin [63, 67, 83–85]. Reporter compounds or chelators are organic chemicals that form two or more coordination bonds with iron ions and improve the stability of spatial dose distribution by reducing the diffusion of iron ions. Historically, the main limitation of the Fricke-type gels was the diffusion of the small iron ions in the gel post-irradiation, degrading the dose distribution, even with the addition of reporter compounds.

Polymer gels date back to at least 1954 with Alexander's use of polymethylmethacrylate [61]. Whereas Fricke-type radiochromic gels depend on the conversion of iron ions, polymer gels depend on

the crosslinking of monomers forming polymers induced by free radicals produced by the radiolysis of water [86–89]. The polymer gel BANG® (N,N' – methylene – bis – acrylamide (BIS), acrylamide, nitrogen, and gelatin) dosimeter has been simulated in the Viewray system to show good agreement between Pinnacle treatment planning system calculated doses and simulated 3D doses from the BANG® gel [59]. The measured 3D doses from BANG® and other polymer gels are dependent on spin-spin relaxation rate R_2 ($=1/T_2$) radiation-induced changes due to polymerization of monomers inside the gel [88]. However, polymer gels require toxic chemicals and an oxygen free environment and have demonstrated energy and dose rate dependence as well as other undesirable characteristics [88, 90–95].

Unlike both the radiochromic and polymer gels, radiochromic plastics do not depend on the radiolysis of water. This most recent class of 3D dosimeters first presented in 2003 consists of a non-water soluble leuco-dye that is dissolved in a halogenated hydrocarbon, such as chloroform, and contained in a polyurethane plastic or silicone matrix [96–100]. Instead of water, radiochromic plastic dosimeters depend on the free radical byproducts of the radiolysis of halogenated hydrocarbons, resulting in the oxidation of the leuco dyes. Radiochromic plastic dosimeters do not require a container but cannot be imaged using MRI. Radiochromic plastic dosimeters require an optical read-out technique such as an optical computed tomography (optical-CT) device [89, 101–107]. While radiochromic plastic dosimeters cannot be read-out using MRI, their preservation of signal with minimal diffusion has allowed for remote dosimetry of the Viewray system demonstrating agreement with generated plans [108–110].

Previously, Fricke-type dosimeters were not favored for clinical quality assurance practices due to a faster rate of diffusion compared to polymer gels. However, with the MR-Linac and other MR-IGRT systems, Fricke-type dosimeters can now be imaged in real-time during irradiation and immediately post-irradiation without moving the dosimeters to a separate MRI or optical scanner [111–114]. Fricke-type gels are easier to make in-house compared to polymer gels, which require a hypoxic environment and toxic chemicals. While Fricke-type gels cannot be completely containerless like

radiochromic plastic dosimeters (which have no MR-visible response), they can fill any shaped molds allowing for the possible inclusion of heterogeneous components. As a result, this dissertation revisited Fricke-type dosimeters for MR-IGRT applications. And as mentioned previously, since the goal of this dissertation work was to identify and develop a suitable volumetric gel for MR-IGRT and to demonstrate the proof of concept of applying the gel to MR-IGRT systems, the signal intensities from T1-weighted images were used rather than acquiring a long series of MR images to quantitatively calculate R_1 or T_1 values.

1.3 Outline of the dissertation

The purpose of this dissertation was to investigate volumetric, MR-visible, and radio-sensitive detectors for dosimetry and quality assurance for integrated MR radiation therapy systems. The MR-IGRT system used for this dissertation was the 1.5 T – 7 MV Elekta MR-Linac. However, the work in this dissertation are relevant and can be translated to any other existing MR-IGRT system.

Chapter 2 investigates candidate volumetric gel formulations, both those already presented in the literature and novel formulations explored for this dissertation, for dosimetric value on MR-IGRT systems. This dissertation solely investigated radiochromic type volumetric dosimeters and primarily those based on iron. The optimal formulation for MR-IGRT applications was identified.

Chapter 3 presents the characterization of the optimal radiochromic gel formulation identified in Chapter 2. Dose linearity, radiological properties, reproducibility, time stability, energy dependence, reusability of a formulation, dose rate dependence, fractionation dependence, gel matrix dependence, and diffusion were quantified.

Chapter 4 investigates strong magnetic field and gradient field/radiofrequency effects on the response of the optimal radiochromic gel formulation as well as optimization of MR sequences for the purposes of real-time imaging during irradiation and immediate post-irradiation imaging for volumetric dose quantification. Other MR considerations that are true for any MRI read-out technique, such as MRI artifacts, are also discussed.

Chapter 5 examines the performance of the optimal radiochromic gel formulation as an end-to-end quality assurance device both in heterogeneous and homogeneous phantoms for 3D plans and step-and-shoot intensity-modulated radiation therapy (IMRT) commissioning plans. Irradiations were completed alongside the quasi-3D ArcCHECK-MR QA system.

A summary and general discussion of the unique contributions of this work are presented in Chapter 6.

Chapter 2 – Comparison of radiochromic systems for MR-IGRT applications

2.1 Rationale

With the advent of MR-IGRT systems, interest in 3D gel dosimeters has grown [108–126]. In particular, polymer gels have gained popularity over radiochromic gels due to the high diffusion rate of radiochromic gels. With the new possibility for real-time and immediate post-irradiation MRI in an MR-IGRT system, I revisited already existing radiochromic gel formulations and proposed new ones created in-house for MR-IGRT applications. Due to the timeline of this dissertation, some irradiations were conducted in clinical conventional linacs, using a Cobalt-60 (Co-60) source, or an orthovoltage x-ray unit (Philips RT-250) when the Elekta MR-Linac was not available. All irradiations in the MR-Linac were conducted following an initial calibration of the MR-Linac. Consequently, the doses given are approximate but are within 5% of the dose determined at a subsequent full calibration. Calibration of the MR-Linac was done following IAEA TRS-398 guidelines [127]. TRS-398 used the tissue maximum ratio (TMR), a special case of tissue phantom ratio (TPR), with a source to axis distance (SAD) set-up unlike the requirement of percent depth dose (PDD) measurements with a source to surface distance (SSD) set-up in the AAPM TG-51 protocol. The use of TMR was preferred over PDD due to the preservation of the ratio of dose per incident photon at 10 cm and 20 cm depths with and without a 1.5 T B_0 field whereas the PDD curve behavior is different in a 1.5 T B_0 field (maximum dose is at a shallower depth than with no B_0 field for example) [55]. The calibration of the MR-Linac was conducted using an MR-compatible Standard Imaging Exradin A1SL ionization chamber and cross-verified using a PTW Farmer chamber with both measurements in modified MR-compatible water tanks. For this dissertation work on relative dosimetry, the exact dose is not necessary to demonstrate the proof of concept of dose-response and other characteristics. For all irradiations, a control sample of each dosimeter was either an un-irradiated region of the dosimeter or an un-irradiated cuvette that was exposed to the same environment as the irradiated samples (except for receiving radiation).

2.2 Iron(II) oxidation gel formulations

Based on the conventional FXG formulation, three additional iron(II) sources were compared with the conventional FAS iron(II) source to determine differences in optical and MR contrast.

2.2.1 Dosimeter fabrication

Radiochromic dosimeters consist of a radiochromic reporter component, free radical source, solvent, iron source, and a gelling agent. Four iron(II) oxidation gel formulations were investigated, referred to as FXG, FOX (ferrous oxide – xylene orange), FCX (ferrous chloride – xylene orange), and FPX (ferrous phthalocyanine – xylene orange) with the compositions outlined below. Iron(III) binds to xylene orange (reporter component) with a 1:1 ratio forming a purple complex. To improve uniform mixing, the iron source was added to the solvent before the reporter component. All samples were prepared in a low-light area to prevent extraneous environmental exposure prior to irradiation. All gel samples were prepared approximately 24 hours prior to irradiation to allow for gel solidification.

The conventional FXG formulation consisted of xylene orange disodium salt, deionized water, and ammonium iron(II) sulfate hexahydrate (or ferrous ammonium sulfate) (Sigma-Aldrich) (Table 1). The FXG formulation was modified from the original Fricke formulation by adding xylene orange and was included as a comparison to the other three newly developed formulations [60, 84]. A small amount of sulfuric acid (Sigma-Aldrich) was added to stabilize the formulation. The FXG formulation in gel was prepared using 300 bloom gelatin from porcine skin. 75-80% of the total water volume was used to first dissolve gelatin. The gelatin mixture was heated to at least 40 °C then cooled to 25 °C prior to adding the concentrated chemical solution containing the reporter component and iron source. The gels were then stored at 4 °C then acclimated to room temperature prior to irradiation.

Table 1: Chemical components of FXG formulation.

Component	Chemical formula	Concentration
Xylenol orange disodium salt	$C_{31}H_{30}N_2Na_2O_{13}S$	0.05 mM
Water	H_2O	~96 wt %
Ammonium iron(II) sulfate hexahydrate	$(NH_4)_2[Fe(SO_4)_2] \cdot 6H_2O$	1 mM
Sulfuric acid	H_2SO_4	50 mM
Gelatin	$(C_{17}H_{32}H_5O_6)_x$	4 wt %

The FOX formulation consisted of xylenol orange disodium salt (Sigma-Aldrich), deionized water, and iron(II) oxide (Sigma-Aldrich) (Table 2). The same gel procedures described for FXG were used for the FOX, FCX, and FPX formulations.

Table 2: Chemical components of FOX formulation.

Component	Chemical formula	Concentration
Xylenol orange disodium salt	$C_{31}H_{30}N_2Na_2O_{13}S$	0.05 mM
Water	H_2O	~96 wt %
Iron(II) oxide	FeO	1 mM
Sulfuric acid	H_2SO_4	50 mM
Gelatin	$(C_{17}H_{32}H_5O_6)_x$	4 wt %

The FCX formulation consisted of xylenol orange disodium salt (Sigma-Aldrich), deionized water, and iron(II) chloride (Sigma-Aldrich) (Table 3).

Table 3: Chemical components of FCX formulation.

Component	Chemical formula	Concentration
Xylenol orange disodium salt	$C_{31}H_{30}N_2Na_2O_{13}S$	0.05 mM
Water	H_2O	~96 wt %
Iron(II) chloride	$FeCl_3$	1 mM
Sulfuric acid	H_2SO_4	50 mM
Gelatin	$(C_{17}H_{32}H_5O_6)_x$	4 wt %

The FPX formulation consisted of xylenol orange disodium salt (Sigma-Aldrich), deionized water, and iron(II) phthalocyanine (Sigma-Aldrich) (Table 4).

Table 4: Chemical components of FPX formulation.

Component	Chemical formula	Concentration
Xylenol orange disodium salt	$C_{31}H_{30}N_2Na_2O_{13}S$	0.05 mM
Water	H_2O	~96 wt %
Iron(II) phthalocyanine	$C_{32}H_{16}FeN_8$	0.1 mM
Sulfuric acid	H_2SO_4	50 mM
Gelatin	$(C_{17}H_{32}H_5O_6)_x$	4 wt %

2.2.2 Optical methods

Samples of gel were prepared in standard size cuvettes with an optical path length of 1 cm (Fisher Scientific) for optical read-out. The optical density (OD, unit cm^{-1} , as explained above in Chapter 1 as absorbance/sample length in equation (10)) of the gel was read-out with wavelengths in the visible range of the spectrum using a GENESYST™ 10S UV-VIS spectrophotometer (Thermo Scientific). The spectrophotometer outputs an absorbance value, and with the use of 1 cm dimension standard cuvettes, absorbance can directly be related to OD as absorbance = OD (cm^{-1}). The net OD was calculated by subtracting the OD value of un-irradiated samples from that of irradiated samples for each wavelength. The standard deviation of repeat spectrophotometer measurements for a single cuvette was no more than 0.004 OD with up to 30 repeat readings, as will be shown in Chapter 3 (Figure 27). While the overall goal of this dissertation was for MR-IGRT applications, access to the MR-Linac was not available at the beginning of this work, and access to a clinical MRI system was not possible within the timeframe of irradiations using clinical radiation therapy machines. Also, the standard deviation of 30 consecutive spectrophotometer measurements was no more than $\pm 0.5\%$ of the mean OD, a much smaller uncertainty than might be expected from measurements of MR signal intensity (up to $\pm 10\%$ standard deviation from the mean MR signal). For these reasons, any investigations that required low signal read-out uncertainty to assess the performance of the dosimeter used optical absorbance measurements instead of MR signal intensities (for example, B_0 field dependence and others later described in Chapter 3).

2.2.3 Magnetic resonance methods

All gels were contained in polyethylene terephthalate (PET) plastic containers (PAPER MART™) for irradiation and MR imaging. For the iron comparison portion of the study, all gels were contained in a 45 mm diameter cylindrical PET container.

The radiation isocenter and MR isocenter of the pre-clinical MR-Linac system are located 143.5 cm from the linac target and are approximately 14.3 cm above the surface of the couch (the couch has no vertical motion in the pre-clinical system). The center of each gel was positioned close to isocenter distance (within 5 mm). For the iron comparison portion of the study, the 45 mm diameter gels were positioned on top of 12.2 cm of water-equivalent plastic backscatter material. No build-up material was added on top of the gels since measurements were taken at the central cross-section of the gels and this was an initial investigation to compare radiation sensitivities. These gels were imaged with a balanced fast field echo (bFFE) sequence of repetition time/echo time (TR/TE) = 5/2.4 ms during irradiation and a T₁-weighted turbo spin echo (TSE) sequence of TR/TE = 500/20 ms pre-irradiation and post-irradiation. The real-time temporal resolution was 275 ms for a single slice per acquisition. All images were acquired with 5 mm slice thickness using a body coil. For all of the real-time 2D MR images, a resolution of 1.17 pixels per mm with pixel size of 0.86 x 0.86 mm² and field of view of 328.56 x 328.56 mm² were used.

2.2.3 Iron(II) oxidation results and discussion

The physical dosimeters, snapshot of the real-time acquisition, and post-irradiation (approximately 17 Gy) images of the four iron compounds investigated (A – FOX, B – FCX, C – FPX, and D – FXG) are shown in Figure 3.

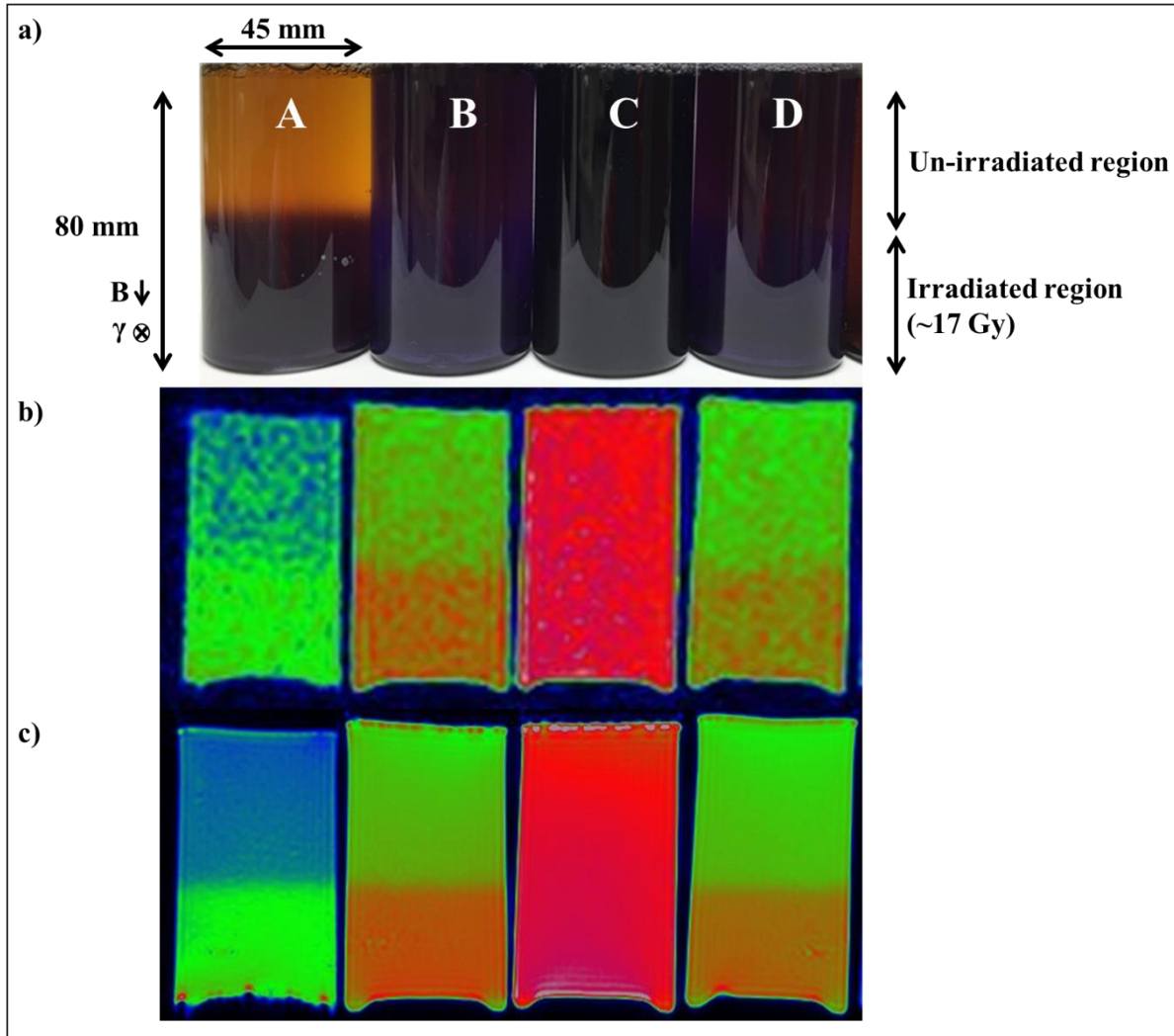


Figure 3: a) Pictures of physical dosimeters where A – FOX, B – FCX, C – FPX, and D – FXG. The top half of each gel was not irradiated, and the bottom half was irradiated to approximately 17 Gy. b) Snapshots of bFFE acquisitions with $TR/TE = 5/2.4$ ms. c) Post-irradiation acquisitions with TSE $TR/TE = 500/20$ ms. MR images shown with color instead of grayscale to emphasize contrast.

As shown in Figure 3, B – FCX and D – conventional FXG responded to irradiation, both optically and MRI. In contrast, C – FPX showed minimal MR change after irradiation. The real-time net change in MR signal is shown in Figure 4. The relative MR signal intensity was plotted from a region of interest taken within the irradiated region of each dosimeter, demonstrating a near-linear change with dose delivered constantly over time ($R^2 = 0.93$ to 0.97). The relative MR signal intensity was calculated for each dosimeter by dividing all net signal intensities (irradiated signal intensity – un-

irradiated signal intensity) by the net signal intensity at the time beam was turned off (225 s). The error bars in Figure 4 represent the propagated standard deviation from the regions of interest measured within the irradiated region and outside the irradiated region in each dosimeter.

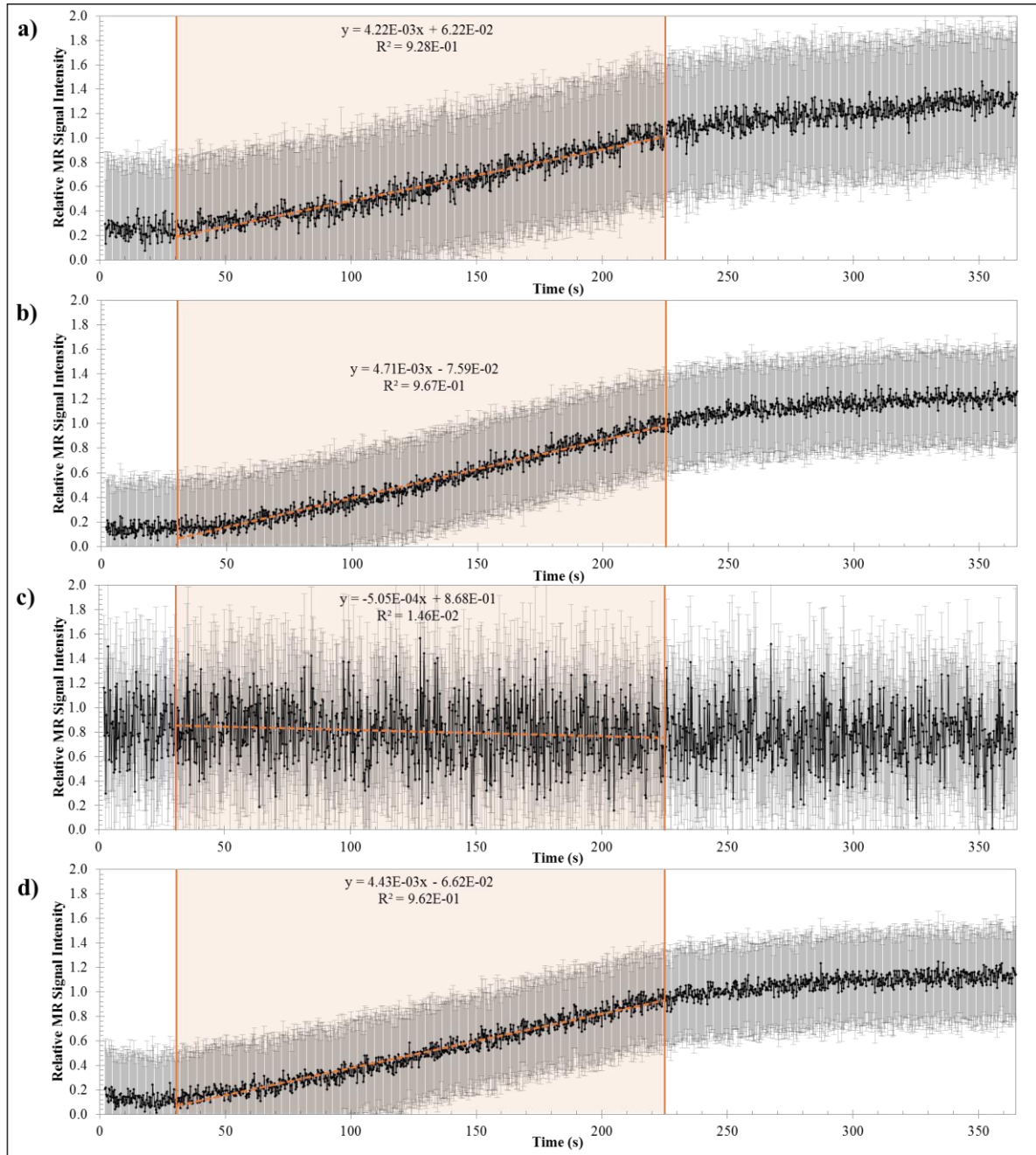


Figure 4: Relative MR signal intensities during real-time acquisition of a) FOX, b) FCX, c) FPX, and d) FXG. The orange shaded regions indicate beam-on times. Linear fits in the beam-on sections are also indicated. The error bars in Figure 4 represent the propagated standard deviation from the regions of interest measured within the irradiated region and outside the irradiated region in each dosimeter.

Unlike visual inspection of the gels' optical and MRI response, real-time relative MR signal intensity plots demonstrated that a) FOX and d) conventional FXG were similar in terms of slope and linearity. Again, c) FPX showed minimal MR change during and after irradiation (slope during irradiation was -0.0005 relative MR signal intensity/time). The significant result of this first demonstration of 2D real-time dose acquisition with iron-based gels (except for c) FPX) in the MR-Linac was that the real-time relative MR signal intensity change was linear with respect to time and therefore dose with a constant dose rate of approximately 540 ± 10 cGy/minute ($R^2 = 0.928, 0.967$, and 0.962 for a) FOX, b) FCX, and d) FXG, respectively). This result indicated that the conversion of iron(II) to iron(III) due to free radicals produced from irradiation of water molecules occurred quickly enough to capture their production in real-time in MR-IGRT systems [62]. The overall net percent signal intensity increases in real-time were $24.4 \pm 10\%$, $21.0 \pm 5\%$, $3.1 \pm 5\%$, and $22.2 \pm 6\%$ for a) FOX, b) FCX, c) FPX, and d) FXG, respectively (Figure 4). The net percent signal intensity increases from the post-irradiation T1-weighted images were $47.1 \pm 2\%$, $32.7 \pm 1\%$, $6.3 \pm 1\%$, and $32.2 \pm 1\%$ for a) FOX, b) FCX, c) FPX, and d) FXG, respectively (Figure 3).

FOX and FXG were further compared optically after irradiations using a Co-60 source (Figure 5). The Co-60 doses were calculated accounting for exponential decay of the source and PDD using BJR Supplement 25 depending on the SSD, depth of measurement, and field size [128]. Complete spectra were acquired for several different dose levels, and the dose responses at each of the two peaks observed with both gels were evaluated. The optical results for FOX and FXG again agreed that FOX was more sensitive to megavoltage irradiation when compared to FXG at both of their respective spectral peaks. The optical calibration curves for FOX and FXG were fit linearly ($R^2 = 0.98$ to 1.00) at their spectral peaks of 430 nm and 585 nm for FOX and 445 nm and 585 nm for FXG. Since the control measurements of 0 Gy were included in the linear fit calculation, the fits were not forced to intercept at 0. 430 nm and 445 nm are both near the wavelengths absorbed for an observed color of yellow. 585 nm is near the wavelengths absorbed for an observed color of purple. As the irradiated dosimeters undergo an optical color change from yellow to purple after iron(III) forms a complex with xylenol orange, the

contribution of yellow decreases while the contribution of purple increases (therefore the signal at 430 nm and at 445 nm for FOX and FXG, respectively, decrease while the opposite is true at 585 nm). The optical spectra and spectral peaks differ between FOX and FXG due to their different chemical contributions of iron, resulting in differences in the absorbance of light. The calibration curves for FOX were 114% and 54% greater for the yellow and purple spectral peaks, respectively, compared to FXG. The error bars in the calibration curves were smaller than the symbols and represented the standard deviation of three spectrophotometer readings per sample. Uncertainties due to batch (within and between) variabilities were further investigated for FOX only in Chapter 3 (Figure 26).

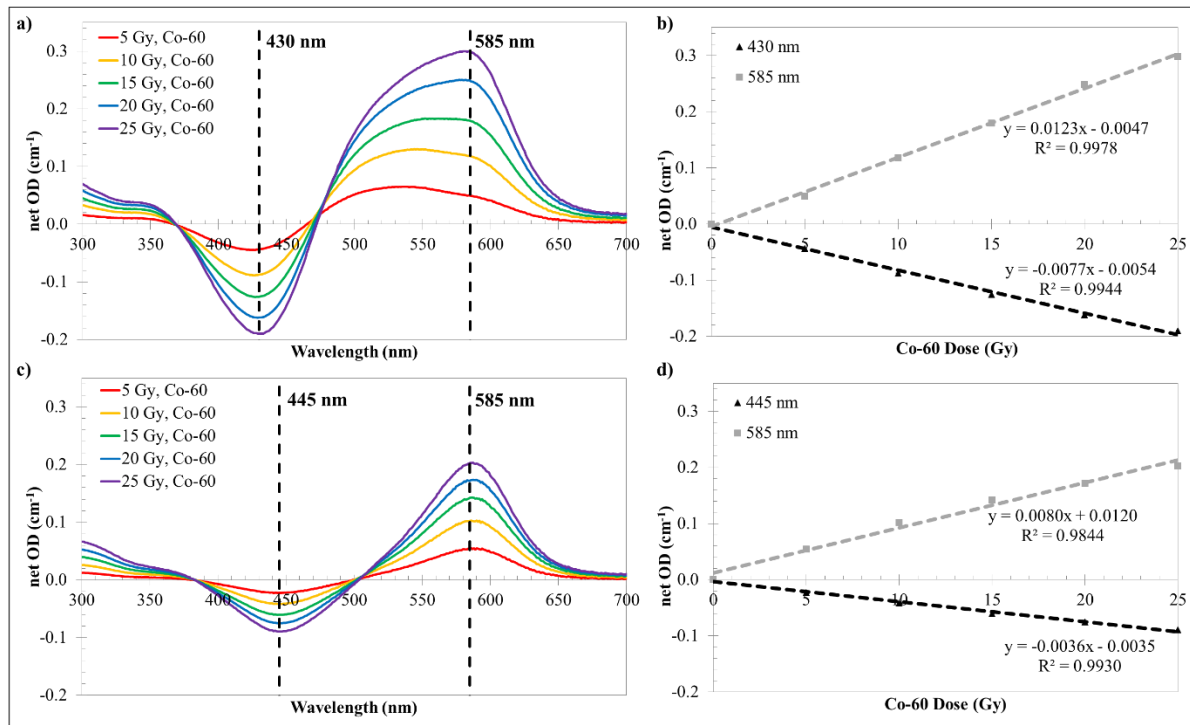


Figure 5: Optical response of FOX and FXG. a) Spectral response of FOX, b) linear optical response of FOX at spectral peaks of 430 nm and 585 nm ($R^2 = 0.9944$ and 0.9978 , respectively), c) spectral response of FXG, and d) linear optical response of FXG at spectral peaks of 445 nm and 585 nm ($R^2 = 0.9930$ and 0.9844 , respectively). The error bars in the calibration curves were smaller than the symbols and represented the standard deviation of three spectrophotometer readings per sample.

The overall comparison of the four iron types demonstrated that the FOX formulation was the best candidate from the iron(II) oxidation formulations for future MR-IGRT studies. The FOX

formulation demonstrated greater optical and MR contrast when compared to the other iron(II) oxidation formulations (up to 114% greater optical response, 10% greater real-time MR response, and 46% greater post-irradiation T1-weighted MR response when compared to conventional FXG).

All of the above iron(II) oxidation formulations were then tested using sodium thiocyanate as the reporter compound instead of xylenol orange to investigate changes in optical and MR contrast. These four iron(II) oxidation gel formulations were referred to as FASST (ferrous ammonium sulfate – sodium thiocyanate), FOST (ferrous oxide – sodium thiocyanate), FCST (ferrous chloride – sodium thiocyanate), and FPST (ferrous phthalocyanine – sodium thiocyanate) with the compositions the same as FXG, FOX, FCX, and FPX except for replacing 0.05 mM xylenol orange with 1.0 mM sodium thiocyanate. Sodium thiocyanate formed a red complex in the presence of iron(III) due to the formation of $[\text{Fe}(\text{SCN}) \cdot (\text{H}_2\text{O})_5]^{2+}$ while remaining colorless clear in the presence of iron(II) (Figure 6).

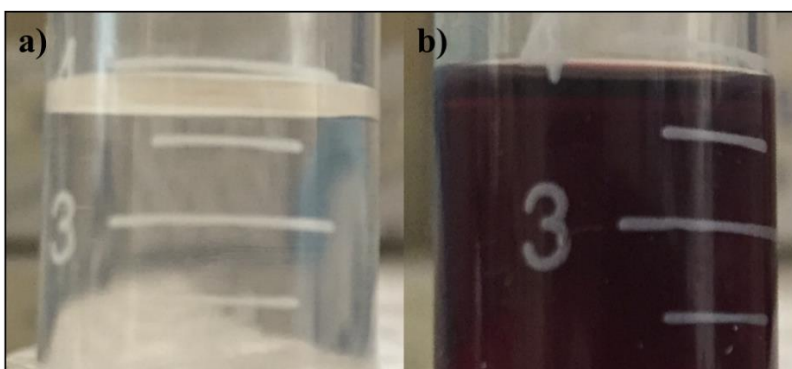


Figure 6: Sample of FCST in solution (without gelatin) with a) un-irradiated iron(II)-containing sample and b) approximately 40 Gy irradiated iron(III)-containing sample using Co-60 source showing color change from a) colorless to b) blood red characteristic of thiocyanate indicators in the presence of iron(III).

Unlike xylenol orange, using sodium thiocyanate did not result in any MR changes when irradiated to the same doses, suggesting that the sensitivity of this formulation was inadequate for conventional radiation therapy dosimetry (Figure 7). The optical changes were also minimal for this dose range, so again, the FOX formulation remained the ideal candidate for further MR-IGRT applications. The net percent signal intensity increases from the post-irradiation T1-weighted images

were $6.1 \pm 2\%$, $6.9 \pm 1\%$, $4.6 \pm 2\%$, and $6.0 \pm 2\%$ for a) FOST, b) FCST, c) FPST, and d) FASST, respectively. In the future, other thiocyanate compounds and their interactions with gelling agents could be investigated for improved optical and MR changes post-irradiation.

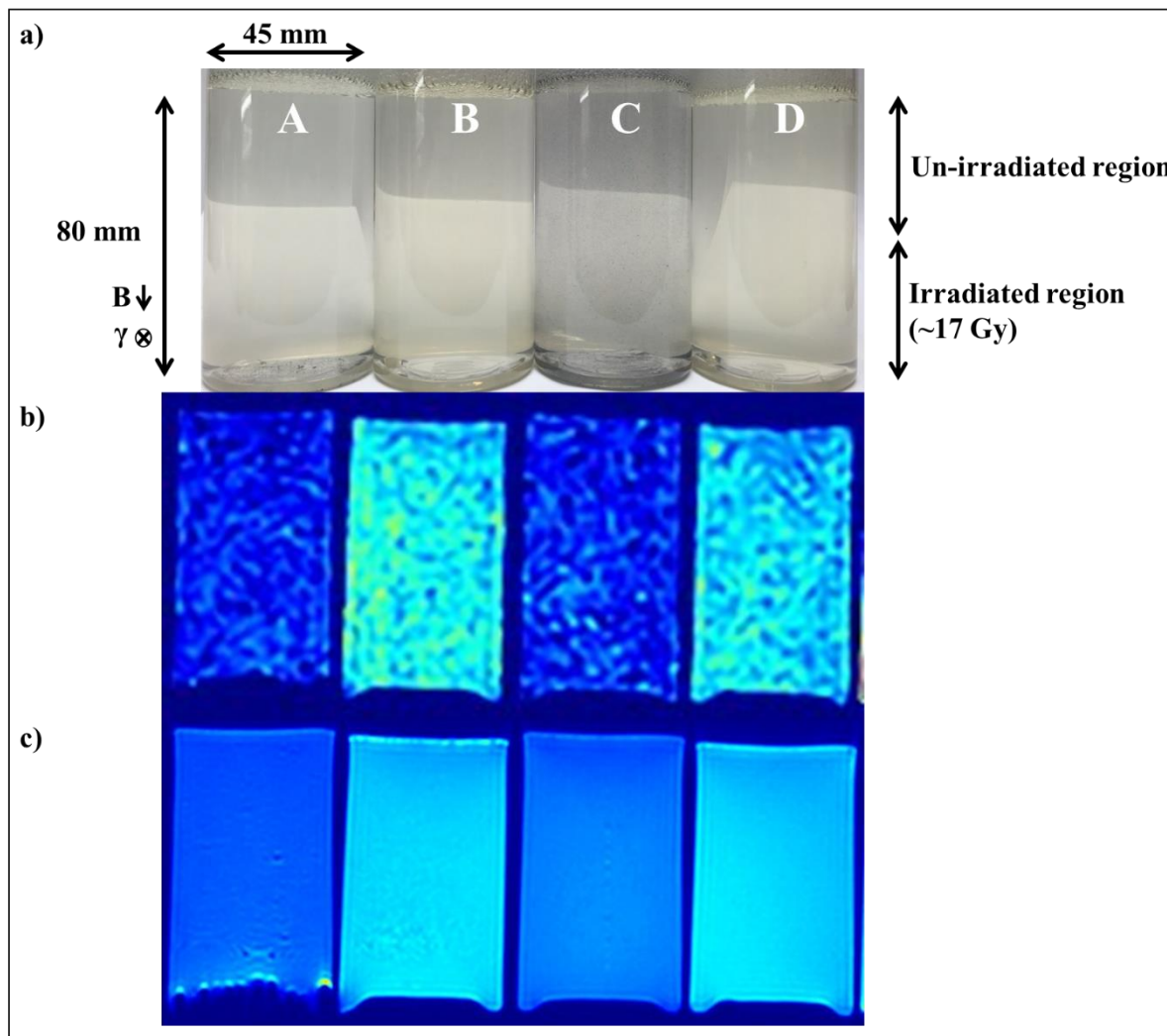


Figure 7: a) Pictures of physical dosimeters where A – FOST, B – FCST, C – FPST, and D – FASST. The top half of each gel was not irradiated, and the bottom half was irradiated to approximately 17 Gy. b) Snapshots of bFFE acquisitions with $TR/TE = 5/2.4$ ms. c) Post-irradiation acquisitions with TSE $TR/TE = 500/20$ ms. MR images shown with color instead of grayscale to emphasize contrast.

2.3 Iron(III) reduction gel formulations

The rationale for investigating iron(III) reduction gel formulations was due to the instability of iron(II) oxidation gels (such as shown by the already oxidized purple FXG and FCX gels prior to

irradiation) (Figure 3) and due to previous studies suggesting slower diffusion [129, 130]. The overall iron(III) reduction gel fabrication, irradiation set-up, and MRI techniques were the same as those listed above for the iron(II) oxidation gel formulations. One already existing iron(III) reduction formulation was assessed (Turnbull blue (TBG)) along with two additional iron(III) sources.

The TBG formulation was created based on photography film processing reactions [131–133]. The Turnbull blue or Prussian blue color was formed during the cyanotype process first invented by John Frederick William Herschel. The TBG formulation consists of potassium ferricyanide, iron(III) chloride, and iron(III) ammonium citrate. After irradiation, organic free radicals are created and reduce iron(III) to iron(II), which then interact with potassium ferricyanide (red prussiate of iron), ultimately forming the dye Turnbull blue or Prussian blue by following two possible pathways:



with the iron(III) components in orange and the iron(II) components in blue and the **Turnbull blue** $\text{Fe}[\text{Fe}(\text{CN})_6]^-$ product in bold font.

Several different combinations of concentrations of the chemical components in TBG were presented by previous studies, and the formulation listed in Table 5 was found to be the most sensitive to megavoltage irradiation [129, 130, 134, 135]. Initial investigations of TBG were done in solution (no gelling agent).

Table 5: Chemical components of TBG formulation.

Component	Chemical formula	Concentration
Potassium ferricyanide	$\text{K}_3\text{Fe}(\text{CN})_6$	1.5 mM
Iron(III) chloride	FeCl_3	0.45 mM
Iron(III) ammonium citrate	$\text{C}_6\text{H}_8\text{O}_7 \cdot \text{FeNH}_3$	1.5 mM
Water	H_2O	~97-100 wt %
Hydrochloric acid	HCl	5 mM
Gelatin	$(\text{C}_{17}\text{H}_{32}\text{H}_5\text{O}_6)_x$	0-3 wt %

The FT (ferric chloride – triphenylamine) formulation consisted of iron(III) chloride (Sigma-Aldrich), triphenylamine (Sigma-Aldrich), and chloroform (Sigma-Aldrich) (Table 6). The FT formulation was only investigated in solution form due to using chloroform as the solvent. Future work could investigate the FT formulation in micelle form in a gelatin-based gel. After iron(III) is converted to iron(II), it forms a complex with triphenylamine that appears green.

Table 6: Chemical components of FT formulation.

Component	Chemical formula	Concentration
Iron(III) chloride	FeCl_3	2 mM
Triphenylamine	$(\text{C}_6\text{H}_5)_3\text{N}$	81 mM
Chloroform	CHCl_3	~100 wt %
Hydrochloric acid	HCl	276 mM

The FO (ferric ammonium oxalate – *o*-phenanthroline) formulation consisted of iron(III) ammonium oxalate trihydrate (Sigma-Aldrich), *o*-phenanthroline or 1,10-phenanthroline (Sigma-Aldrich), and water (Table 7). *o*-phenanthroline must first be dissolved in ethanol before combining with the other chemical components. After iron(III) is converted to iron(II), it forms a complex with *o*-phenanthroline that appears red with a 1:3 ratio.

Table 7: Chemical components of FO formulation.

Component	Chemical formula	Concentration
Iron(III) ammonium oxalate trihydrate	$(\text{NH}_4)_3[\text{Fe}(\text{C}_2\text{O}_4)_3] \cdot 3\text{H}_2\text{O}$	28 mM
<i>o</i> -phenanthroline	$\text{C}_{12}\text{H}_8\text{N}_2 \cdot \text{FeNH}_3$	26 mM
Ethanol	$\text{C}_2\text{H}_6\text{O}$	5 wt %
Water	H_2O	~91 wt %
Sulfuric acid	H_2SO_4	17 mM
Gelatin	$(\text{C}_{17}\text{H}_{32}\text{H}_5\text{O}_6)_x$	4 wt %

2.3.2 Iron(III) reduction results and discussion

The TBG formulation responded linearly optically (OD) with respect to Co-60 dose at its spectral peak of 690 nm. 690 nm is within the absorbed wavelength range for an observed color of green/blue. However, this optical response was not immediately linear and took at least 72 hours to develop (Figure 8). The appearance of an offset in the dose response curve even after 72 hours may be

due to a gradual darkening of the gel with time following preparation, rather than a nonlinearity of response at low dose levels. The error bars in the calibration curve were smaller than the symbols and represented the standard deviation of three spectrophotometer readings per sample.

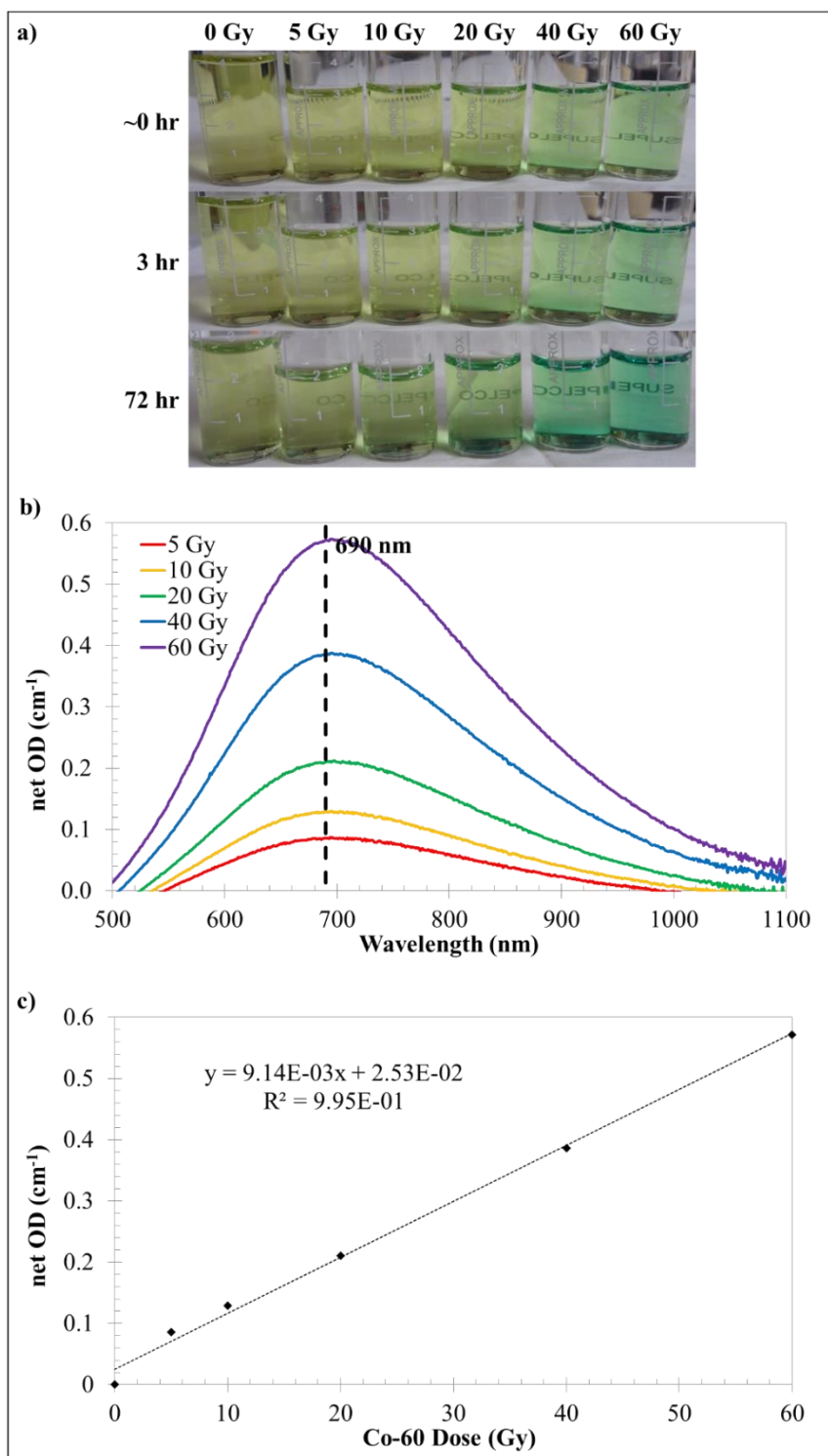


Figure 8: Post-irradiation response of TBG in solution (no gelatin). a) Pictures of TBG irradiated to 0, 5, 10, 20, 40, and 60 Gy using a Co-60 source immediately post-irradiation, 3 hours post-irradiation, and 72 hours post-irradiation. b) Spectral response of TBG 72 hours after irradiation. c) Calibration curve of TBG 72 hours after irradiation at the spectral peak 690 nm. The error bars in the calibration curve were smaller than the symbols and represented the standard deviation of three spectrophotometer readings per sample.

The TBG formulation was then tested in the MR-Linac in 2 wt % and 3 wt % gelatin to investigate whether any MR contrast could be detected after approximately 30 Gy (Figure 9). TBG in 2 wt % gelatin showed an increase in MR signal intensity of approximately 0.6% post-irradiation of approximately 30 Gy. TBG in 3 wt % gelatin showed an increase in MR signal intensity of approximately 5.1% after absorbing the same dose of 30 Gy. Due to the delayed optical dose response over time (Figure 8) and the minimal MR changes post-irradiation (Figure 9), the TBG formulation was not further investigated for MR-IGRT applications.

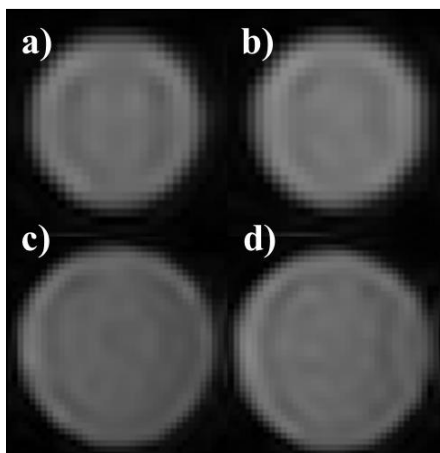


Figure 9: MR images of TBG. a) TBG in 2 wt % gelatin pre-irradiation, b) TBG in 2 wt % gelatin post-irradiation of approximately 30 Gy, c) TBG in 3 wt % gelatin pre-irradiation, and d) TBG in 3 wt % gelatin post-irradiation of approximately 30 Gy.

While the TBG formulation was not found to be useful for MR-IGRT applications, future investigations of TBG could involve incorporating it into gel matrixes other than gelatin as an ultraviolet (UV) light dosimeter (Figure 10). A preliminary evaluation of the response of TBG to UV exposure demonstrated that a visible optical response took place following exposure when incorporated into different matrixes (sodium polyacrylate ball and powder and Encapso® K rubber) (Figure 10).

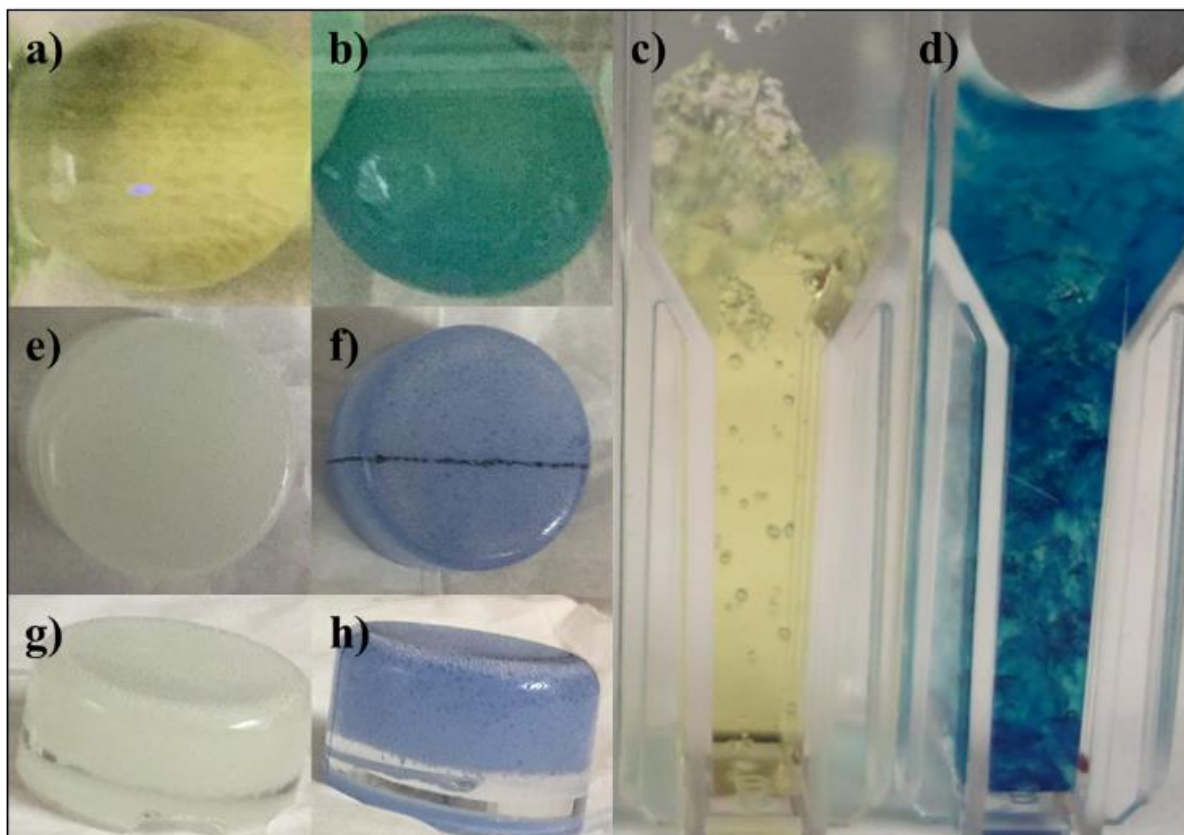


Figure 10: a) TBG incorporated into sodium polyacrylate ball prior to UV exposure, b) TBG post UV exposure, c) TBG incorporated into sodium polyacrylate powder prior to UV exposure, d) TBG post UV exposure, e) TBG incorporated into Encapso® K rubber prior to UV exposure, f) TBG post UV exposure, g) side view of e, and h) side view of f.

Similar to the TBG formulation, the FT formulation was also found to have a delayed linear optical response to irradiation. Unlike TBG, FT's spectral response had three peaks (407 nm, 485 nm, and 650 nm). 407 nm is bordering the ultraviolet light absorption wavelength range and therefore cannot necessarily be correlated to optical observed color. 485 nm is in the absorbed wavelength range for an observed color of yellow/orange, and 650 nm is in the absorbed wavelength range for an observed color of green/blue. The calibration curve is plotted below for the spectral peak of 650 nm with a near-linear fit with $R^2 = 0.98$ (Figure 11) The error bars in the calibration curve were smaller than the symbols and represented the standard deviation of three spectrophotometer readings per sample.

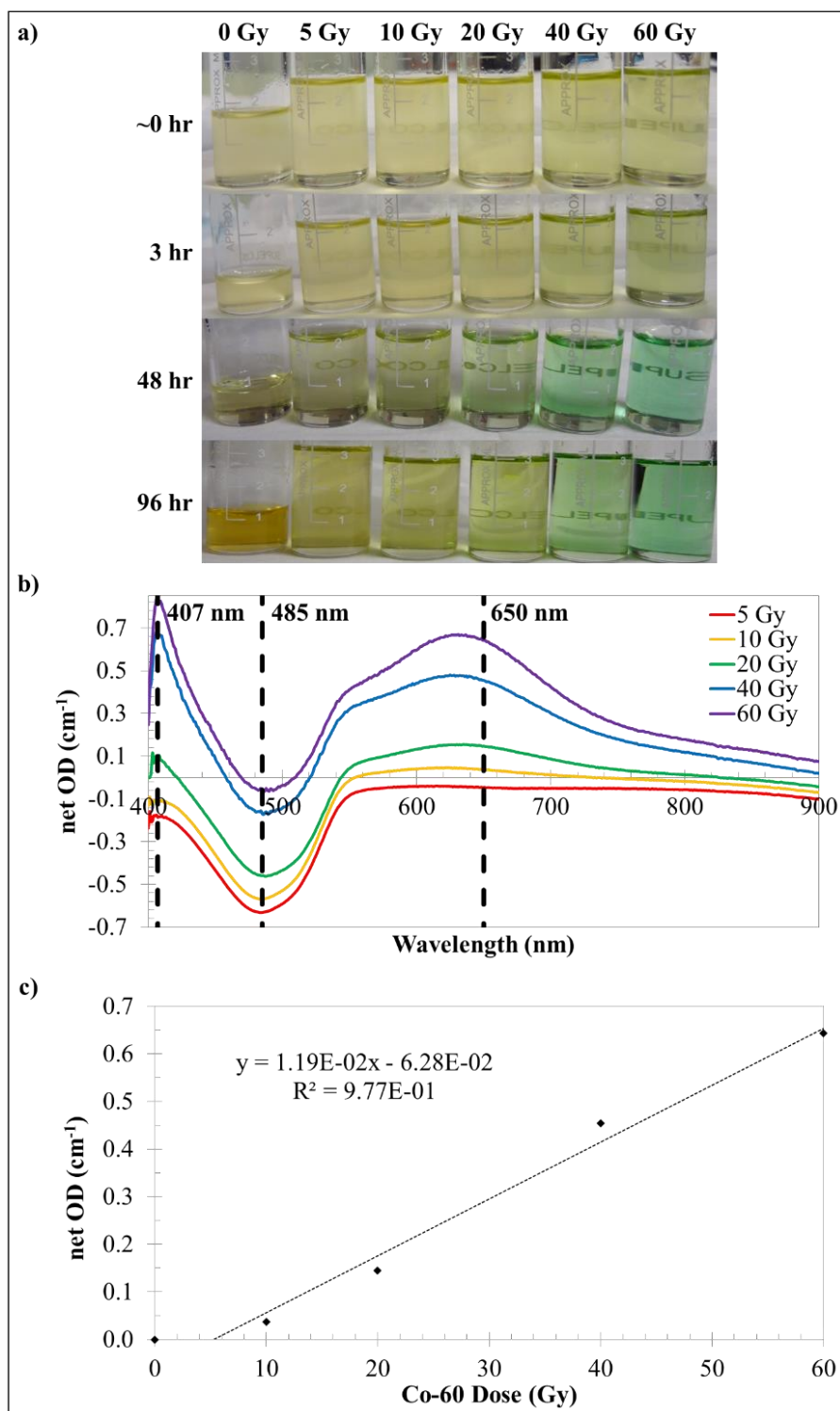


Figure 11: Post-irradiation response of FT in solution. a) Pictures of FT irradiated to 0, 5, 10, 20, 40, and 60 Gy using a Co-60 source immediately post-irradiation, 3 hours post-irradiation, 48 hours post-irradiation, and 96 hours post-irradiation. b) Spectral response of FT 96 hours after irradiation. c) Calibration curve of FT 96 hours after irradiation at the spectral peak 650 nm. The error bars in the calibration curve were smaller than the symbols and represented the standard deviation of three spectrophotometer readings per sample.

Since FT was found to have a delayed optical response and could not easily be incorporated into a gel matrix, it was not further investigated for MR contrast. However, future investigations of FT could involve incorporating it into other matrixes as an ultraviolet light dosimeter (Figure 12).

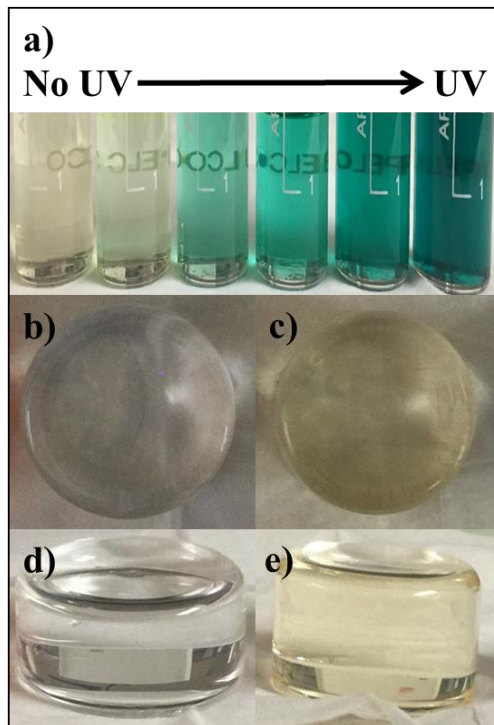


Figure 12: a) FT in solution showing color change from colorless clear to dark green with increasing UV exposure, b) FT incorporated into Encapso® K rubber prior to UV exposure, c) FT post UV exposure (yellow color change), d) side view of b, and e) side view of c.

Unlike the TBG and FT formulations, the FO formulation was found to give an immediate linear optical response post-irradiation up to at least 100 Gy at its spectral peak of 512 nm (Figure 13). 512 nm is within the absorbed wavelength range for an observed color of red. Since one of polymer gel's main disadvantages was its oxygen dependence, the oxygen dependence of FO was investigated along with its dose rate dependence, shelf-life time, and gelatin percentage dependence on sensitivity. In order to test oxygen dependence, FO in solution was degassed with N₂ for 10 minutes per sample to remove dissolved O₂ (Figure 14). While the exact concentration of O₂ was not measured after degassing, the bubbling of a chemically inert gas (such as N₂ used in this case) can remove dissolved gases such as O₂ from solution (degasification is also commonly called sparging in chemistry). After removal of

O₂, the sensitivity of FO to irradiation was increased about 6.0%. Deoxygenation of PRESAGE® was found to increase the sensitivity by approximately 30% whereas deoxygenation of FXG was found to decrease the sensitivity [136, 137]. The linearity of the dose response was not affected for FO or for PRESAGE® and FXG in the literature. The error bars in the calibration curves in Figure 13 and Figure 14 represented the standard deviation of spectrophotometer measurements averaged for three cuvettes per dose level.

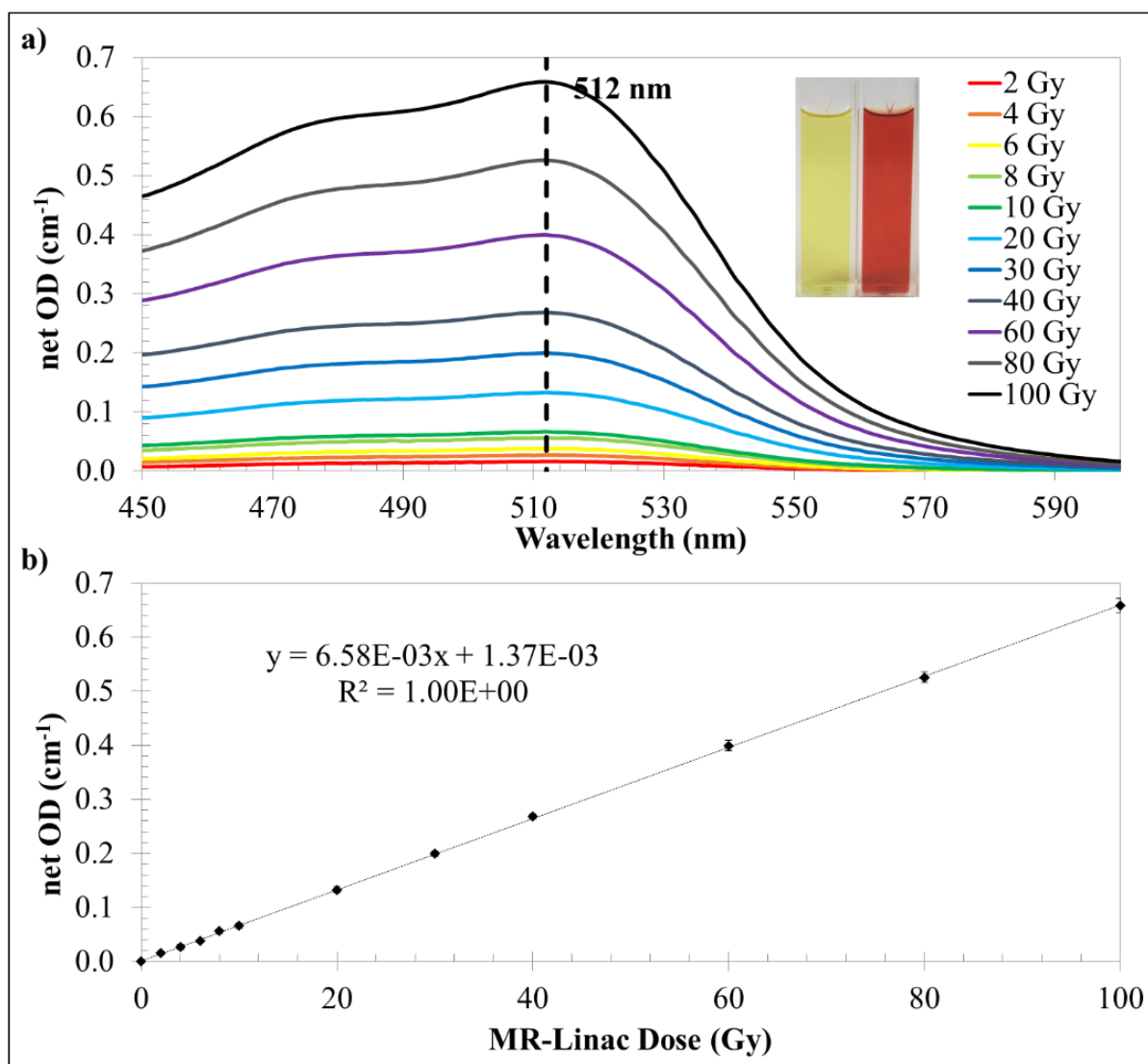


Figure 13: a) Spectral response of FO immediately after irradiation (inset image shows FO before irradiation – yellow and after irradiation – red). c) Calibration curve of FO at the spectral peak 650 nm. The error bars in the calibration curve represented the standard deviation of spectrophotometer measurements averaged for three cuvettes per dose level.

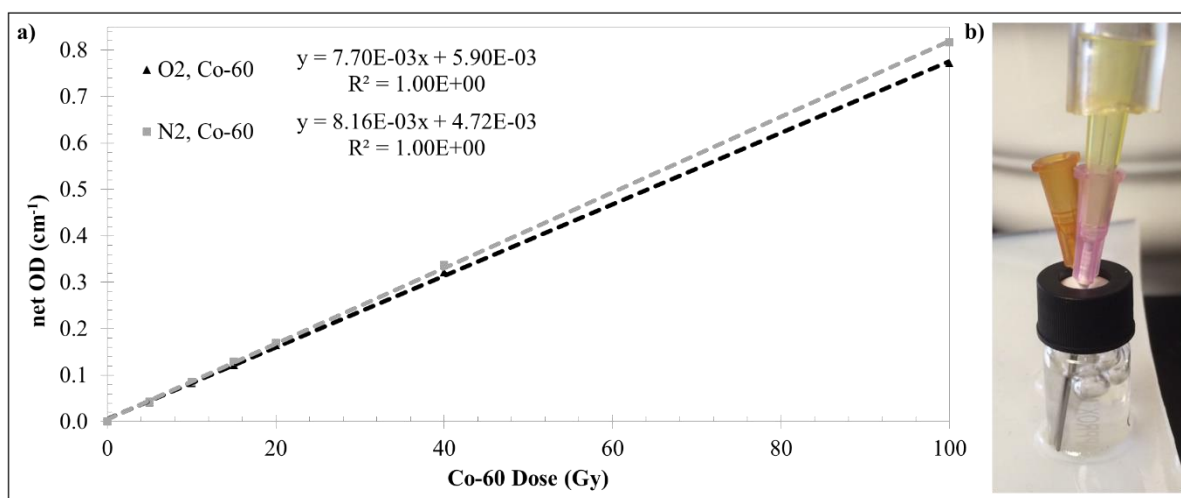


Figure 14: Oxygen dependence test of FO in solution by O₂ degassing with N₂ for 10 minutes. a) Calibration curves of FO with and without O₂ and b) example set-up for degassing with N₂ into the solution with a vent (actual set-up was covered to prevent light affecting the samples). The error bars in the calibration curves represented the standard deviation of spectrophotometer measurements averaged for three cuvettes per dose level.

The dose rate dependence of FO was tested using a Co-60 source at different distances from the source (Figure 15). The dose rate was approximated relative to distance from the source using the inverse square law ($\text{dose rate}_2 = \text{dose rate}_1 * (\text{distance}_1/\text{distance}_2)^2$), so the dose rate at 100 cm source to surface distance (SSD) was 0.64 of the dose rate at 80 cm SSD. The error bars in the calibration curves in Figure 15 represented the standard deviation of spectrophotometer measurements averaged for three cuvettes per dose level.

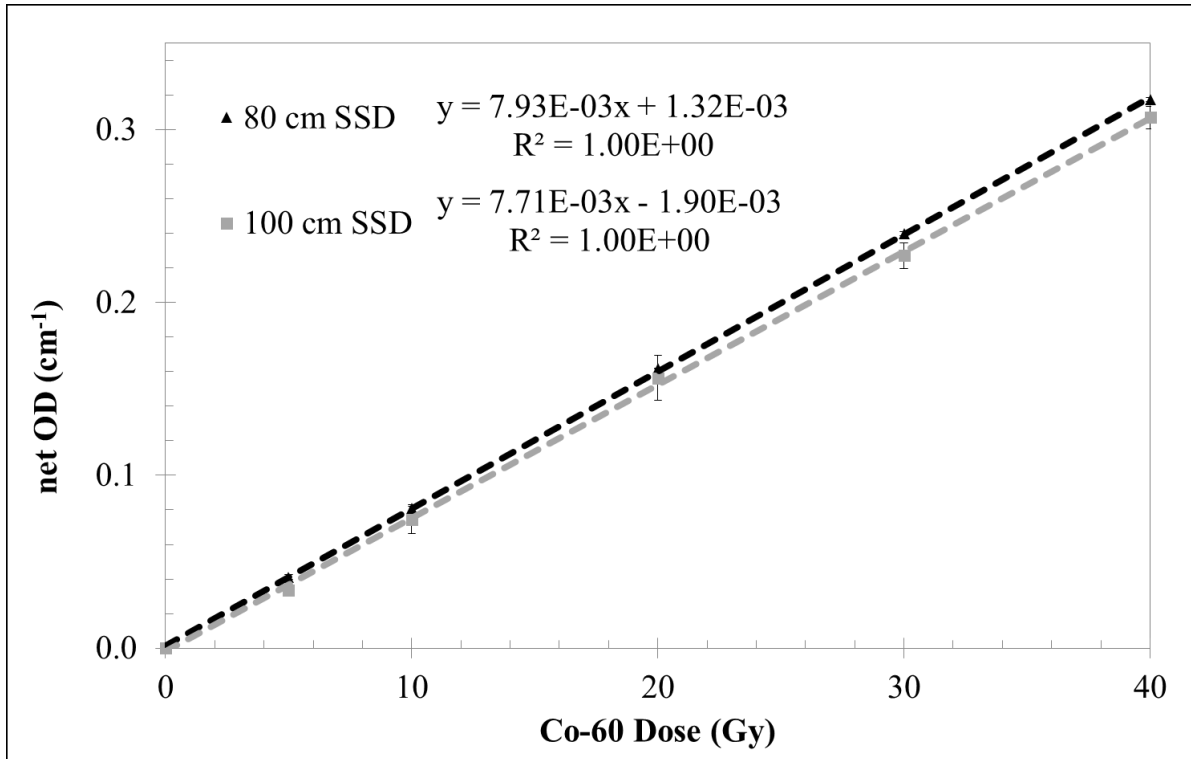


Figure 15: Dose rate dependence of FO. The error bars in the calibration curve represented the standard deviation of spectrophotometer measurements averaged for three cuvettes per dose level.

The shelf-life of FO and its effect on dose response sensitivity was tested in light-tight environments both at room temperature (RT) and at 4 °C (Figure 16). After 1 week of storage, the calibration curves after irradiation were 2.3% and 0.8% decreased in slope for RT and 4 °C, respectively, when compared to immediate preparation of FO prior to irradiation. After 2 weeks of storage, the calibration curves after irradiation were 4.6% and 2.1% decreased in slope for RT and 4 °C, respectively, when compared to immediate preparation of FO prior to irradiation. Future work should include batch uncertainties to better quantify the uncertainties in the changes of these calibration curves. The calibration curves decreased in slope more for RT than for 4 °C after both 1 week and 2 weeks of storage. The calibration curves decreased in slope, regardless of storage temperature, when compared to immediate preparation prior to irradiation.

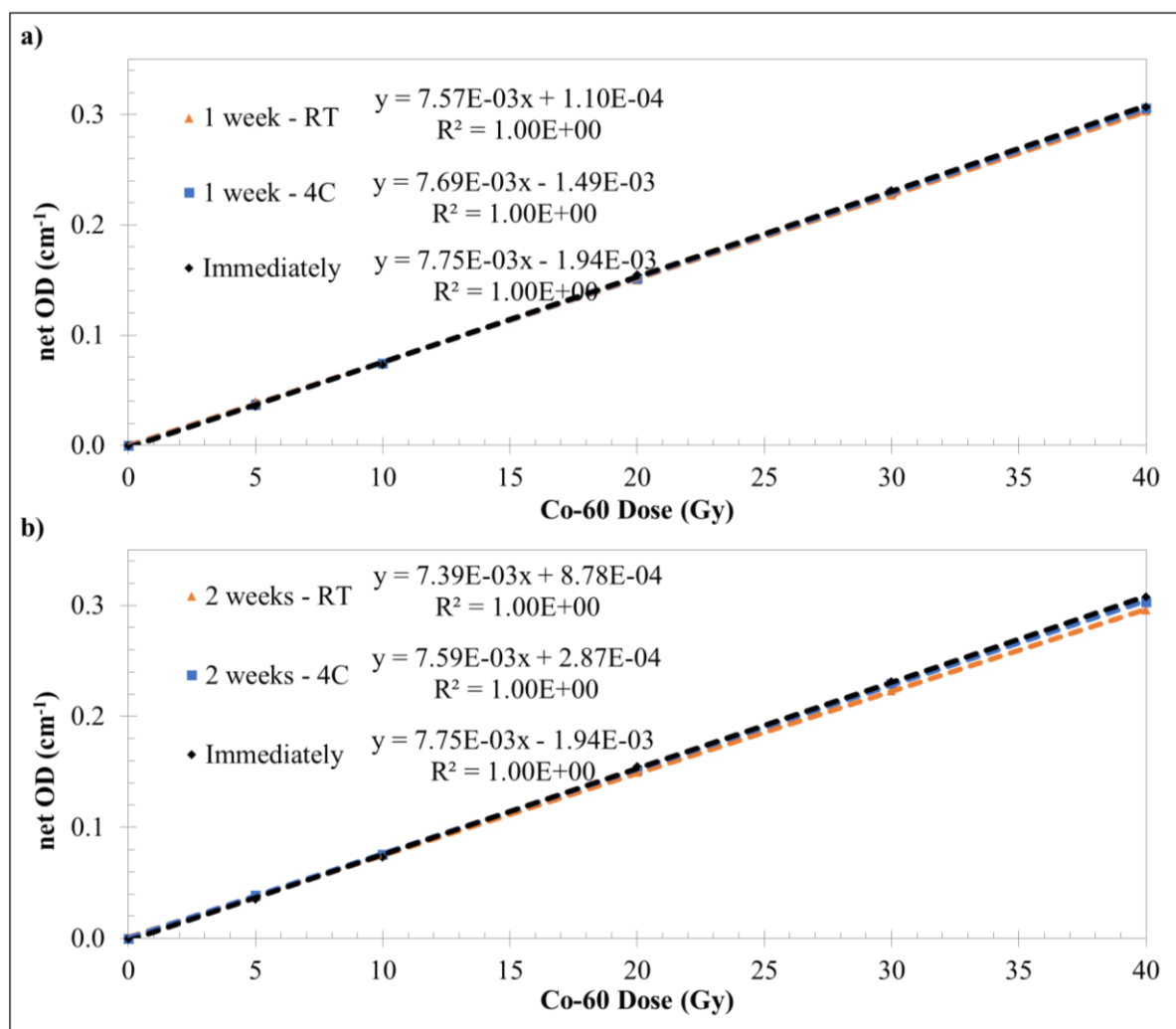


Figure 16: a) Calibration curves of FO in solution (no gelatin) after storage at room temperature (RT) and 4 °C (4C) for 1 week compared to immediately prior to irradiation and b) after storage for 2 weeks. The error bars in the calibration curves represented the standard deviation of spectrophotometer measurements averaged for three cuvettes per dose level.

The dependence of sensitivity of FO on gelatin concentration was then investigated between 1.5 and 5 wt %. Greater gelatin concentrations increased the background OD of samples prior to irradiations (Figure 17). The post-irradiation sensitivities were most similar for 1.5 and 2 wt % and for 3 and 5 wt % gelatin. The overall calibration curve slopes decreased with increasing gelatin concentration, which agreed with the literature for FXG [137].

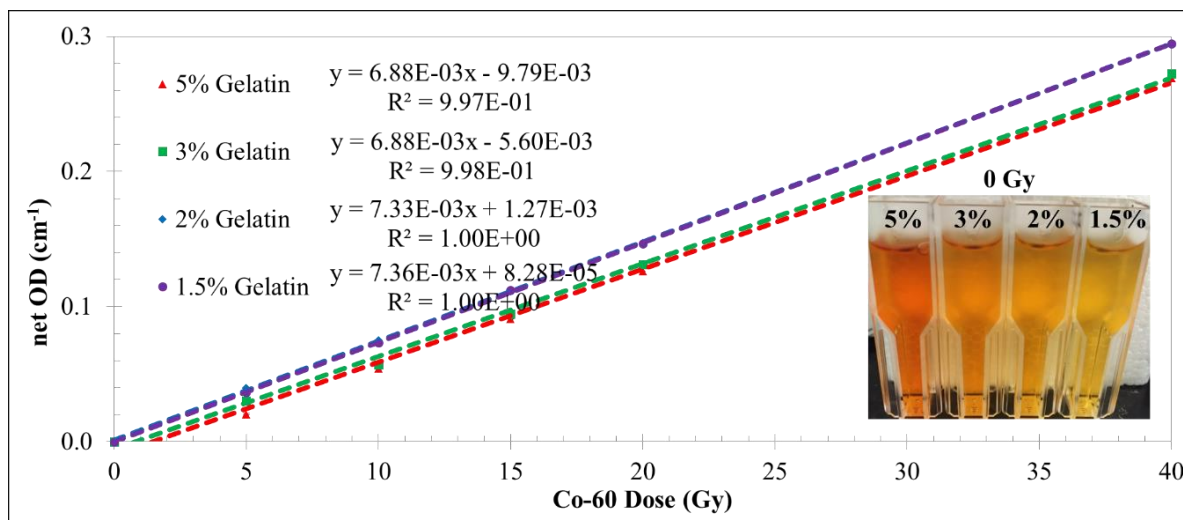


Figure 17: Gelatin percentage dependence on FO sensitivity (inset image shows differences in OD of samples prior to irradiations depending on gelatin percentage). The error bars in the calibration curves represented the standard deviation of spectrophotometer measurements averaged for three cuvettes per dose level.

After characterizing the FO formulation for optical linearity with radiation dose, oxygen dependence, dose rate dependence, shelf-life, and gelatin percentage dependence with no effects on the linearity of the response for all the above, FO was then imaged with MRI in the MR-Linac. Alongside FO, the following combinations were investigated for MR contrast (Table 8). 2,2'-Bipyridine was a similar reporter component to *o*-phenanthroline that also formed complexes with iron(II) resulting in a red color post-irradiation.

Table 8: Iron(III) combinations for investigation in the MR-Linac.

Iron(III) component	Reporter component	Name of formulation
Iron(III) ammonium oxalate trihydrate	<i>o</i> -phenanthroline	FO
Iron(III) citrate	<i>o</i> -phenanthroline	FCO
Iron(III) ammonium oxalate trihydrate	2,2'-Bipyridine	FB
Iron(III) citrate	2,2'-Bipyridine	FCB

However, similar to TBG, FO also did not result in a clearly distinguishable MR signal intensity change post-irradiation of approximately 34 Gy (Figure 18). The net percent signal intensity increases from the post-irradiation T1-weighted images were $8.8 \pm 1\%$, $11.0 \pm 1\%$, $8.1 \pm 1\%$, and $8.8 \pm 2\%$ for a) FO,

b) FCO, c) FB, and d) FCB, respectively. Similarly to TBG and FT, future investigations of FO could involve incorporating it into other matrixes as an ultraviolet light dosimeter (Figure 19).

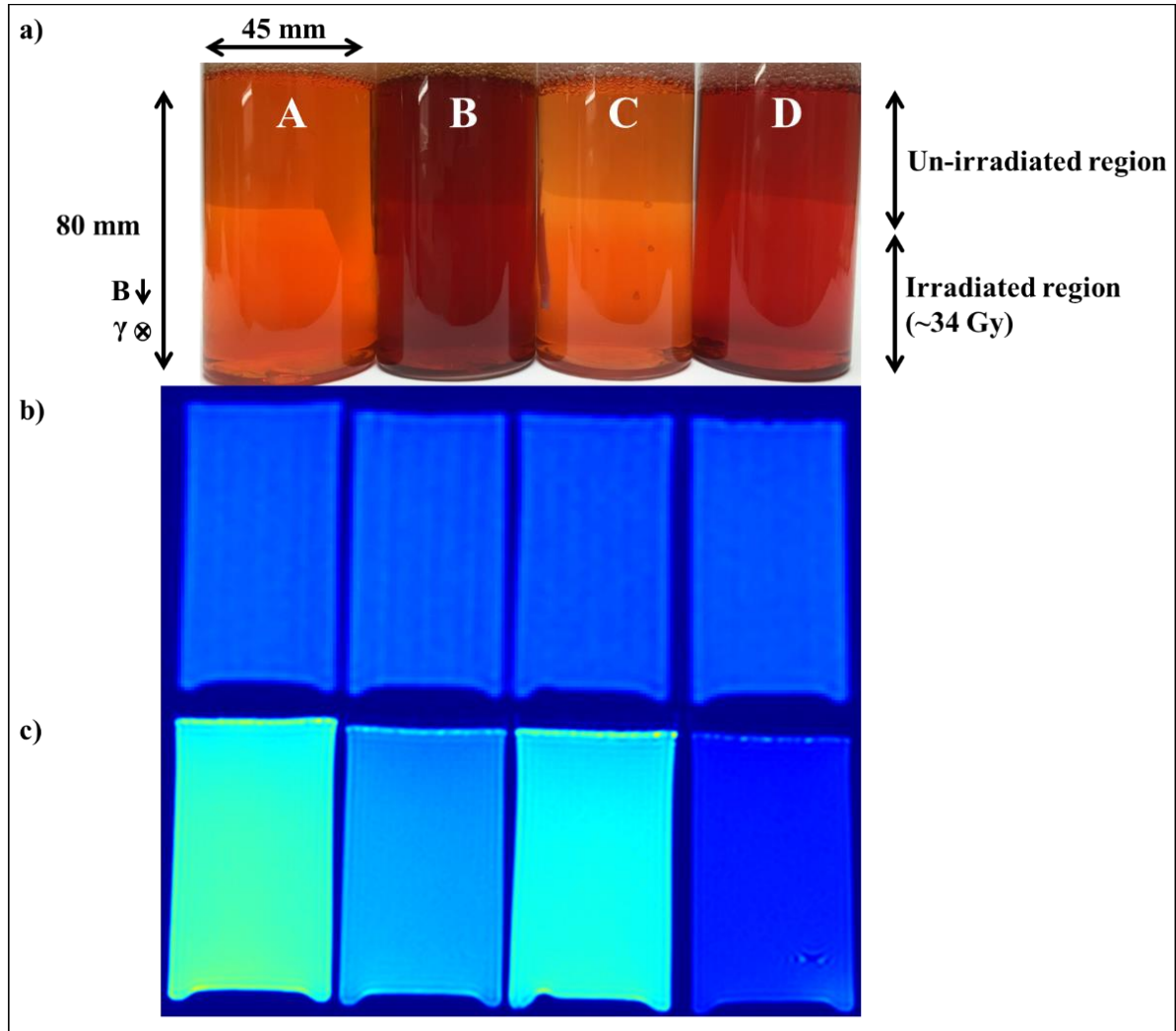


Figure 18: a) Pictures of physical dosimeters where A – FO, B – FCO, C – FB, and D – FCB. The top half of each gel was not irradiated, and the bottom half was irradiated to approximately 34 Gy. b) Snapshots of bFFE acquisitions with $TR/TE = 5/2.4$ ms. c) Post-irradiation acquisitions with TSE $TR/TE = 500/20$ ms. MR images shown with color instead of grayscale to emphasize contrast.

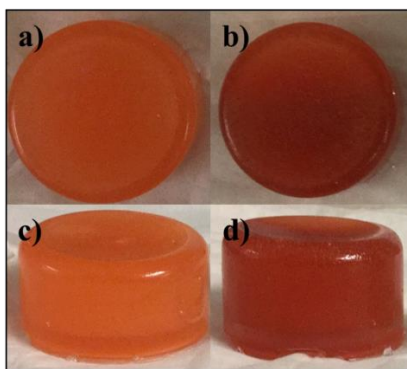


Figure 19: a) FO incorporated into Encapso® K rubber prior to UV exposure, b) FO post UV exposure (red color change), c) side view of a, and d) side view of b.

2.4 Summary

After comparisons of iron(II) and iron(III) formulations optically and with MRI, the iron(II) formulation FOX had the greatest optical and MR contrast. FOX changed linearly with respect to dose for both optical and MR read-out, both immediately post-irradiation and in real-time during irradiation. Whereas iron(III) formulations, such as FO, responded linearly with respect to dose up to at least 100 Gy, its response could not be accurately measured using MRI at clinically relevant quality assurance dose levels. Overall, iron(II) formulations are recommended for MR-IGRT applications, and iron(III) formulations are recommended for UV applications (preliminary results shown in Figure 10, Figure 12, and Figure 19). Further characterization of FOX is presented in Chapter 3.

Chapter 3 – Characterization of optimal radiochromic formulation

3.1 Rationale

Following identification of the most ideal candidate gel formulation for MR-IGRT applications in Chapter 2, the FOX and a reusable version of FOX (rFOX) formulations were characterized for their dose response. Since FOX depends on the oxidation of iron(II) after the radiolysis of water, rFOX was created with the addition of a reducing agent. Further explanation on the behavior of rFOX with respect to the reducing agent is presented in this chapter. Most importantly, for volumetric dose comparisons with planned dose presented in Chapter 5, the linearity of the dose response should be preserved regardless of the irradiation scenario to allow for linear scaling of MR signal intensity to relative dose. The dose linearity, radiological properties, reproducibility, time stability, energy dependence, reusability of rFOX, dose rate dependence, fractionation dependence, gel matrix dependence, and diffusion are presented in this chapter.

3.2 Dose linearity

As was mentioned in Chapter 2, dose linearity of FOX were important characteristics for eventual relative scaled dose comparisons with treatment planning system planned doses. A more detailed characterization of the linearity of FOX and rFOX are presented in this chapter.

3.2.1 Optical linearity

FOX is linear with radiation dose optically at its spectral peaks of 440 nm and 585 nm up to approximately 15 Gy and plateaus above 30 Gy up to at least 100 Gy (Figure 20). The error bars in the calibration curves represented the standard deviation of spectrophotometer measurements averaged for three cuvettes per dose level.

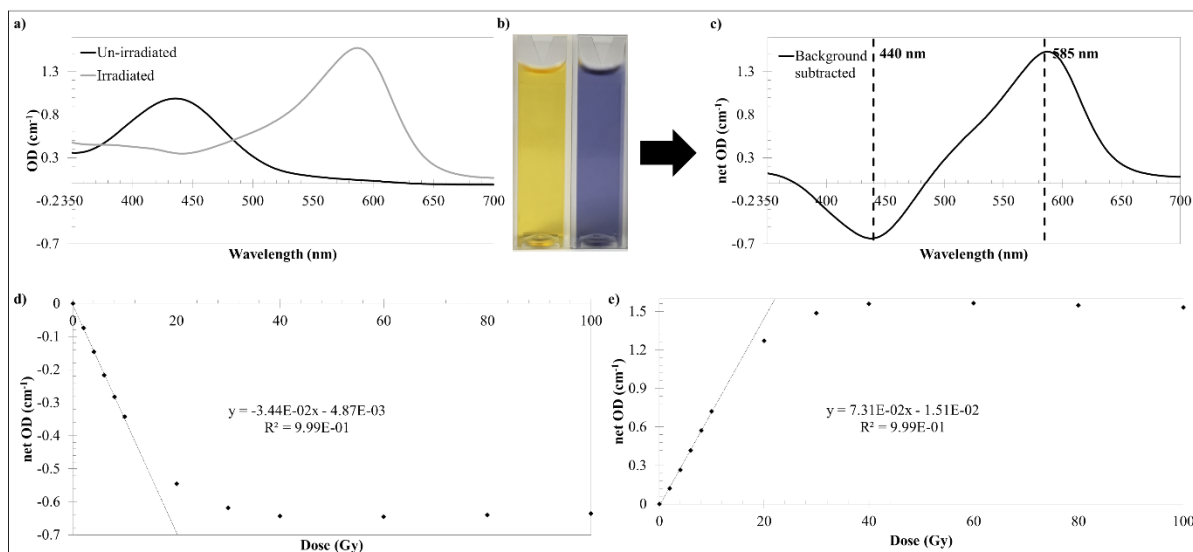


Figure 20: a) Representative absorption spectra of un-irradiated and irradiated FOX, b) un-irradiated yellow FOX on the left and irradiated purple FOX on the right, c) background subtracted spectrum with peaks at 440 nm and 585 nm, d) calibration curve at 440 nm, and e) calibration curve at 585 nm. The error bars in the calibration curves represented the standard deviation of spectrophotometer measurements averaged for three cuvettes per dose level.

Initial optical testing for rFOX was conducted using a clinical orthovoltage unit since immediate optical readings were not possible using the MR-Linac (and rFOX's signal decay had not yet been carefully investigated for optical read-out). Similarly to previous irradiation using a Co-60 source, orthovoltage doses were calculated using PDD tables in BJR Supplement 25[138]. Doses up to approximately 20 Gy were delivered to rFOX containing different levels of reducing agent (RA) that was responsible for making rFOX reusable (1 wt %, 3 wt %, and 5 wt %). The error bars in the calibration curves in Figure 21 represented the standard deviation of spectrophotometer measurements averaged for three cuvettes per dose level. The RA released iron(III) from its complex with xylenol orange and reduced it back to iron(II). For all concentrations of RA, rFOX was linear with respect to orthovoltage dose (Figure 21). The sensitivity of rFOX was reduced with increasing concentrations of RA. All calibration curve slopes dropped most significantly in the first 24 hours and continued to drop close to 0 (indicating the complete reversal of optical signal) up to 96 hours post-irradiation and was dependent on RA concentration (faster reversal for higher concentrations of RA). From these results,

an RA concentration of 9 wt % were used for larger volumetric rFOX dosimeters to ensure reversal of signal by at least 24 hours.

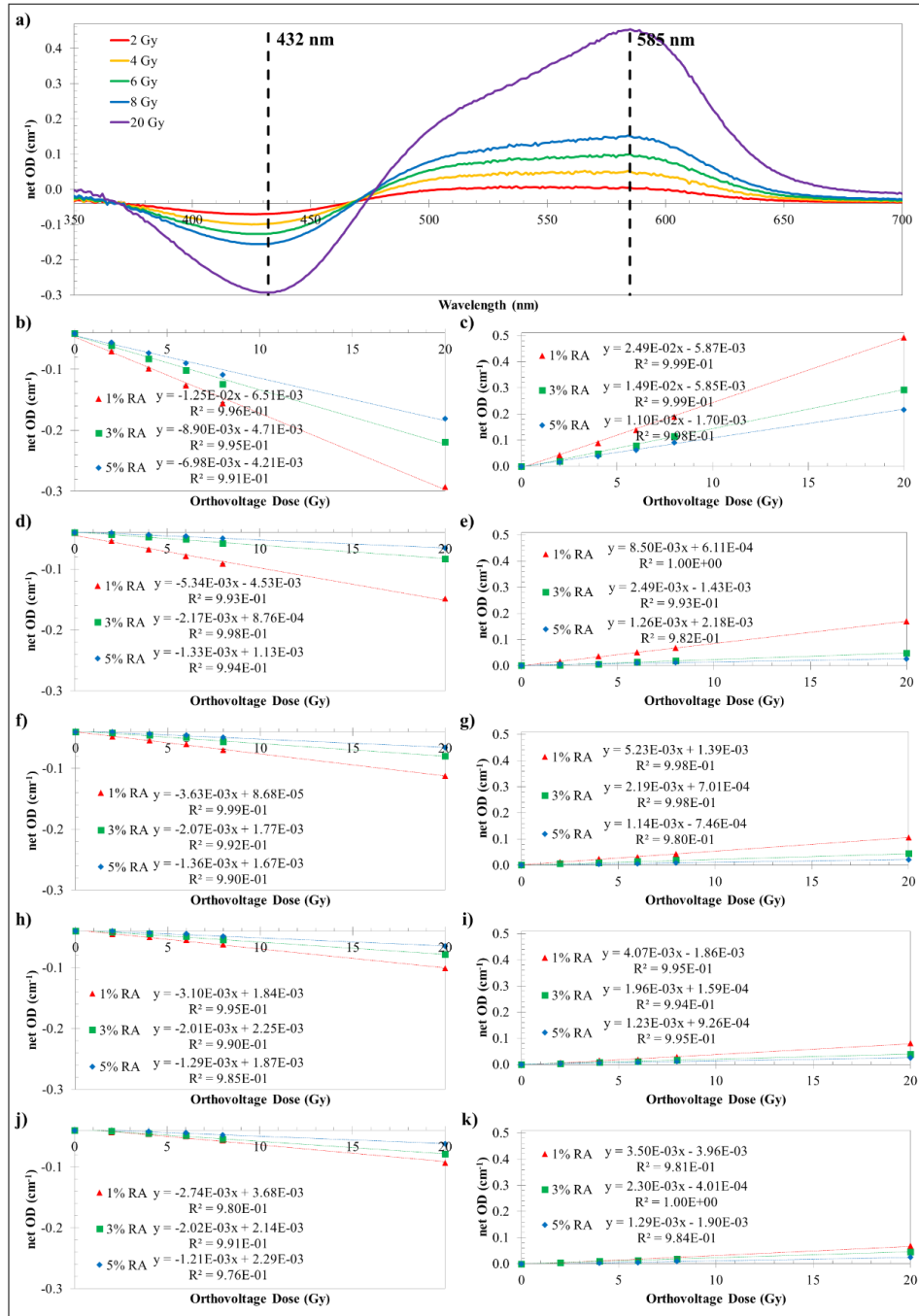


Figure 21: a) Spectral response of rFOX immediately (as realistically possible) after irradiation with peaks at 432 nm and 585 nm. Calibration curves at 432 nm b) immediately post-irradiation, d) 24 hours post-irradiation, f) 48 hours post-irradiation, h) 72 hours post-irradiation, and j) 96 hours post-irradiation. Calibration curves at 585 nm c) immediately, e) 24 hours, g) 48 hours, i) 72 hours, and k) 96 hours. The error bars in the calibration curves represented the standard deviation of spectrophotometer measurements averaged for three cuvettes per dose level.

3.2.2 Post-irradiation MR linearity

Post-irradiation MR linearity was only measured for rFOX up to approximately 20 Gy with $R^2 = 0.99$ (Figure 22). The error bars represent the standard deviation from the regions of interest measured within the irradiated region in each dosimeter. The raw MR signal intensities are shown in Figure 22 without subtraction of the 0 Gy sample (so intercept of linear fit is not close to 0). The standard deviations of the raw MR signal intensities were on average $\pm 4.8\%$ of the mean raw MR signal intensity.

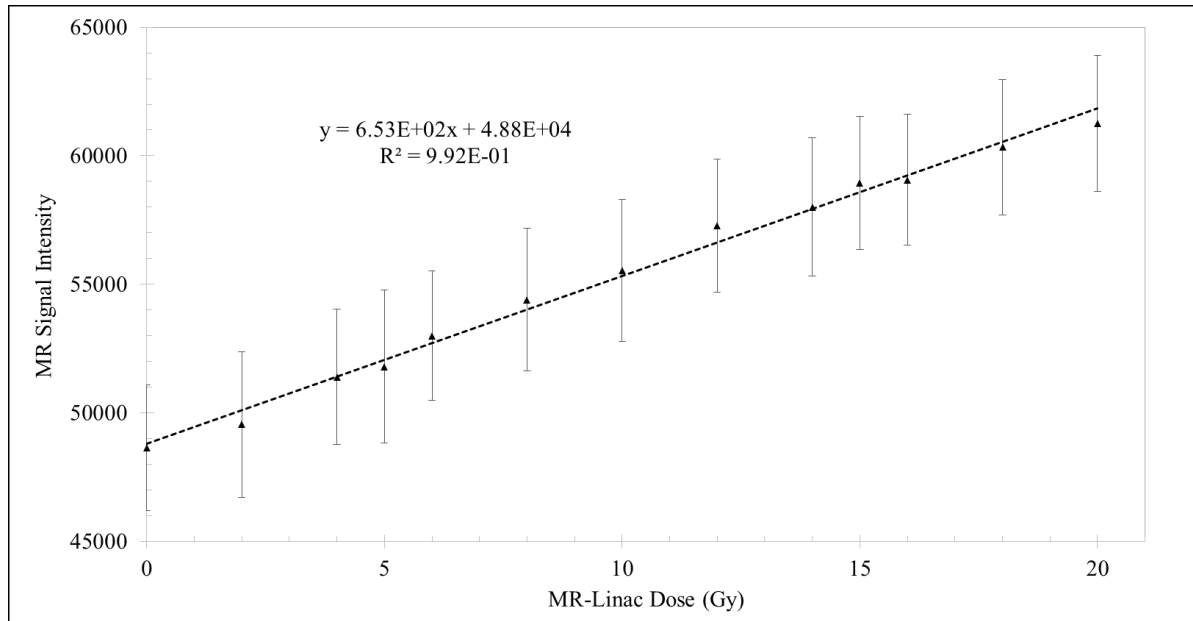


Figure 22: Post-irradiation MR linearity of rFOX. The error bars represent the standard deviation from the regions of interest measured within the irradiated region in each dosimeter.

3.2.3 Real-time MR linearity

Real-time MR linearity was measured for FOX and rFOX in the same irradiation set-up and bFFE sequence (TR/TE = 5/2.4 ms) with temporal resolution of 275 ms. The real-time MR signal intensity was linear with respect to time and dose (constant dose rate delivered) for FOX in gelatin, FOX in gelatin and agarose, and rFOX in gelatin and agarose ($R^2 = 0.82$ to 0.87) (Figure 23). The relative MR signal intensity was calculated for each dosimeter by dividing all MR signal intensities by the un-irradiated MR signal intensity at the start of image acquisition. The error bars represent the

propagated standard deviation from the regions of interest measured within the irradiated region and outside the irradiated region in each dosimeter. Further results on the real-time MR linearity and bFFE sequences will be discussed in Chapter 4.

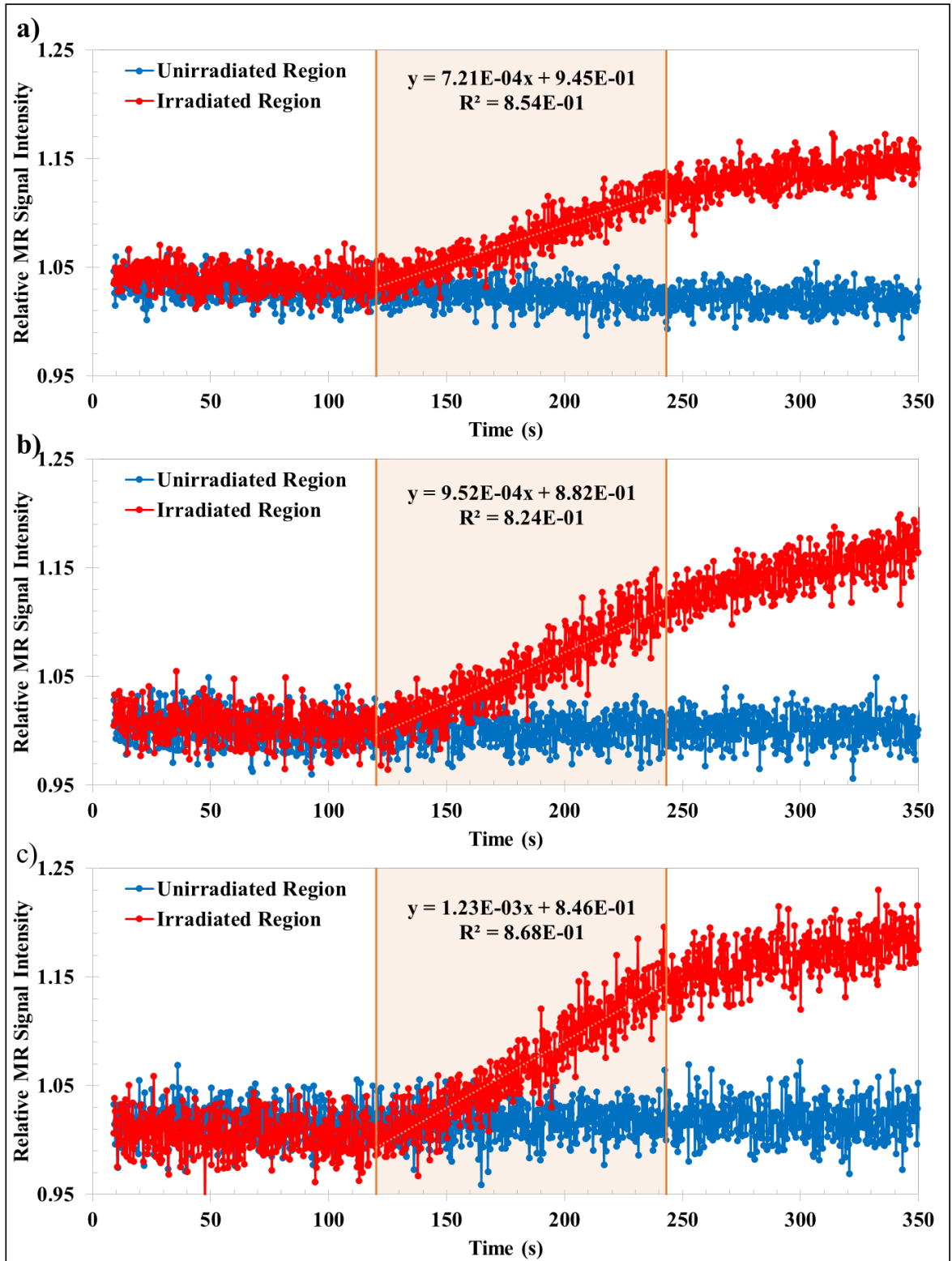


Figure 23: Real-time MR signal intensity linearity with dose for a) FOX in gelatin, b) FOX in gelatin and agarose), and c) rFOX in gelatin and agarose. The error bars represent the propagated standard deviation from the regions of interest measured within the irradiated region and outside the irradiated region in each dosimeter.

3.3 Radiological properties

The radiological properties and water equivalence of other 3D dosimeters have been presented in the past [139–141]. The interaction probability, mass attenuation coefficient ratio, mass energy absorption coefficient ratio, mass collision stopping power ratio, and mass radiative stopping power ratio were calculated using the National Institute of Standards and Technology (NIST) XCOM (photon cross sections database) and NIST ESTAR (stopping power and range tables for electrons) using the elemental composition of FOX in comparison with water (Figure 24 and Figure 25). All radiological properties demonstrated that FOX was nearly water-equivalent, with interaction probabilities nearly overlapping that of water (Figure 24) and ratios within 3.5% of water (Figure 25)

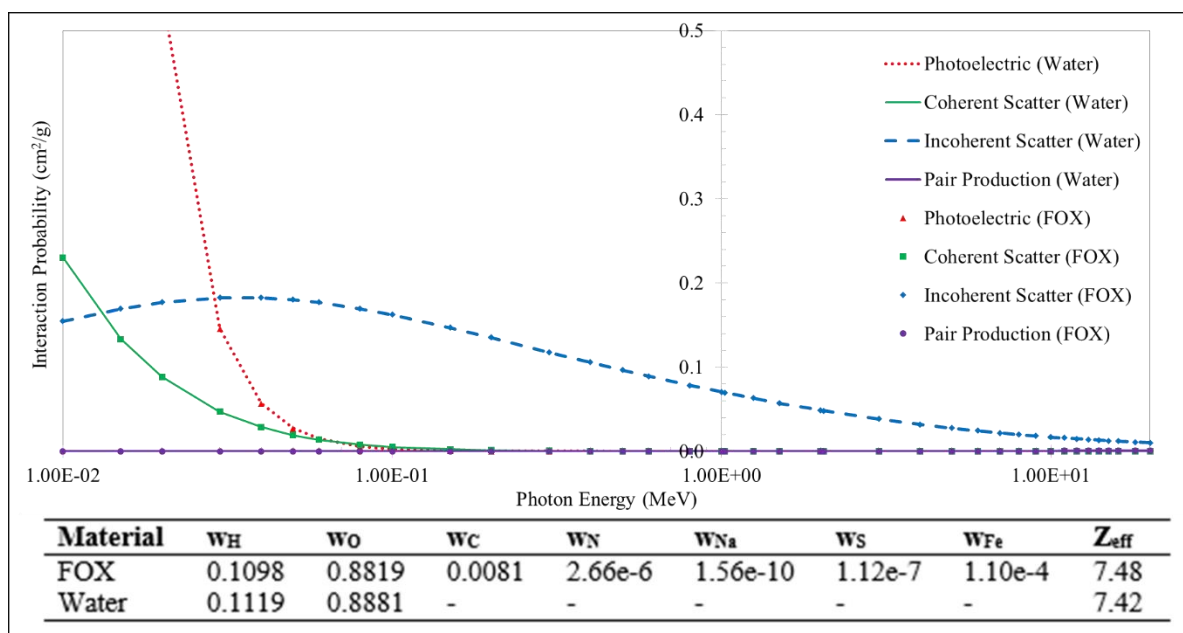


Figure 24: Interaction properties for water and FOX.

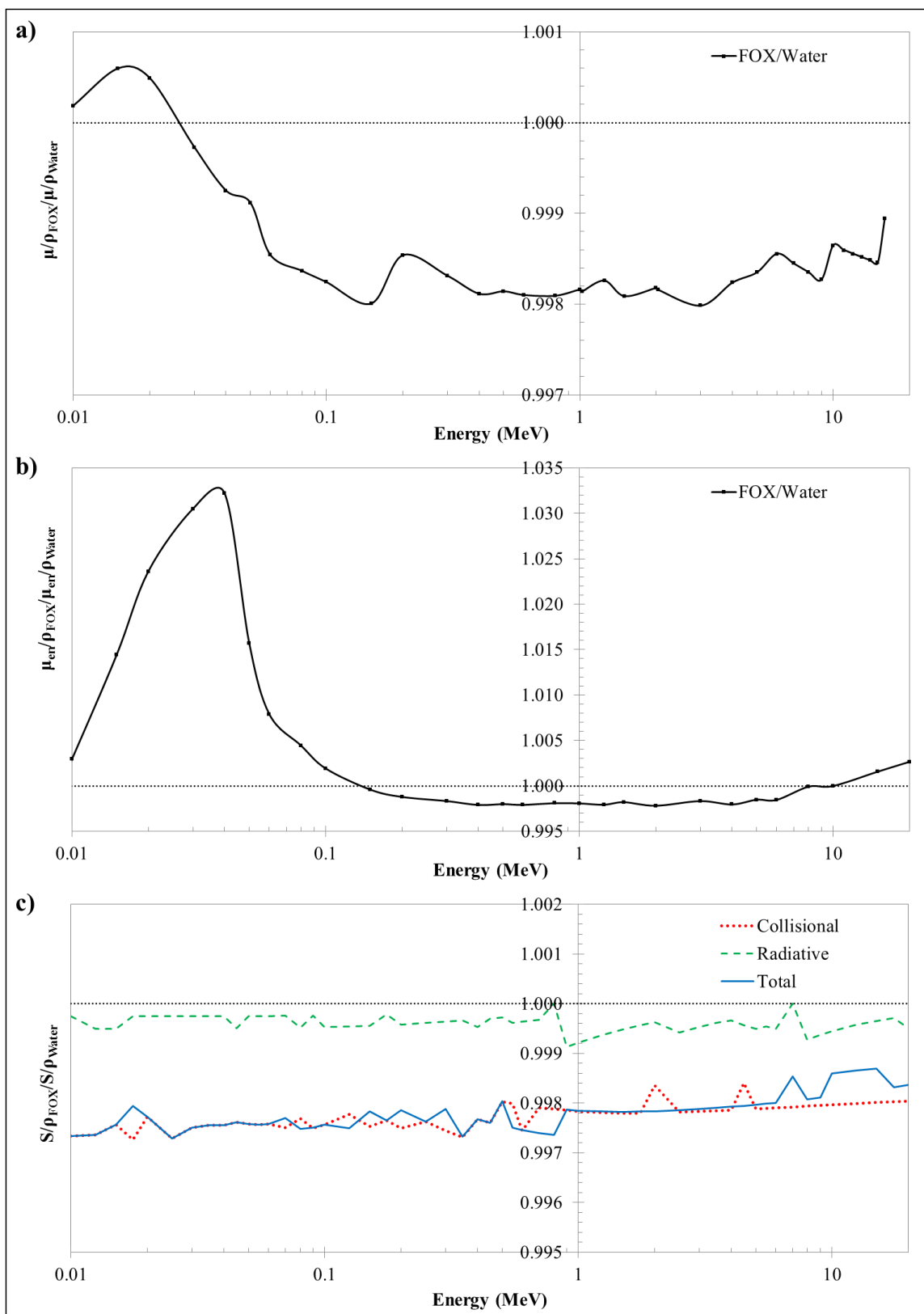


Figure 25: a) Mass attenuation coefficient ratio, b) mass energy absorption coefficient ratio, and stopping power ratios (collisional, radiative, and total) for FOX and water.

The mass attenuation coefficients, mass energy absorption coefficients, and stopping power ratios for FOX were calculated by summing the individual values for each element and multiplying by their fractional mass (elemental composition by weight fraction given in Figure 24). As mentioned above, the elemental coefficients were calculated using the NIST XCOM database. The approximations using these calculations were estimated to have a maximum error of 5% [141–144]. FOX has a higher mass attenuation coefficient ratio and mass energy absorption coefficient ratio for energies less than 0.1 MeV due to iron's photoelectric cross section (Figure 25). Above energies of 0.1 MeV, these ratios closely approximate the relative electron density due to the higher interaction probability of Compton scatter (or incoherent scatter, which depends on number of electrons) (Figure 24). Similarly, the collisional stopping power ratios were approximately the electron density ratios (collisional stopping power is proportional to electron density). On the other hand, the radiative stopping power ratios were proportional to the atomic number(atomic number + 1). Overall, the radiological properties demonstrated that FOX was nearly water-equivalent, with interaction probabilities nearly overlapping that of water (Figure 24) and ratios within 3.5% of water (Figure 25)

3.4 Reproducibility

For reproducibility testing, intra-batch (within one batch) and inter-batch (between batch) variability were tested. For intra-batch variability, the same dose of approximately 4 Gy was delivered 10 times from one batch in both without and with 1.5 T B_0 field present using a Co-60 source. A linear fit was applied for intra-batch comparison (a slope of 0 was expected for a zero intra-batch variability). For inter-batch variability, the same doses up to approximately 8.2 Gy were delivered to 6 separate batches. As expected, the inter-batch variability was greater than the intra-batch variability (Figure 26). The linearity of the dose response was preserved across all batches. The error bars in the calibration curves represented the standard deviation of spectrophotometer measurements averaged for three cuvettes per dose level. The greatest intra-batch variability was 5% measured at 440 nm. The greatest inter-batch variability was 10% measured at 440 nm for the calibration slope and 13% measured at 440

nm for a single dose point (2 Gy dose point). The greatest intra-batch variability was 4% measured at 585 nm. The greatest inter-batch variability was 7% measured at 585 nm for the calibration slope and 7% at 585 nm for a single dose point (8 Gy dose point).

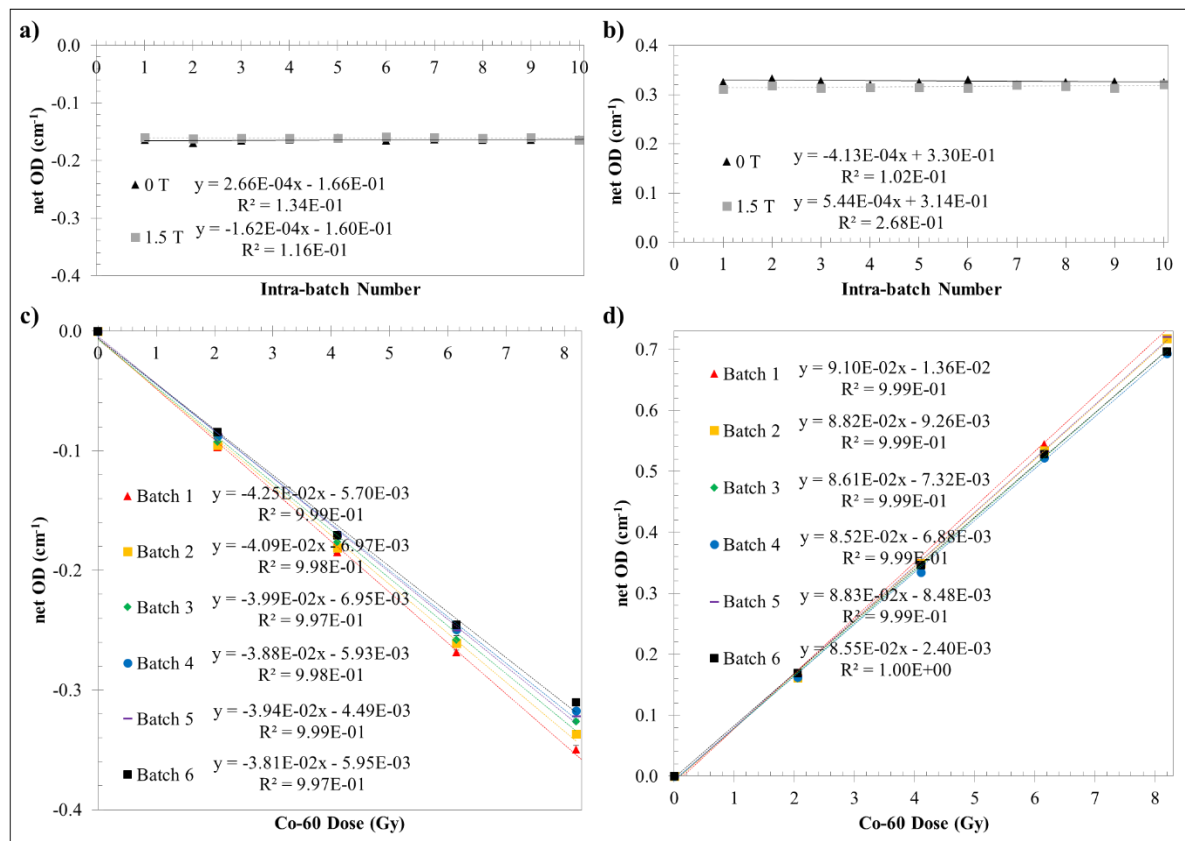


Figure 26: Reproducibility testing for FOX. a) Intra-batch variability with 10 irradiations from one batch of approximately 4 Gy (measured at spectral peak of 440 nm), b) intra-batch variability (585 nm), c) inter-batch variability from 6 batches (440 nm), and d) inter-batch variability (585 nm). The error bars in the calibration curves represented the standard deviation of spectrophotometer measurements averaged for three cuvettes per dose level.

3.5 Time stability

To ensure that repeat measurements for time stability studies were not affected from repeat exposure to the xenon lamp in the spectrophotometer for the range of wavelengths relevant for the FO gel formulation, which were also in the range of wavelengths used for the FOX gel (Figure 27). With repeat exposure to a broad range of wavelengths in the spectrophotometer, conversions of iron ions may occur (and appeared to be near-linearly related to the number of exposure, $R^2 = 0.99$). The standard

deviation of 30 consecutive spectrophotometer measurements was no more than $\pm 0.5\%$ of the mean OD, compared to up to $\pm 10\%$ standard deviation from the mean MR signal.

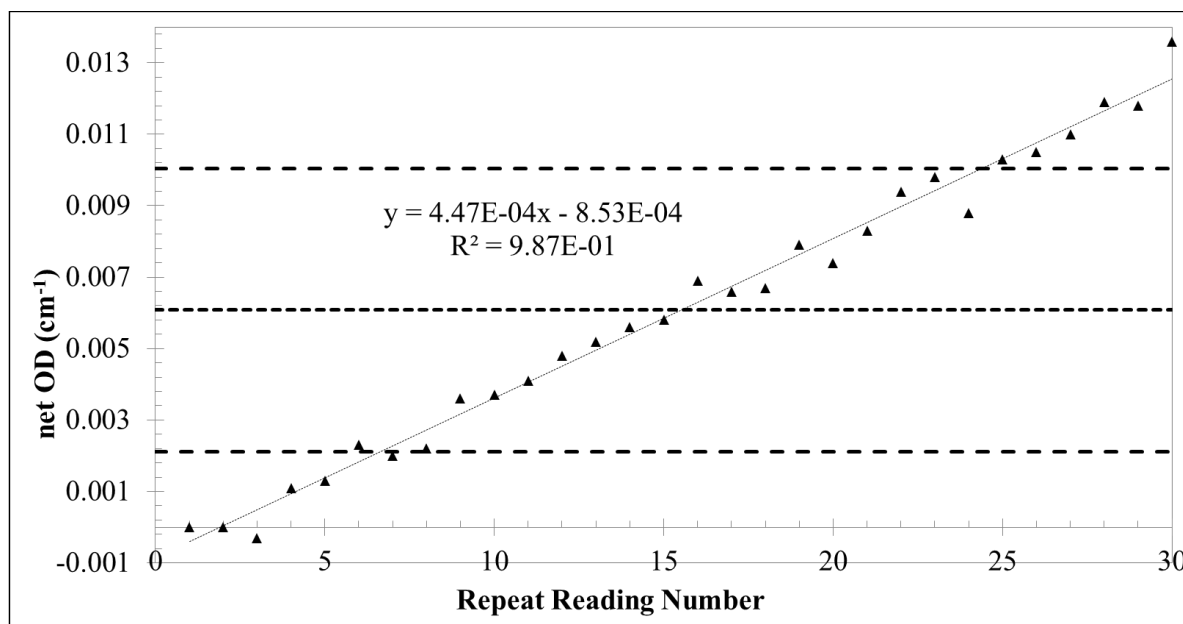


Figure 27: The effect of repeat spectrophotometer xenon lamp exposures on consecutive optical read-out of FO gel measured at 512 nm. The center dotted line represents the mean value from the 30 readings. The surrounding dotted lines show the bounds from the mean value considering the standard deviation of the 30 readings. The increase in net OD with repeat exposure to the xenon lamp was found to be linear ($R^2 = 0.987$).

To investigate time stability post-irradiation, FOX was irradiated to approximately 4 Gy then repeatedly measured for up to 68 days when stored at either room temperature or at 4 °C with three cuvette samples per environment (stored with covers to minimize the evaporation of water) (Figure 28). The stability for 4 Gy, 0 Gy, and net 4 Gy (4 Gy – 0 Gy) was best preserved over 68 days when stored at 4 °C and measured at the spectral peak of 440 nm. The stability of FOX when stored at room temperature plateaued after irradiation for up to 12 days then changed over the course of 56 days (Figure 28). Although both room temperature and 4 °C samples were stored in boxes to prevent stray light affecting the samples, it was possible that more stray light reached the room temperature FOX. Also, gelatin lost its rigidity over time when stored at room temperature, which would also affect the OD values (by affecting the amount of light absorbed, scattered, and transmitted). These results encourage

the storage of FOX at 4 °C. Although the OD values remained fairly stable at 4 °C storage in cuvettes, for volumetric studies, this would not be sufficient for preventing diffusion of the signal, eventually distorting the dose distribution. Overall, the OD values were not expected to remain 100% stable for any scenario of storage due to spontaneous chemical oxidation of iron(II) to iron(III) over time in the presence of dissolved oxygen (the oxidation reaction could not occur in the presence of irradiation if oxygen is purged, so this is an unavoidable consequence of Fricke-type gels) [145].

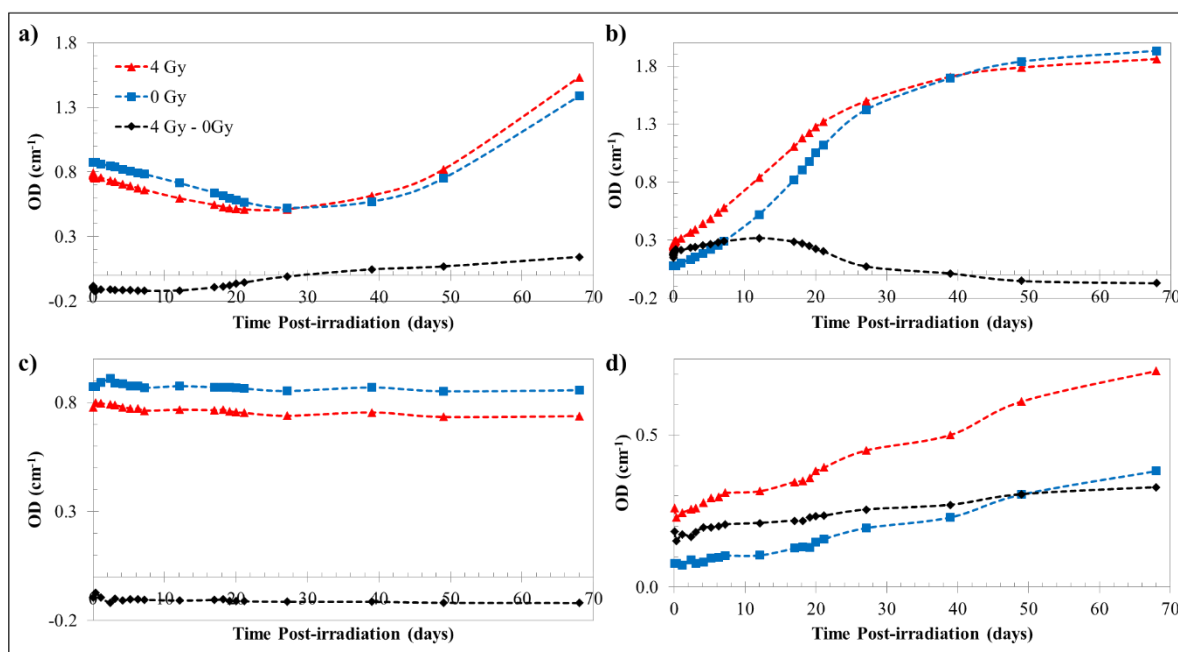


Figure 28: Time stability of FOX measured for 4 Gy (red triangles), 0 Gy (blue squares), and net 4 Gy (black diamonds) when stored at a) room temperature (measured at spectral peak 440 nm), b) room temperature (585 nm), c) 4 °C (440 nm), and d) 4 °C (585 nm). The error bars in the curves represented the standard deviation of spectrophotometer measurements averaged for three cuvettes per time point and per dose level.

3.6 Energy dependence

The energy dependence of FOX was tested using a clinical Varian TrueBeam™ linac with 6 MV and 18 MV radiation beams, a clinical Elekta Versa HD™ linac with 6 MV and 10 MV radiation beams, a 1.25 MeV Co-60 source (1.17 MeV and 1.33 MeV gamma rays), 250 kVp using an orthovoltage unit, and a pre-clinical 7 MV Elekta MR-Linac. The percent differences in net OD relative

to 7 MV (MR-Linac) were $-1\pm2.5\%$, $+1\pm2.5\%$, $+2\pm6.5\%$, $+5\pm6.5\%$, $+4\pm6.5\%$, and $-11\pm6.5\%$ at 440 nm for 6 MV (Varian), 18 MV (Varian), 6 MV (Versa), 10 MV (Versa), 1.25 MeV (Co-60), and 250 kVp (Orthovoltage), respectively. The percent differences in net OD relative to 7 MV (MR-Linac) were $-2\pm2\%$, $+2\pm2\%$, $+6\pm3.5\%$, $+9\pm3.5\%$, $+8\pm3.5\%$, and $-10\pm3.5\%$ at 585 nm for 6 MV (Varian), 18 MV (Varian), 6 MV (Versa), 10 MV (Versa), 1.25 MeV (Co-60), and 250 kVp (Orthovoltage), respectively. Some differences between machines were due to intra-batch variability (up to 5% at 440 nm and 4% at 585 nm) and inter-batch variability (up to 13% at 440 nm and 7% at 585 nm across 6 batches for a single dose level) (one batch was used for Varian and MR-Linac irradiations, and one batch was used for Versa, Co-60, and orthovoltage irradiations). Uncertainties stated above were plus or minus half of the maximum variability for intra-batch (Varian and MR-Linac values) and inter-batch (Versa, Co-60, and orthovoltage values) irradiations.

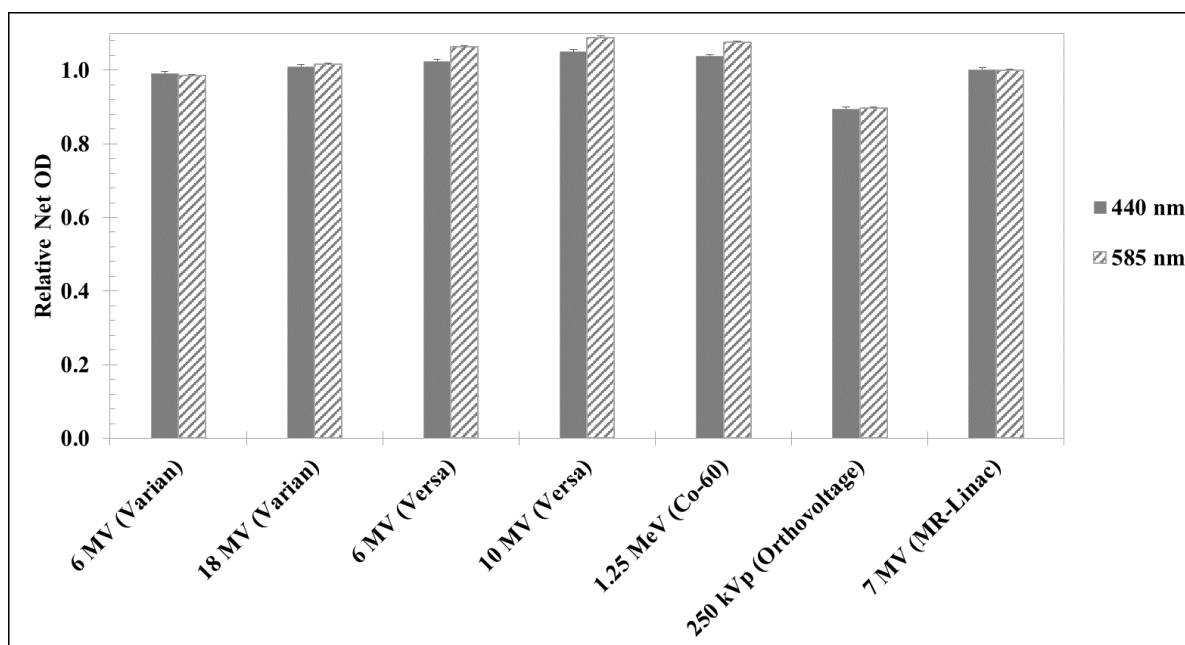


Figure 29: Energy dependence of FOX relative to net OD measured for 7 MV (MR-Linac). The error bars in the curves represented the standard deviation of spectrophotometer measurements averaged for three cuvettes per irradiation.

3.7 Reusability

The reproducibility of the reusable version of FOX, rFOX, was tested with repeat irradiations of approximately 10 Gy separated by at least 24 hours between each irradiation (Figure 30). The relative net MR signal intensity was calculated as the irradiated region's signal intensity divided by the un-irradiated region's signal intensity for each repeat irradiation. The initial net MR signal intensity response was lower when compared to following repeat irradiations due to irradiating the gel while still cold, having recently removed it from 4° C storage. Temperature of the gel can affect the overall sensitivity to irradiation as well as the weak magnetic interactions affecting temperature-dependent magnetic moments [64, 146]. Fluctuations in the relative net signal intensity between repeat irradiations may also be due to incomplete reversion of iron(III) to iron(II) inside the gel. Between all repeat irradiations, rFOX was stored at room temperature away from bright lights. The real-time response of rFOX remained linear throughout these repeat irradiations and will be discussed in further detail in Chapter 4.

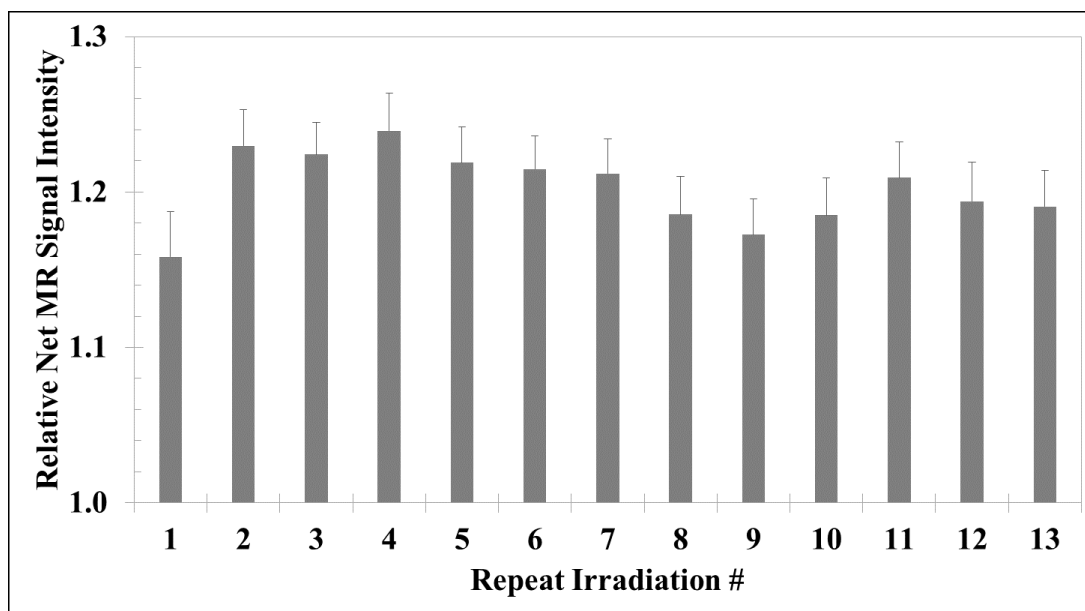


Figure 30: Reproducibility of net MR signal intensity response shown for rFOX irradiated with approximately 10 Gy each time with at least 24 hours separating each repeat irradiation. The relative net MR signal intensity was calculated as the irradiated region's signal intensity divided by the un-irradiated region's signal intensity for each repeat irradiation. The error bars represent the propagated standard deviation from the regions of interest measured within the irradiated region and outside the irradiated region in each dosimeter.

3.8 Dose rate dependence

Dose rate dependence was tested for FOX and rFOX by changing the gun duty cycle from 100% down to 50% (Figure 31). Unlike the dose rate dependence tested in Figure 15 of FO using different distances from the radiation source, this method of changing the gun duty cycle does not change the instantaneous dose rate (amplitude of each pulse). The monitor unit (MU) rate at 100% gun duty cycle was roughly 500 MU/min (~ 500 cGy/min at calibration depth). rFOX was imaged with MR using two different sequences: T1 contrast enhancement (CE) and no CE. T1 CE and no CE are Philips-specific terminology for their 3D fast field echo (FFE) sequences and do not indicate that an MR contrast agent was injected. The T1 CE sequences spoiled the transverse magnetization using pulse phase cycling of the radiofrequency excitation pulses. Therefore, the no CE images included a mixed signal of the free induction decay (FID) and spin echo, and the T1 CE images only contained the FID signal. As a result, no CE images contain more overall MR signal and reduced apparent noise (smaller standard deviations). The relative values were calculated as the net value divided by the net value at 100% gun duty cycle. For FOX, the percent differences were $-2 \pm 2.5\%$ and $-1 \pm 2.5\%$ at 440 nm and $-1 \pm 2\%$ and $-0.1 \pm 2\%$ at 585 nm for 80% and 50% gun duty cycle, respectively. The uncertainties in the percent differences for FOX were half of the maximum uncertainty in intra-batch measurements for 440 nm (5%) and 585 nm (4%), respectively. For rFOX, the percent differences were $1 \pm 4\%$ and $1 \pm 5\%$ for no CE and $2 \pm 12\%$ and $3 \pm 11\%$ for T1 CE for 80% and 50% gun duty cycle, respectively.

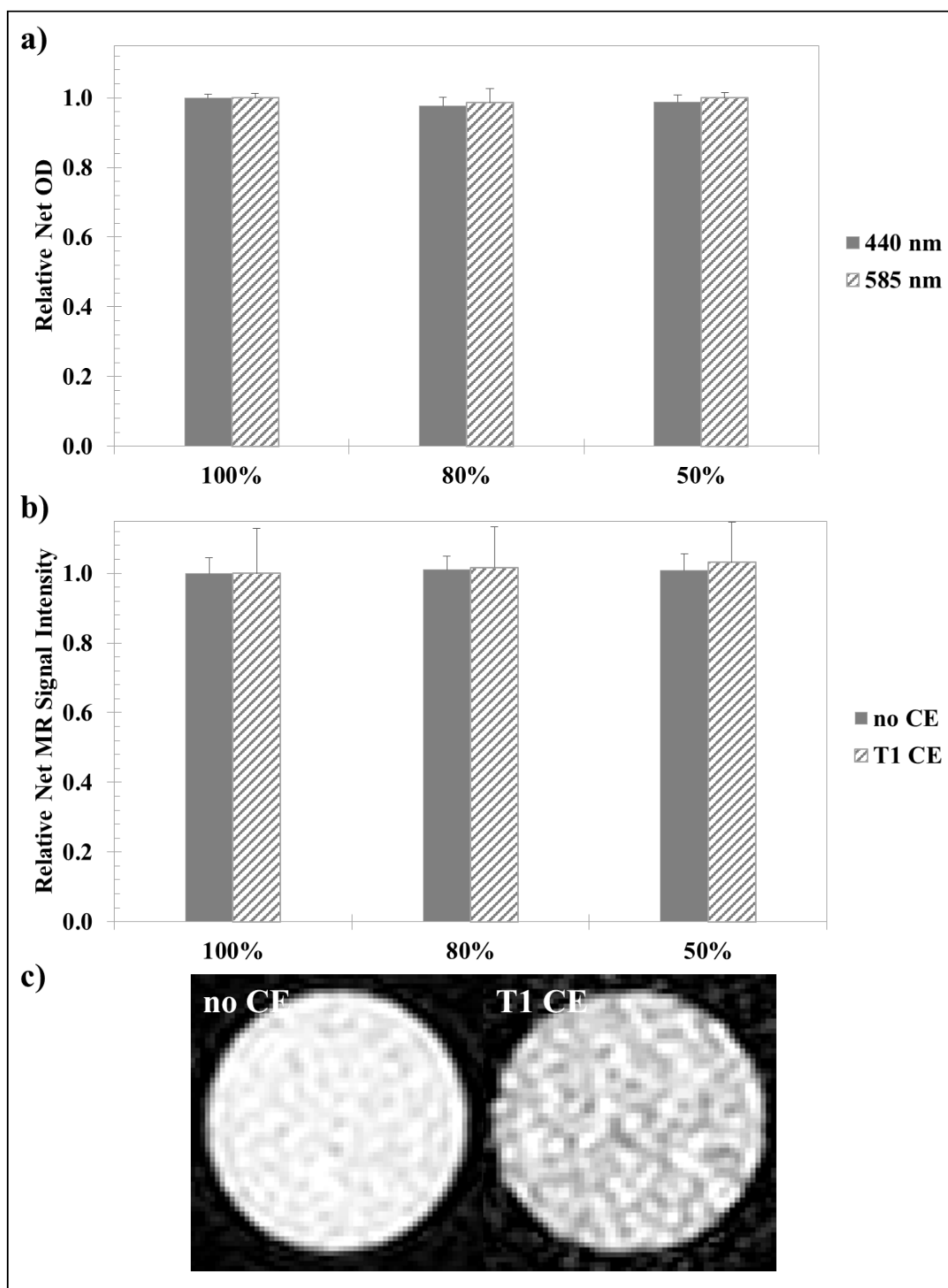


Figure 31: Dose rate dependence of a) FOX and b) rFOX. c) Example MR images of rFOX with no CE and T1 CE acquisitions. MR images acquired with no CE were smoother with lower standard deviation. The relative values were calculated as the net value divided by the net value at 100% gun duty cycle. The error bars in a) represent the standard deviation of spectrophotometer measurements averaged for three cuvettes per dose level and b) represent the propagated standard deviation from the regions of interest measured within the irradiated region and outside the irradiated region in each dosimeter.

3.9 Fractionation dependence

FOX was tested for fractionation dependence up to a total of 12 Gy: 12 Gy delivered in one fraction, 12 Gy delivered in 3 fractions of 4 Gy with no time gap between fractions, and 12 Gy delivered in 3 fractions of 4 Gy with 20 minutes between fractions (Figure 32). rFOX was tested for fractionation dependence up to a total of 20 Gy: 20 Gy in one fraction, two fractions (10 Gy each), four fractions (5 Gy each), five fractions (4 Gy each), and ten fractions (2 Gy each) with the same total time of delivery for all fractionations (Figure 32). The terminology “fractionation” here does not refer to the fractionation scheme of radiation treatment, typically separated by 24 hours. This fractionation was to test the dependence on the delivery of multiple separate beams for a given radiation plan. For FOX, the percent differences compared to 12 Gy x 1 were $-0.4 \pm 2.5\%$ and $-2 \pm 2.5\%$ at 440 nm and $-2 \pm 2\%$ and $-0.3 \pm 2\%$ at 585 nm for 4 Gy x 3 and 4 Gy x 3 (20 min), respectively. The uncertainties in the percent differences for FOX were half of the maximum uncertainty in intra-batch measurements for 440 nm (5%) and 585 nm (4%), respectively. For rFOX, the percent differences for the calibration curve slopes (not plotted in Figure 32) compared to that of 20 Gy x 1 were $-6 \pm 3\%$, $-2 \pm 3\%$, $-2 \pm 3\%$, and $-8 \pm 3\%$ for 2 Gy x 10, 4 Gy x 5, 5 Gy x 4, and 10 Gy x 2, respectively, with $R^2 = 0.99$ to 1. Uncertainties for rFOX were calculated from the standard deviation of all of the calibration curve slopes and for the calibration curve slope including all values.

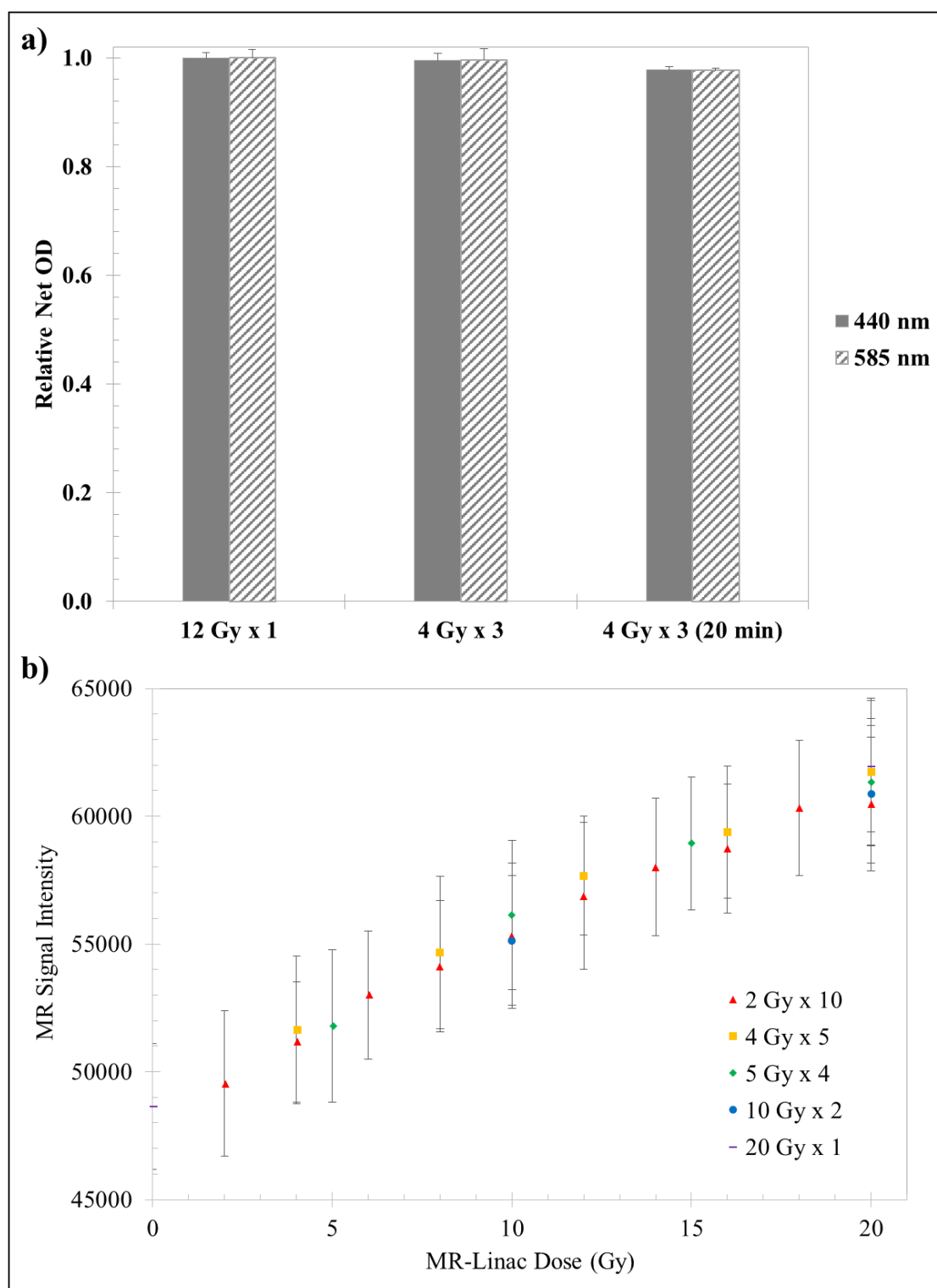


Figure 32: Fractionation dependence of a) FOX and b) rFOX. The relative net OD values were calculated as the net value divided by the net value at 12 Gy x 1. The error bars in a) represent the standard deviation of spectrophotometer measurements averaged for three cuvettes per irradiation and b) represent the standard deviation from the regions of interest measured within the irradiated region in each dosimeter (raw MR signal intensity given here).

3.10 Gel matrix dependence and diffusion

The FOX gel formulation was further modified in-house with the addition of a reducing agent (9 wt %, water content reduced to ~87 wt %) to produce a reusable gel (rFOX). However, the reducing agent in rFOX was also found to affect the rigidity of gelatin, so the gel matrix was changed to 3 wt % gelatin and 1 wt % agarose. The FOX gel was created in both 4 wt % gelatin and 3 wt % gelatin and 1 wt % agarose to compare changes in radiation sensitivity with rFOX in 3 wt % gelatin and 1 wt % agarose. All gels were contained in 4.5 cm diameter cylindrical PET plastic containers for irradiation and MR imaging. FOX in gelatin and agarose, and rFOX in gelatin and agarose were assessed with irradiation of approximately 10 Gy (Figure 33). The net percent signal intensity increases determined from the post-irradiation T1-weighted images were $20.5 \pm 2\%$, $26.0 \pm 2\%$, and $21.4 \pm 2\%$ for a) FOX in gelatin (4 wt %), b) FOX in gelatin (3 wt %) and agarose (1 wt %), and c) rFOX in gelatin (3 wt %) and agarose (1 wt %), respectively. Optically, the use of agarose instead of gelatin had previously been shown to decrease the sensitivity of FXG [147]. The results of this study indicated that the incorporation of agarose with gelatin slightly increased the radiation sensitivity of FOX measured using MRI.

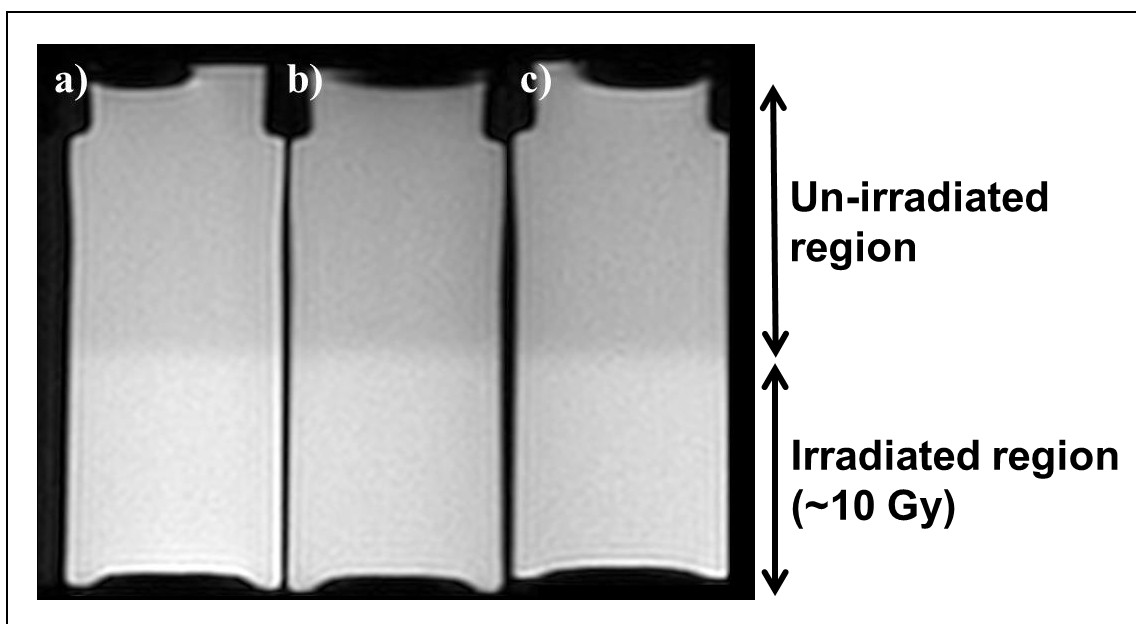


Figure 33: Gel matrix dependence. Post-irradiation T1-weighted images ($TR/TE = 500/20$ ms) of a) FOX in gelatin (4 wt %), b) FOX in gelatin (3 wt %) and agarose (1 wt %), and c) rFOX in gelatin (3 wt %) and agarose (1 wt %).

Diffusion of FOX and rFOX (same samples imaged and shown in Figure 33) were measured up to 28 days post-irradiation (Figure 34). As shown in Figure 34, the radiation beam edge regions were approximately linear. The change in slopes over time are also listed in Table 9 as well as the percent differences in slopes relative to the slope measured at 14 minutes post-irradiation for FOX and 0 minutes post-irradiation for rFOX in Table 10 since they were difficult to distinguish from Figure 34. Overall, the slopes decrease over time. Notably for FOX in gelatin or gelatin and agarose, the overall signal also gradually rose due to spontaneous oxidation of FOX at room temperature. On the other hand, for rFOX, the overall signal gradually decreased as expected as the signal reverted. The change in the irradiated region's signal for rFOX was shown over time to demonstrate the speed of reversal of signal (Figure 35). The first two hours of signal change for rFOX were found to be linear and are recommended for volumetric relative dose measurements (Figure 35).

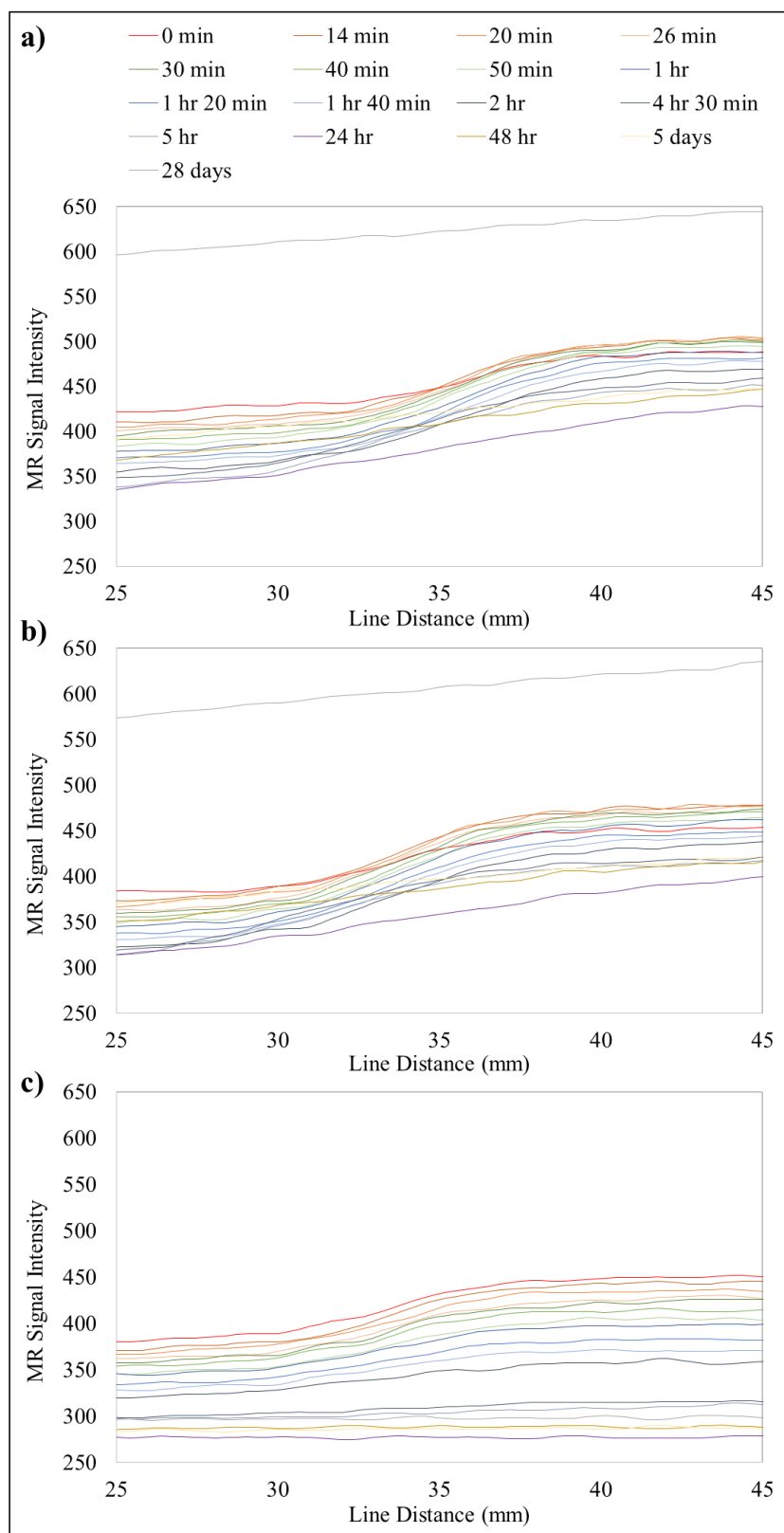


Figure 34: Diffusion of signal for a) FOX in gelatin, b) FOX in gelatin and agarose, and c) rFOX in gelatin and agarose for up to 28 days.

Table 9: Slopes of radiation field edge over time for FOX and rFOX.

Time	FOX (gelatin)	FOX (gelatin and agarose)	rFOX (gelatin and agarose)
0 min	9.85	6.28	6.08
14 min	13.41	10.64	6.25
20 min	14.26	10.51	7.38
26 min	13.25	10.44	5.04
30 min	14.13	11.77	4.64
40 min	14.47	11.87	4.80
50 min	14.00	11.97	5.30
1 hr	13.73	10.77	6.01
1 hr 20 min	16.08	10.38	5.15
1 hr 40 min	12.86	9.90	4.18
2 hr	12.18	10.73	1.81
4 hr 30 min	9.63	5.67	1.57
5 hr	8.22	5.60	1.70
24 hr	6.39	4.44	-0.53
48 hr	5.16	4.22	-0.05
5 days	3.34	1.99	-0.03
28 days	3.42	2.79	-0.55

Table 10: Percent differences in slopes of radiation field edge over time for FOX and rFOX relative to slope measured at 14 min post-irradiation for FOX and 0 min post-irradiation for rFOX.

Time	FOX (gelatin)	FOX (gelatin and agarose)	rFOX (gelatin and agarose)
0 min	-26.5%	-41.0%	0.0%
14 min	0.0%	0.0%	2.8%
20 min	6.3%	-1.2%	21.4%
26 min	-1.2%	-1.9%	-17.1%
30 min	5.4%	10.6%	-23.7%
40 min	7.9%	11.6%	-21.1%
50 min	4.4%	12.5%	-12.8%
1 hr	2.4%	1.2%	-1.2%
1 hr 20 min	19.9%	-2.4%	-15.3%
1 hr 40 min	-4.1%	-7.0%	-31.3%
2 hr	-9.2%	0.8%	-70.2%
4 hr 30 min	-28.2%	-46.7%	-74.2%
5 hr	-38.7%	-47.4%	-72.0%
24 hr	-52.3%	-58.3%	-108.7%
48 hr	-61.5%	-60.3%	-100.8%
5 days	-75.1%	-81.3%	-100.5%
28 days	-74.5%	-73.8%	-109.0%

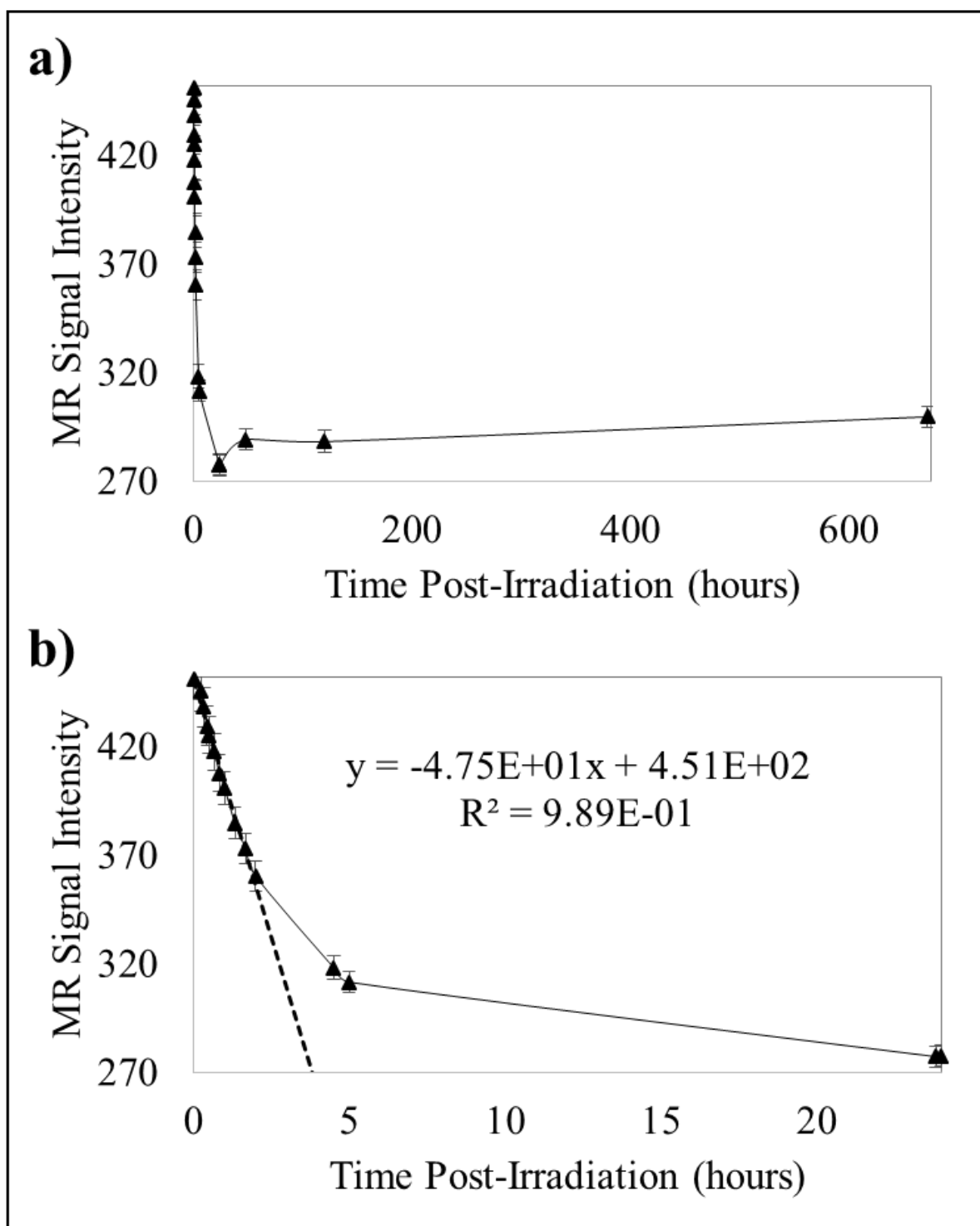


Figure 35: rFOX reversal of raw MR signal intensity. a) Change in signal up to 28 days and b) zoomed in view to first 24 hours. The decrease in signal in the first two hours was found to be linear. The error bars represent the standard deviation from the regions of interest measured within the irradiated region at each time point.

Other gel matrixes were tested for FOX but resulted in oxidation of iron(II) during the curing process, did not cure, or resulted in no optical or MR visible changes after irradiation (Table 11). For non-water based matrixes, a variety of solvents and surfactants were tested: chloroform, acetone, Triton X-100, ethanol, and methanol. All tested gel matrixes were optically clear materials on their own.

Table 11: Gel matrixes tested for FOX formulation.

Name of matrix	Type of matrix	Reason(s) for failure
Encapso® K	Encapsulation rubber	Oxidation, did not cure
SS-5060	Silicone	No change post-irradiation
QSi1 216	Silicone	Oxidation, did not cure
Sylgard® 184	Silicone	Did not cure
Clear Flex 30	Urethane rubber	No change post-irradiation
Crystal Clear 202	Urethane resin	No change post-irradiation
Crystal Clear 206	Urethane resin	Oxidation
Epoxy Hydrogel	Hydrogel	No change post-irradiation
Sodium polyacrylate	Super-absorbing polymer	No change post-irradiation
Xanthan gum	Polysaccharide polymer	Did not gel firmly
Gellan gum (Phytigel)	Polysaccharide polymer	Did not gel firmly

3.11 Summary

The dose linearity, radiological properties, reproducibility, time stability, energy dependence, reusability of rFOX, dose rate dependence, fractionation dependence, gel matrix dependence, and diffusion were investigated for FOX and rFOX. Both FOX and rFOX were found to be linear with respect to radiation dose optically and with MR. Radiological properties of FOX demonstrated that it was nearly water-equivalent. The intra-batch and inter-batch variabilities were quantified (up to 5% intra-batch and up to 13% inter-batch) to demonstrate the reproducibility of FOX, which can be affected by batch-to-batch differences in concentrations of chemicals due to scale and human uncertainties. The time stability of FOX was most ideal when stored at 4 °C. Up to $11 \pm 6.5\%$ energy dependence, up to $3 \pm 11\%$ dose rate dependence, and up to $8 \pm 3\%$ fractionation dependence were found for FOX and rFOX for energies and doses relevant for the MR-Linac. The reusability of rFOX was also demonstrated over repeated irradiations of rFOX separated by at least 24 hours. The addition of agarose to FOX increased its MR signal intensity change post-irradiation by 27% compared to gelatin alone. The change in MR signal intensity for rFOX was -18% compared to FOX in gelatin and agarose (same gel matrix as

rFOX). Within the first hour of measurement, changes in the slope at the radiation field edge due to diffusion (as well as iron(III) reversal for rFOX) were less than 8% for FOX (gelatin), 13% for FOX (gelatin and agarose), and 24% for rFOX (gelatin and agarose). One hour is within the timescale of MR-Linac irradiations and immediate post-irradiation imaging. The decrease in MR signal intensity for rFOX (correlating to the reversal of iron(III) to iron(II)) was linear within the first two hours ($R^2 = 0.99$). Indicating that the linear scaling of MR signal intensity from T1-weighted MR images to relative dose can reliably be calculated for rFOX within the first two hours of measurement (disregarding diffusion and only considering the fading of the MR signal intensity).

Chapter 4 – Magnetic field effects on volumetric dosimeters

4.1 Rationale

The perpendicular orientation of the strong magnetic field (B_0) with respect to the radiation beam in systems integrating an MRI with a linac or Co-60 unit influences secondary electrons resulting in changes in dose deposition in three dimensions [56, 57]. However, conventional quality assurance (QA) tools lack the ability to report changes in volumetric dose distributions and discrepancies out of the plane of measurement [85, 148]. Conventional QA tools such as ionization chambers, film, and other detectors also exhibit varying degrees of B_0 field dependence [55, 57, 116, 149–155]. The effect of B_0 field on newer detectors, such as plastic scintillators, have also been recently investigated due to the growing interest in applying such detectors for MR-IGRT applications [156–158]. To meet the need for volumetric and potentially B_0 field-independent dose evaluations, several 3D dosimeter types have been applied to MR-IGRT systems to assess the electron return effect, B_0 field effects on the radiation field penumbra, and the feasibility of 3D dosimeters for assessing treatment planning system (TPS) calculations and treatment plan deliveries [108, 114–116, 121, 124–126]. Prior to full volumetric dose distribution analysis using 3D dosimeters, it was necessary to investigate whether the presence of a B_0 field and gradient/radiofrequency fields present during MR imaging would require correction factors to be applied for MR-IGRT applications. Other MR imaging considerations that could impact calculated dose distributions were also discussed (these MR considerations are relevant to any MRI system and not specific to the MR-Linac).

4.2 Strong magnetic field dependence

To reduce variability due to inter-batch and day-to-day differences, an electromagnet (GMW Dipole Electromagnet Model #3472-70, GMW, San Carlos, CA, USA) was used for same-day irradiations with and without a B_0 field for all dosimeters (Figure 36). The B_0 field strength inside the

electromagnet was measured using a gaussmeter at the beginning and end of each set of irradiations (Gaussmeter Model GM2, AlphaLab, Inc., Salt Lake City, UT, USA). A B_0 field of 1.5 T with 50 mm pole caps was used for FOX. FOX dosimeters were positioned consistently inside an acrylic phantom (80 cm SSD at the surface of the phantom) and were irradiated with a $5 \times 13 \text{ cm}^2$ field using a Co-60 source. The distance between the pole caps with the acrylic phantom between the pole caps was approximately 3 cm. The acrylic phantom served as a scatter medium providing 5 cm of build-up and 5 cm of backscatter material for the dosimeters. The cuvette insert dimensions inside the acrylic phantom were $12.5 \times 12.5 \text{ mm}^2$, and the outer dimensions of the cuvettes were $12.5 \times 12.5 \text{ mm}^2$. This resulted in no measurable air gap between the acrylic phantom and cuvette to prevent the presence of electron return effects in the dosimeters. The Co-60 doses were calculated accounting for exponential decay of the source and PDD using BJR Supplement 25 depending on the SSD, depth of measurement, and field size [128].

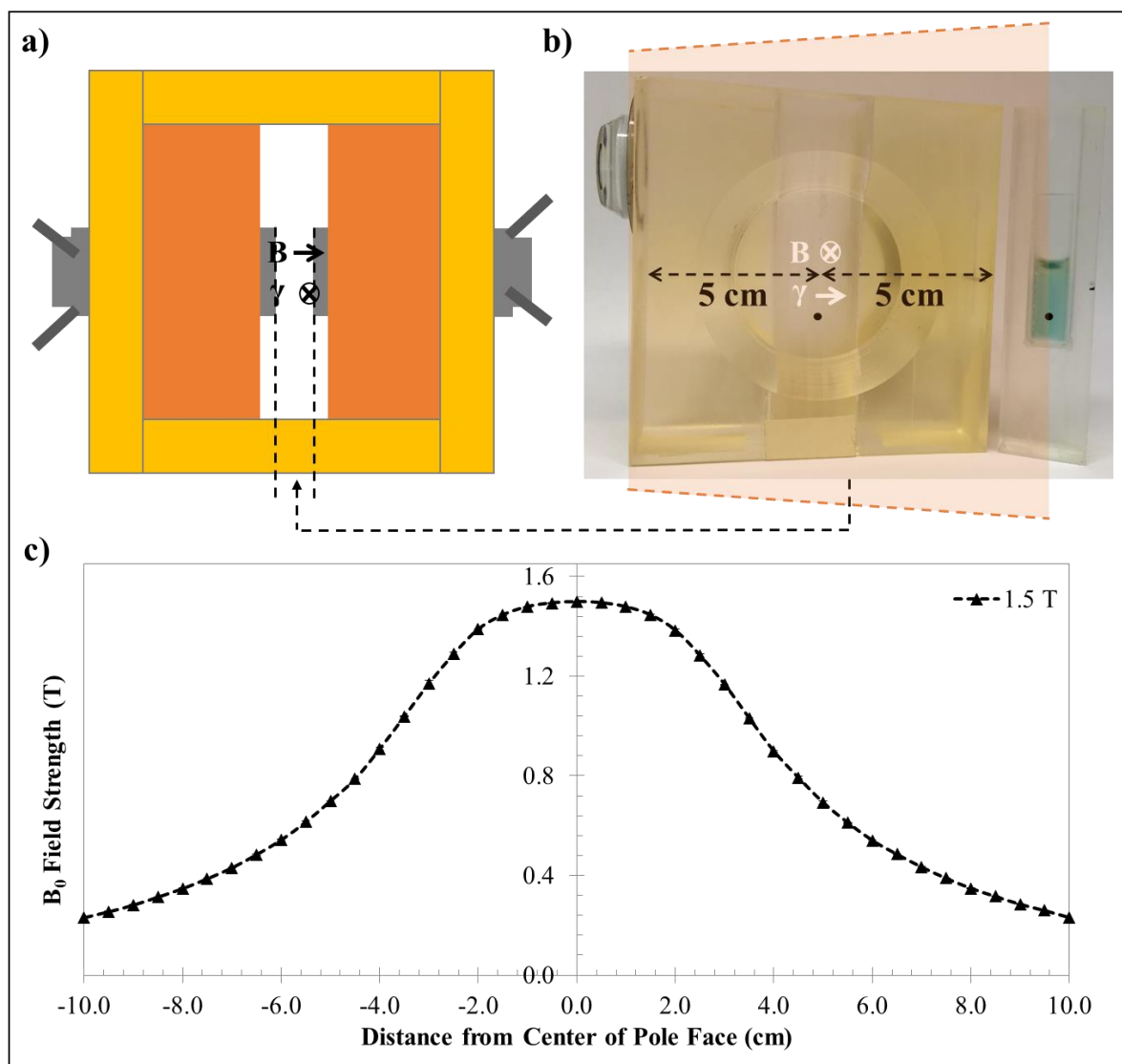


Figure 36: a) Schematic of electromagnet and location of phantoms when inserted between pole caps with the directions of the B_0 field and radiation beam noted; b) acrylic phantoms with cuvette inserts used for FOX irradiations (sample cuvette in insert). Black dots in phantom and in sample cuvette indicate region of optical measurement using a spectrophotometer in relation to the radiation field (shaded region); and c) profile of 1.5 T B_0 field strength in between pole faces (50 mm) of electromagnet. The error bars represent the standard deviation from three readings of the B_0 field strength.

FOX dosimeters were measured at spectral peaks of 440 nm and 585 nm (Figure 37). The full dose calibration curves and each dose level were compared. Percent differences in slope of $1.6 \pm 2.5\%$ and $0.5 \pm 2\%$ were calculated for the full dose curves at 440 nm and 585 nm, respectively. The greatest percent difference at a given dose level was $2.3 \pm 2.5\%$ at 6 Gy at 440 nm (Figure 37). Because FOX

and other iron-based radiochromic gels contain a ferromagnetic iron component, the B_0 field effect was evaluated for time dependence with FOX dosimeters at the 4 Gy dose point with five different lengths of time in the 1.5 T B_0 field (0, 6, 7, 10, and 30 minutes) (Figure 37). The percent differences for measurements at the spectral peak 440 nm were $1.9 \pm 2.5\%$, $4.1 \pm 2.5\%$, $2.1 \pm 2.5\%$, and $3.3 \pm 2.5\%$ for 6, 7, 10, and 30 minutes when compared to 0 minutes, respectively. Likewise at the spectral peak 585 nm, the percent differences were $2.5 \pm 2\%$, $-0.9 \pm 2\%$, $2.5 \pm 2\%$, and $0.2 \pm 2\%$ for 6, 7, 10, and 30 minutes, respectively. The data at neither spectral peak trended with respect to time of exposure to the 1.5 T B_0 field, supporting no significant dependence on the B_0 field.

FOX dosimeters consisted of ferromagnetic iron(II) oxide and polarized oxygen molecules with intermediate radicals [63]. While the presence of B_0 fields could potentially alter the response and sensitivity of iron-based radiochromic gels, I found that this was not the case at 1.5 T with dosimeters having been exposed to the B_0 field for up to 30 minutes and for doses up to 8 Gy. FOX and other iron-based radiochromic gels may have B_0 field dependence at greater than 1.5 T but this was not tested with the electromagnet used for this study or the 1.5 T MR-Linac.

Although the geometry and beam quality were different, at depths beyond the build-up region (5-25 cm), the difference in dose per incident photon with and without a 1.5 T B_0 field was on the order of 0.5% (lower dose with B_0 field beyond build-up region) [55]. For FOX (440 nm), the calibration curve slopes decreased in the presence of a B_0 field. This agreed with the literature for findings with PRESAGE® and with the 0.5% lower dose beyond the build-up region [116, 149, 150]. While irradiating in a B_0 field shifts the lateral edges of a radiation field, the measurements in this study were well within the central region of the radiation field to minimize the contribution of penumbra changes in a B_0 field [117, 159, 160]. Unlike air-filled ionization chambers, the 3D dosimeters used in this study filled their respective containers without the presence of air within the beam's path. While small air gaps between the acrylic phantom and silicone phantom and the 3D dosimeters could result in dose enhancement due to the electron return effect, these effects were not within the scope of this study since the radiation dose response measurements were averaged over an optical length of 1 cm for FOX [54,

161]. Air cavities purposefully incorporated into PRESAGE® and FOX dosimeters have demonstrated measurements of the electron return effect with good agreement with literature [116, 120]. Considering the scale of dose differences beyond the build-up region and potential dose differences due to the presence of small air gaps between the dosimeters and phantoms, the percent differences in response with and without B_0 fields were minimal for FOX [161].

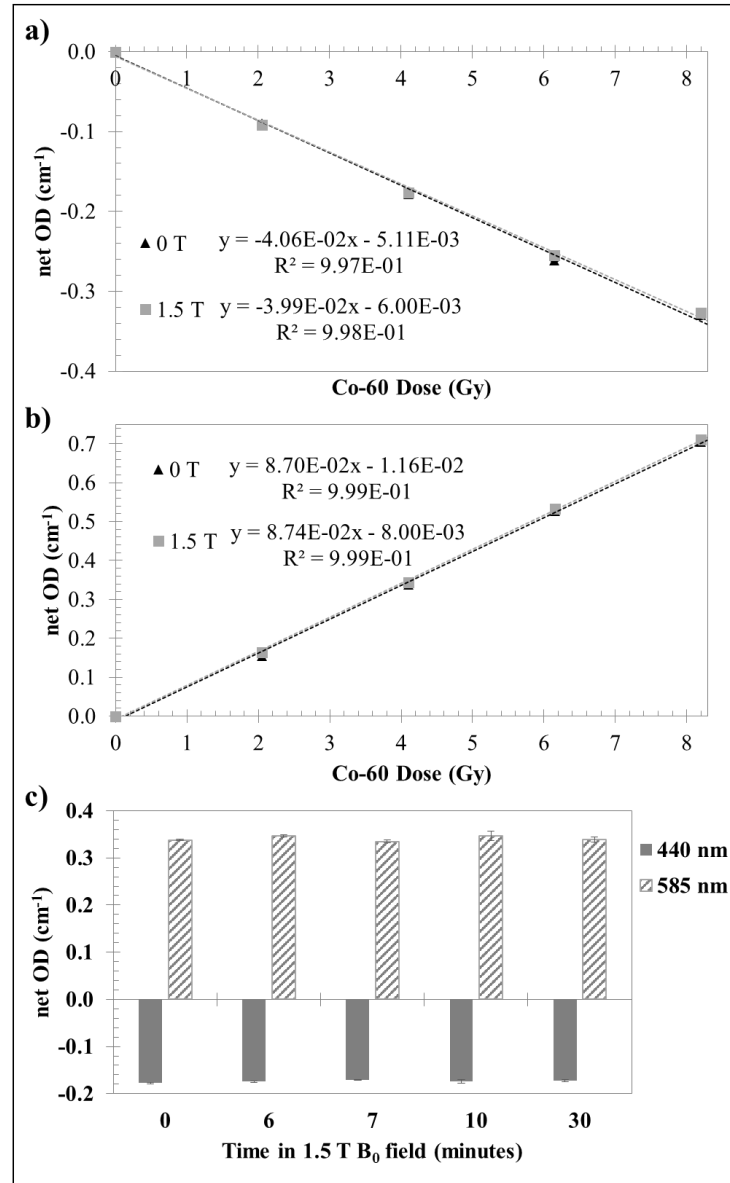


Figure 37: a) net OD versus dose linear calibration curves without ($R^2 = 1.00$) and with ($R^2 = 1.00$) 1.5 T B_0 field at spectral peak of 440 nm, b) linear calibration curves ($R^2 = 1.00$) at spectral peak of 585 nm, and c) net OD for FOX dosimeters at 440 nm and 585 nm for varying lengths of time in the 1.5 T B_0 field during irradiation to 4 Gy absorbed dose. The error bars represented the standard deviation of spectrophotometer measurements averaged for three cuvettes per data point.

B_0 field dependence was repeated for FOX inside the MR-Linac with 0 T and 1.5 T measurements separated by 9 days (1.5 T measurements were collected for the same batch of FOX used for 0 T stored at 4 °C in between irradiations and for a new batch of FOX prepared approximately 24 hours prior to 1.5 T irradiations) (Figure 38). Similar findings to the electromagnet irradiations were found in the MR-Linac (Figure 38). At 440 nm, the calibration curve slopes were different from 0 T by $2 \pm 2.5\%$ for the same batch at 1.5 T and $4 \pm 5\%$ for the new batch at 1.5 T. The largest difference between a single dose level was $7 \pm 6.5\%$ at 2 Gy. At 585 nm, the calibration curve slopes were different from 0 T by $3 \pm 2\%$ for the same batch at 1.5 T and $0 \pm 3.5\%$ for the new batch at 1.5 T. The largest difference between a single dose level was $8 \pm 3.5\%$ at 2 Gy.

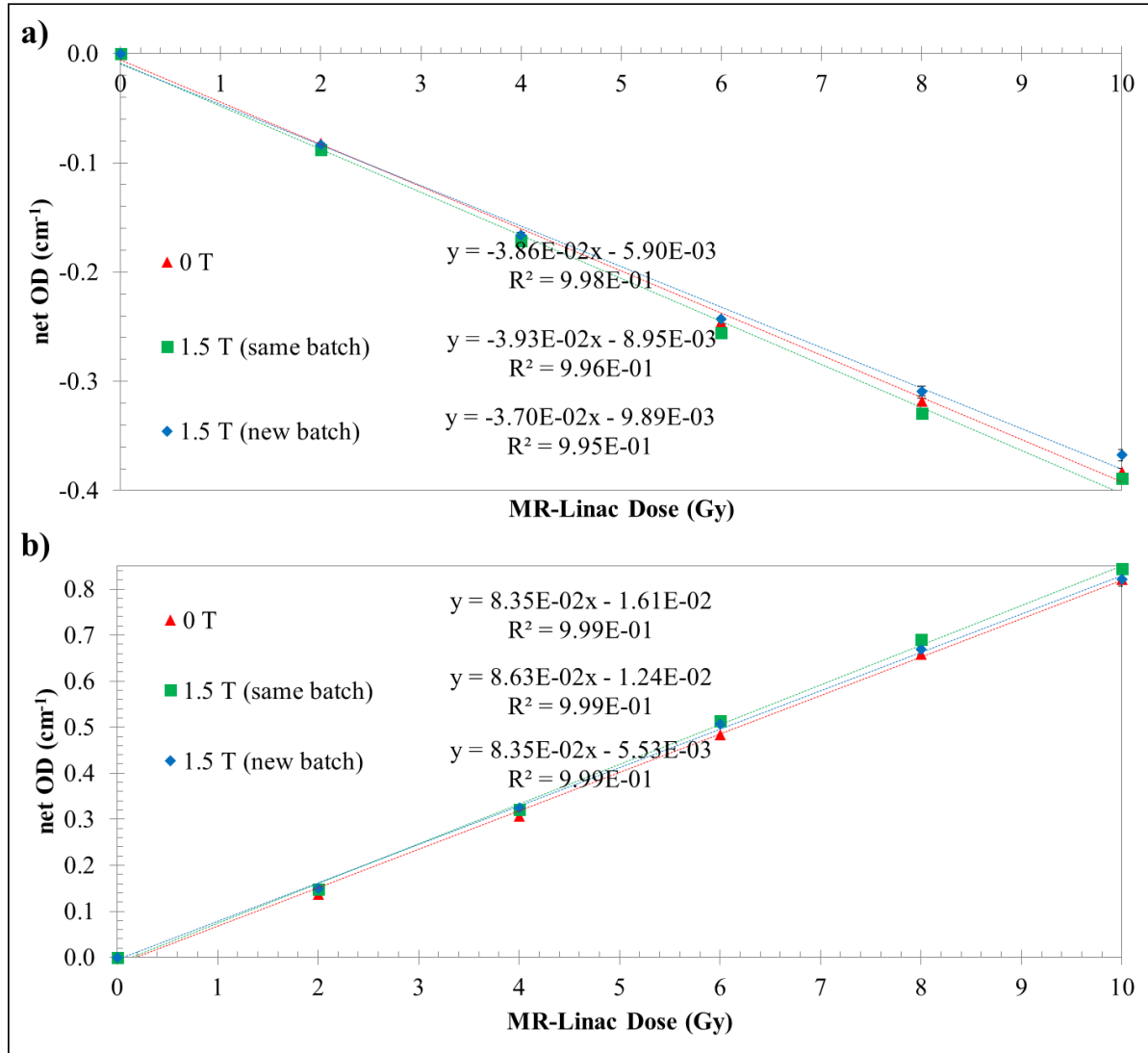


Figure 38: a) net OD versus dose linear calibration curves without and with 1.5 T B_0 field in MR-Linac at spectral peak of 440 nm and b) linear calibration curves at spectral peak of 585 nm. The error bars in the curves represented the standard deviation of spectrophotometer measurements averaged for three cuvettes per data point.

4.3 Gradient and radiofrequency field dependence

For the gradient/radiofrequency (B_1 /RF) field dependence portion of the study, cuvettes were placed inside a high impact polystyrene cuvette insert that was 1.3 cm thick. Water-equivalent plastic backscatter material of 13.2 cm and build-up water-equivalent plastic of 6 cm were placed underneath and above the cuvette insert plate, respectively. The cuvettes were irradiated with the same $10 \times 10 \text{ cm}^2$

field and approximately 4 Gy for each B_1 /RF field scenario. The cuvettes were irradiated with 4 different real-time imaging sequences: (1) no imaging during irradiation, (2) $TR/TE = 8/3.6$ ms, $B_1 = 20$ μ T, maximum gradient mode, $dB/dt = 20.5$ T/s, (3) $TR/TE = 8/3.6$ ms, $B_1 = 20$ μ T, regular gradient mode, $dB/dt = 7.3$ T/s, and (4) $TR/TE = 8/3.6$ ms, $B_1 = 3$ μ T, maximum gradient mode, $dB/dt = 14.0$ T/s (Figure 39). All real-time acquisitions had temporal resolutions of 400 ms. Relative to no real-time MRI during irradiation (only B_0 field present), the relative net OD was different by $-1 \pm 2.5\%$ for scenario (2), $-1 \pm 2.5\%$ for (3), and $-1 \pm 2.5\%$ for (4) at 440 nm and by $-1 \pm 2\%$ for scenario (2), $-1 \pm 2\%$ for (3), and $-2 \pm 2\%$ for (4) at 585 nm.

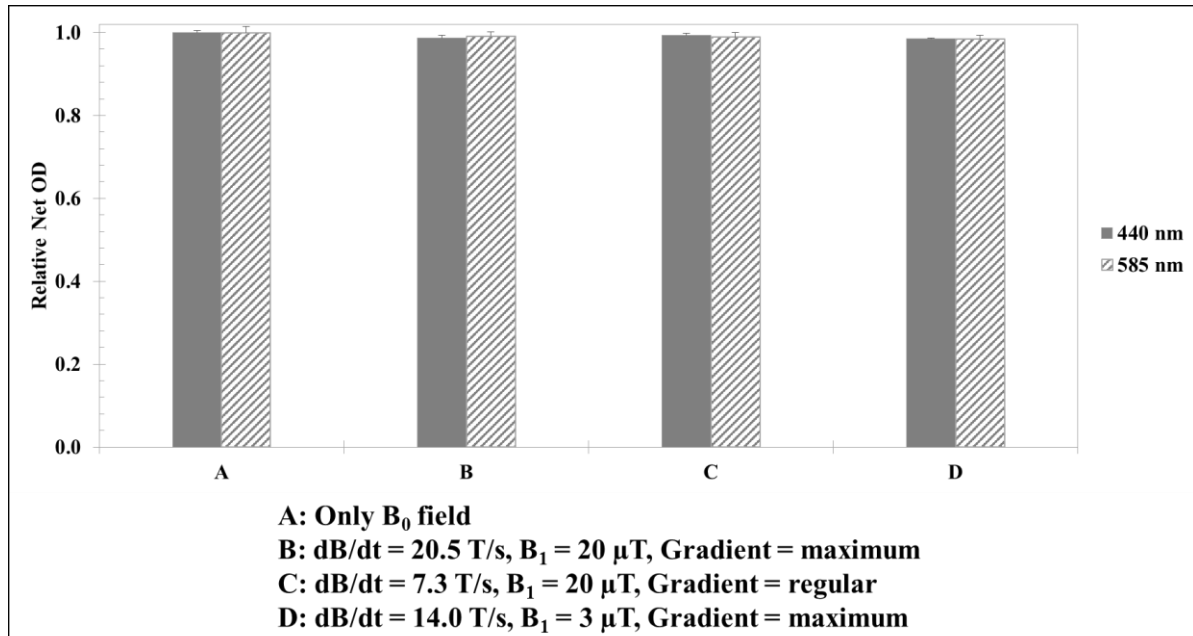


Figure 39: Assessment of potential B_1 /RF dependence on FOX gel using 4 different real-time bFFE sequences at both 440 nm and 585 nm optical peaks: A) no real-time MRI during irradiation, B) $TR/TE = 8/3.6$ ms, $B_1 = 20$ μ T, maximum gradient mode, $dB/dt = 20.5$ T/s, C) $TR/TE = 8/3.6$ ms, $B_1 = 20$ μ T, regular gradient mode, $dB/dt = 7.3$ T/s, and D) $TR/TE = 8/3.6$ ms, $B_1 = 3$ μ T, maximum gradient mode, $dB/dt = 14.0$ T/s. Values for B, C, and D were normalized to A for both wavelengths. All real-time acquisitions had temporal resolutions of 400 ms. The error bars represented the standard deviation of spectrophotometer measurements averaged for three cuvettes per data point.

4.4 Other MR considerations

Real-time plots of MR signal intensity change previously shown demonstrated that after the radiation beam was turned off, the signal continued to drift upwards, with lower slope. Since bFFE

images produce more banding artifacts (or Gibbs ringing artifacts) than post-irradiation T₁-weighted images, the effect of the number of signal averages (NSA, also known as number of excitations NEX) on the MR signal intensity was investigated (Figure 40). The temporal resolutions for NSA of 1, 2, 3, and 4 were 231 ms, 476 ms, 710 ms, and 947 ms, respectively. NSA and its effect on banding artifact on the real-time bFFE acquisition was assessed using only the rFOX gel with TR/TE = 3.8/1.92 ms for all NSA. Gibbs ringing artifacts are deterministic and could be reduced but could never be completely removed due to arising from the fundamental consequence of using Fourier transform to reconstruct MR signals into images (Figure 47).

The standard deviation for the real-time relative MR signal intensity decreased with increasing NSA (average standard deviation of 0.057, 0.033, 0.027, 0.024 for NSA = 1, 2, 3, and 4, respectively) (Figure 40). However, the temporal resolution worsened with increasing NSA (the time for MR image acquisition increases linearly with increasing NSA). The benefit of increasing NSA seemed to diminish for NSA > 3. The linear fit was no longer improved for NSA = 4 and the signal within the irradiated region began to decrease slightly during acquisition post-irradiation. The stability of the acquisition pre-irradiation and post-irradiation was further investigated using NSA = 2 up to 10 minutes pre-irradiation and 20 minutes post-irradiation (Figure 41). While the MR signal intensity gradually drifts downward prior to irradiation, the MR signal intensity remains relatively stable post-irradiation for up to 20 minutes (Figure 41).

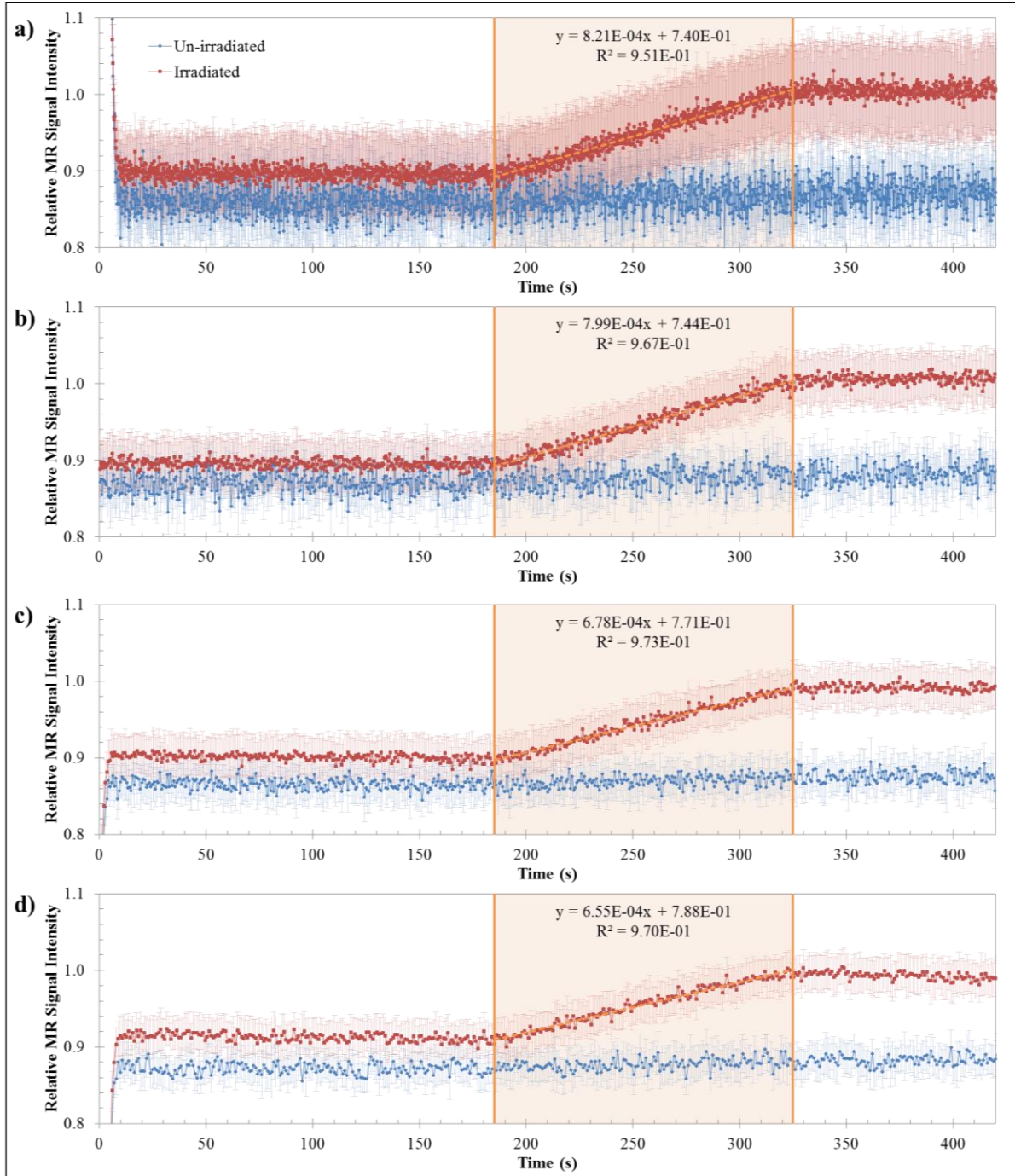


Figure 40: Real-time relative MR signal intensity for a) NSA = 1, b) NSA = 2, c) NSA = 3, and d) NSA = 4. The temporal resolution for NSA = 1, 2, 3, and 4 were 231 ms, 476 ms, 710 ms, and 947 ms, respectively. The orange shaded regions indicate beam on times. The red lines indicate the relative MR signal intensity in the irradiated region and the blue lines show the intensity in the un-irradiated region. The error bars represent the propagated standard deviation from the regions of interest measured within the irradiated region and outside the irradiated region in each dosimeter.

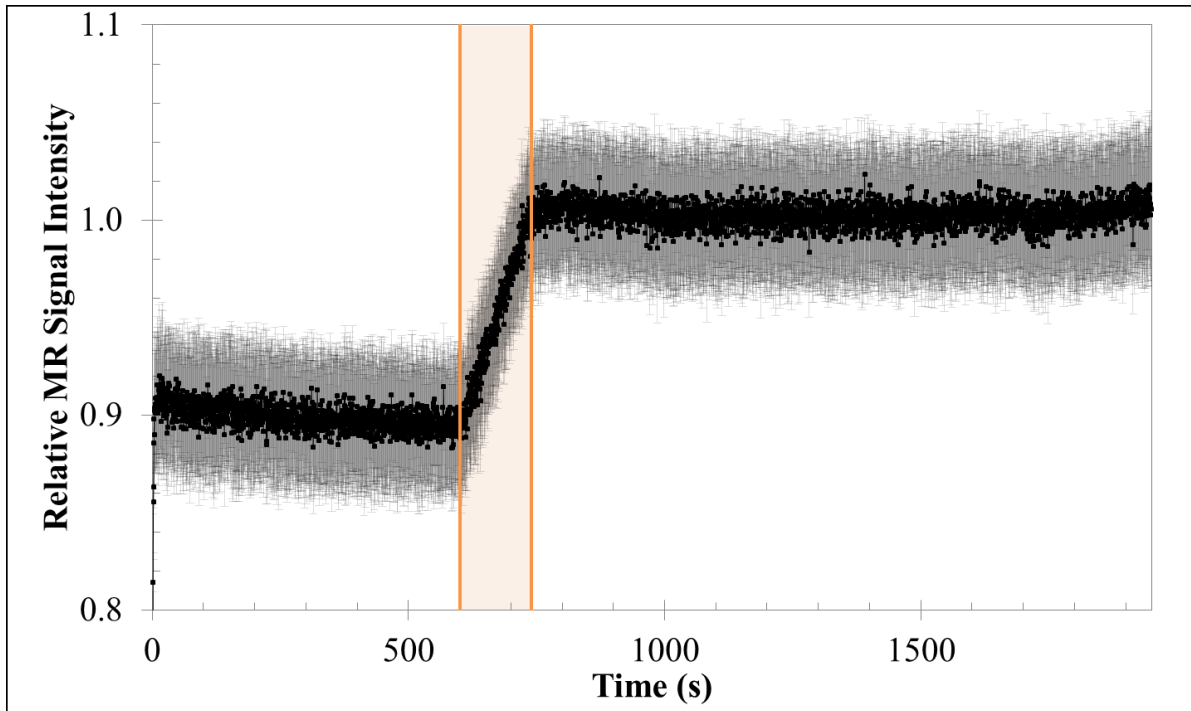


Figure 41: Real-time relative MR signal intensity for NSA = 2 with temporal resolution of 476 ms demonstrating stability of signal intensity pre-irradiation and post-irradiation for up to 10 minutes and 20 minutes, respectively. The orange shaded region indicates beam-on time. The error bars represent the propagated standard deviation from the regions of interest measured within the irradiated region and outside the irradiated region in each dosimeter.

A 3D dose distribution was acquired by irradiating a FOX gel with two gantry angles (0° and 270°). The two beams were separated by approximately 24 seconds, including time for gantry rotation. A central slice was imaged during irradiation to confirm the linear increase in MR signal intensity with time (and dose with constant rate of approximately 540 ± 10 cGy/minute). The regions of interest within and outside the beam path and change in MR signal intensity are also shown. Quantification of regions of interest within the central slice demonstrate that the gel again responded linearly with time (and dose with a constant dose rate) ($R^2 = 0.98$ and 0.99). Volumetric snapshots for the FOX gel are shown below.

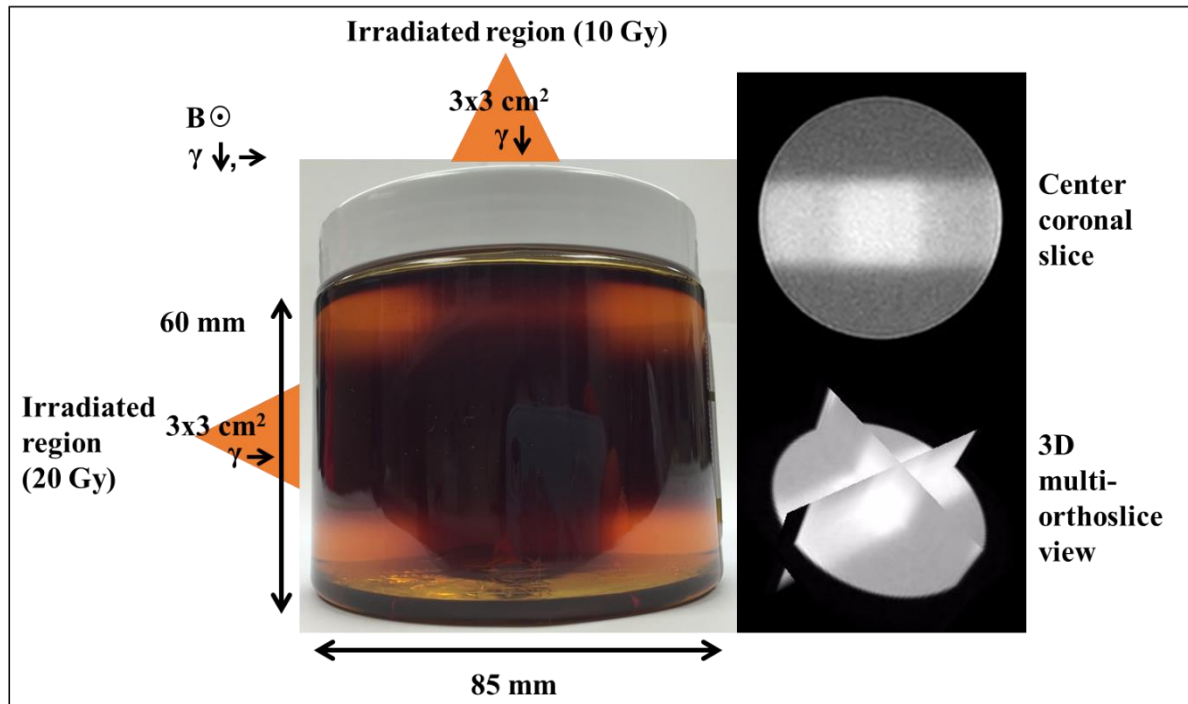


Figure 42: FOX gel used for 3D dose acquisition in an 85 mm diameter and 60 mm tall PET container. Post-irradiated T_1 -weighted images are shown to the right of the physical dosimeter (irradiated and imaged in MR-Linac).

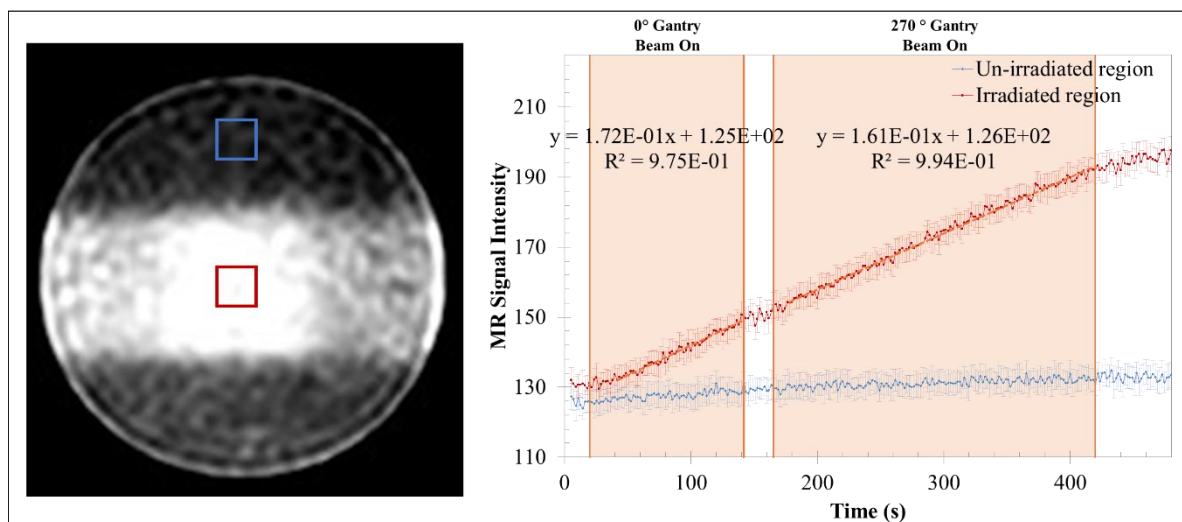


Figure 43: Real-time snapshot of FOX gel showing regions of interest used to assess un-irradiated and irradiated regions. Images were acquired using a bFFE sequence of $TR/TE = 4.4/2.2$ ms with 12 slices per acquisition, $NSA = 1$, and temporal resolution of 1800 ms. The red line indicates the relative MR signal intensity in the irradiated region and the blue line shows the signal in the un-irradiated region. The error bars represent the propagated standard deviation from the regions of interest measured within the irradiated region and outside the irradiated region.

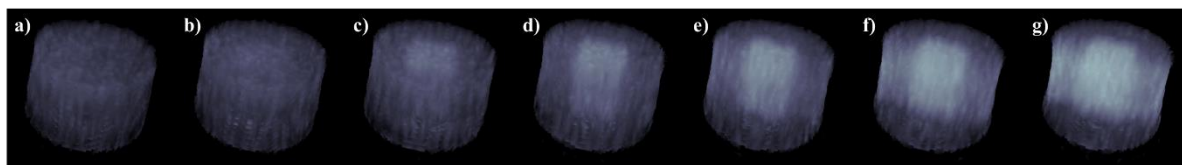


Figure 44: Real-time volumetric snapshots of FOX gel after irradiating to approximately a) 0 Gy, b) 5 Gy, c) 10 Gy, d) 15 Gy, e) 20 Gy, f) 25 Gy, and g) 30 Gy delivered to the center of the gel. The first 10 Gy were delivered with gantry angle 0° and the last 20 Gy with gantry angle 270°.

The volume dependence of FOX was investigated using 16 oz, 12 oz, and 4 oz PET containers irradiated to the same doses. The percent increase in MR signal intensity post-irradiation was $26.7 \pm 3\%$, $27.4 \pm 2\%$, and $26.1 \pm 2\%$ for 16 oz, 12 oz, and 4 oz FOX, respectively (Figure 45). These MR images were acquired with TR/TE = 500/20 ms, turbo spin echo (TSE), and with reconstructed voxels of $0.35 \times 0.35 \times 3.00 \text{ mm}^3$.

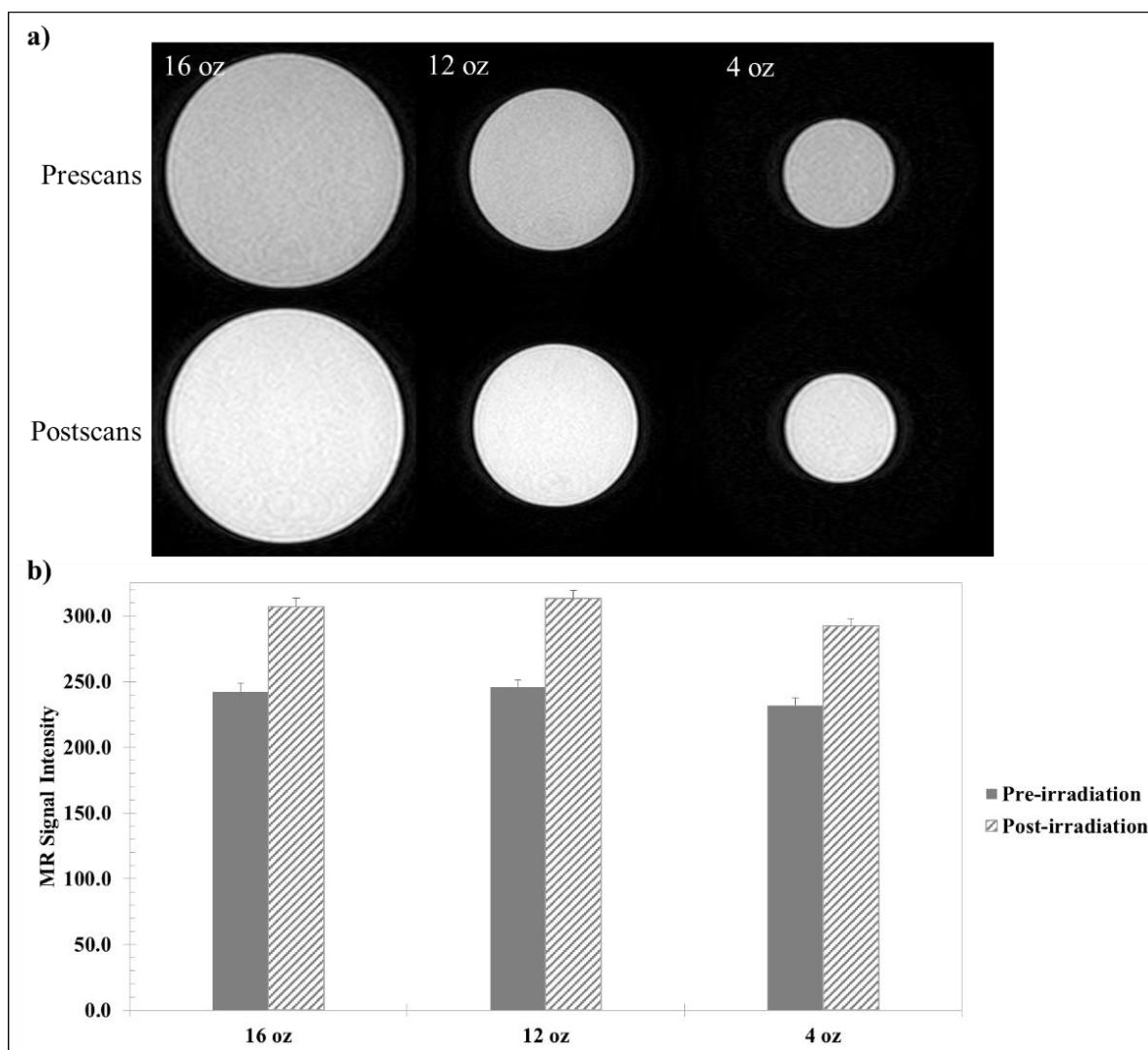


Figure 45: a) MR images of FOX gels in 16 oz, 12 oz, and 4 oz containers pre-irradiation and post-irradiation and b) MR signal intensities of those images. The error bars represent the standard deviation from the regions of interest measured within the pre-irradiated and post-irradiated regions in each dosimeter.

The MR images of FOX were also tested for gantry angle dependence since imaging could be acquired at arbitrary gantry angle during and after plan delivery in Chapter 5. Gantry angles 0°, 90°, 180°, and 270° were investigated (Figure 46). These MR images were acquired with TR/TE = 11/4.6 ms, T1 CE 3D FFE, and with reconstructed voxels of 0.83 x 0.83 x 1.00 mm³. The percent MR signal intensity increases were 42.3±3%, 43.1±3%, 42.8±3%, and 40.7±3% for gantry angles 0°, 90°, 180°, and 270°, respectively.

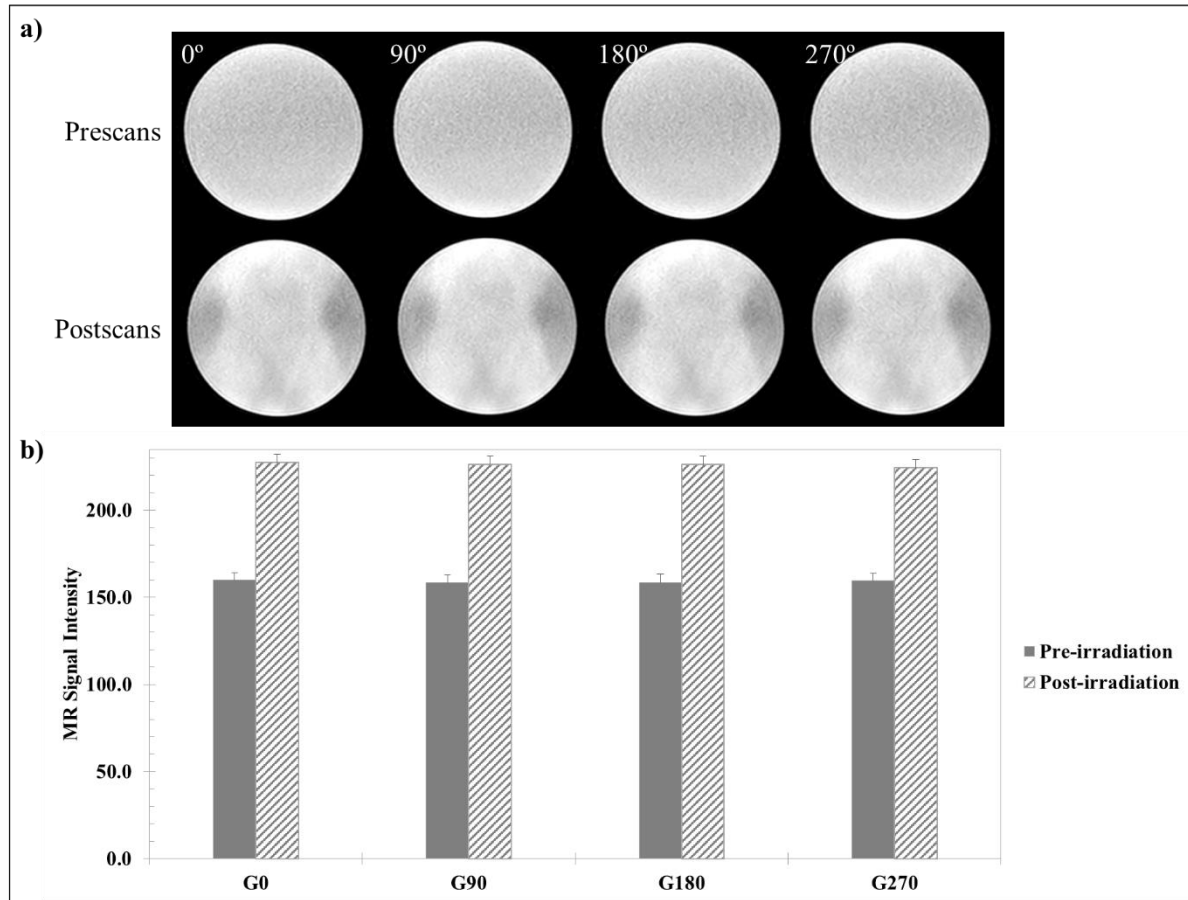


Figure 46: a) MR images of FOX gels for gantry angles 0°, 90°, 180°, and 270° pre-irradiation and post-irradiation and b) MR signal intensities of those images. The error bars represent the standard deviation from the regions of interest measured within the pre-irradiated and post-irradiated regions in each dosimeter.

MR-sequence specific artifacts included fold-over artifacts, Gibbs ringing artifacts at interfaces, zipper artifacts from PET plastic, and artifacts from super glue. These artifacts would arise regardless of the MRI system and were not specific to the MR-Linac. Examples of such artifacts are shown below in Figure 47. The presence of such artifacts could result in mis-analysis of dose when converting the MR images to relative doses. Fold-over artifacts could be mitigated by increasing the fold over suppression oversampling or by increasing the field of view acquired. Gibbs ringing artifacts could be reduced in the gel on the right of Figure 47b but could never be completely removed due to arising from the fundamental consequence of using Fourier transform of a truncated sinc function to

reconstruct MR signals into images. Zipper artifacts that generally occur with radiofrequency contamination from electronic devices occurred with spin echo sequences in PET plastic (with gel or water) but could be removed with a turbo spin echo sequence. The presence of super glue resulted in an MR signal void (whether the jar was filled with gel or water) but was not true with the use of hot glue. The main component of super glue is ethyl cyanoacrylate or another cyanoacrylate ester, which consists of carbon, hydrogen, nitrogen, and oxygen. The MR signal void was most likely due to a proprietary metal component that was not indicated in any technical data sheets.

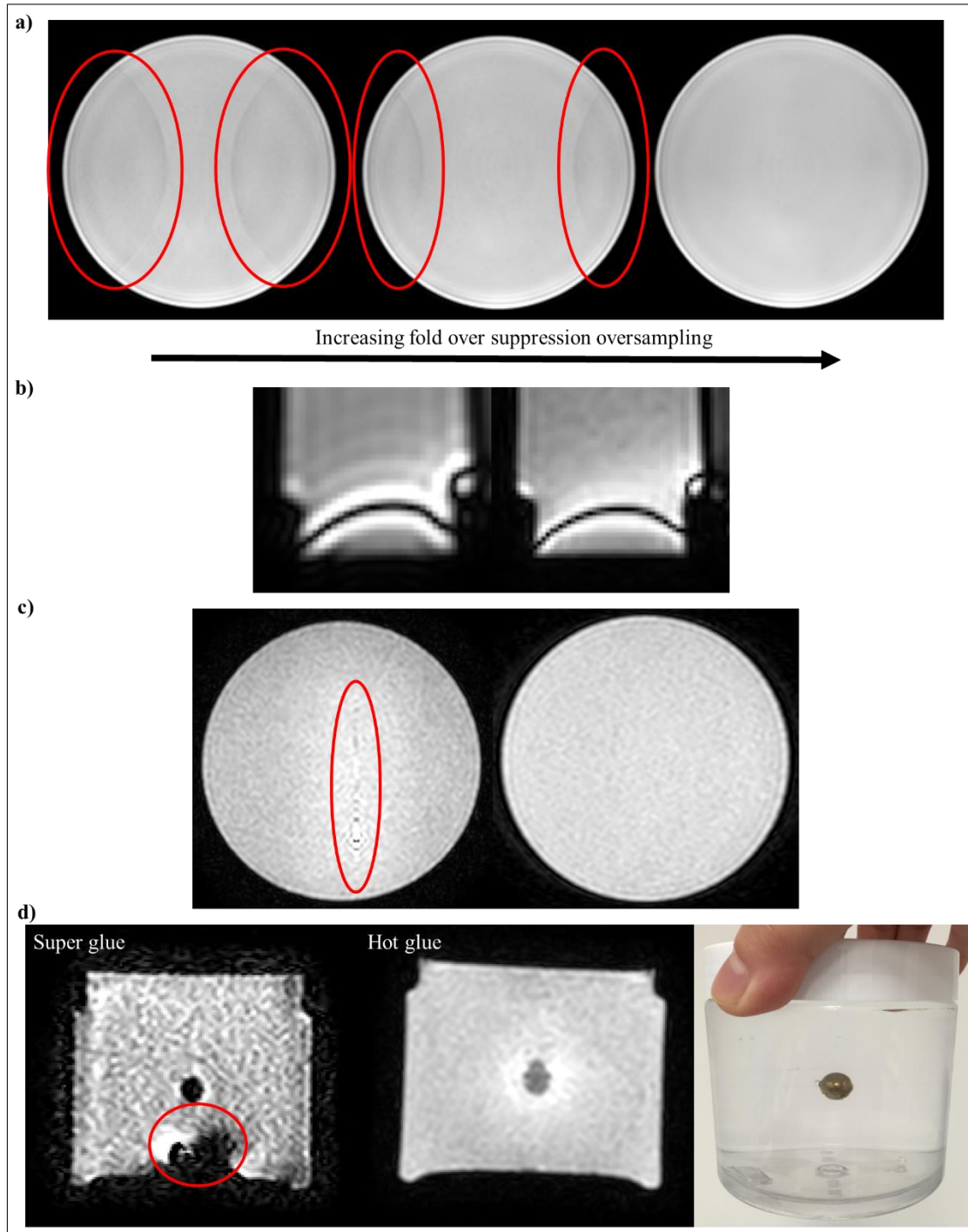


Figure 47: Examples of MRI artifacts. a) Fold over artifacts that could be remedied with suppression oversampling or increased field of view, b) Gibbs ringing artifact that could be reduced in the gel on the right but could never be completely removed due to arising from the fundamental consequence of using Fourier transform to reconstruct MR signals into images, c) zipper artifact that generally occurs with radiofrequency contamination from electronic devices occurred with spin echo sequences in PET plastic (with gel or water) and remedied on the right with a turbo spin echo sequence, and d) MR artifact due to super glue on bottom of jar (regardless of gel or water) but not present when hot glue was used. Central black region was due to brass ball bearing.

4.5 Summary

This chapter investigated MR-related considerations for volumetric dosimetry using MR images including B_0 field dependence, B_1 /RF field dependence, and potentials for MRI artifacts. Overall FOX was found to have up to $4\pm 5\%$ B_0 field dependence and up to $2\pm 2\%$ B_1 /RF field dependence. The real-time MR signal intensity change with radiation dose remained linear for FOX and rFOX regardless of the real-time bFFE sequence used. Example MRI artifacts that could affect the conversion of MR signal intensities scaled to relative volumetric dose distributions were also discussed for fold-over artifacts, Gibbs ringing artifacts at interfaces, zipper artifacts from PET plastic, and artifacts from super glue.

Chapter 5 – Volumetric phantom study

5.1 Rationale

MR-IGRT systems require a modified clinical workflow to integrate MR images for daily adaptive re-planning. Conventional treatment plan delivery checks are conducted using quasi-3D arrays such as the ArcCHECK or with 2D arrays. These are valuable clinical tools for quality assurance since they are not time consuming to set-up and take measurements from (compared to having to process and scan film for planar measurements). Dosimetry panels such as the IC Profiler (Sun Nuclear) and Starcheck (PTW) allow for measurements in two perpendicular profiles and two diagonal profiles. The detectors for these devices are distributed evenly over a surface. Investigations on the use of such devices in a B_0 field have been done [151, 153, 162]. The IC Profiler consists of 251 parallel plate ionization chambers (0.05 cm^3 sensitive volume per chamber) in its panel, with intrinsic build-up of 0.9 g/cm^2 and backscatter of 2.3 g/cm^2 . A 1.5 T B_0 field was found to affect the IC Profiler's profile measurements, but normalization profiles were comparable with that of film [151, 153]. The Starcheck consists of 527 vented ionization chambers, again in two perpendicular profiles and two diagonal profiles. The reference detector at the center position of the Starcheck was not always in the same orientation of nearby detectors, depending on the profile measured, resulting in a discontinuity in the profile [151, 153]. Similar to the IC Profiler, care must be taken when normalizing the Starcheck ionization chamber measurement values. Quasi-3D arrays such as the ArcCHECK (Sun Nuclear) and Delta-4 (Scandidos) have also been investigated in a B_0 field [151, 153, 163, 164]. The ArcCHECK is a cylindrical water-equivalent phantom consisting of an array of diodes near its perimeter with a 15 cm wide center cavity (with an assortment of available plugs, including a plug for ionization chamber reference dosimetry). The performance of the ArcCHECK in the 1.5 T MR-Linac was found to be within 1% of its performance in a conventional linac [151, 153]. The Delta-4 is not yet commercially available as an MR-compatible device. However, these devices cannot be MR imaged nor would they

provide valuable MRI information. Ideally, a fully anthropomorphic MR-visible and radiation-sensitive phantom would be used for a complete end-to-end clinical workflow assessment. While commissioning phantoms including CT and MR-visible materials are currently in development, these depend on point and planar measurements using thermoluminescent dosimeters (TLDs) and film, which can miss dose information in three dimensions [165, 166]. Compared to 3D gels, the implementation of a phantom for multi-institutional and remote dosimetry is of course simplified with a commissioning phantom with TLD and film inserts, with the understanding that volumetric dose distributions cannot be quantified. Conventional plan verification anthropomorphic phantoms only included planar film and point dosimeters (such as TLDs or ion chambers) and generally produced at best poor MR image quality. For example, MR imaging of an anthropomorphic Rando phantom required placing an MR-bright substance on top of the phantom and MR-visible PinPoint® #128 markers (Beekley Corporation, Bristol, CT) to assist with fusion of the MRI with CT (Figure 48).

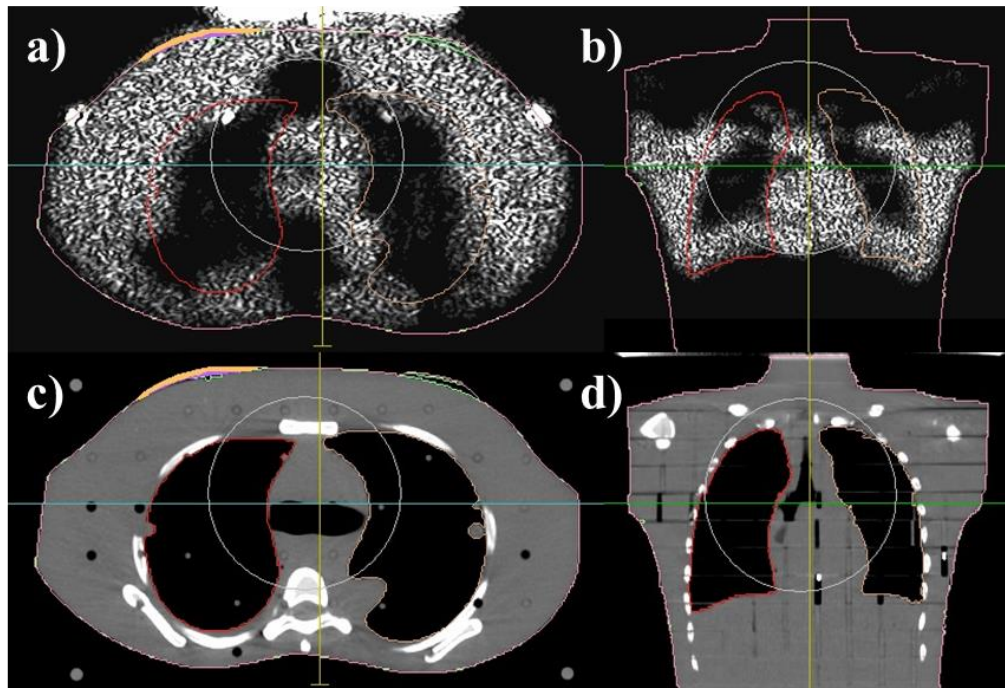


Figure 48: a) and b) The anthropomorphic Rando phantom imaged in the 1.5 T MR-Linac using the following parameters: 300 slices with FOV of $400 \times 400 \times 300 \text{ mm}^3$, reconstructed voxel $0.83 \times 0.83 \times 1 \text{ mm}^3$, T1-weighted $TR/TE = 11/4.6 \text{ ms}$, 3D FFE, and 30° flip angle. c) and d) CT of same phantom.

To fill the need for a large volumetric, MR-visible, and radiation-sensitive phantom for end-to-end assessment of MR-IGRT workflow, I utilized my rFOX and conventional FXG gel formulations in both heterogeneous and homogeneous phantom studies.

5.2 Heterogeneous rFOX phantom results and discussion

The first investigation of end-to-end testing on the MR-Linac using a volumetric phantom was done with a modified IROC-Houston head and neck phantom, commonly used for IMRT plan delivery validation, with an rFOX insert (Figure 49). The rFOX gel insert was created with four different heterogeneous components and one uniform homogeneous gel insert. The four heterogeneous components were a 1.3 cm diameter solution, a 1.3 cm diameter gel, a 1.3 cm diameter air, and a 3 cm diameter air (examples of 1.3 cm diameter and 3.0 cm diameter components shown in Figure 49). These heterogeneous components were selected to mimic anatomical heterogeneities present in the human body that can produce dose perturbations in a strong magnetic field. Relevant examples include tissues similar to what was generalized as soft-tissue such as various soft organs and blood vessels (rationale for including solution heterogeneity). Other examples include air cavities such as the sinuses and trachea (rationale for including air heterogeneities of different sizes). The remainder of the head and neck phantom was composed of plastic filled with water.

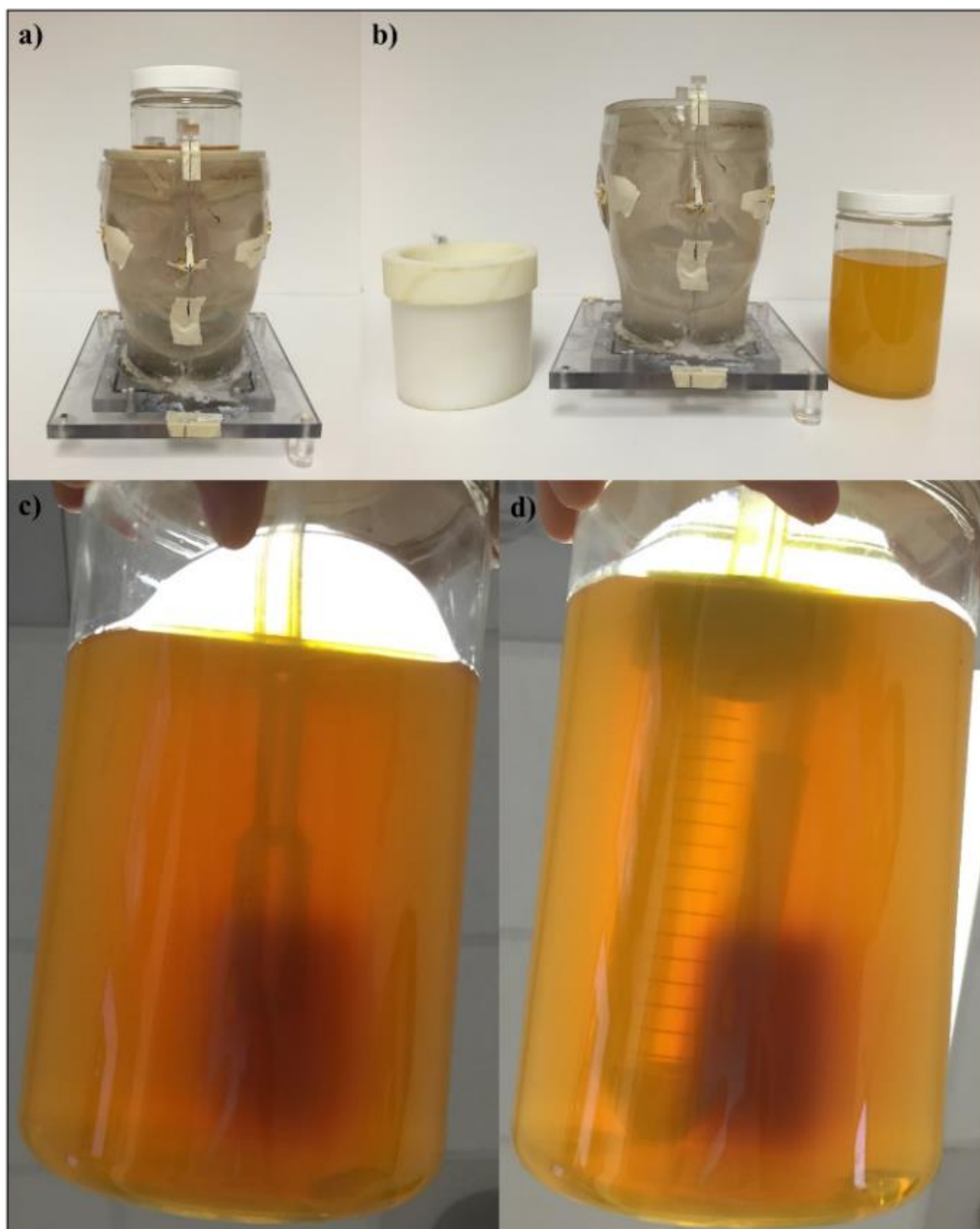


Figure 49: Pictures of head and neck phantom and rFOX inserts. a) rFOX inside of phantom, b) rFOX outside of phantom, c) example of 1.3 cm diameter heterogeneous component in rFOX, and d) example of 3.0 cm diameter heterogeneous component in rFOX (purple regions were irradiated areas).

All of the combinations of rFOX inserts inside the head and neck phantom were initially CT scanned with 120 kV, 250 mAs/slice, and 1 mm slice thickness. The CT number to electron density (used for dose calculations in treatment planning systems) for 120 kV and the Philips Brilliance Big Bore CT scanner are plotted below (Figure 50). The average CT numbers of the rFOX gels, water in the phantom, and air were 20.3 ± 9.2 , 3.2 ± 7.9 , and -1002.6 ± 3.9 , respectively. These CT numbers could then be used to calculate the linear attenuation coefficient of each material, which was energy dependent. The x-ray mass attenuation coefficient of water provided by NIST (μ/ρ) and the density of water 1 g/cm^3 were used to calculate the linear attenuation coefficients of rFOX and air using the equation: $\mu_{\text{material}} = (\text{CT number} \times \mu_{\text{water}} / 1000) + \mu_{\text{water}}$, where $\mu_{\text{water}} = 0.142 \text{ cm}^{-1}$ for 120 kV. μ_{rFOX} and μ_{air} were calculated to be 0.145 cm^{-1} and 0.00036 cm^{-1} , respectively, under these conditions. The electron densities for all materials were calculated within Monaco TPS.

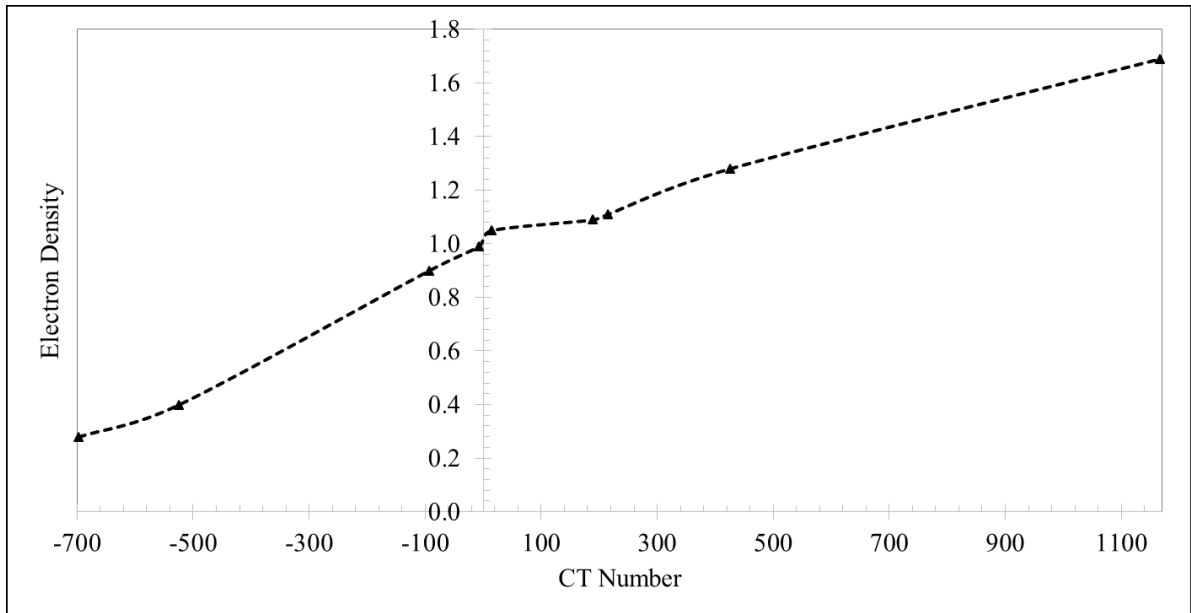


Figure 50: CT number to electron density conversion.

Reference plans were made in the Monaco TPS (research version 5.19.02) using the CT images acquired of the rFOX inserts in the head and neck phantom. Complete cross-validation of the Monaco TPS in a B_0 field environment had not yet been done at the time of this dissertation work, so some

uncertainties in dose are expected as a result (conventional TPS calculations include up to 3% dose uncertainties in clinical use due to many different factors, including conversions of CT numbers to electron density for dose calculations). Monaco TPS used Monte Carlo dose calculations in a graphical processing unit environment that incorporated a 1.5 T B_0 field. Daily T2-weighted, T1-weighted T1 CE, and T1-weighted no CE MR images were acquired for fusion with the CT to create the daily adapted plan based on the phantom position in the MR-Linac. These daily adapted plans were then delivered in the MR-Linac and post-irradiation MR images were acquired of the gels in the same position. Prior to MR-IGRT systems, it was not possible to pre-scan, irradiate, and post-scan 3D dosimeters all in the same position. With the MR-Linac and other MR-IGRT systems, we now have the ability for delivering a treatment plan to a 3D dosimeter in the exact position that it was planned for with the possibility for real-time onboard MR imaging during irradiation and immediate MR imaging post-irradiation. The overall MR-IGRT workflow is shown below (Figure 51).

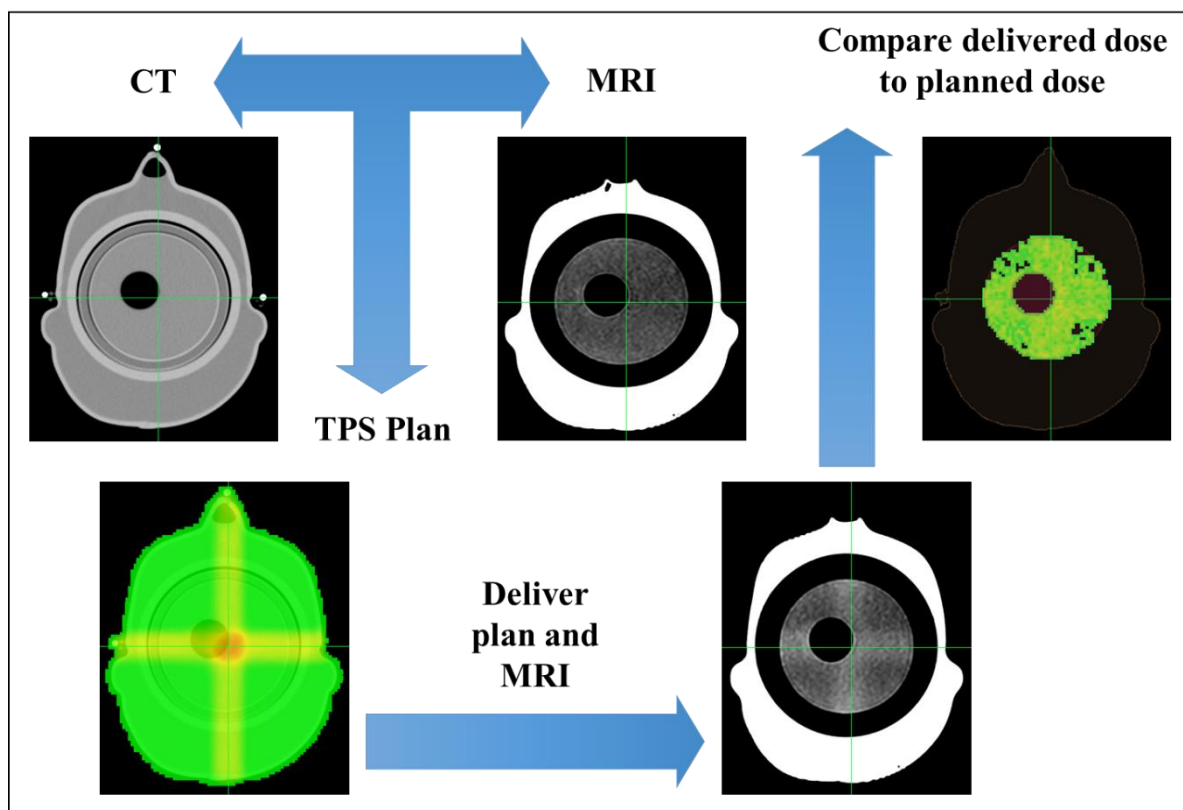


Figure 51: Overall MR-Linac workflow. First, make a reference TPS plan from the CT. Next, fuse the daily MRI with the CT and make an adapted plan. Next, deliver this plan and obtain a post-irradiation MRI. Finally, compare the relative delivered dose with the planned dose.

Small differences (<0.3 mm) in fusion coordinates were found depending on the MR image sequence used (T2-weighted, T1-weighted T1 CE, and T1-weighted no CE) (Table 12). Overall, T2-weighted MR images were not recommended for fusion with CT due to greater distortions at interfaces, distorting the geometric accuracies of sharp edges in the images (Figure 52). No differences in fusion coordinates were found for MR images acquired at different gantry angles (Table 12), which agreed with previous results of investigating MR signal intensities at different gantry angles (Figure 46). MR images acquired with T1-weighted no CE were used for all fusion for adapted plans due to its superior visibility of edges and reduced noise compared to T2-weighted and T1-weighted T1 CE (Figure 52).

Table 12: Fusion translation coordinates for MRI with CT.

MRI sequence type	Gantry angle	x (cm)	y (cm)	z (cm)
T2-weighted	0°	-0.0595	-49.2979	-8.1302
T1-weighted T1 CE	0°	-0.0595	-49.2979	-8.1591
T1-weighted no CE	0°	-0.0695	-49.2879	-8.1591
T1-weighted no CE	90°	-0.0695	-49.2879	-8.1591
T1-weighted no CE	180°	-0.0695	-49.2879	-8.1591
T1-weighted no CE	270°	-0.0695	-49.2879	-8.1591

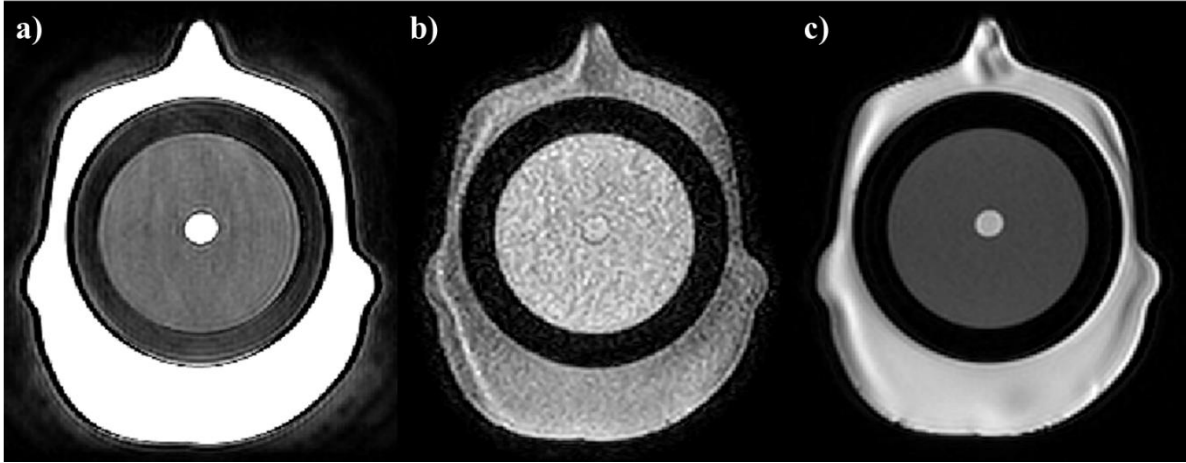


Figure 52: a) T2-weighted MRI, b) T1-weighted T1CE MRI, and c) T1-weighted no CE MRI.

Regardless of the NSA used for a given MRI acquisition, T2-weighted sequences used 3D TSE, $TR/TE = 1535/278$ ms, field of view of $400 \times 400 \times 300 \text{ mm}^3$, and reconstructed voxels of $0.83 \times 0.83 \times 1.00 \text{ mm}^3$. T2-weighted acquisitions took 1:57 minutes with NSA = 1. T1-weighted T1 CE and T1-weighted no CE sequences used 3D FFE and $TR/TE = 11/4.6$ ms with the same field of view and reconstructed voxels dimensions as T2-weighted sequences. Both T1 CE and no CE acquisitions took 1:54 minutes, 5:42 minutes, and 9:29 minutes for NSA = 1, 3, and 5, respectively.

Due to some initial bugs in Monaco TPS that were addressed after this portion of the study, rectangular 3D fields of $4 \times 2 \text{ cm}^2$ were delivered to the phantom; consequently, the adapted plans did not perfectly match the irradiation conditions used so lower agreement between the rFOX calculated relative dose and the Monaco TPS calculated dose were expected. 3D fields of $4 \times 2 \text{ cm}^2$ were delivered as 1 beam (gantry angle 0°), 2 beams (0° and 180°), 3 beams (60°, 180°, and 300°), 4 beams (0°, 90°, 180°, and 270°), and 5 beams (0°, 60°, 180°, 270°, and 300°).

180°, and 270°), and 7 beams (306°, 255°, 204°, 0°, 51°, 102°, and 153°). After acquisition of the pre-irradiation and post-irradiation MR images, the relative volumetric dose distributions quantified in the gels were compared to Monaco TPS's calculated doses using 3D Slicer (version 4.6.2) [167, 168]. 3D Slicer was an open source software platform that could be used for a wide variety of applications and has been validated for TPS plan comparisons using gamma analysis [116, 169]. The 3D Slicer workflow is described below.

Step 1: Install 3D Slicer software from <http://download.slicer.org/> (the latest version available at the time of this dissertation work was 4.6.2).

Step 2: Install the “SlicerRT” extension.

Step 3: Import dicom files (planned dose, structures, prescan, postscan, and etc.) using the “DICOM Browser”. I preferred to use “Add link” rather than “Copy” due to the size of my files.

Step 4: Load the imported dicom files. If the prescan and postscan were acquired in the same study set, load each series separately. If they are loaded at the same time from the same study set, then the values will not appear as single scalar values for each, which means the prescan values cannot be subtracted from the postscan values. After each piece is loaded, the screen will clear. Click on the “DCM” transfer button to load the next series.

Step 5: Double check that everything was loaded by going to “Subject Hierarchy” (Figure 53).

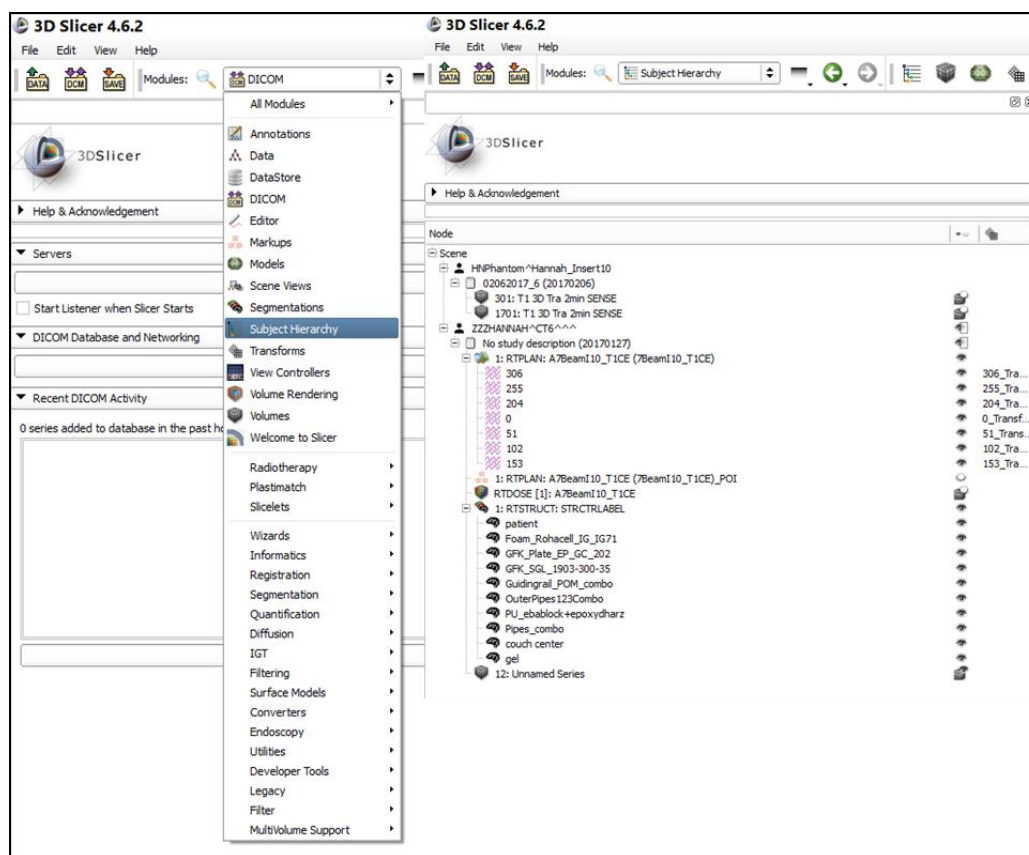


Figure 53: “Subject Hierarchy” in 3D Slicer.

Step 6: Go to “Subtract Scalar Volumes”. Select your postscan for “Input Volume 1” and prescan for “Input Volume 2”, enter new output volume name, and click “Apply”. Wait until “Status: Completed” (Figure 54).

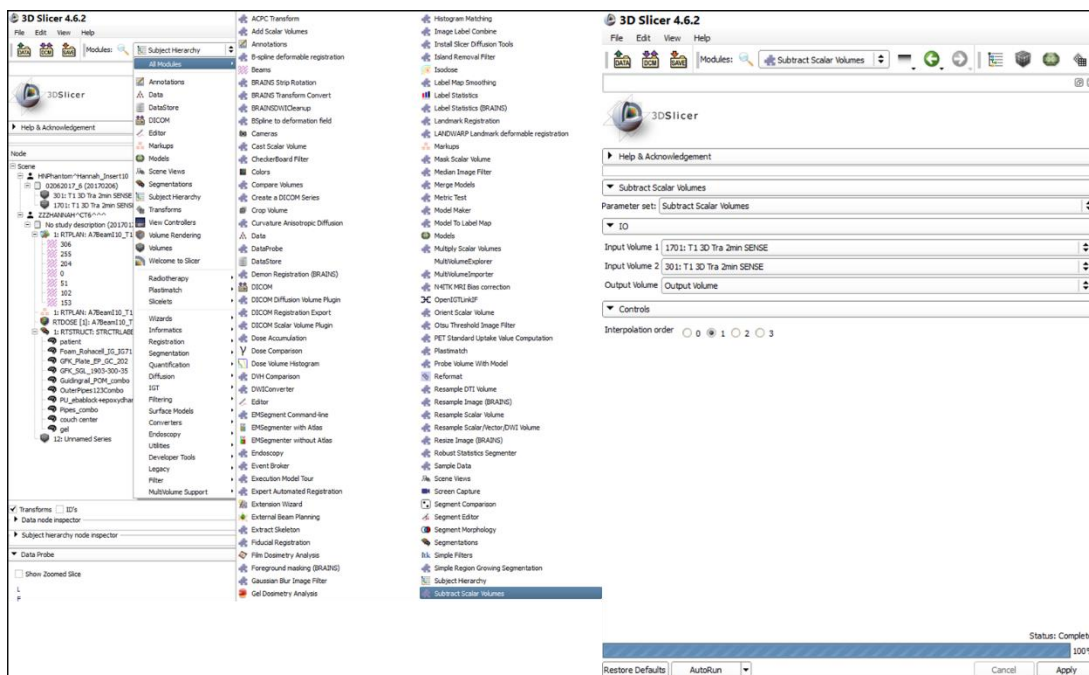


Figure 54: “Subtract Scalar Volumes” in 3D Slicer.

Step 7: Go to “Transforms” to align your MRI volumes with your plan volumes (based on CT coordinates). Depending on the coordinate systems of your MRI, CT and TPS, you may need to press “Identity” or the image planes may be mismatched (for example, the sagittal plane will appear in the axial plane and rotated incorrectly). You can then manually adjust the translation for LR, PA, and IS. If using the MR-Linac system for acquiring your MR images and Monaco TPS, you may enter your MR-Linac isocenter coordinates from Monaco TPS adapted plan (fusion translation coordinates already applied from the daily MR images) as the following into 3D Slicer: X (cm) \rightarrow -LR (mm) (may or may not be +/-LR depending on how the MR images were exported, can be easily checked using the axial plane view), Z (cm) \rightarrow PA (mm), and Y (cm) \rightarrow IS (mm). After you are satisfied with the transform coordinates, go to “Convert”, select a reference volume (any of the MRI volumes), enter a name for the “Output Displacement Field”, and press “Apply” (Figure 55).

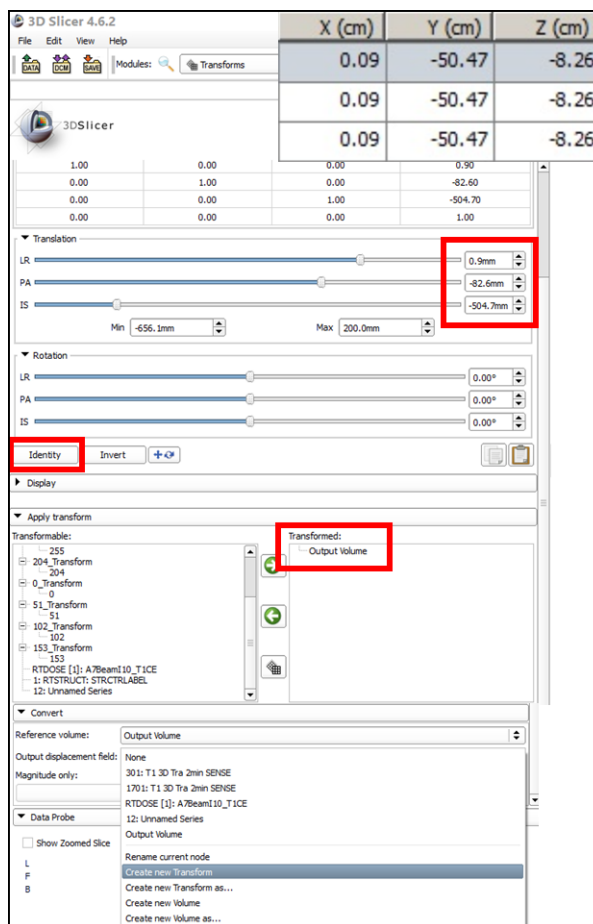


Figure 55: “Transforms” in 3D Slicer.

Step 8: Go to “Simple Filters”. Here you can select any post-processing image filters for denoising (such as “MedianImageFilter” and others). Make sure to create a new “Output Volume” name to not over-write your currently existing volumes. After creating any new volumes, you will need to go back to “Transforms” and push those volumes over to the right side to be transformed. You will also do your image scaling to a relative dose here using “ShiftScaleImageFilter”. “Shift” should be used for background values first and then “Scale” for the relative dose inside irradiated regions. Make sure to reset “Shift” to 0 and “Scale” to 1 after making any changes (and again, you may choose to over-write a volume or create a new volume each time and then transform the new volume). In order to know what values to enter, you may visualize the planned dose and your gel image as an overlay and see the values of each pixel under “Data Probe” (Figure 56).

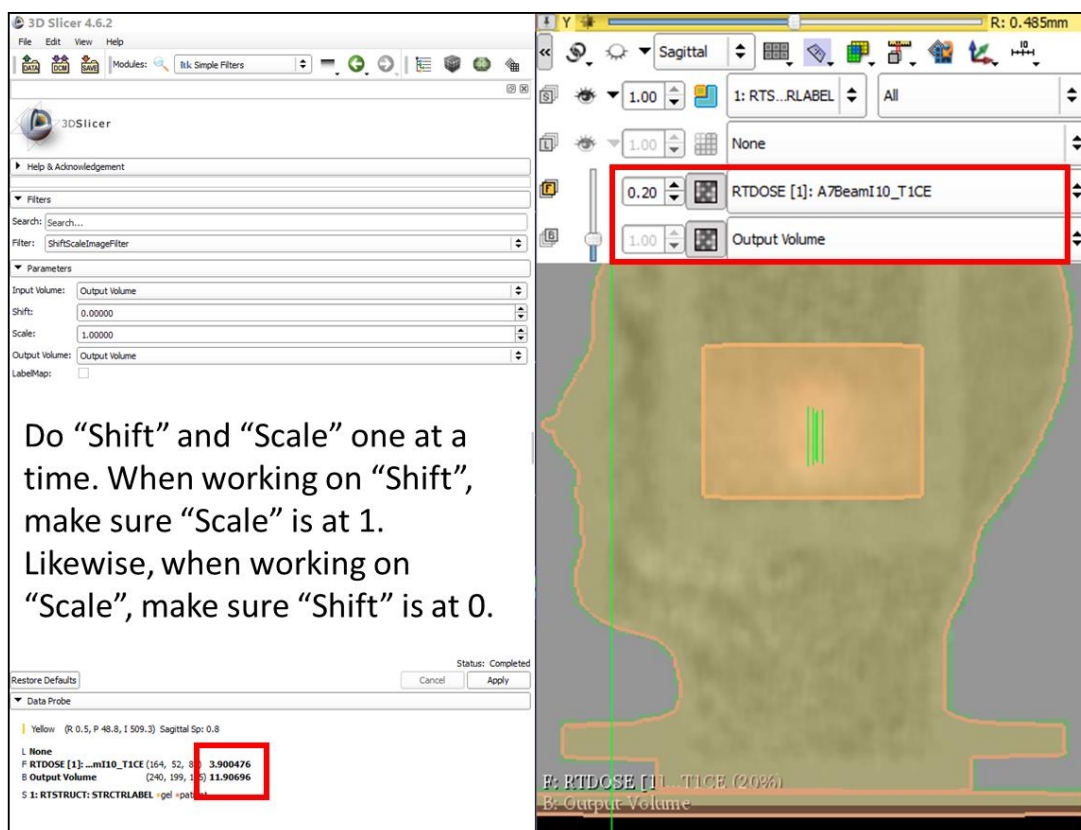


Figure 56: “Simple Filters” in 3D Slicer.

Step 9: Once you have shifted and scaled your desired relative dose volume, go back to “Subject Hierarchy” and make sure that this volume is under a study (notepad icon to left of study). If it is not, then drag the series under a study (any study). Then right click on the gel series and select “Convert to RT dose volume”. The icon to the left of the series should change from a gray cube to a multi-colored cube (Figure 57).

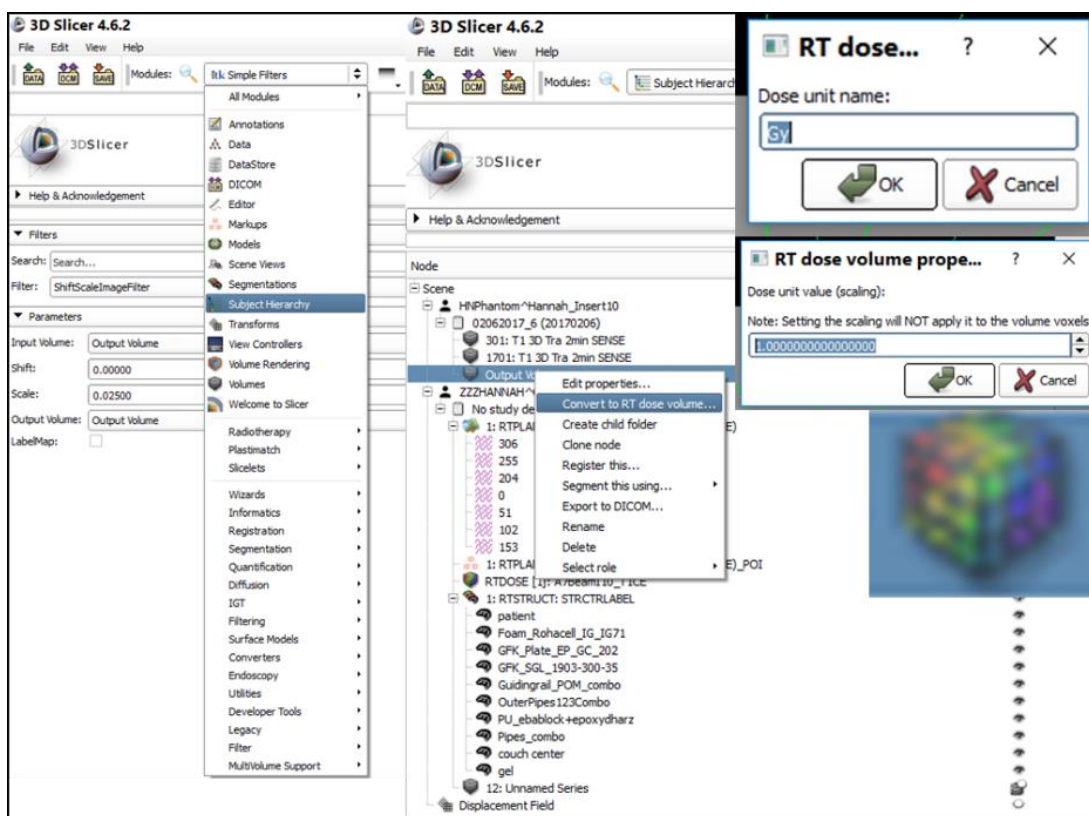


Figure 57: “Subject Hierarchy” to convert to RT dose volume in 3D Slicer.

Step 10: Once you have converted your desired relative dose volumes into RT dose volumes, go to “Radiotherapy” then “Dose Comparison”. You may then enter in your 3D gamma criteria and dose thresholds. You can select a “Mask structure” to only analyze dose within the gel and not for the entire patient structure set. Again, enter in a new volume name for “Gamma volume” to not over-write any existing volumes. Once you press “Calculate gamma”, you have your gamma analysis results (Figure 58)!

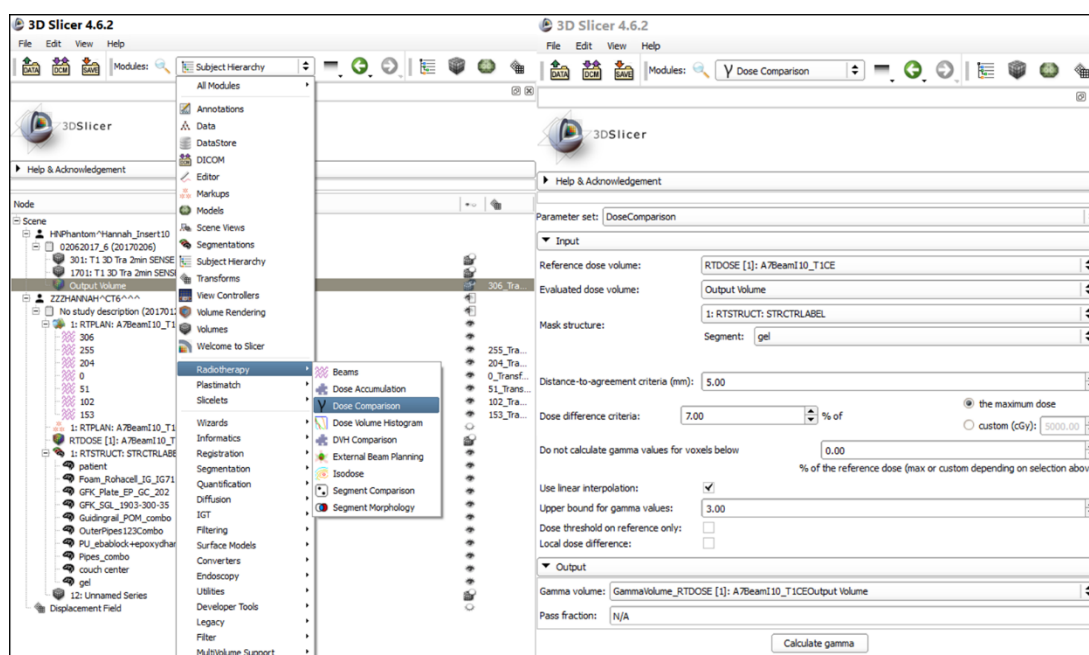


Figure 58: “Dose Comparison” in 3D Slicer.

Step 11: Helpful shortcuts for manipulating your images are available here:

<https://www.slicer.org/wiki/Documentation/4.4/SlicerApplication/MouseandKeyboardShortcuts>.

Gamma analysis was used for comparison of the two dose distributions in this dissertation work (relative dose calculated from MR images of gel and dose calculated from Monaco TPS). Gamma analysis was developed by Low *et al.* to combine comparisons of dose and spatial information [170]. The minimum distance from a reference point from the reference dose (calculated from TPS) to the measured point of the comparison dose (relative dose calculated from 3D dosimeter) is the gamma index. A gamma index greater than 1 indicated a failing value. A gamma criteria of 7%/4mm distance to agreement (DTA) was used by IROC for IMRT head and neck plans for 2D gamma analysis of film [171]. While 3D dosimetry studies have used other gamma criteria for 3D gamma analysis (which added another spatial dimension to 2D gamma analysis), 7%/4mm was used along with stricter gamma constraints (5%/3mm and 3%/3mm) as a comparison with passing cutoffs of 80% [170–173]. While 85% is the typical passing cutoff, up to 5% differences in gamma pass rates were found depending on

small changes to scaling for relative doses. As mentioned earlier, lower than normal gamma passing rates (and therefore lower agreement between the two dose distributions) were expected for this portion of the study due to initial bugs in Monaco TPS not allowing for the full MR-Linac workflow. A 10% dose threshold was applied for all of the gamma analysis, regardless of the gamma criteria. Because of the standard deviation due to the noise in the MR images (up to ~10% of the mean MR signal intensity), it is important to note that there is a risk of voxels passing with 3D gamma analysis using loose criteria (such as 7%/4mm used in this dissertation work). However, since the purpose of this development project was to demonstrate the proof of concept of the end-to-end testing workflow using a 3D dosimeter and to demonstrate the feasibility of doing so with heterogeneous and homogeneous 3D dosimeters, both loose and tighter gamma criteria were used to analysis the relative volumetric dose distributions.

As mentioned in the 3D Slicer Workflow, several image post-processing tools are built into the software, including noise reduction filters, such as the MedianImageFilter and MeanImageFilter. The MedianImageFilter (Figure 59) and MeanImageFilter (Figure 60) computed values of each output pixel as a statistical median/mean of neighborhood values around a corresponding input pixel. The radius of neighborhood pixel values to search can be specified in all three dimensions. While increasing the radius of neighborhood pixel values to search improves the smoothness of the image, this could remove thin structures and cause blurring of signal, such as in areas with steep dose gradients. Since noise in the images were more prevalent in T1-weighted T1 CE images, an analysis of the ideal radius (same radius value applied in all three dimensions) to use to post-process T1 CE images with NSA = 1 was investigated for only the heterogeneous rFOX phantom with 1.3 cm solution insert for 1 beam delivery.

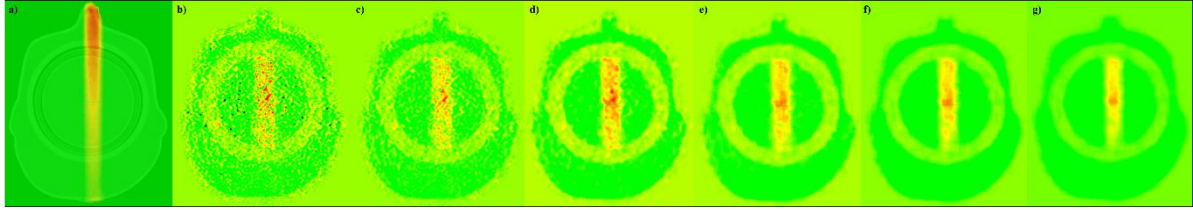


Figure 59: a) Planned dose overlaid on CT image, b) calculated relative dose from rFOX (T1 CE, NSA = 1) with no post-processing filter, c) MedianImageFilter radius 1, d) MedianImageFilter radius 2, e) MedianImageFilter radius 3, f) MedianImageFilter radius 4, and g) MedianImageFilter radius 5. The central region of rFOX that appears like a hot spot is due to the heterogeneous component and was not used for dose comparisons since that region cannot be scaled appropriately.

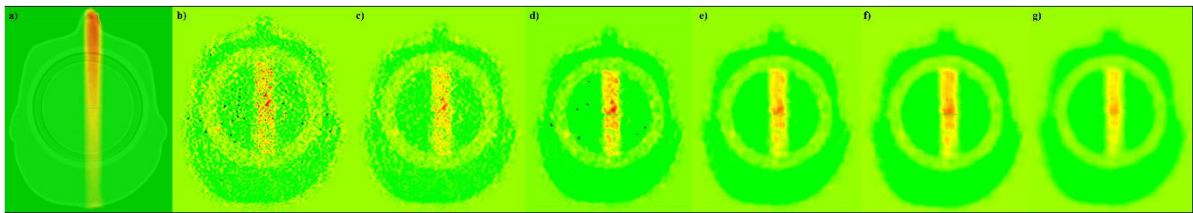


Figure 60: a) Planned dose overlaid on CT image, b) calculated relative dose from rFOX (T1 CE, NSA = 1) with no post-processing filter, c) MeanImageFilter radius 1, d) MeanImageFilter radius 2, e) MeanImageFilter radius 3, f) MeanImageFilter radius 4, and g) MeanImageFilter radius 5. The central region of rFOX that appears like a hot spot is due to the heterogeneous component and was not used for dose comparisons since that region cannot be scaled appropriately.

Table 13: 3D gamma pass rates for heterogeneous rFOX phantom with 1.3 cm solution insert with image post-processing. Pass rates above the 80% cutoff are highlighted in green.

Post-processing	Radius (pixel)	7%/4mm	5%/3mm	3%/3mm
No filter	--	99.39%	86.38%	69.59%
MedianImageFilter	1	98.30%	87.85%	74.95%
MedianImageFilter	2	93.28%	78.375%	67.81%
MedianImageFilter	3	85.09%	66.30%	56.62%
MedianImageFilter	4	84.78%	70.07%	59.63%
MedianImageFilter	5	82.37%	69.84%	58.27%
MeanImageFilter	1	97.94%	87.72%	75.30%
MeanImageFilter	2	91.16%	77.04%	65.89%
MeanImageFilter	3	85.71%	70.54%	60.76%
MeanImageFilter	4	82.67%	65.38%	54.69%
MeanImageFilter	5	82.04%	64.68%	52.38%

Analysis of post-processing with both the MedianImageFilter (Figure 59) and MeanImageFilter (Figure 60) for T1-weighted T1 CE NSA = 1 images showed that the pass rate was

similar for no filter and with filters of radius 1 (Table 13). This indicated that careful shifting and scaling of the original postscan – prescan images could be used for gamma analysis without any post-processing. However, the addition of a filter with radius 1 did improve more strict gamma criteria pass rates, so the MedianImageFilter with radius 1 was applied for all following T1 CE NSA = 1 images. Overall, no CE gamma pass rates were higher than those for T1 CE for tighter gamma criteria even if the looser 7%/4mm gamma pass rates were lower by less than 1.5% (could potentially be improved with better scaling of relative dose). This indicated that the no CE images resulted in more informative relative dose pixels spatially compared to T1 CE, which were noisier. no CE was also more accurate with subtracting the prescan from the postscan as can be seen where the heterogeneous region appeared black from being completely subtracted (Figure 61d). The 3D gamma pass rates and representative images for the rFOX gel are below for 1.3 cm diameter solution heterogeneity (Table 14 and Figure 61), a 1.3 cm diameter gel heterogeneity (Table 15 and Figure 62), a 1.3 cm diameter air heterogeneity (Table 16 and Figure 63), a 3 cm diameter air heterogeneity (Table 17 and Figure 64), and a uniform gel (Table 18 and Figure 65). Representative images were shown with 1 beam irradiation for the 1.3 cm diameter solution insert (Figure 61), 2 beams irradiation for the 1.3 cm diameter gel insert (Figure 62), 3 beams irradiation for the 1.3 cm diameter air insert (Figure 63), 4 beams irradiation for the 3 cm diameter air insert (Figure 64), and 7 beams irradiation for the uniform gel. All gels, regardless of the heterogeneous insert, were irradiated with 1 beam, 2 beams, 3 beams, 4 beams, and 7 beams, separated by at least 24 hours for the rFOX gel to revert to background levels. Before and after irradiation, all rFOX gels were MR imaged with T1-weighted T1 CE and no CE sequences. For all images, the raw pre-irradiated images were subtracted from the raw post-irradiated images. This was due to higher MR signal intensities closer to the body and anterior coils in the MRI bore (as expected for any MRI system). The purpose of subtracting the pre-irradiated images from the post-irradiated images was to mitigate the influence of these signal non-uniformities in the MR images. After this subtraction, the T1-weighted MR images were then scaled to the Monaco planned doses to obtain a relative volumetric dose distribution. For future work, absolute volumetric dose distributions could be calculated from T1-

weighted MR images or from quantitative T_1 -mapped MR images from planar and point dosimetry values using calibrated film and ionization chamber values.

Table 14: 3D gamma pass rates for heterogeneous rFOX phantom with 1.3 cm solution insert. Pass rates above the 80% cutoff are highlighted in green.

MRI	NSA	# Beams	7%/4mm	5%/3mm	3%/3mm
T1 CE	1	1	99.39%	86.38%	69.59%
T1 CE	1	2	98.09%	79.28%	61.63%
T1 CE	1	3	97.92%	79.85%	63.10%
T1 CE	1	4	97.52%	80.56%	64.33%
T1 CE	1	7	98.30%	79.39%	61.63%
no CE	1	1	97.97%	87.68%	76.63%
no CE	1	2	97.48%	84.42%	69.39%
no CE	1	3	98.06%	80.84%	62.95%
no CE	1	4	97.52%	87.39%	74.13%
no CE	1	7	97.41%	77.63%	59.91%

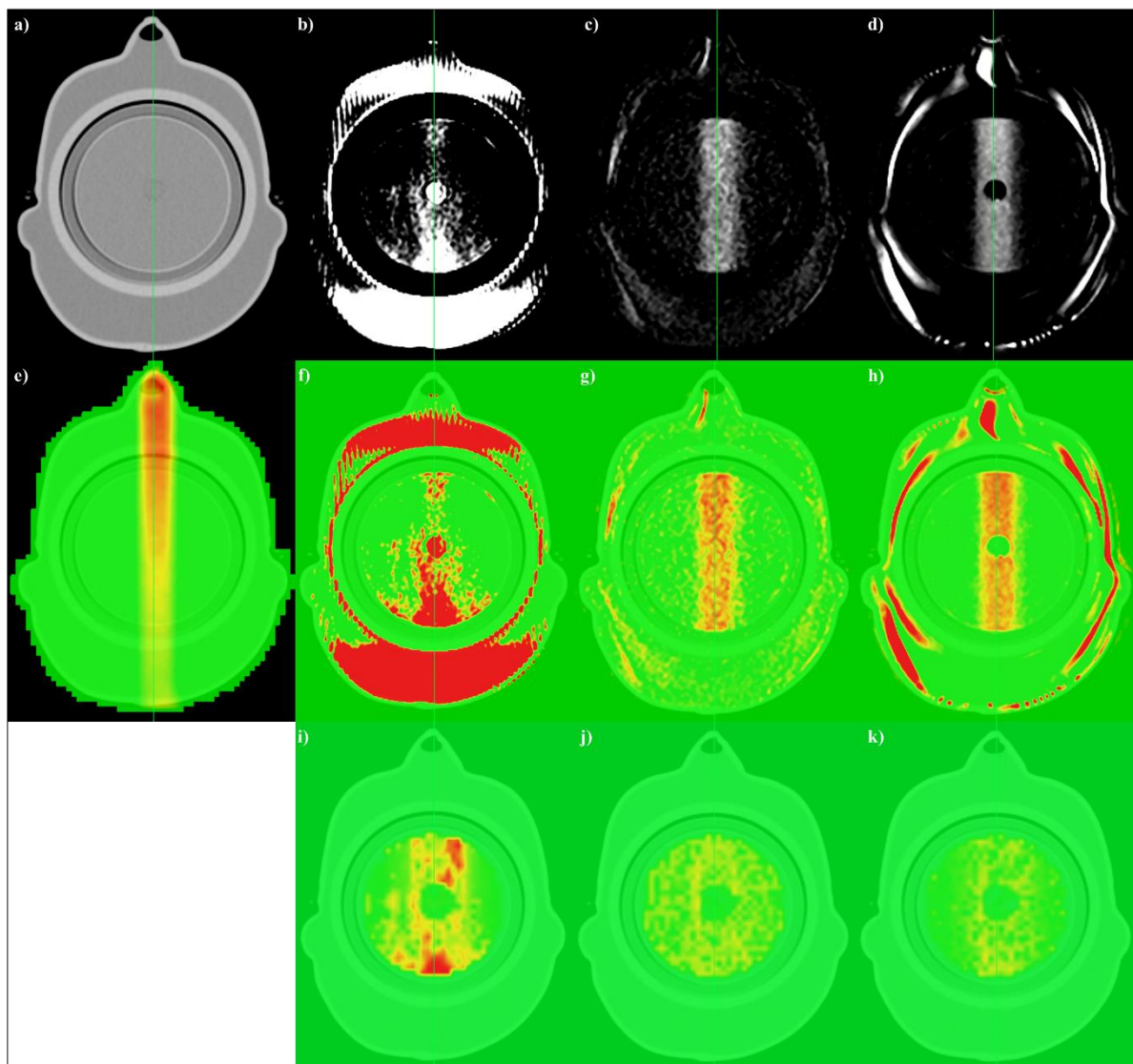


Figure 61: a) CT of rFOX with 1.3 cm solution insert, b) T2-weighted image, c) T1-weighted T1 CE image, d) T1-weighted no CE image, e) Monaco TPS dose overlaid on CT, f) T2-weighted relative dose (non-linear dose so not analyzed with gamma criteria), g) T1 CE relative dose, h) no CE relative dose, i) gamma map of T2-weighted dose, j) gamma map of T1 CE dose, and k) gamma map of no CE dose.

Table 15: 3D gamma pass rates for heterogeneous rFOX phantom with 1.3 cm gel insert. Pass rates above the 80% cutoff are highlighted in green.

MRI	NSA	# Beams	7%/4mm	5%/3mm	3%/3mm
T1 CE	1	1	98.15%	85.24%	70.72%
T1 CE	1	2	96.02%	74.40%	56.87%
T1 CE	1	3	89.98%	63.57%	47.08%
T1 CE	1	4	87.71%	57.35%	41.35%
T1 CE	1	7	94.16%	81.58%	68.69%
no CE	1	1	97.01%	86.19%	75.51%
no CE	1	2	96.03%	83.20%	68.41%
no CE	1	3	92.74%	78.23%	51.06%
no CE	1	4	97.61%	85.16%	69.82%
no CE	1	7	98.38%	85.70%	69.74%

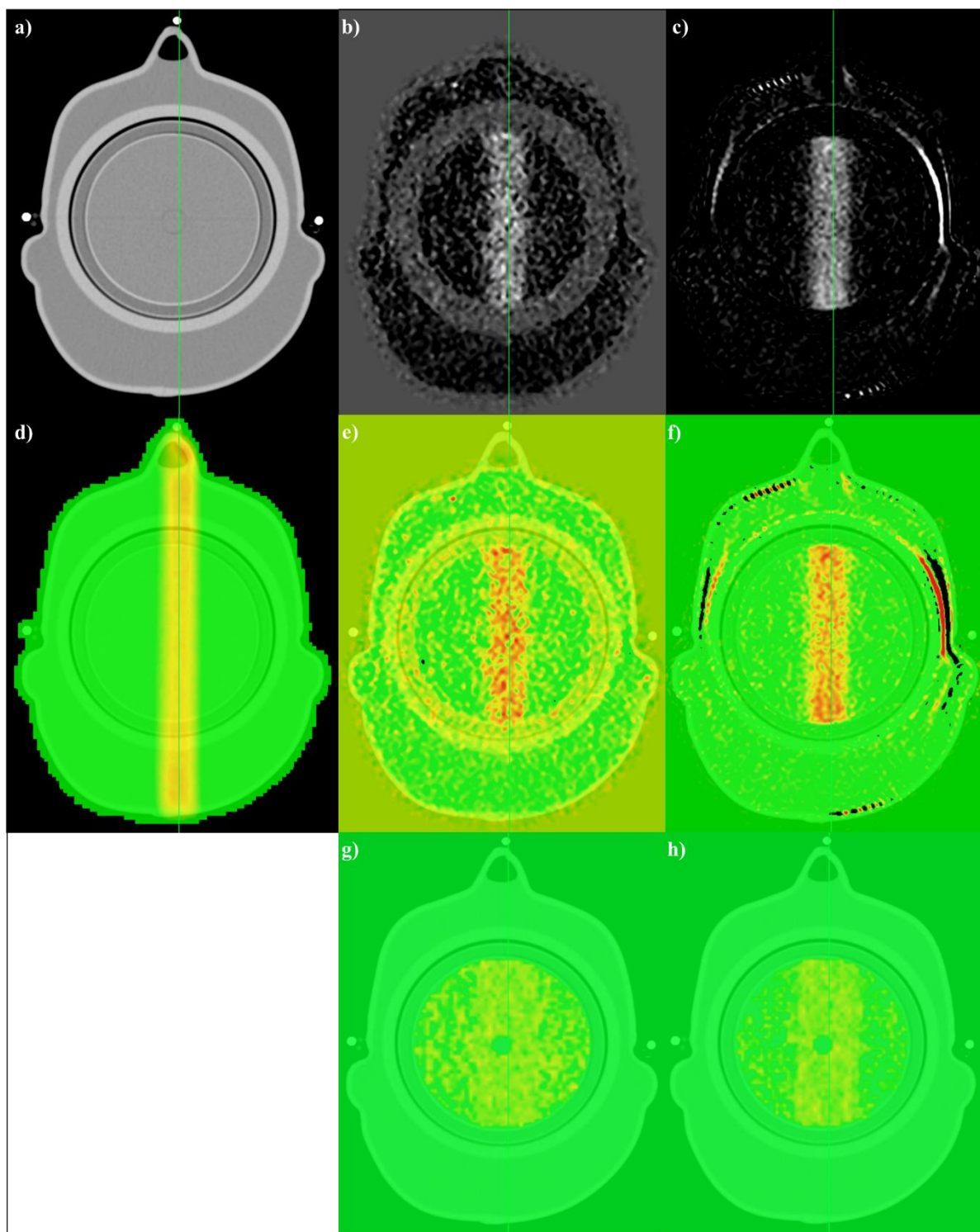


Figure 62: a) CT of rFOX with 1.3 cm gel insert, b) T1-weighted T1 CE image, c) T1-weighted no CE image, d) Monaco TPS dose overlaid on CT, e) T1 CE relative dose, f) no CE relative dose, g) gamma map of T1 CE dose, and h) gamma map of no CE dose.

Table 16: 3D gamma pass rates for heterogeneous rFOX phantom with 1.3 cm air insert. Pass rates above the 80% cutoff are highlighted in green.

MRI	NSA	# Beams	7%/4mm	5%/3mm	3%/3mm
T1 CE	1	1	98.57%	86.77%	72.43%
T1 CE	1	2	97.40%	78.14%	60.53%
T1 CE	1	3	95.15%	82.13%	68.79%
T1 CE	1	4	95.62%	76.74%	60.71%
T1 CE	1	7	92.34%	71.24%	55.52%
no CE	1	1	96.64%	86.12%	75.30%
no CE	1	2	96.92%	84.06%	69.62%
no CE	1	3	99.14%	86.12%	70.11%
no CE	1	4	98.07%	84.97%	69.66%
no CE	1	7	98.77%	86.58%	70.86%

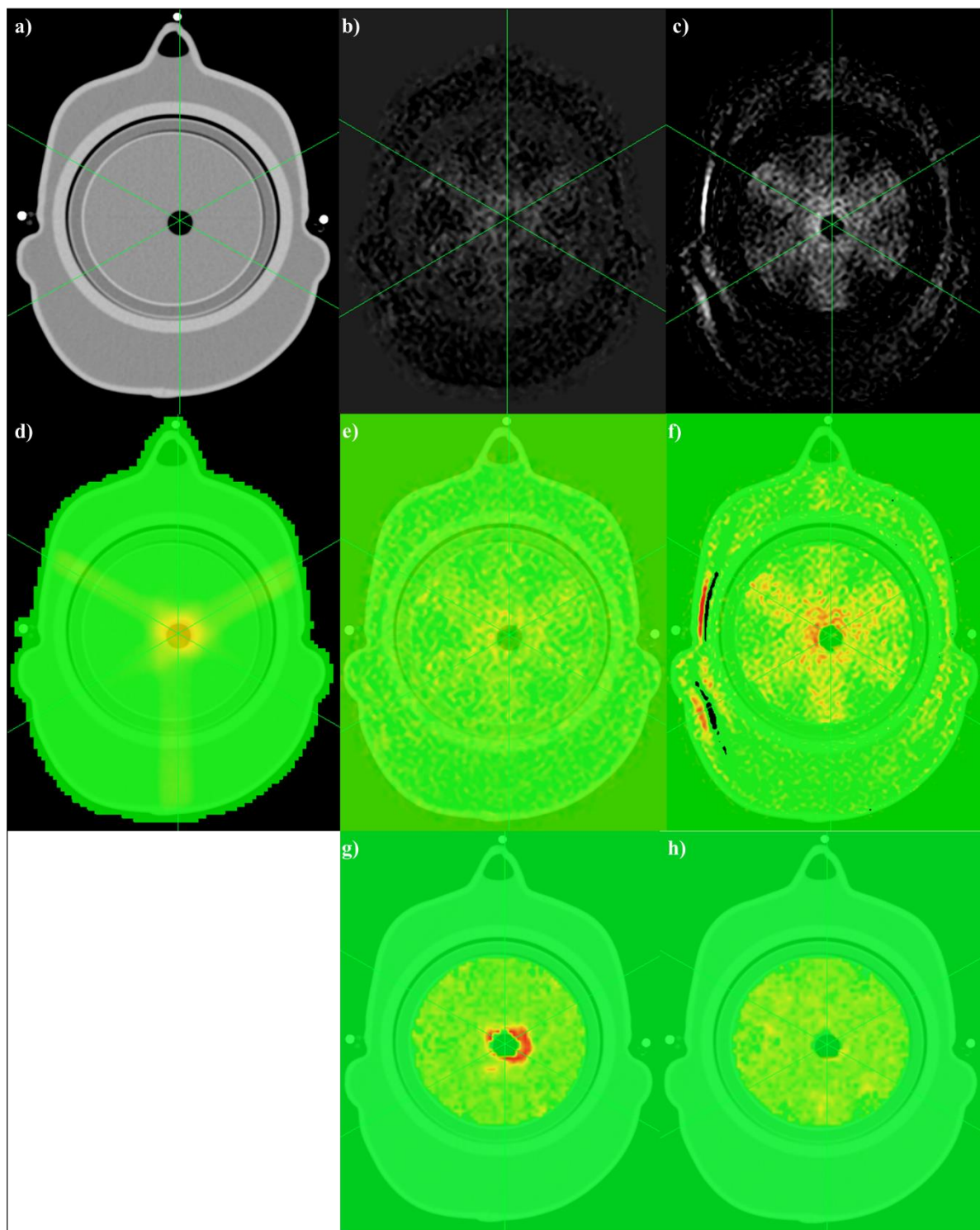


Figure 63: a) CT of rFOX with 1.3 cm air insert, b) T1-weighted T1 CE image, c) T1-weighted no CE image, d) Monaco TPS dose overlaid on CT, e) T1 CE relative dose, f) no CE relative dose, g) gamma map of T1 CE dose, and h) gamma map of no CE dose.

Table 17: 3D gamma pass rates for heterogeneous rFOX phantom with 3.0 cm air insert. Pass rates above the 80% cutoff are highlighted in green.

MRI	NSA	# Beams	7%/4mm	5%/3mm	3%/3mm
T1 CE	1	1	95.39%	77.74%	61.89%
T1 CE	1	2	95.55%	71.90%	54.13%
T1 CE	1	3	92.49%	71.86%	58.06%
T1 CE	1	4	95.04%	75.62%	60.04%
T1 CE	1	7	91.61%	70.09%	54.51%
no CE	1	1	94.89%	84.30%	74.91%
no CE	1	2	95.40%	82.46%	67.78%
no CE	1	3	99.13%	87.64%	72.43%
no CE	1	4	98.27%	84.55%	68.43%
no CE	1	7	97.62%	83.56%	67.20%

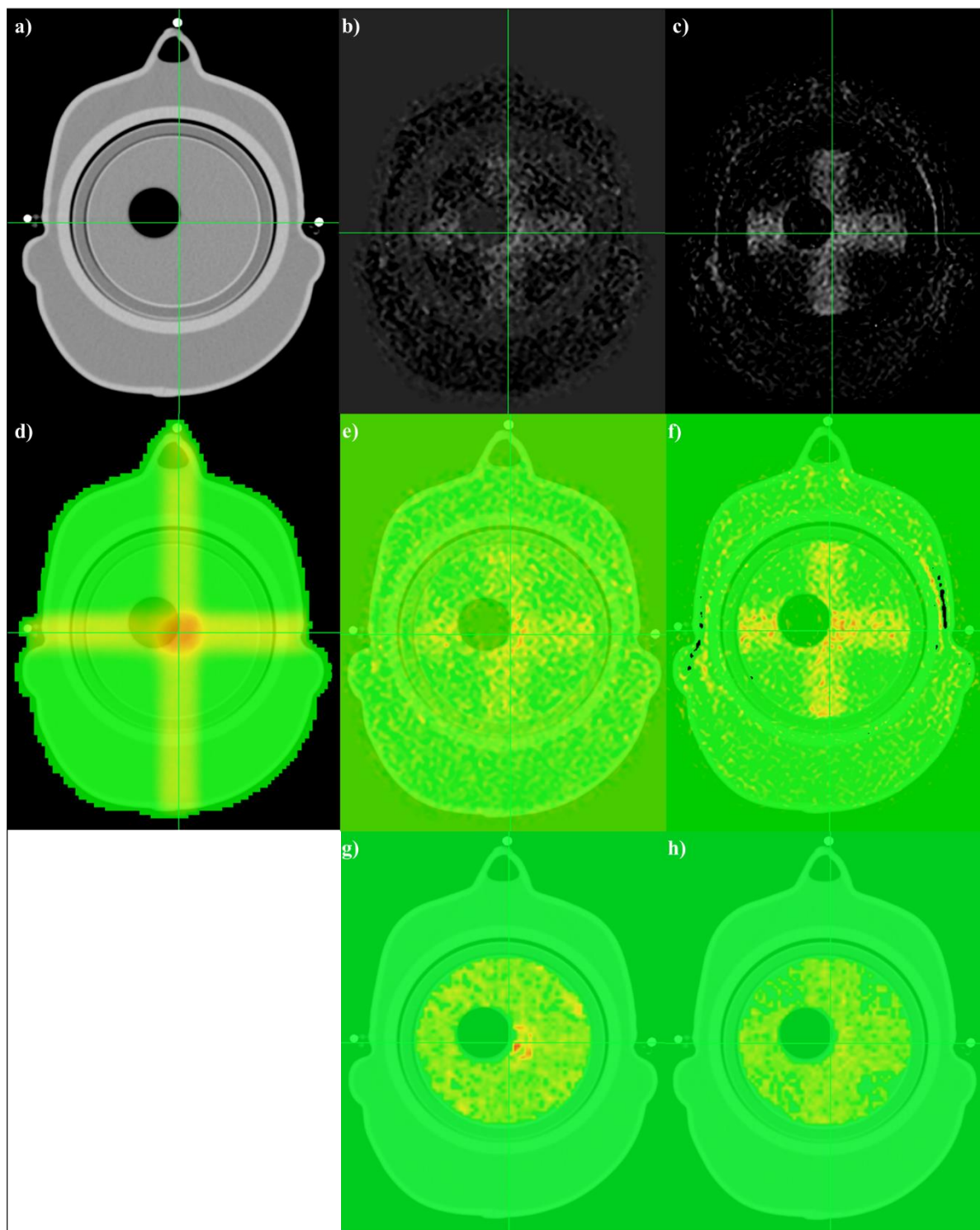


Figure 64: a) CT of rFOX with 3.0 cm air insert, b) T1-weighted T1 CE image, c) T1-weighted no CE image, d) Monaco TPS dose overlaid on CT, e) T1 CE relative dose, f) no CE relative dose, g) gamma map of T1 CE dose, and h) gamma map of no CE dose.

Table 18: 3D gamma pass rates for homogeneous rFOX phantom. Pass rates above the 80% cutoff are highlighted in green.

MRI	NSA	# Beams	7%/4mm	5%/3mm	3%/3mm
T1 CE	1	1	97.61%	83.97%	69.21%
T1 CE	1	2	96.75%	75.02%	57.31%
T1 CE	1	3	94.83%	76.94%	62.18%
T1 CE	1	4	95.07%	77.02%	61.70%
T1 CE	1	7	93.24%	75.51%	61.13%
no CE	1	1	95.20%	84.56%	74.11%
no CE	1	2	96.50%	82.81%	67.96%
no CE	1	3	98.17%	83.03%	66.43%
no CE	1	4	97.98%	84.32%	68.73%
no CE	1	7	97.70%	84.73%	68.90%

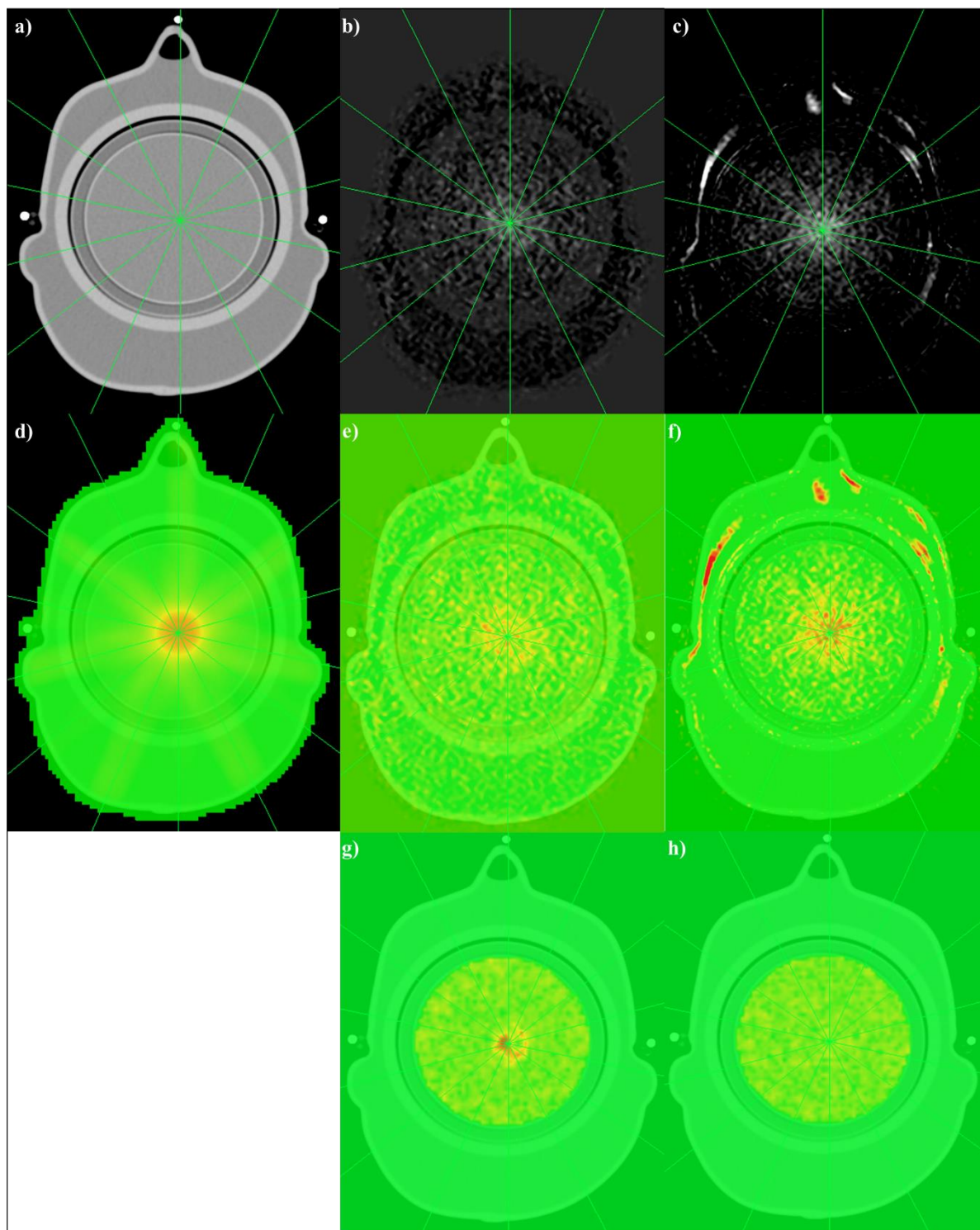


Figure 65: a) CT of uniform rFOX with no heterogeneous insert, b) T1-weighted T1 CE image, c) T1-weighted no CE image, d) Monaco TPS dose overlaid on CT, e) T1 CE relative dose, f) no CE relative dose, g) gamma map of T1 CE dose, and h) gamma map of no CE dose.

As mentioned earlier in Chapter 3, the T1 CE sequences spoiled the transverse magnetization using pulse phase cycling of the radiofrequency excitation pulses. Therefore, the no CE images included a mixed signal of the free induction decay (FID) and spin echo, and the T1 CE images only contained the FID signal. As a result, no CE images contain more overall MR signal and reduced apparent noise (smaller standard deviations). This was evident in the heterogeneous gel results because T1 CE-calculated relative dose comparisons failed more with tighter gamma criteria (5%/3mm and 3%/3mm) compared to no CE 3D gamma pass rates (Table 14, Table 15, Table 16, Table 17, and Table 18). Overall, the pass rates between the heterogeneous inserts and the uniform gel were comparable, suggesting the validity of Monaco TPS calculations for heterogeneous environments when comparing relatively to a scaled dose from T1-weighted MR signal intensities. Future work should include more rigorous cross-validation of Monaco TPS with absolute dose calculations.

5.3 Homogeneous FXG phantom and ArcCHECK-MR results and discussion

After delivery of 3D plans onto rFOX inside an anthropomorphic head and neck phantom, step-and-shoot IMRT plans were investigated next based off of TG-119 IMRT Commissioning Tests [174, 175]. These plans were delivered onto two liter-sized uniform FXG phantoms. Some difficulties with using rFOX in large sizes above one liter resulted in the use of the FXG formulation for this proof of concept study of delivering TG-119 plans onto volumetric, MR-visible, and radiation-sensitive dosimeters. Because rFOX was not stable in just gelatin, agarose was added as a gel matrix component. The advantage of the addition of agarose for gel stability was due to its higher melting point and greater rigidity; however, in the context of making gels larger than one liter, this higher melting point make it more difficult to dissolve the rFOX components in a uniform manner and uniform distribution of the formulation during cooling. For these reasons, as an initial proof of concept of using a Fricke-type gel for more complex plan assessment, the FXG formulation was used instead. The FXG formulation has been fully characterized for dose distribution calculations from both MR signal intensities and from quantified T_1 or R_1 values in the literature [176–181]. Alongside the FXG phantoms, the plans were

delivered onto quasi-3D ArcCHECK-MR for comparison. Sun Nuclear provided an MR-compatible ArcCHECK-MR for MR-IGRT systems and had been previously investigated for such applications [163, 164, 182]. Without the guidance of lasers and a light field and since the ArcCHECK cannot be MR imaged, radio-opaque ceramic BB markers were positioned on its isocenter crosshairs to position in the MR-Linac using the electronic portal imaging device (EPID) (Figure 66). Although the ArcCHECK-MR does not provide a fully 3D dose distribution, it was included in this comparison with FXG as a benchmark for acceptable gamma pass rates since the MR-Linac was still a pre-clinical system. Most notably, rigorous MLC calibration and MR to MV isocenter registration had not yet been completed at the time of this dissertation work, affecting the delivery of IMRT plans and the accuracy of adapted plans based on daily MR images.

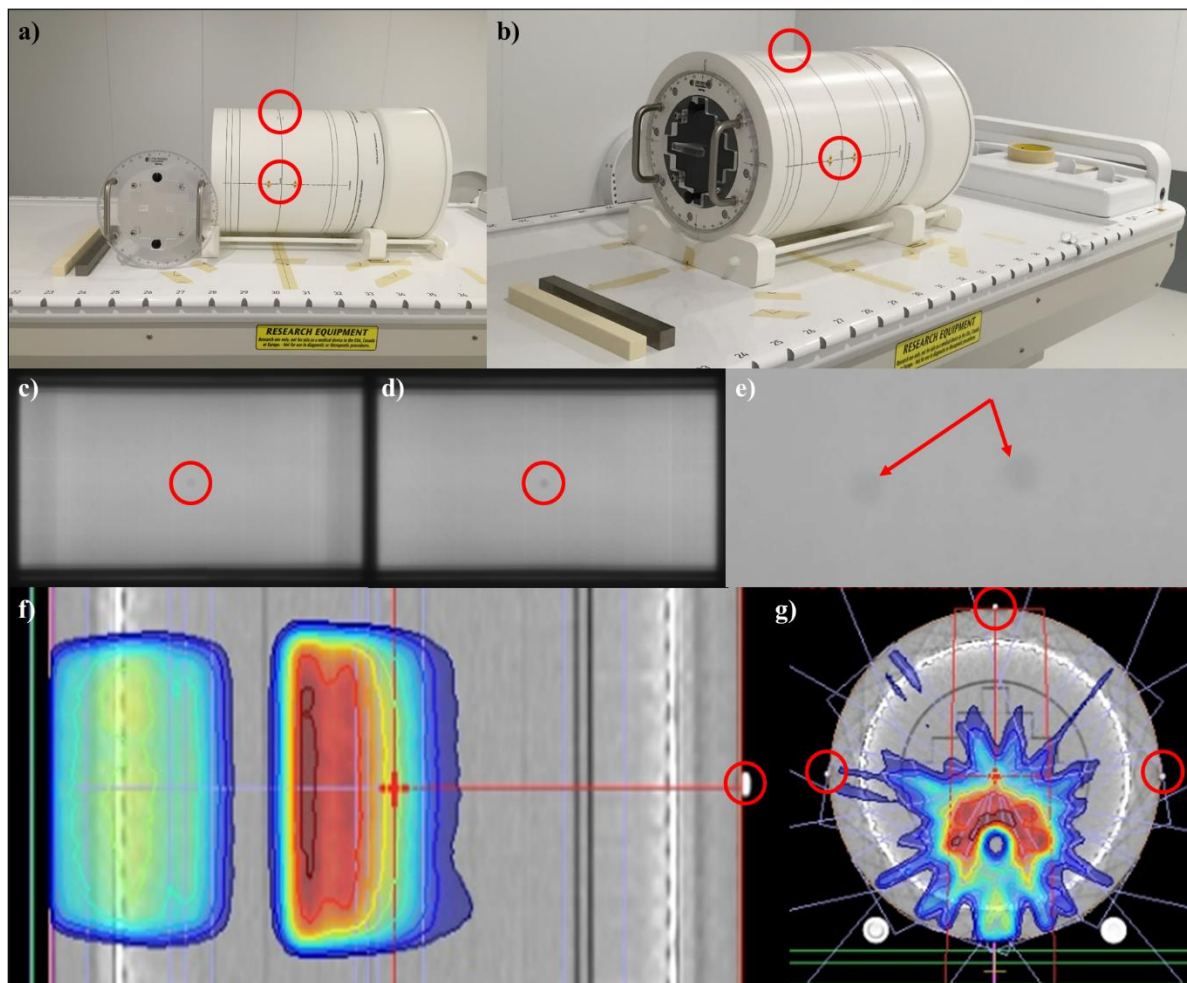


Figure 66: a) and b) Images of ArcCHECK-MR showing locations of radio-opaque ceramic BB markers, c) view of BB on EPID with gantry angle at 0° (BB should be in center of field of view if positioned correctly, side BBs not visible in this acquisition due to size of EPID field of view), d) view of BB on EPID with gantry angle at 90° or 270° (BBs should be centered and overlap if positioned correctly), e) example of mis-aligned ArcCHECK-MR with BBs not overlapping, f) CT of BB used for initial isocenter positioning in Monaco TPS, and g) CT of BBs on ArcCHECK-MR used for initial isocenter positioning in Monaco TPS.

Similar to the heterogeneous rFOX phantom study, the FXG gel was MR imaged prior to irradiation and post-irradiation using T2-weighted, T1-weighted T1 CE, and T1-weighted no CE sequences with the same sequence parameters as for rFOX. Contrary to rFOX, the FXG had a greater T2-weighted change and an insignificant T1-weighted no CE change (nearly all voxels failed using gamma comparison with the Monaco TPS plan) (Figure 71). However, the post-irradiation T2-weighted images were not used for dose distribution analysis since previous studies have shown the T2 response

to be non-linear with respect to dose [82]. The overall 3D gamma pass rates are listed in Table 19. Figures including the CT of large uniform FXG, T1-weighted T1 CE image, Monaco TPS dose overlaid on CT, T1 CE relative dose, example gamma map of T1 CE dose, Monaco TPS dose on CT of ArcCHECK-MR, and delivered and planned relative dose comparisons are presented below for the AP PA plan (Figure 67), MultiTarget plan (Figure 68), Prostate plan (Figure 69), Head/Neck plan (Figure 70), and C-shape plan (Figure 71). The AP PA plan is a simple rectangular plan that could be delivered in the shortest amount of time with only 2 parallel opposing beams (gantry angles 0° and 180°). The MultiTarget plan consisted of 7 beams (gantry angles 0° , 50° , 100° , 150° , 210° , 260° , and 310°) and dose constraints identified for three cylindrical targets (central, superior, and inferior). The Prostate plan consisted of 7 beams (gantry angles 0° , 50° , 100° , 150° , 210° , 260° , and 310°) and dose constraints identified for the prostate planning target volume (PTV), rectum, and bladder. The Head/Neck plan consisted of 9 beams (gantry angles 0° , 40° , 80° , 120° , 160° , 200° , 240° , 280° , and 320°) and dose constraints identified for the head/neck PTV, spinal cord, and parotids. The C-shape plan consisted of 9 beams (gantry angles 0° , 40° , 80° , 120° , 160° , 200° , 240° , 280° , and 320°) and dose constraints identified for the C-shape PTV and core. The MultiTarget plan had a total of 36 segments; the Prostate plan had a total of 28 segments; the Head/Neck plan had a total of 65 segments; and the C-shape plan had a total of 55 segments. The plans were all delivered as step-and-shoot IMRT plans, so the greater the number of segments, the overall time of treatment delivery was also longer.

Table 19: 3D gamma pass rates for TG-119 plans. Pass rates above the 80% cutoff are highlighted in green.

	MRI	NSA	TG-119 Plan	7%/4mm	5%/3mm	3%/3mm
FXG	T1 CE	1	AP PA	98.68%	92.24%	82.01%
FXG	T1 CE	2	AP PA	98.98%	92.65%	81.23%
FXG	T1 CE	3	AP PA	99.06%	94.06%	84.61%
FXG	T1 CE	4	AP PA	99.02%	94.34%	85.92%
FXG	T1 CE	5	AP PA	99.01%	94.07%	85.88%
Arc-CHECK	-----	--	AP PA	-----	-----	100.0%
FXG	T1 CE	1	MultiTarget	96.07%	48.50%	30.62%
FXG	T1 CE	2	MultiTarget	96.15%	46.70%	29.19%
FXG	T1 CE	3	MultiTarget	95.99%	50.07%	31.56%
FXG	T1 CE	4	MultiTarget	96.73%	54.15%	34.87%
FXG	T1 CE	5	MultiTarget	96.38%	56.35%	36.02%
Arc-CHECK	-----	--	MultiTarget	-----	-----	91.6%
FXG	T1 CE	1	Prostate	96.12%	47.16%	29.12%
FXG	T1 CE	2	Prostate	95.57%	42.86%	26.36%
FXG	T1 CE	3	Prostate	97.21%	54.56%	34.87%
FXG	T1 CE	4	Prostate	97.94%	61.04%	39.78%
Arc-CHECK	-----	--	Prostate	-----	-----	94.5%
FXG	T1 CE	1	Head/Neck	94.28%	44.82%	27.56%
Arc-CHECK	-----	--	Head/Neck	-----	-----	93.8%
FXG	T1 CE	1	C-Shape	94.79%	47.94%	29.99%
Arc-CHECK	-----	--	C-Shape	-----	-----	86.8%

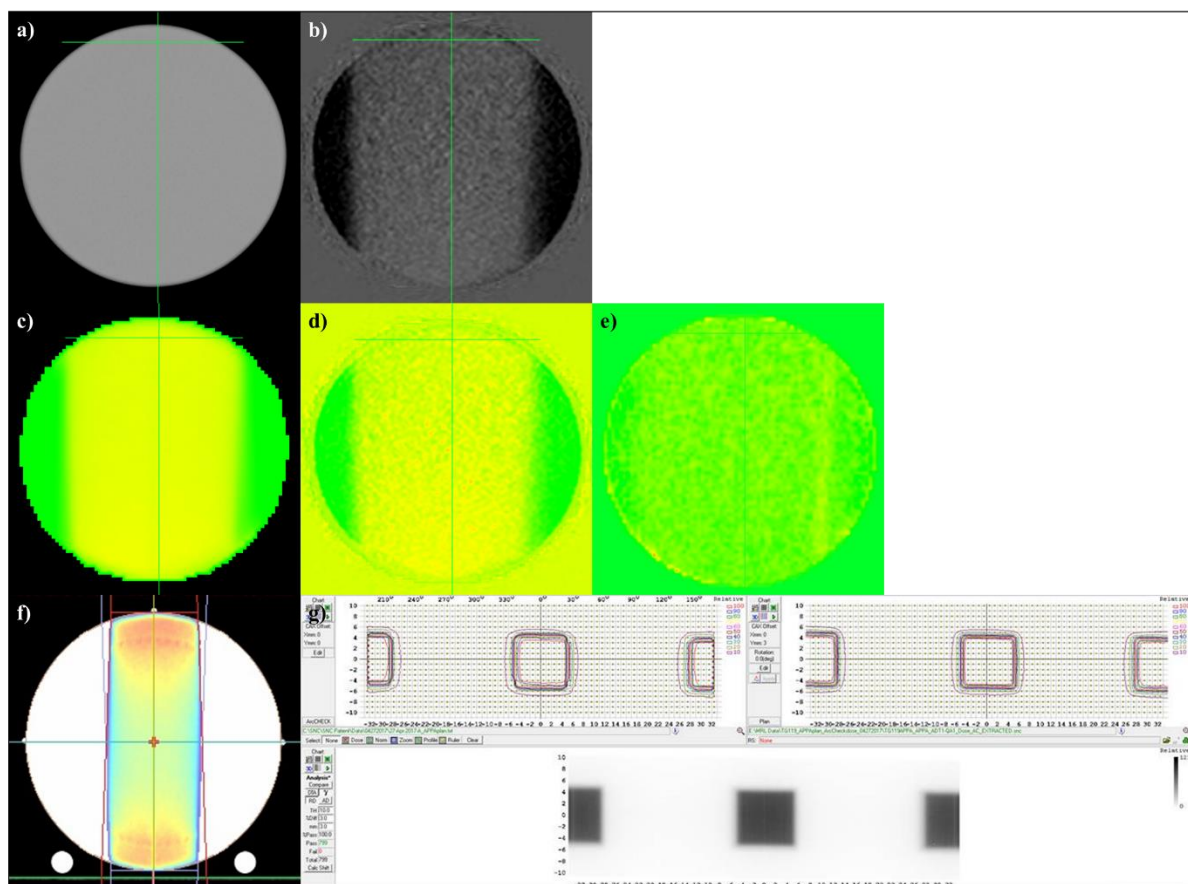


Figure 67: a) CT of large uniform FXG, b) T1-weighted T1 CE image, c) Monaco TPS dose overlaid on CT, d) T1 CE relative dose, e) gamma map of T1 CE dose, f) Monaco TPS dose on CT of ArcCHECK-MR, and g) delivered and planned relative dose comparisons for AP PA TG-119 plan.

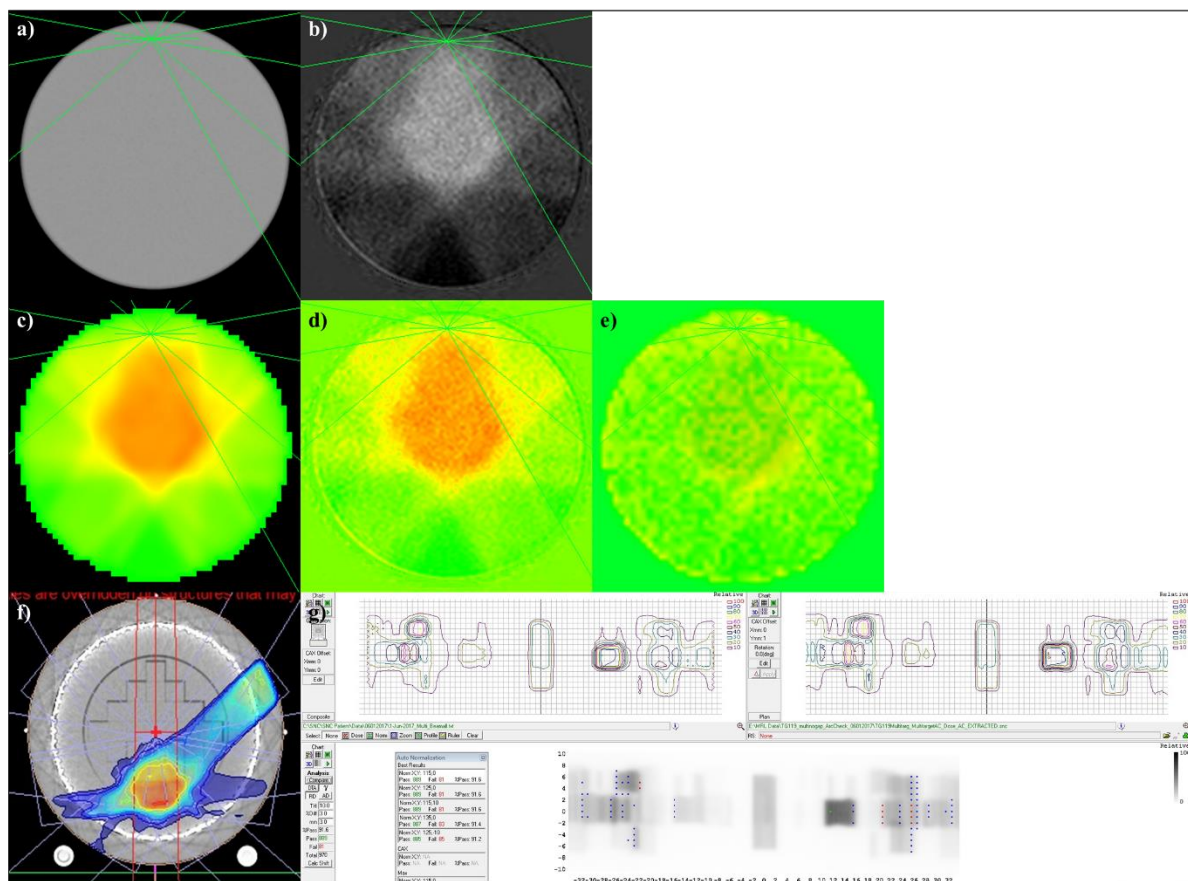


Figure 68: a) CT of large uniform FXG, b) T1-weighted T1 CE image, c) Monaco TPS dose overlaid on CT, d) T1 CE relative dose, e) gamma map of T1 CE dose, f) Monaco TPS dose on CT of ArcCHECK-MR, and g) delivered and planned relative dose comparisons for MultiTarget TG-119 plan.

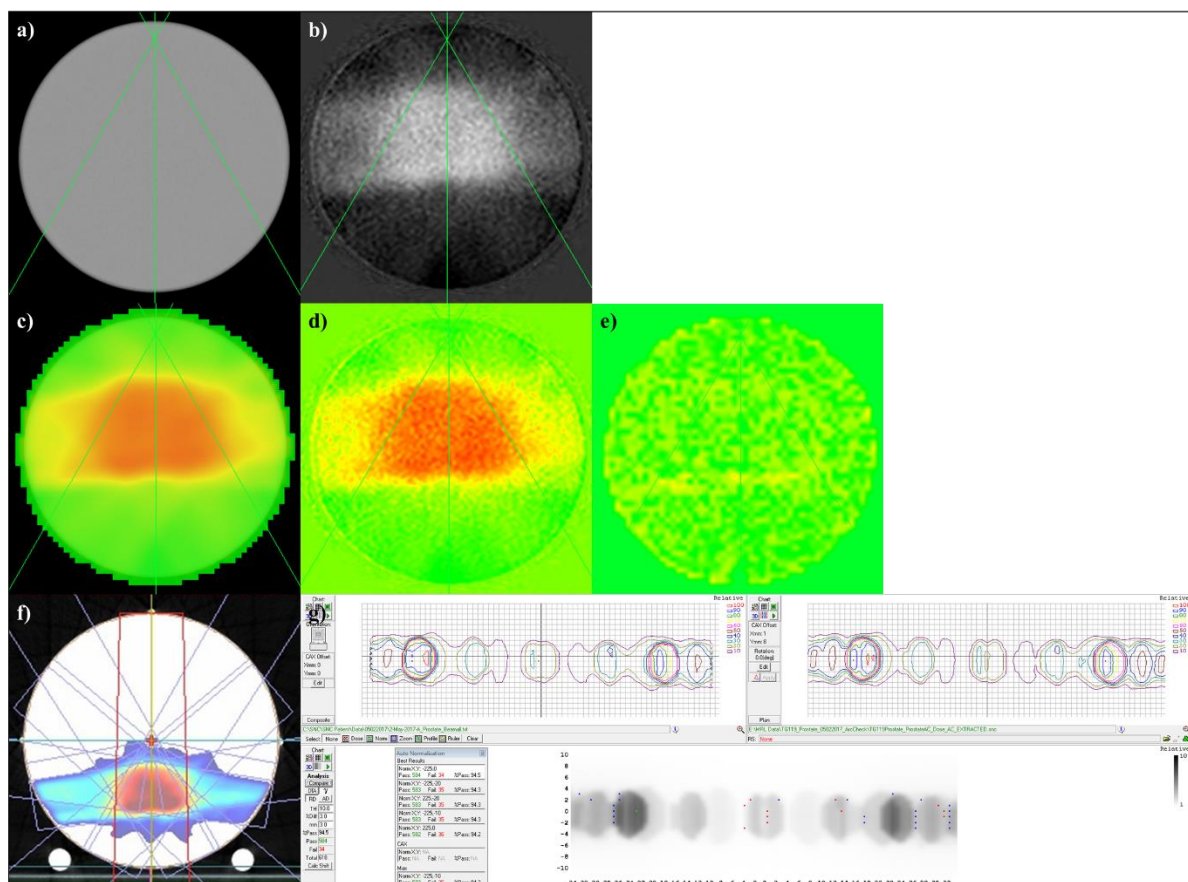


Figure 69: a) CT of large uniform FXG, b) T1-weighted T1 CE image, c) Monaco TPS dose overlaid on CT, d) T1 CE relative dose, e) gamma map of T1 CE dose, f) Monaco TPS dose on CT of ArcCHECK-MR, and g) delivered and planned relative dose comparisons for Prostate TG-119 plan.

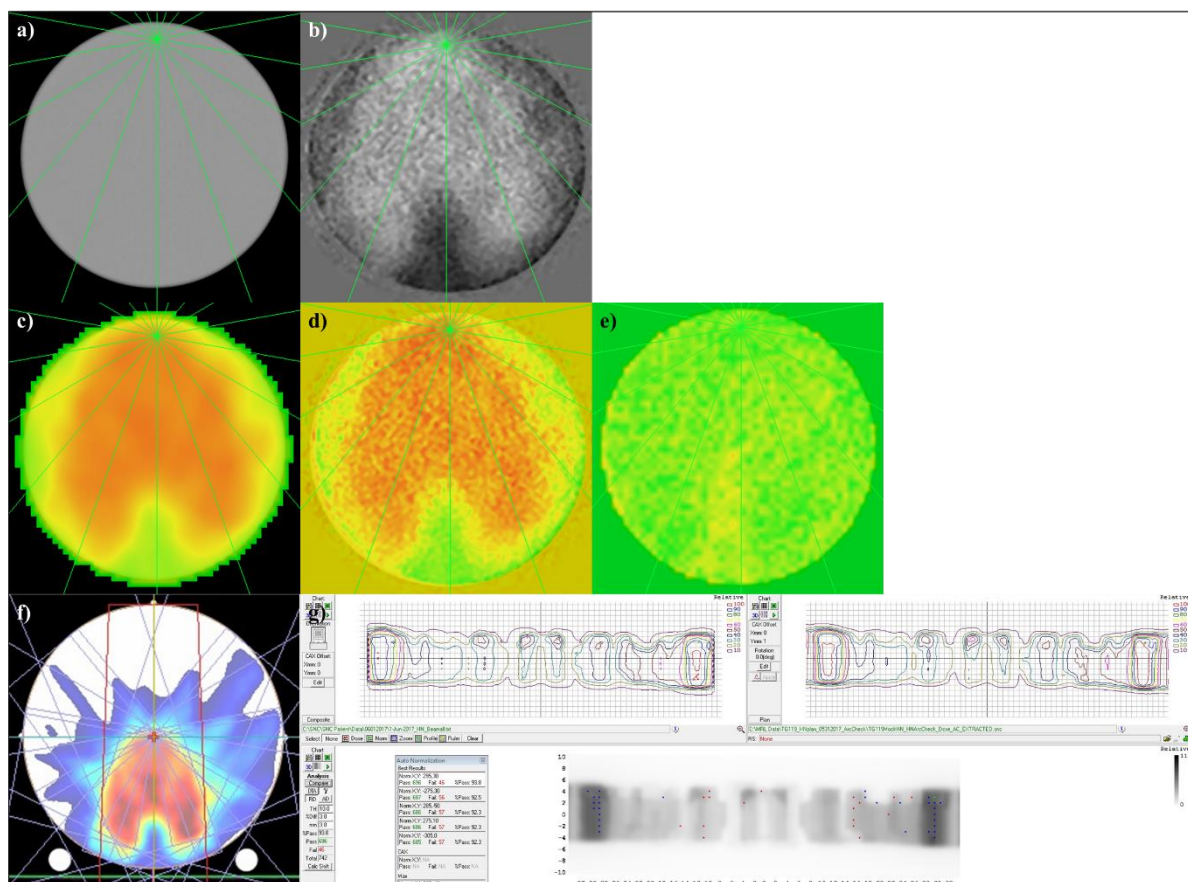


Figure 70: a) CT of large uniform FXG, b) T1-weighted T1 CE image, c) Monaco TPS dose overlaid on CT, d) T1 CE relative dose, e) gamma map of T1 CE dose, f) Monaco TPS dose on CT of ArcCHECK-MR, and g) delivered and planned relative dose comparisons for Head/Neck TG-119 plan.

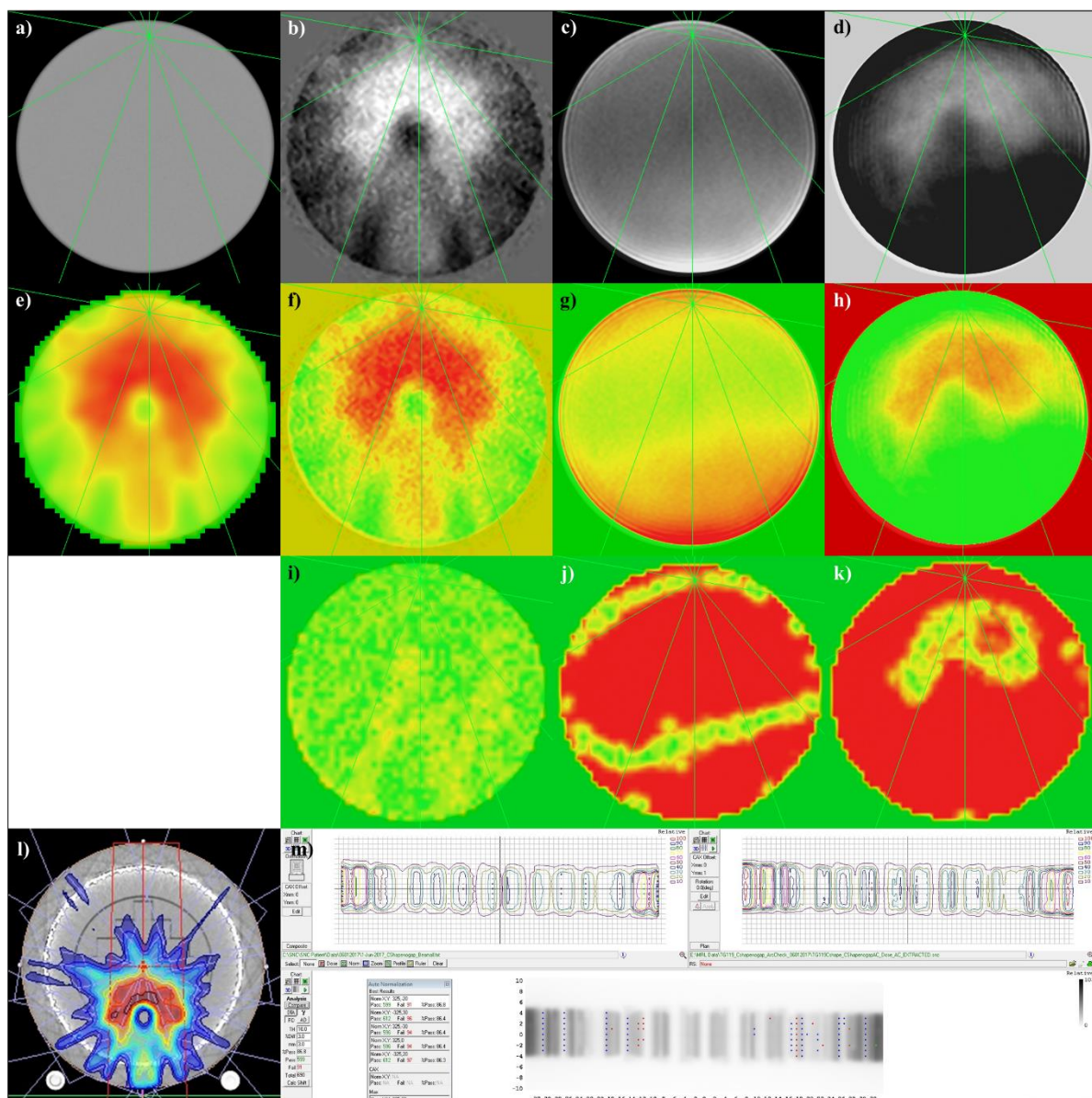


Figure 71: a) CT of large uniform FXG, b) T1-weighted T1 CE image, c) T1-weighted no CE image, d) T2-weighted image, e) Monaco TPS dose overlaid on CT, f) T1 CE relative dose, g) no CE relative dose, h) T2-weighted relative dose, i) gamma map of T1 CE dose, j) gamma map of no CE dose, k) gamma map of T2-weighted dose, l) Monaco TPS dose on CT of ArcCHECK-MR, and m) delivered and planned relative dose comparisons for C-Shape TG-119 plan.

5.4 Summary

This work was the first to use heterogeneous MR-visible and radiation-sensitive 3D dosimeters for full end-to-end testing in an MR-IGRT system. All heterogeneous rFOX dosimeters' relative doses passed for gamma criteria of 7%/4mm, more than half passed for 5%/3mm, and none passed for 3%/3mm. As mentioned previously, the heterogeneous rFOX dosimeter work was completed prior to bug fixes in Monaco TPS so the adapted plans were not created and delivered exactly through the planned workflow; as a result, lower gamma pass rates were expected. Since heterogeneous phantoms were more susceptible to spatial dose accuracy, this work would be beneficial to be repeated once the MR-Linac is no longer pre-clinical. However, the 7%/4mm gamma criteria pass rates (>90%) were sufficient to demonstrate the proof of concept of using heterogeneous anthropomorphic rFOX dosimeters for 3D dose distribution assessment with the MR-IGRT workflow.

The homogeneous large FXG dosimeters used for TG-119 IMRT plan evaluation passed for all 7%/4mm gamma criteria. However, compared to the rFOX 3D plan results, the FXG gamma pass rates dropped more steeply for 5%/3mm and 3%/3mm for all IMRT plans except for the AP PA plan. This rapid drop in gamma pass rates with tighter gamma criteria could be attributed to the longer plan delivery times for the complex step-and-shoot IMRT plans compared to the AP PA plan and 3D plans used with rFOX. During this time frame, some diffusion of signal may have occurred; a rigorous assessment of dose rate dependence, fractionation, and other characteristics was also not completed in this dissertation work for FXG. Since the gamma pass rates were above 94% with 7%/4mm gamma criteria, it could be assumed that FXG responded linearly with dose for these plans. Future work should either utilize fewer control points for the TG-119 plans or incorporate FXG or another formulation into a gel matrix that has less diffusion compared to only gelatin.

The effect of NSA on gamma pass rates was also investigated for the homogeneous large FXG dosimeters. NSA = 3 or 4 resulted in the greatest pass rates by up to 1.8% compared to NSA = 1 with the MedianImageFilter with radius 1 applied. However, the MRI acquisition time rose linearly with NSA (NSA = 3 required 3 x length of time required for NSA = 1). With only an increase in pass rate

by up to 1.8% for NSA = 3 or 4, applying post-processing filters to images acquired with NSA = 1 would be recommended when diffusion was of concern.

This work was the first to use a homogeneous MR-visible 3D dosimeter for full end-to-end testing in an MR-IGRT system. Previous work used non-MR-visible 3D dosimeters, indicating that the clinical adaptive plan workflow could not be used [108]. However, previous work with non-MR-visible 3D dosimeters did result in higher gamma pass rates with tighter criteria (3%/3mm), those results were acquired with optical CT scanning methods that could measure high resolution signal with less noise when compared to MRI. The benefit of using an MR-visible 3D dosimeter in this proof of concept was to eliminate registration errors between prescans of the dosimeter, delivery of plan based on the prescans orientation, and postscans of the dosimeter. The entire clinical workflow including daily MR imaging for adaptive planning and all scans of the dosimeters could be completed in one MR-IGRT system using an MR-visible 3D dosimeter, eliminating the need for an outside read-out system such as an optical CT scanner. However, one advantage of non-MR-visible plastic dosimeters included reduced diffusion, resulting in higher gamma pass rates for tighter criteria [108].

At the time of this dissertation work, the MR and MV isocenters had not yet been registered, the MLCs had not yet undergone a rigorous calibration, and the MR-Linac had not yet been fully commissioned and calibrated. For these reasons, the pass rates were not as high as expected for a fully clinical system. Updates to the Monaco TPS and workflow were also still underway at the time of this dissertation work. Under these limitations, the feasibility of using both heterogeneous and homogeneous MR-visible and radiation-sensitive 3D dosimeters were confirmed with encouraging 3D pass rates with gamma criteria of 7%/4mm.

Limitations of using Fricke-type gels, including rFOX and FXG, for volumetric dose calculations include noise in the MR images. Reducing MR image noise requires longer scan times (for example by acquiring with larger NSA). However, for rFOX, the MR signal intensities were continuously dropping post-irradiation, making it difficult to acquire dosimetrically valuable MR images with significantly longer scan times (on the scale of hours for a volumetric scan) (Figure 35).

For FXG, while the MR signal intensity is not dropping, diffusion of iron ions distort the dose distribution on the scale of hours for Fricke-type gels (Figure 34, Table 9, and Table 10).

Chapter 6 – Conclusion

6.1 Summary and conclusion

The purpose of this dissertation was to demonstrate the feasibility and benefit of volumetric, MR-visible, and radiation-sensitive detectors for MR-IGRT applications.

In Chapter 2, I investigated candidate volumetric gel formulations, both already presented in the literature and novel formulations explored for this dissertation, for dosimetric value on MR-IGRT systems. The FOX formulation was found to be the most optimal, both optically and with MRI, for MR-IGRT applications (up to 114% greater optical response, 10% greater real-time MR response, and 46% greater post-irradiation T1-weighted MR response when compared to conventional FXG). I also demonstrated for the first time that iron(III) reduction formulations were more sensitive to UV exposure compared to megavoltage irradiations, and that iron(II) oxidation formulations were more sensitive to megavoltage irradiations than UV exposure [114, 183].

In Chapter 3, I presented the characterization of my novel formulations FOX and rFOX. Dose linearity, radiological properties, reproducibility, time stability, energy dependence, reusability of a formulation, dose rate dependence, fractionation dependence, gel matrix dependence, and diffusion were quantified. In all scenarios, FOX and rFOX were found to respond linearly with respect to dose in real-time during irradiation and immediately post-irradiation.

In Chapter 4, I investigated strong magnetic field and gradient field/radiofrequency effects on the response of FOX as well as optimization of MR sequences for the purposes of real-time imaging during irradiation and immediate post-irradiation imaging for volumetric dose quantification of rFOX. Minimal magnetic field and gradient field/radiofrequency field effects were found for FOX. Volume dependence and gantry angle dependence were also investigated with minimal effects. Gantry angle dependence was a new concept specific to MR-IGRT systems, where the gantry may not necessarily be in the same position each time for MR imaging. Other MR considerations that were true for any

MRI read-out technique, such as MRI artifacts, were also discussed. I was the first to investigate strong magnetic field effects on a radiochromic gel dosimeter and was the first to investigate any gradient field/radiofrequency effects on 3D dosimeters. I was also the first to investigate several MR considerations specific to and not specific to MR-IGRT systems, such as gantry angle dependence on MR imaging and the occurrence and mitigations for MR artifacts, respectively.

In Chapter 5, I examined the performance of rFOX and FXG as end-to-end quality assurance devices both in heterogeneous and homogeneous phantoms for 3D plans and step-and-shoot IMRT commissioning plans. TG-119 IMRT plan irradiations were completed alongside the quasi-3D ArcCHECK-MR QA system. This work demonstrated the proof of concept of using rFOX and FXG in both heterogeneous and homogeneous phantoms for end-to-end assessment of the MR-IGRT workflow and relative dose comparisons with the Monaco TPS plan doses. I was the first to investigate heterogeneous 3D dosimeters for MR-IGRT applications and the first to use 3D dosimeters as a full end-to-end quality assurance tool for MR-IGRT, including adapting plans using daily MR images of the dosimeters. Previous work on IMRT plan verification in MR-IGRT systems utilized non-MR-visible radiochromic plastic dosimeters [108]. Again, limitations of using Fricke-type gels, including rFOX and FXG, for volumetric dose calculations include noise in the MR images. Reducing MR image noise requires longer scan times (for example by acquiring with larger NSA). However, for rFOX, the MR signal intensities were continuously dropping post-irradiation, making it difficult to acquire dosimetrically valuable MR images with significantly longer scan times (on the scale of hours for a volumetric scan) (Figure 35). For FXG, while the MR signal intensity is not dropping, diffusion of iron ions distort the dose distribution on the scale of hours for Fricke-type gels (Figure 34, Table 9, and Table 10).

6.3 Future works

Future work suggested include further investigations into other matrixes for radiochromic gels to allow for their use without a container, to reduce diffusion, or as a deformable gel. A polymer gel

based deformable gel was made by encasing in a thin latex material and could easily be translated for radiochromic gel work [184–186]. Although my work was the first to demonstrate the proof of concept of real-time 3D dose acquisition during irradiation, this work should be continued in a deformable gel in a motion phantom [111–114]. There are currently two MRI-compatible motion phantoms available: CIRS dynamic phantom and Modus QUASAR respiratory motion phantom. Respiratory motion has remained a challenge in radiation therapy for reducing organs at risk dose while maintaining or reducing local recurrence [187–189]. Motion phantom studies are necessary for testing translational methodologies using MR-IGRT prior to patient treatment. Also of continued interest in the 3D dosimetry field is a lung equivalent 3D dosimeter as well as in combination with other materials to make realistic heterogeneous phantoms [190–192]. I also encourage further characterization of FOX and rFOX along with improved MR sequences for image quality in order to more accurately assess IMRT plans with tighter gamma criteria. While long MR imaging sequences were avoided for rFOX and FXG due to concerns with signal reversal and signal diffusion for rFOX and FXG, respectively, further investigations into the most efficient MR imaging sequence to balance time with image quality for volumetric dose distribution evaluation are recommended. This dissertation work investigated relative 3D doses for rFOX and FXG; future work could include calibrating the dosimeter for absolute 3D doses. Suggestions have been made for internal calibrations of 3D dosimeters within a single dosimeter for calibration and plan delivery [193].

Overall, this dissertation work encourages further investigations of MR-visible and radiation-sensitive 3D dosimeters for MR-IGRT applications, both as a general quality assurance tool and as an end-to-end test. I have done some initial work on investigating the use of 3D dosimeters for MR-isocenter and MV-isocenter registration since other current methods lack a technique that is both MR-visible and radiation-sensitive [119]. During our initial experience with the MR-Linac workflow, it was extremely beneficial to have an MR-visible and radiation-sensitive tool for following the workflow end-to-end and to visually see where dose was being deposited (both optically and with MR images). Especially since MR-IGRT workflows are not the same as conventional linac workflows, I especially

encourage the use of 3D dosimeters for initial end-to-end experience before patient treatments are delivered. My rFOX dosimeter can be imaged with CT and MRI, used for reference and adapted planning practice, tracked with MRI in a motion phantom, can be incorporated into heterogeneous anthropomorphic or homogeneous phantoms, irradiated with a plan, its relative 3D dose distribution can be compared with the planned dose, and can be reused.

Bibliography

1. Jaffray DA, Siewerdsen JH, Wong JW, Martinez AA (2002) Flat-panel cone-beam computed tomography for image-guided radiation therapy. *Int J Radiat Oncol Biol Phys* 53:1337–49.
2. Groh BA, Siewerdsen JH, Drake DG, Wong JW, Jaffray DA (2002) A performance comparison of flat-panel imager-based MV and kV cone-beam CT. *Med Phys* 29:967–975. doi: 10.1118/1.1477234
3. White EA, Cho J, Vallis KA, Sharpe MB, Lee G, Blackburn H, Nageeti T, McGibney C, Jaffray DA, Pradier O, Visvikis D (2007) Cone Beam Computed Tomography Guidance for Setup of Patients Receiving Accelerated Partial Breast Irradiation. *Int J Radiat Oncol* 68:547–554. doi: 10.1016/j.ijrobp.2007.01.048
4. Gilles M, Fayad H, Miglierini P, Clement JF, Scheib S, Cozzi L, Bert J, Boussion N, Schick U, Pradier O, Visvikis D (2016) Patient positioning in radiotherapy based on surface imaging using time of flight cameras. *Med Phys* 43:4833–4841. doi: 10.1118/1.4959536
5. Thilmann C, Nill S, Tücking T, Höss A, Hesse B, Dietrich L, Bendl R, Rhein B, Häring P, Thieke C, Oelfke U, Debus J, Huber P (2006) Correction of patient positioning errors based on in-line cone beam CTs: clinical implementation and first experiences. *Radiat Oncol* 1:16. doi: 10.1186/1748-717X-1-16
6. Bostel T, Nicolay NH, Grossmann JG, Mohr A, Delorme S, Echner G, Häring P, Debus J, Sterzing F (2014) MR-guidance--a clinical study to evaluate a shuttle- based MR-linac connection to provide MR-guided radiotherapy. *Radiat Oncol* 9:12. doi: 10.1186/1748-717X-9-12
7. Leech M, Coffey M, Mast M, Moura F, Osztaivics A, Pasini D, Vaandering A (2017) ESTRO ACROP guidelines for positioning, immobilisation and position verification of head and neck patients for radiation therapists. *Tech Innov Patient Support Radiat Oncol*. doi:

- 10.1016/j.tipsro.2016.12.001
8. Jin J-Y, Yin F-F, Tenn SE, Medin PM, Solberg TD (2008) Use of the BrainLAB ExacTrac X-Ray 6D System in Image-Guided Radiotherapy. *Med Dosim* 33:124–134. doi: 10.1016/j.meddos.2008.02.005
 9. Owen R, Kron T, Foroudi F, Milner A, Cox J, Duchesne G, Cleeve L, Zhu L, Cramb J, Sparks L, Laferlita M (2009) Comparison of CT on Rails With Electronic Portal Imaging for Positioning of Prostate Cancer Patients With Implanted Fiducial Markers. *Int J Radiat Oncol* 74:906–912. doi: 10.1016/j.ijrobp.2009.01.054
 10. Oh SA, Park JW, Yea JW, Kim SK, Alterio D (2017) Evaluations of the setup discrepancy between BrainLAB 6D ExacTrac and cone-beam computed tomography used with the imaging guidance system Novalis-Tx for intracranial stereotactic radiosurgery. *PLoS One* 12:e0177798. doi: 10.1371/journal.pone.0177798
 11. Josipovic M, Persson GF, Logadottir Á, Smulders B, Westmann G, Bangsgaard JP (2012) Translational and rotational intra- and inter-fractional errors in patient and target position during a short course of frameless stereotactic body radiotherapy. *Acta Oncol (Madr)* 51:610–617. doi: 10.3109/0284186X.2011.626448
 12. Fuller CD, Scarbrough TJ, Sonke J-J, Rasch CRN, Choi M, Ting JY, Wang SJ, Papanikolaou N, Rosenthal DI (2009) Method comparison of automated matching software-assisted cone-beam CT and stereoscopic kilovoltage x-ray positional verification image-guided radiation therapy for head and neck cancer: a prospective analysis. *Phys Med Biol* 54:7401–15. doi: 10.1088/0031-9155/54/24/010
 13. Juhler-Nøttrup T, Korreman SS, Pedersen AN, Persson GF, Aarup LR, Nyström H, Olsen M, Tarnavski N, Specht L (2008) Interfractional changes in tumour volume and position during entire radiotherapy courses for lung cancer with respiratory gating and image guidance. *Acta Oncol (Madr)* 47:1406–1413. doi: 10.1080/02841860802258778
 14. Schmidt ML, Hoffmann L, Kandi M, Møller DS, Poulsen PR (2013) Dosimetric impact of

- respiratory motion, interfraction baseline shifts, and anatomical changes in radiotherapy of non-small cell lung cancer. *Acta Oncol (Madr)* 52:1490–1496. doi: 10.3109/0284186X.2013.815798
15. Müller BS, Duma MN, Kampfer S, Nill S, Oelfke U, Geinitz H, Wilkens JJ (2015) Impact of interfractional changes in head and neck cancer patients on the delivered dose in intensity modulated radiotherapy with protons and photons. *Phys Medica* 31:266–272. doi: 10.1016/j.ejmp.2015.02.007
 16. Sonke J-J, Belderbos J (2010) Adaptive Radiotherapy for Lung Cancer. *Semin Radiat Oncol* 20:94–106. doi: 10.1016/j.semradonc.2009.11.003
 17. Perkins CL, Fox T, Elder E, Kooby DA, Staley CA, Landry J (2006) Image-guided radiation therapy (IGRT) in gastrointestinal tumors. *JOP* 7:372–81.
 18. Jensen AD, Grehn C, Nikoghosyan A, Thieke C, Krempien R, Huber PE, Debus J, Mütter MW (2009) Catch Me if You Can – the Use of Image Guidance in the Radiotherapy of an Unusual Case of Esophageal Cancer. *Strahlentherapie und Onkol* 185:469–473. doi: 10.1007/s00066-009-1935-6
 19. Raaymakers BW, Lagendijk JJW, Overweg J, Kok JGM, Raaijmakers AJE, Kerkhof EM, van der Put RW, Meijsing I, Crijs SPM, Benedosso F, van Vulpen M, de Graaff CHW, Allen J, Brown KJ (2009) Integrating a 1.5 T MRI scanner with a 6 MV accelerator: proof of concept. *Phys Med Biol* 54:N229–N237. doi: 10.1088/0031-9155/54/12/N01
 20. Keall PJ, Barton M, Crozier S (2014) The Australian Magnetic Resonance Imaging–Linac Program. *Semin Radiat Oncol* 24:203–206. doi: 10.1016/j.semradonc.2014.02.015
 21. Fallone BG, Murray B, Rathee S, Stanescu T, Steciw S, Vidakovic S, Blosser E, Tymofichuk D (2009) First MR images obtained during megavoltage photon irradiation from a prototype integrated linac-MR system. *Med Phys* 36:2084–2088. doi: 10.1118/1.3125662
 22. Lagendijk JJW, Raaymakers BW, Raaijmakers AJE, Overweg J, Brown KJ, Kerkhof EM, van der Put RW, Hårdemark B, van Vulpen M, van der Heide UA (2008) MRI/linac integration. *Radiother Oncol* 86:25–9. doi: 10.1016/j.radonc.2007.10.034

23. Mutic S, Dempsey JF (2014) The ViewRay System: Magnetic Resonance–Guided and Controlled Radiotherapy. *Semin Radiat Oncol* 24:196–199. doi: 10.1016/j.semradonc.2014.02.008
24. Wegner CS, Hauge A, Gaustad J-V, Andersen LMK, Simonsen TG, Galappathi K, Rofstad EK (2017) Dynamic contrast-enhanced MRI of the microenvironment of pancreatic adenocarcinoma xenografts. *Acta Oncol (Madr)* 1–9. doi: 10.1080/0284186X.2017.1343494
25. Wong KH, Panek R, Bhide SA, Nutting CM, Harrington KJ, Newbold KL (2017) The emerging potential of magnetic resonance imaging in personalizing radiotherapy for head and neck cancer: an oncologist’s perspective. *Br J Radiol* 90:20160768. doi: 10.1259/bjr.20160768
26. Toft J, Hadden WJ, Laurence JM, Lam V, Yuen L, Janssen A, Pleass H (2017) Imaging modalities in the diagnosis of pancreatic adenocarcinoma: A systematic review and meta-analysis of sensitivity, specificity and diagnostic accuracy. *Eur J Radiol* 92:17–23. doi: 10.1016/j.ejrad.2017.04.009
27. To DT, Kim JP, Price RG, Chetty IJ, Glide-Hurst CK (2016) Impact of incorporating visual biofeedback in 4D MRI. *J Appl Clin Med Phys* 17:128–137. doi: 10.1120/jacmp.v17i3.6017
28. Kersemans V, Beech JS, Gilchrist S, Kinches P, Allen PD, Thompson J, Gomes AL, D’Costa Z, Bird L, Tullis IDC, Newman RG, Corroyer-Dulmont A, Falzone N, Azad A, Vallis KA, Sansom OJ, Muschel RJ, Vojnovic B, Hill MA, Fokas E, Smart SC (2017) An efficient and robust MRI-guided radiotherapy planning approach for targeting abdominal organs and tumours in the mouse. *PLoS One* 12:e0176693. doi: 10.1371/journal.pone.0176693
29. Leu K, Ott GA, Lai A, Nghiemphu PL, Pope WB, Yong WH, Liao LM, Cloughesy TF, Ellingson BM (2017) Perfusion and diffusion MRI signatures in histologic and genetic subtypes of WHO grade II–III diffuse gliomas. *J Neurooncol*. doi: 10.1007/s11060-017-2506-9
30. Salerno M, Sharif B, Arheden H, Kumar A, Axel L, Li D, Neubauer S (2017) Recent Advances in Cardiovascular Magnetic Resonance. *Circ Cardiovasc Imaging* 10:e003951. doi: 10.1161/CIRCIMAGING.116.003951

31. Christen T, Lemasson B, Pannetier N, Farion R, Segebarth C, Remy C, Barbier EL (2010) Evaluation of a quantitative blood oxygenation level-dependent (qBOLD) approach to map local blood oxygen saturation. *NMR Biomed* 24:n/a-n/a. doi: 10.1002/nbm.1603
32. Christen T, Bouzat P, Pannetier N, Coquery N, Moisan A, Lemasson B, Thomas S, Grillon E, Detante O, Remy C, Payen J-F, Barbier EL (2014) Tissue Oxygen Saturation Mapping with Magnetic Resonance Imaging. *J Cereb Blood Flow Metab* 34:1550–1557. doi: 10.1038/jcbfm.2014.116
33. An H, Lin W (2000) Quantitative Measurements of Cerebral Blood Oxygen Saturation Using Magnetic Resonance Imaging. *J Cereb Blood Flow Metab* 20:1225–1236. doi: 10.1097/00004647-200008000-00008
34. He X, Yablonskiy DA (2007) Quantitative BOLD: Mapping of human cerebral deoxygenated blood volume and oxygen extraction fraction: Default state. *Magn Reson Med* 57:115–126. doi: 10.1002/mrm.21108
35. Frackowiak RS, Lenzi GL, Jones T, Heather JD (1980) Quantitative measurement of regional cerebral blood flow and oxygen metabolism in man using ^{15}O and positron emission tomography: theory, procedure, and normal values. *J Comput Assist Tomogr* 4:727–36.
36. Goyal S, Kataria T (2014) Image guidance in radiation therapy: techniques and applications. *Radiol Res Pract* 2014:705604. doi: 10.1155/2014/705604
37. Jaffray DA (2012) Image-guided radiotherapy: from current concept to future perspectives. *Nat Rev Clin Oncol* 9:688–699. doi: 10.1038/nrclinonc.2012.194
38. Metcalfe P, Liney GP, Holloway L, Walker A, Barton M, Delaney GP, Vinod S, Tome W (2013) The potential for an enhanced role for MRI in radiation-therapy treatment planning. *Technol Cancer Res Treat* 12:429–46. doi: 10.7785/tcrt.2012.500342
39. Musunuru H, Rosenberg S, Bayouth J, Mitteur K, Ritter M, Paliwal B, Witek M, Baschnagel A, Uboha N, Lubner S, Loconte N, Harari P, Bassetti M (2017) PV-0322 Rapid Early Response of Gastroesophageal Junction Tumors During Real-time MRI-Guided Radiotherapy. In: *Int. J.*

- Radiat. Oncol. <https://cld.bz/bookdata/19T1ww/basic-html/page-180.html>. Accessed 30 Jun 2017
40. Bruynzeel A, Lagerwaard F, Bohoudi O, Tetar S, Haasbeek N, Oei SS, Slotman B, Meijerink M, Senan S, Palacios M (2017) OC-0425 Clinical experience with stereotactic MR- guided adaptive radiation therapy for pancreatic tumors. <https://cld.bz/bookdata/19T1ww/basic-html/page-235.html>. Accessed 30 Jun 2017
 41. Edmund JM, Nyholm T (2017) A review of substitute CT generation for MRI-only radiation therapy. *Radiat Oncol* 12:28. doi: 10.1186/s13014-016-0747-y
 42. Kim J, Glide-Hurst C, Doemer A, Wen N, Movsas B, Chetty IJ (2015) Implementation of a Novel Algorithm For Generating Synthetic CT Images From Magnetic Resonance Imaging Data Sets for Prostate Cancer Radiation Therapy. *Int J Radiat Oncol* 91:39–47. doi: 10.1016/j.ijrobp.2014.09.015
 43. Kim J, Garbarino K, Schultz L, Levin K, Movsas B, Siddiqui MS, Chetty IJ, Glide-Hurst C (2015) Dosimetric evaluation of synthetic CT relative to bulk density assignment-based magnetic resonance-only approaches for prostate radiotherapy. *Radiat Oncol* 10:239. doi: 10.1186/s13014-015-0549-7
 44. Koivula L, Wee L, Korhonen J (2016) Feasibility of MRI-only treatment planning for proton therapy in brain and prostate cancers: Dose calculation accuracy in substitute CT images. *Med Phys* 43:4634–4642. doi: 10.1118/1.4958677
 45. Korhonen J, Kapanen M, Keyriläinen J, Seppälä T, Tenhunen M (2013) A dual model HU conversion from MRI intensity values within and outside of bone segment for MRI-based radiotherapy treatment planning of prostate cancer. *Med Phys* 41:11704. doi: 10.1118/1.4842575
 46. Demol B, Boydev C, Korhonen J, Reynaert N (2016) Dosimetric characterization of MRI-only treatment planning for brain tumors in atlas-based pseudo-CT images generated from standard T 1-weighted MR images. *Med Phys* 43:6557–6568. doi: 10.1118/1.4967480

47. Kapanen M, Tenhunen M (2013) T1/T2*-weighted MRI provides clinically relevant pseudo-CT density data for the pelvic bones in MRI-only based radiotherapy treatment planning. *Acta Oncol (Madr)* 52:612–618. doi: 10.3109/0284186X.2012.692883
48. Dowling JA, Lambert J, Parker J, Salvado O, Fripp J, Capp A, Wratten C, Denham JW, Greer PB (2012) An Atlas-Based Electron Density Mapping Method for Magnetic Resonance Imaging (MRI)-Alone Treatment Planning and Adaptive MRI-Based Prostate Radiation Therapy. *Int J Radiat Oncol* 83:e5–e11. doi: 10.1016/j.ijrobp.2011.11.056
49. Guerreiro F, Burgos N, Dunlop A, Wong K, Petkar I, Nutting C, Harrington K, Bhide S, Newbold K, Dearnaley D, deSouza NM, Morgan VA, McClelland J, Nill S, Cardoso MJ, Ourselin S, Oelfke U, Knopf AC (2017) Evaluation of a multi-atlas CT synthesis approach for MRI-only radiotherapy treatment planning. *Phys Medica* 35:7–17. doi: 10.1016/j.ejmp.2017.02.017
50. Uh J, Merchant TE, Li Y, Li X, Hua C (2014) MRI-based treatment planning with pseudo CT generated through atlas registration. *Med Phys* 41:51711. doi: 10.1118/1.4873315
51. van Heijst TCF, den Hartogh MD, Lagendijk JJW, van den Bongard HJGD, van Asselen B (2013) MR-guided breast radiotherapy: feasibility and magnetic-field impact on skin dose. *Phys Med Biol* 58:5917–5930. doi: 10.1088/0031-9155/58/17/5917
52. van Zijp HM, van Asselen B, Wolthaus JWH, Kok JMG, de Vries JHW, Ishakoglu K, Beld E, Lagendijk JJW, Raaymakers BW (2016) Minimizing the magnetic field effect in MR-linac specific QA-tests: the use of electron dense materials. *Phys Med Biol* 61:N50–N59. doi: 10.1088/0031-9155/61/3/N50
53. Chen X, Prior P, Chen G-P, Schultz CJ, Li XA (2016) Technical Note: Dose effects of 1.5 T transverse magnetic field on tissue interfaces in MRI-guided radiotherapy. *Med Phys* 43:4797–4802. doi: 10.1118/1.4959534
54. Hackett SL, van Asselen B, Wolthaus JWH, Kok JGM, Woodings SJ, Lagendijk JJW, Raaymakers BW (2016) Consequences of air around an ionization chamber: Are existing solid

- phantoms suitable for reference dosimetry on an MR-linac? *Med Phys* 43:3961–3968. doi: 10.1118/1.4952727
55. O'Brien DJ, Roberts DA, Ibbott GS, Sawakuchi GO (2016) Reference dosimetry in magnetic fields: formalism and ionization chamber correction factors. *Med Phys* 43:4915–4927. doi: 10.1118/1.4959785
 56. Raaijmakers AJE, Raaymakers BW, Lagendijk JJW (2005) Integrating a MRI scanner with a 6 MV radiotherapy accelerator: dose increase at tissue–air interfaces in a lateral magnetic field due to returning electrons. *Phys Med Biol* 50:1363–1376. doi: 10.1088/0031-9155/50/7/002
 57. Raaijmakers AJE, Raaymakers BW, Lagendijk JJW (2008) Magnetic-field-induced dose effects in MR-guided radiotherapy systems: dependence on the magnetic field strength. *Phys Med Biol* 53:909–23. doi: 10.1088/0031-9155/53/4/006
 58. Smit K, van Asselen B, Kok JGM, Aalbers AHL, Lagendijk JJW, Raaymakers BW (2013) Towards reference dosimetry for the MR-linac: magnetic field correction of the ionization chamber reading. *Phys Med Biol* 58:5945–5957. doi: 10.1088/0031-9155/58/17/5945
 59. Houweling AC, de Vries JHW, Wolthaus J, Woodings S, Kok JGM, van Asselen B, Smit K, Bel A, Lagendijk JJW, Raaymakers BW (2016) Performance of a cylindrical diode array for use in a 1.5 T MR-linac. *Phys Med Biol* 61:N80-9. doi: 10.1088/0031-9155/61/3/N80
 60. Fricke H, Morse S (1927) The chemical action of Roentgen rays on dilute ferrous sulfate solutions as a measure of radiation dose. *J Roentgenol Radium Ther Nucl Med* 18:430–2.
 61. Fricke H, Morse S (1929) The action of X-rays on ferrous sulphate solutions. London, Edinburgh, Dublin *Philos Mag J Sci* 7:129–141. doi: 10.1080/14786440108564721
 62. Dobson G, Hughes G (1961) Effect of ferric ion on the gamma-ray induced oxidation of ferrous ion. *Trans Faraday Soc* 57:1117. doi: 10.1039/tf9615701117
 63. Schreiner LJ (2004) Review of Fricke gel dosimeters. *J Phys Conf Ser* 3:9–21. doi: 10.1088/1742-6596/3/1/003
 64. Van Vleck JH (1965) The theory of electric and magnetic susceptibilities. Oxford University

Press

65. Doran SJ (2009) The history and principles of chemical dosimetry for 3-D radiation fields: Gels, polymers and plastics. *Appl Radiat Isot* 67:393–398. doi: 10.1016/j.apradiso.2008.06.026
66. Watanabe Y, Warmington L, Gopishankar N (2017) Three-dimensional radiation dosimetry using polymer gel and solid radiochromic polymer: From basics to clinical applications. *World J Radiol* 9:112. doi: 10.4329/wjr.v9.i3.112
67. Oldham M (2015) Radiochromic 3D Detectors. *J Phys Conf Ser* 573:12006. doi: 10.1088/1742-6596/573/1/012006
68. Jordan K (2010) Review of recent advances in radiochromic materials for 3D dosimetry. *J Phys Conf Ser* 250:12043. doi: 10.1088/1742-6596/250/1/012043
69. Welch M, Foltz WD, Jaffray DA (2015) Timing considerations for preclinical MRgRT: effects of ion diffusion, SNR and imaging times on FXG gel calibration. *J Phys Conf Ser* 573:12045. doi: 10.1088/1742-6596/573/1/012045
70. Bloembergen N, Morgan LO (1961) Proton Relaxation Times in Paramagnetic Solutions. Effects of Electron Spin Relaxation. *J Chem Phys* 34:842–850. doi: 10.1063/1.1731684
71. Bloembergen N (1957) Proton Relaxation Times in Paramagnetic Solutions. *J Chem Phys* 27:572–573. doi: 10.1063/1.1743771
72. Solomon I (1955) Relaxation Processes in a System of Two Spins. *Phys Rev* 99:559–565. doi: 10.1103/PhysRev.99.559
73. Kruk D, Kowalewski J (2009) General treatment of paramagnetic relaxation enhancement associated with translational diffusion. *J Chem Phys*. doi: 10.1063/1.3119635
74. Bertini I, Galas O, Luchinat C, Parigi G (1995) A Computer Program for the Calculation of Paramagnetic Enhancements of Nuclear-Relaxation Rates in Slowly Rotating Systems. *J Magn Reson Ser A* 113:151–158. doi: 10.1006/jmra.1995.1074
75. Kowalewski J, Luchinat C, Nilsson T, Parigi G Nuclear Spin Relaxation in Paramagnetic Systems: Electron Spin Relaxation Effects under Near-Redfield Limit Conditions and Beyond.

doi: 10.1021/jp020608p

76. Lipari G, Szabo A (2002) Model-free approach to the interpretation of nuclear magnetic resonance relaxation in macromolecules. 2. Analysis of experimental results. doi: 10.1021/JA00381A010
77. Lipari G, Szabo A (1982) Model-free approach to the interpretation of nuclear magnetic resonance relaxation in macromolecules. 1. Theory and range of validity. *J Am Chem Soc* 104:4546–4559. doi: 10.1021/ja00381a009
78. Podgorsak MB, Schreiner LJ (1992) Nuclear magnetic relaxation characterization of irradiated Fricke solution. *Med Phys* 19:87–95. doi: 10.1118/1.596901
79. Audet C, Schreiner LJ (1997) Multiple-site fast exchange model for spin-lattice relaxation in the Fricke-gelatin dosimeter. *Med Phys* 24:201–209. doi: 10.1118/1.597926
80. MacDougall ND, Pitchford WG, Smith MA (2002) A systematic review of the precision and accuracy of dose measurements in photon radiotherapy using polymer and Fricke MRI gel dosimetry. *Phys Med Biol* 47:R107-21.
81. Schulz RJ, deGuzman AF, Nguyen DB, Gore JC (1990) Dose-response curves for Fricke-infused agarose gels as obtained by nuclear magnetic resonance. *Phys Med Biol* 35:1611–22.
82. Luciani AM, Di Capua S, Guidoni L, Ragona R, Rosi A, Viti V (1996) Multiexponential T2 relaxation in Fricke agarose gels: implications for NMR dosimetry. *Phys Med Biol* 41:509–21.
83. Abe M, Ohnishi K, Kan C, Ishikawa O (2003) Ultraviolet-B phototherapy is successful in Japanese patients with early-stage mycosis fungoides. *J Dermatol* 30:789–96.
84. Cheng KL (1959) Analytical application of xylenol orange-IV: a spectrophotometric study of the ferric xylenol orange complex. 3:147–150.
85. Schreiner LJ (2015) True 3D chemical dosimetry (gels, plastics): Development and clinical role. *J Phys Conf Ser* 573:12003. doi: 10.1088/1742-6596/573/1/012003
86. Deene Y De (2004) Essential characteristics of polymer gel dosimeters. *J Phys Conf Ser* 3:34–57. doi: 10.1088/1742-6596/3/1/006

87. De Deene Y (2002) Gel dosimetry for the dose verification of intensity modulated radiotherapy treatments. *Z Med Phys* 12:77–88.
88. Baldock C, De Deene Y, Doran S, Ibbott G, Jirasek A, Lepage M, McAuley KB, Oldham M, Schreiner LJ (2010) Polymer gel dosimetry. *Phys Med Biol* 55:R1-63. doi: 10.1088/0031-9155/55/5/R01
89. Ibbott GS, Maryanski MJ, Eastman P, Holcomb SD, Zhang Y, Avison RG, Sanders M, Gore JC (1997) Three-dimensional visualization and measurement of conformal dose distributions using magnetic resonance imaging of BANG polymer gel dosimeters. *Int J Radiat Oncol Biol Phys* 38:1097–103.
90. Sellakumar P, Samuel EJJ, Kumar DS (2010) Dose-rate dependence of PAGAT polymer gel dosimeter evaluated using X-ray CT scanner. *J Phys Conf Ser* 250:12074. doi: 10.1088/1742-6596/250/1/012074
91. Novotny J, Spevacek V, Dvorak P, Novotny J, Cechak T (2001) Energy and dose rate dependence of BANG-2 polymer-gel dosimeter. *Med Phys* 28:2379–2386. doi: 10.1118/1.1414307
92. Adinehvand K, Zahmatkesh MH, Aghamiri M., Akhlaghpour S, Bagheri S (2008) Verification of dose rate and energy dependence of MAGICA polymer gel dosimeter with electron beams. *Int J Radiat Res* 6:31–36.
93. Azadbakht B, Hadad K, Zahmatkesh MH (2009) Response verification of dose rate and time dependence of PAGAT polymer gel dosimeters by photon beams using magnetic resonance imaging. *J Phys Conf Ser* 164:12036. doi: 10.1088/1742-6596/164/1/012036
94. Roed Y, Tailor R, Pinsky L, Ibbott G (2014) SU-F-BRE-15: Verification of Energy Dependence of MAGAT Polymer Gel at Orthovoltage Energies. *Med Phys* 41:394–394. doi: 10.1118/1.4889053
95. Roed Y, Tailor R, Pinsky L, Ibbott G (2015) SU-E-T-716: Suitability Study of a Unique 3D Dosimeter for Commissioning Radiation Treatment Machines. *Med Phys* 42:3501–3501. doi:

10.1118/1.4925080

96. Adamovics J, Maryanski M (2003) New 3D radiochromic solid polymer dosimeter from leuco dyes and a transparent polymeric matrix. *Med. Phys.*
97. Adamovics J, Maryanski MJ (2004) A new approach to radiochromic three-dimensional dosimetry-polyurethane. *J Phys Conf Ser* 3:172–175. doi: 10.1088/1742-6596/3/1/020
98. Adamovics J, Guo P, Burgess D, Manzoor A, Oldham M (2006) PRESAGE™ - Development and optimization studies of a 3D radiochromic plastic dosimeter–Part 2. *J Phys Conf Ser* 56:176–178. doi: 10.1088/1742-6596/56/1/021
99. Adamovics J, Jordan K, Dietrich J (2006) PRESAGE™ - Development and optimization studies of a 3D radiochromic plastic dosimeter–Part 1. *J Phys Conf Ser* 56:172–175. doi: 10.1088/1742-6596/56/1/020
100. Alqathami M, Blencowe A, Qiao G, Butler D, Geso M (2012) Optimization of the sensitivity and stability of the PRESAGE™ dosimeter using trihalomethane radical initiators. *Radiat Phys Chem* 81:867–873. doi: 10.1016/j.radphyschem.2012.03.022
101. Gore JC, Ranade M, Maryański MJ, Schulz RJ (1996) Radiation dose distributions in three dimensions from tomographic optical density scanning of polymer gels: I. Development of an optical scanner. *Phys Med Biol* 41:2695–704.
102. Maryański MJ, Zastavker YZ, Gore JC (1996) Radiation dose distributions in three dimensions from tomographic optical density scanning of polymer gels: II. Optical properties of the BANG polymer gel. *Phys Med Biol* 41:2705–17.
103. Oldham M, Siewerdsen JH, Kumar S, Wong J, Jaffray DA (2003) Optical-CT gel-dosimetry I: Basic investigations. *Med Phys* 30:623–634. doi: 10.1118/1.1559835
104. Oldham M, Kim L (2004) Optical-CT gel-dosimetry. II: Optical artifacts and geometrical distortion. *Med Phys* 31:1093–104. doi: 10.1118/1.1655710
105. Xu Y, Wu C-S, Maryanski MJ (2004) Performance of a commercial optical CT scanner and polymer gel dosimeters for 3-D dose verification. *Med Phys* 31:3024–3033. doi:

10.1118/1.1803674

106. Islam KTS, Dempsey JF, Ranade MK, Maryanski MJ, Low DA (2003) Initial evaluation of commercial optical CT-based 3D gel dosimeter. *Med Phys* 30:2159–2168. doi: 10.1118/1.1593636
107. Xu Y, Wu C-S, Maryanski MJ (2010) Sensitivity calibration procedures in optical-CT scanning of BANG[®] 3 polymer gel dosimeters. *Med Phys* 37:861–868. doi: 10.1118/1.3298017
108. Rankine LJ, Mein S, Cai B, Curcuru A, Juang T, Miles D, Mutic S, Wang Y, Oldham M, Li HH (2017) Three-Dimensional Dosimetric Validation of a Magnetic Resonance Guided Intensity Modulated Radiation Therapy System. *Int J Radiat Oncol* 97:1095–1104. doi: 10.1016/j.ijrobp.2017.01.223
109. Mein S, Rankine L, Miles D, Juang T, Cai B, Curcuru A, Mutic S, Fenoli J, Adamovics J, Li H, Oldham M (2017) How feasible is remote 3D dosimetry for MR guided Radiation Therapy (MRgRT)? *J Phys Conf Ser* 847:12056. doi: 10.1088/1742-6596/847/1/012056
110. Mein S, Stewart (2013) MRI-Guided Radiation Therapy: Investigating the Accuracy of Treatment Delivery.
111. Lee HJ, Alqathami M, Kadbi M, Wang J, Blencowe A, Ibbott GS (2016) Feasibility of Using 3-Dimensional (3D) Radiochromic Dosimeters for Real-Time 2-Dimensional and 3D Dose Distribution Measurements in Magnetic Resonance–Guided Radiation Therapy. *Int J Radiat Oncol* 96:E631. doi: 10.1016/j.ijrobp.2016.06.2208
112. Lee HJ, Alqathami M, Wang J, Blencowe A, Ibbott G (2016) PO-0800: Fricke-type dosimetry for “real-time” 3D dose measurements using MR-guided RT: a feasibility study. *Radiother Oncol* 119:S377–S378. doi: 10.1016/S0167-8140(16)32050-3
113. Lee H, Alqathami M, Kadbi M, Wang J, Blencowe A, Ibbott G (2016) SU-G-JeP2-04: Comparison Between Fricke-Type 3D Radiochromic Dosimeters for Real-Time Dose Distribution Measurements in MR-Guided Radiation Therapy. *Med Phys* 43:3660–3660. doi: 10.1118/1.4957024

114. Lee H, Alqathami M, Kadbi M, Wang J, Blencowe A, Ibbott G (2016) TH-CD-BRA-08: Novel Iron-Based Radiation Reporting Systems as 4D Dosimeters for MR-Guided Radiation Therapy. *Med Phys* 43:3874–3875. doi: 10.1118/1.4958151
115. Choi GW, Lee H, Alqathami M, Ibbott G (2016) TH-AB-BRA-11: Using 3D Dosimeters for the Investigation of the Electron Return Effect (ERE) in MR-Guided Radiation Therapy: A Feasibility Study. *Med Phys* 43:3856–3856. doi: 10.1118/1.4958062
116. Choi GW (2016) Measurement of the Electron Return Effect Using PRESAGE Dosimeter. UT GSBS Diss. Theses (Open Access)
117. Ibbott GS, Roed Y, Lee H, Alqathami M, Wang J, Pinsky L, Blencowe A (2016) Gel dosimetry enables volumetric evaluation of dose distributions from an MR-guided linac. *AIP Conf Proc.* doi: 10.1063/1.4954102
118. Lee H J, Roed Y, Venkataraman S, Carroll M, Ibbott G (2017) OC-0258 Investigation of magnetic field effects on 3D dosimeters for MR-IGRT applications. In: *Int. J. Radiat. Oncol.* <https://cld.bz/bookdata/19T1ww/basic-html/page-143.html>. Accessed 30 Jun 2017
119. Lee H, Bosco G, Kadbi M, Ibbott G (2017) Use of 3D Gels for Determining MR and Radiation Isocenters in MR-Guided Radiation Therapy. <http://www.aapm.org/meetings/2017AM/PRAbs.asp?mid=127&aid=37534>. Accessed 23 Jul 2017
120. Lee HJ, Choi GW, Alqathami M, Kadbi M, Ibbott G (2017) Using 3D dosimetry to quantify the Electron Return Effect (ERE) for MR-image-guided radiation therapy (MR-IGRT) applications. *J Phys Conf Ser* 847:12057. doi: 10.1088/1742-6596/847/1/012057
121. Mein S, Rankine L, Adamovics J, Li H, Oldham M (2016) TH-CD-BRA-11: Implementation and Evaluation of a New 3D Dosimetry Protocol for Validating MRI Guided Radiation Therapy Treatments. *Med Phys* 43:3875–3876. doi: 10.1118/1.4958154
122. Roed Y, Wang J, Pinsky L, Ibbott G (2016) EP-1513: Polymer gels enable volumetric dosimetry of dose distributions from an MR-guided linac. *Radiother Oncol* 119:S699–S700. doi:

- 10.1016/S0167-8140(16)32763-3
123. Roed Y, Ding Y, Wen Z, Wang J, Pinsky L, Ibbott G (2017) The potential of polymer gel dosimeters for 3D MR-IGRT quality assurance. *J Phys Conf Ser* 847:12059. doi: 10.1088/1742-6596/847/1/012059
 124. Roed Y, Kadbi M, Wang J, Pinsky L, Ibbott G (2016) SU-G-JeP2-11: Polymer Gels as 3D QA Devices in Magnetic Resonance-Guided Radiation Therapy. *Med Phys* 43:3661–3662. doi: 10.1118/1.4957031
 125. Zhang L, Du D, Green O, Rodriguez V, Wooten H, Xiao Z, Yang D, Hu Y, Li H (2014) TU-C-BRE-04: 3D Gel Dosimetry Using ViewRay On-Board MR Scanner: A Feasibility Study. *Med Phys* 41:455–455. doi: 10.1118/1.4889267
 126. Zhang L, Hu Y, Du D, Green OL, Wooten HO, Li HH (2015) Three-dimensional polymer gel dosimetry using an onboard 0.35 T magnetic resonance imaging scanner: A simulation study. *J Med Phys* 40:176–80. doi: 10.4103/0971-6203.165081
 127. Andreo P, Burns DT, Hohlfeld K, Huq MS, Kanai T, Laitano F, Smyth VG, Vynckier S (2006) IAEA TRS-398 Absorbed Dose Determination in External Beam Radiotherapy: An International Code of Practice for Dosimetry based on Standards of Absorbed Dose to Water.
 128. McKenzie AL (1996) Cobalt-60 gamma-ray beams. *BJR Suppl* 25:46–61.
 129. Solc J, Špeváček V (2009) New radiochromic gel for 3D dosimetry based on Turnbull blue: basic properties. *Phys Med Biol* 54:5095–107. doi: 10.1088/0031-9155/54/17/002
 130. Šolc J, Špeváček V (2009) New 3D radiochromic gel dosimeters with inhibited diffusion. *J Phys Conf Ser* 164:12047. doi: 10.1088/1742-6596/164/1/012047
 131. Lawrence GD, Fishelson S (1999) Blueprint Photography by the Cyanotype Process. *J Chem Educ* 76:1216A. doi: 10.1021/ed076p1216A
 132. Dusan C, Stulik C, Kaplan A (2013) The Atlas of Analytical Signatures of Photographic Processes. J. Paul Getty Trust
 133. Hansen LD, Litchman WM, Daub GH (1969) Turnbull's blue and Prussian blue:

- KFe(III)[Fe(II)(CN)₆]. J Chem Educ 46:46. doi: 10.1021/ed046p46
134. Kozubikova P, Solc J, Novotny J, Pilarova K, Pipek J, Koncekova J (2015) Assessment of radiochromic gel dosimeter based on Turnbull Blue dye for relative output factor measurements of the Leksell Gamma Knife[®] Perfexion[™]. J Phys Conf Ser 573:12049. doi: 10.1088/1742-6596/573/1/012049
 135. Šolc J, Sochor V, Kozubíková P (2015) Energy dependence of Fricke-xylene orange gel and gel based on Turnbull blue for low-energy photons. J Phys Conf Ser 573:12069. doi: 10.1088/1742-6596/573/1/012069
 136. Alqathami M, Blencowe A, Ibbott G (2016) Experimental determination of the influence of oxygen on the PRESAGE[®] dosimeter. Phys Med Biol 61:813–824. doi: 10.1088/0031-9155/61/2/813
 137. Davies JB, Baldock C (2008) Sensitivity and stability of the Fricke–gelatin–xylene orange gel dosimeter. Radiat Phys Chem 77:690–696. doi: 10.1016/j.radphyschem.2008.01.007
 138. Smith CW (1996) Orthovoltage X-ray beams (0.5 mm–4.0 mm Cu HVL). BJR Suppl 25:24–38.
 139. Brown S, Venning A, De Deene Y, Vial P, Oliver L, Adamovics J, Baldock C (2008) Radiological properties of the PRESAGE and PAGAT polymer dosimeters. Appl Radiat Isot 66:1970–4. doi: 10.1016/j.apradiso.2008.06.005
 140. Venning AJ, Nitschke KN, Keall PJ, Baldock C (2005) Radiological properties of normoxic polymer gel dosimeters. Med Phys 32:1047–1053. doi: 10.1118/1.1881812
 141. Keall P, Baldock C (1999) A theoretical study of the radiological properties and water equivalence of Fricke and polymer gels used for radiation dosimetry. Australas Phys Eng Sci Med 22:85–91.
 142. Berger MJ, Coursey JS, Zucker MA, Chang J (1998) Stopping-Power & Range Tables for Electrons, Protons, and Helium Ions. Radiat. Phys. Div. PML, NIST NISTIR 499:
 143. Hubbell JH, Seltzer SM (1996) X-Ray Mass Attenuation Coefficients. Radiat. Phys. Div. PML, NIST NISTIR 5632:

144. Seltzer SM (1993) Calculation of Photon Mass Energy-Transfer and Mass Energy-Absorption Coefficients. *Radiat Res* 136:147. doi: 10.2307/3578607
145. Morgan B, Lahav O (2007) The effect of pH on the kinetics of spontaneous Fe(II) oxidation by O₂ in aqueous solution – basic principles and a simple heuristic description. *Chemosphere* 68:2080–2084. doi: 10.1016/j.chemosphere.2007.02.015
146. Selwood PW (1905-1986). (2015) *Magnetochemistry*. Swinburne Press
147. Bero MA, Gilboy WB, Glover PM, El-masri HM (2000) Tissue-equivalent gel for non-invasive spatial radiation dose measurements. *Nucl Instruments Methods Phys Res Sect B Beam Interact with Mater Atoms* 166–167:820–825. doi: 10.1016/S0168-583X(99)00873-3
148. Lafratta R, Ibbott G, Adamovics J, Followill D, al BC et, al AJ et, al PLC et, al WM et, al MA et, al TA et, al DJO et (2015) Comparison of 2D and 3D Gamma calculations for an IMRT QA phantom. *J Phys Conf Ser* 573:12055. doi: 10.1088/1742-6596/573/1/012055
149. Mathis M, Sawakuchi G, Flint D, Tailor R, Beddar S, Ibbott G, Wen Z (2014) Effects of a strong magnetic field on selected radiation dosimeters (TLD, OSLD, EBT3 film, PRESAGE). 2014 Comb Sci Meet 1–8. doi: 10.1594/RANZCR2014/R-0175
150. Mathis M, Wen Z, Tailor R, Sawakuchi G, Flint D, Beddar S, Ibbott G (2014) SU-E-T-368: Effect of a Strong Magnetic Field On Select Radiation Dosimeters. *Med Phys* 41:309–309. doi: 10.1118/1.4888701
151. Smit K, Kok JGM, Lagendijk JJW, Raaymakers BW (2014) Performance of a multi-axis ionization chamber array in a 1.5 T magnetic field. *Phys Med Biol* 59:1845–1855. doi: 10.1088/0031-9155/59/7/1845
152. Reynolds M, Fallone BG, Rathee S (2015) Technical Note: Response measurement for select radiation detectors in magnetic fields. *Med Phys* 42:2837–2840. doi: 10.1118/1.4919681
153. Smit K (2015) Dosimetry for the MR-linac. 1–139.
154. Reynoso FJ, Curcuru A, Green O, Mutic S, Das IJ, Santanam L (2016) Technical Note: Magnetic field effects on Gafchromic-film response in MR-IGRT. *Med Phys* 43:6552–6556.

doi: 10.1118/1.4967486

155. Wen Z, Wang J, Jiang W, O'Brien D, Sawakuchi G, Ibbott G (2016) SU-G-BRB-08: Investigation On the Magnetic Field Effect On TLDs, OSLDs, and Gafchromic Films Using An MR-Linac. *Med Phys* 43:3632–3632. doi: 10.1118/1.4956915
156. Therriault-Proulx F, Wen Z, Ibbott G, Beddar S (2016) TH-CD-BRA-12: Impact of a Magnetic Field On the Response From a Plastic Scintillation Detector. *Med Phys* 43:3876–3876. doi: 10.1118/1.4958155
157. Wen Z, Therriault-Proulx F, Owens C, Ibbott G, Beddar S (2016) SU-F-J-50: Study On the Magnetic Field Effect On the Exradin W1 Plastic Scintillation Detector. *Med Phys* 43:3417–3417. doi: 10.1118/1.4955958
158. Stefanowicz S, Latzel H, Lindvold LR, Andersen CE, Jäkel O, Greilich S (2013) Dosimetry in clinical static magnetic fields using plastic scintillation detectors. *Radiat Meas* 56:357–360. doi: 10.1016/j.radmeas.2013.03.012
159. Vandecasteele J, Deene Y De (2013) Polymer gel dosimetry of an electron beam in the presence of a magnetic field. *J Phys Conf Ser* 444:12104. doi: 10.1088/1742-6596/444/1/012104
160. Raaijmakers BW, Raaijmakers AJE, Kotte ANTJ, Jette D, Lagendijk JJW (2004) Integrating a MRI scanner with a 6 MV radiotherapy accelerator: dose deposition in a transverse magnetic field. *Phys Med Biol* 49:4109–4118. doi: 10.1088/0031-9155/49/17/019
161. O'Brien DJ, Sawakuchi GO (2017) Monte Carlo study of the chamber-phantom air gap effect in a magnetic field. *Med Phys*. doi: 10.1002/mp.12290
162. Green OP, Goddu S, Mutic S (2012) SU-E-T-352: Commissioning and Quality Assurance of the First Commercial Hybrid MRI-IMRT System. *Med Phys* 39:3785–3785. doi: 10.1118/1.4735439
163. Ellefson ST, Culbertson WS, Bednarz BP, DeWerd LA, Bayouth JE (2017) An analysis of the ArcCHECK-MR diode array's performance for ViewRay quality assurance. *J Appl Clin Med Phys* 18:161–171. doi: 10.1002/acm2.12107

164. Li HH, Rodriguez VL, Green OL, Hu Y, Kashani R, Wooten HO, Yang D, Mutic S (2015) Patient-Specific Quality Assurance for the Delivery of ^{60}Co Intensity Modulated Radiation Therapy Subject to a 0.35-T Lateral Magnetic Field. *Int J Radiat Oncol* 91:65–72. doi: 10.1016/j.ijrobp.2014.09.008
165. Steinmann A, Followill D Characterizing tissue equivalent materials used for an end-to-end QA phantom for MR-guided RT. doi: 10.3252/pso.eu.ESTRO36.2017
166. Steinmann A, Stafford R, Yung J, Followill D (2015) SU-E-J-210: Characterizing Tissue Equivalent Materials for the Development of a Dual MRI-CT Heterogeneous Anthropomorphic Phantom Designed Specifically for MRI Guided Radiotherapy Systems. *Med Phys* 42:3313–3314. doi: 10.1118/1.4924296
167. Fedorov A, Beichel R, Kalpathy-Cramer J, Finet J, Fillion-Robin J-C, Pujol S, Bauer C, Jennings D, Fennessy F, Sonka M, Buatti J, Aylward S, Miller J V, Pieper S, Kikinis R (2012) 3D Slicer as an image computing platform for the Quantitative Imaging Network. *Magn Reson Imaging* 30:1323–41. doi: 10.1016/j.mri.2012.05.001
168. 3D Slicer. <https://www.slicer.org/>. Accessed 22 Jul 2017
169. Pinter C, Lasso A, Wang A, Jaffray D, Fichtinger G (2012) SlicerRT: Radiation therapy research toolkit for 3D Slicer. *Med Phys* 39:6332–6338. doi: 10.1118/1.4754659
170. Low DA, Harms WB, Mutic S, Purdy JA (1998) A technique for the quantitative evaluation of dose distributions. *Med Phys* 25:656–661. doi: 10.1118/1.598248
171. Ibbott GS, Followill DS, Molineu HA, Lowenstein JR, Alvarez PE, Roll JE (2008) Challenges in Credentialing Institutions and Participants in Advanced Technology Multi-institutional Clinical Trials. *Int J Radiat Oncol* 71:S71–S75. doi: 10.1016/j.ijrobp.2007.08.083
172. Hussein M, Clark CH, Nisbet A (2017) Challenges in calculation of the gamma index in radiotherapy – Towards good practice. *Phys Medica* 36:1–11. doi: 10.1016/j.ejmp.2017.03.001
173. Pulliam KB, Huang JY, Howell RM, Followill D, Bosca R, O'Daniel J, Kry SF (2014) Comparison of 2D and 3D gamma analyses. *Med Phys* 41:21710. doi: 10.1118/1.4860195

174. Ezzell GA, Burmeister JW, Dogan N, Losasso TJ, Mechalakos JG, Mihailidis D, Molineu A, Palta JR, Ramsey CR, Salter BJ, Shi J, Xia P, Yue NJ, Xiao Y (2009) IMRT commissioning: Multiple institution planning and dosimetry comparisons, a report from AAPM Task Group 119. *Med Phys*. doi: 10.1118/1.3238104
175. (2009) TG-119 IMRT Commissioning Tests Instructions for Planning, Measurement, and Analysis. *Med. Phys.*
176. Yin-Jiun Tseng, Woei-Chyn Chu, Sung-Cheng Huang Measurement of ferric ion diffusion coefficient in Fricke-infused agarose gel from MR image intensity changes. In: 2001 Conf. Proc. 23rd Annu. Int. Conf. IEEE Eng. Med. Biol. Soc. IEEE, pp 2303–2306
177. Marrale M, Brai M, Gagliardo C, Gallo S, Longo A, Tranchina L, Abbate B, Collura G, Gallias K, Caputo V, Lo Casto A, Midiri M, D’Errico F (2014) Correlation between ferrous ammonium sulfate concentration, sensitivity and stability of Fricke gel dosimeters exposed to clinical X-ray beams. *Nucl Instruments Methods Phys Res Sect B Beam Interact with Mater Atoms* 335:54–60. doi: 10.1016/j.nimb.2014.05.012
178. Nazir A, Afzal M, Buzdar SA (2010) Effects of variation of MRI parameters on signal homogeneity: a qualitative analysis for ferrous benzoic xylene orange gel. *J Pak Med Assoc* 60:470–3.
179. Galante AMS, Cervantes HJ, Cavinato CC, Campos LL, Rabbani SR (2008) MRI study of radiation effect on Fricke gel solutions. *Radiat Meas* 43:550–553. doi: 10.1016/j.radmeas.2007.12.011
180. Kron T, Jonas D, Pope JM (1997) Fast T1 imaging of dual gel samples for diffusion measurements in NMR dosimetry gels. *Magn Reson Imaging* 15:211–21.
181. Back SAJ, Author SA, Bflick J Implementation of MRI gel dosimetry in radiation therapy.
182. Houweling AC, de Vries JHW, Wolthaus J, Woodings S, Kok JGM, van Asselen B, Smit K, Bel A, Lagendijk JJW, Raaymakers BW (2016) Performance of a cylindrical diode array for use in a 1.5 T MR-linac. *Phys Med Biol* 61:N80–N89. doi: 10.1088/0031-9155/61/3/N80

183. Lee H, Alqathami M, Ibbott G (2017) UV versus MV irradiation response of 3D dosimeters. <https://conferences.iaea.org/indico/event/108/session/95/contribution/311>. Accessed 23 Jul 2017
184. Yeo UJ, Taylor ML, Supple JR, Smith RL, Kron T, Franich RD (2013) Deformable gel dosimetry II: experimental validation of DIR-based dose-warping. *J Phys Conf Ser* 444:12107. doi: 10.1088/1742-6596/444/1/012107
185. Yeo UJ, Taylor ML, Supple JR, Smith RL, Kron T, Franich RD (2013) Deformable gel dosimetry I: application to external beam radiotherapy and brachytherapy. *J Phys Conf Ser* 444:12032. doi: 10.1088/1742-6596/444/1/012032
186. Yeo UJ, Taylor ML, Dunn L, Kron T, Smith RL, Franich RD (2012) A novel methodology for 3D deformable dosimetry. *Med Phys* 39:2203–2213. doi: 10.1118/1.3694107
187. Cao Y, Tseng C-L, Balter JM, Teng F, Parmar HA, Sahgal A (2017) MR-guided radiation therapy: transformative technology and its role in the central nervous system. *Neuro Oncol* 19:ii16-ii29. doi: 10.1093/neuonc/nox006
188. Stemkens B, Glitzner M, Kontaxis C, de Senneville BD, Prins FM, Crijns SPM, Kerkmeijer LGW, Lagendijk JJW, Van den Berg CAT, Tijssen RHN (2017) Effect of intra-fraction motion on the accumulated dose for free-breathing MR-guided stereotactic body radiation therapy of renal-cell carcinoma. *Phys Med Biol*. doi: 10.1088/1361-6560/aa83f7
189. Zhao D, Hu Q, Qi L, Wang J, Wu H, Zhu G, Yu H (2017) Magnetic resonance (MR) imaging for tumor staging and definition of tumor volumes on radiation treatment planning in nonsmall cell lung cancer. *Medicine (Baltimore)* 96:e5943. doi: 10.1097/MD.0000000000005943
190. Bache ST, Juang T, Belley MD, Koontz BF, Adamovics J, Yoshizumi TT, Kirsch DG, Oldham M (2015) Investigating the accuracy of microstereotactic-body-radiotherapy utilizing anatomically accurate 3D printed rodent-morphic dosimeters. *Med Phys* 42:846–855. doi: 10.1118/1.4905489
191. Borges J, BenComo J, Ibbott G (2003) A 3 Dimensional Gel Dosimetry Lung Equivalent (WIP).

- Med Phys 30:1478. doi: 10.1118/1.1595296
192. De Deene Y, Vergote K, Claeys C, De Wagter C (2006) Three dimensional radiation dosimetry in lung-equivalent regions by use of a radiation sensitive gel foam: Proof of principle. Med Phys 33:2586–2597. doi: 10.1118/1.2208939
193. Carroll M, Lee H, Venkataraman S, Ibbott G (2017) Investigation of a PRESAGE Three-Dimensional Dosimetry Protocol That Allows for Internal Calibration. <http://www.aapm.org/meetings/2017AM/PRAbs.asp?mid=127&aid=38018>. Accessed 23 Jul 2017

VITA

Hannah Jungeun Lee was born in Manhattan, Kansas on June 25, 1990, the daughter of Young Ae Lee and Kwan Myung Lee. After completing her work at Parkway Central High School, Chesterfield, Missouri in 2008, she entered Washington University in St. Louis in St. Louis, Missouri. She received the degree of Bachelor of Arts, Magna Cum Laude, with double majors in physics and biology with a minor in psychology from Washington University in May, 2012. In August of 2012, she entered The University of Texas MD Anderson Cancer Center UTHHealth Graduate School of Biomedical Sciences.

Permanent address:

15711 Heathercroft Drive, Chesterfield, Missouri 63017, USA